Investigating CO_2 Capture in Ionic Liquids Using *in Situ* Synchrotron Techniques

University of Central Lancashire
UCLan

Jordan Cole

A thesis submitted in partial fulfilment for the requirements for the degree of Doctor of Philosophy at the University of Central Lancashire.

October 2023

RESEARCH STUDENT DECLARATION FORM

Type of Award   Doctor of Philosophy
School   Engineering and Computing

1.   **Concurrent registration for two or more academic awards**

> I declare that while registered as a candidate for the research degree, I have not been a registered candidate or enrolled student for another award of the University or other academic or professional institution.

2.   **Material submitted for another award**

> I declare that no material contained in the thesis has been used in any other submission for an academic award and is solely my own work.

3.   **Collaboration**

Where a candidate's research programme is part of a collaborative project, the thesis must indicate in addition clearly the candidate's individual contribution and the extent of the collaboration. Please state below:

_____

4.   **Use of a Proof-reader**

> No proof-reading service was used in the compilation of this thesis.

Signature of Candidate _____ _J Cole_ _____

Print name: _____ **Jordan Cole** _____

Abstract

This thesis details three *in situ* synchrotron studies probing the interactions of ionic liquid (IL) thin films with CO_2. ILs are liquid salts with bulky ions showing a wide range of interesting properties. An emerging class called superbasic ILs (SBILs) show great promise as alternatives to current carbon capture solvents. However, more fundamental studies delving into the molecular interactions of SBILs with CO_2 are required before they see widescale industrial use. In this work, interfacial interactions were probed using near-ambient pressure X-ray photoelectron spectroscopy (NAP-XPS) and near-edge X-ray absorption fine structure (NEXAFS) at synchrotron facilities. Experimental results were complemented by computational simulations carried out using density functional theory (DFT). The studies presented here aim to explore chemical and physical interactions at the IL/gas interface, examine the reordering of ions upon exposure to gas, and discover how CO_2 competes with other gases at different depths into IL thin films.

Thin films of the SBIL $[P_{66614}][benzim]$ were prepared on a rutile TiO_2 (110) surface and exposed to CO_2 at near-ambient pressures. SBILs show highly structured behaviour when deposited as thin films, and results indicate that reaction with CO_2 causes a reordering of IL molecules. $[benzim]^-$ anions orient $27° \pm 5°$ from the surface normal before exposure to CO_2 and approximately $54° \pm 4°$ from the surface normal when they react with CO_2. NAP-XPS shows evidence of irreversible CO_2 absorption and a greater concentration of CO_2-reacted anions in the deeper layers.

Thin films of the SBIL $[P_{66614}][124Triz]$ were deposited onto rutile TiO_2 (110) using *in situ* electrospray deposition (ESD). To the best of our knowledge, this is the largest IL to be successfully deposited via ESD. Depth profiling NAP-XPS reveals that competitive absorption between CO_2 and H_2O in $[P_{66614}][124Triz]$ varies with depth into the thin film. A greater concentration of CO_2 absorbs in the bulk layers, and does so reversibly, while more H_2O ad/absorbs at the surface reversibly. CO_2 that is ad/absorbed at the surface does so irreversibly.

Depth profiling NAP-XPS and NEXAFS measurements were carried out on an electrosprayed thin film of the SBIL $[P_{66614}][Tetz]$ upon exposure to CO_2, NO, and a CO_2 + NO mixture. The plane of the ring of the $[Tetz]^-$ anion orients $10° \pm 3°$ from the surface normal prior to exposure to gas, before reorienting to $37° \pm 2°$ and $64° \pm 2°$ from the surface normal upon exposure to NO and CO_2, respectively. This corroborates with the orientational behaviour of $[P_{66614}][benzim]$ upon exposure to CO_2. Irreversibly absorbed NO in the bulk layers of the $[P_{66614}][Tetz]$ thin film inhibits CO_2 absorption in these deeper layers. CO_2 was therefore only found to ad/absorb at the surface layers, but this reaction is reversible.

These results provide new insights into CO_2 absorption in SBILs by studying fundamental interactions at the liquid/gas interface, the reversibility of chemical reactions, and the reordering of ions. Understanding interfacial behaviour is an important step towards implementing ILs into gas capture applications. Results may also inform designs of IL-based technologies such as SCILL/SILP catalysts.

Table of Contents

Chapter 5. Near-Ambient Pressure XPS and NEXAFS Study of [P$_{66614}$][benzim] with CO$_2$ 95

Chapter 6. *In Situ* Depth Profiling Study of Competitive CO$_2$/H$_2$O Absorption in [P$_{66614}$][124Triz] 135

Acknowledgements

I would first and foremost like to thank my supervisor Karen for all of her help and guidance over the years. Thank you for your constant support and positivity, for all the mid-meeting hot chocolates, Danish cherry beers, impromptu yoga lessons, 90's music listening parties, and for helping me navigate chemistry labs like a real physicist. It's been so fun working with you! I would also like to thank my second supervisor Joe for his help and all of our career talks. I wish you all the best in your future STM'ing!

I send my gratitude to Tom and all of our collaborators at the University of Manchester and beyond who have aided in this work. A special thanks to Zoe who has always been so kind, funny and supportive over the years. Thanks to Eric and Kejian who joined us on our beamtime and had to endure the struggle of our noisy nitrogen scans. To Jack, thank you for all the meals in Denmark and for catching that eldritch horror of a massive wasp. I wish you all the best for the future!

Thank you to Tim for all your advice, stories, and laughs over my time in the basement. My best wishes go to the staff and students of the JHI, and to all past, present, and future Basement Dwellers. This leads me to thank my academic brothers Cal and Adam (V). I can't believe we met in first year undergraduate physics and are now submitting our PhD theses together! Thank you (and our rogue shadow Zak) for all of the amazing memories throughout our time at university. Thanks for all the lunchtime chess games, board games nights, "are people ravioli?"-esque debates, and especially all the blubbs and other made-up gubbins.

A final special thanks goes to my friends, family and loved ones. You have all been so supportive and encouraging – I'm so lucky to have such a wonderful and caring family. I'm definitely ready for our next curry night! My love goes to the Shmoles for everything you have done for me. Thanks for our Preston days, games nights, cinnamon spices, and all the laughs that kept me smiling through my time at university.

– For Holly and the Rose Queen –

List of Figures

Figure 3.2. Energy level diagram of a core level electron in a sample that is in electrical contact with an electron energy analyser. Adapted from [2].

Figure 3.3. Experimental data of the inelastic mean free path of electrons as a function of their kinetic energy for various materials. Reproduced from [3].

Figure 3.4. Sampling depth, d, changing with emission angle, θ, of the photoelectron for grazing and normal emission. Adapted from [4].

Figure 3.5. Schematic cross section of a hemispherical electron energy analyser. Electrons collected from the sample are focused using an electrostatic lens. Dotted lines show the trajectory of electrons deflected by the potential difference between the two hemispherical electrodes before reaching the detector. Adapted from [3].

Figure 3.6. XPS Si 2p doublet of a Si(111) surface. The two peaks $2p_{1/2}$ and $2p_{3/2}$ have the same full width at half maximum (0.32 eV), a spin orbit separation of 0.608 eV and an area ratio of 1:2. Reproduced from [3].

Figure 3.7. Illustration (not to scale) of a NAP-cell containing the sample and gas (a) and a schematic cross section of a NAP analyser (b). The aperture of the analyser cone is a small distance, z, away from the sample surface. A series of pumps reduce the pressure from mbar at the aperture to ultra-high vacuum in the analyser. Dotted lines show electron trajectories as they are focused between each pumping stage. Adapted from [8].

Figure 3.8. Survey scan (a) and a high-resolution C 1s spectrum (b) of polyethylene terephthalate (PET). Chemical assignment of the three C 1s components is also shown. Reproduced from [2].

Figure 3.9. Examples of the Linear, Shirley and Tougaard background subtraction for a Fe 2p XPS peak. Reproduced from [1].

Figure 3.10. XPS binding energy values of common chemical species are known within a narrow energy range. Reproduced from [9].

Figure 3.11. Energy level diagram depicting the excitation of a core level electron into an unoccupied molecular orbital (NEXAFS) or into the continuum of free states

(EXAFS) (a). NEXAFS and EXAFS regions near the absorption edge (b). Adapted from [13].

Figure 3.12. σ and π bonding and antibonding (*) molecular orbitals made by interactions of 2p atomic orbitals in a diatomic molecule. Reproduced from [15].

Figure 3.13. A schematic K-shell NEXAFS spectrum (a) and the potential well of a diatomic molecule (b). 1s electrons are excited into π* or Rydberg states below the vacuum level (ionisation potential), or into the continuum of free states above the vacuum level. Adapted from [17].

Figure 3.14. Energy level diagram showing the creation of an Auger electron or fluorescence photon after the decay of a core hole. The Auger decay process can involve either the originally excited electron (participator method) or another electron (spectator method).

Figure 3.15. Yield window settings showing the energy ranges used in Auger, partial and total electron yield detection. E_a is the energy of the Auger peak while E_p is the user-controlled pass energy. Photoemission spectra are shown above, where VB is a valence band peak. Reproduced from [17].

Figure 3.16. Coordinate system showing the geometry of a π* or σ* MO on a surface. $\vec{O}$ is the direction of the MO vector described by a polar angle α and azimuthal angle ϕ. X-rays are incident at an angle θ from the surface, equal to the polar angle of the $\vec{E^{\parallel}}$ vector. Reproduced from [17].

Figure 3.17. Angle-resolved NEXAFS showing the angular dependence of π* and σ* peaks with X-ray incidence angle for benzene. π* orbitals point out-of-plane while σ* orbitals are in-plane. Overlap of the electric field vector with the direction of the orbital changes the intensity of the resonance. Reproduced from [18].

Figure 3.18. Ratio of resonance intensities taken at normal incidence and grazing incidence (5 – 30°) as a function of orbital polar angle α. If an experimental intensity ratio is known, it can be compared to the theoretical intensity ratio using Equation 3.7 to obtain a value of α. Reproduced from [17].

Figure 3.19. Radiation patterns of synchrotron light emitted from an electron travelling in a circular orbit at non-relativistic ($\beta = v/c << 1$) and relativistic ($\beta = v/c \approx 1$) speeds. Acc. denotes the direction of centripetal acceleration. Reproduced from [20].

Figure 3.20. Illustration of the SOLEIL synchrotron facility (a) where electrons (blue) travelling around the outer storage ring emit synchrotron light (yellow) down beamlines. Scheme showing a simplified configuration of a synchrotron storage ring (b). The grey cones depict the emission of synchrotron radiation from bending magnets, wiggler and undulator insertion devices. Reproduced from [21,22].

Figure 3.21. Experimental setup of a wiggler insertion device. Alternating dipole magnets cause the electrons to oscillate and produce more intense synchrotron radiation. Adapted from [21].

Figure 3.22. Schematic illustration of the electron trajectory through a wiggler and the emission angle of the SR $1/\gamma$. Reproduced from [20].

Figure 3.23. Schematic of a monochromator used to select the photon energy of synchrotron light. A curved quartz crystal diffracts the light, which is refocused on a point on the Rowland circle. Reproduced from [25].

Figure 3.24. Schematic illustration of the rotors and stators used in a turbomolecular pump. Adapted from [26].

Figure 3.25. Illustration of the electrospray ionisation deposition process. The solution for deposition escapes the capillary in the form of a Taylor cone jet. A scheme shows Coulomb explosion of droplets into small molecular clusters. Reproduced from [33].

Figure 3.26. Photograph of a Molecularspray UHV4 electrospray system mounted to a UHV chamber.

Figure 3.27. Schematic diagram of the B07 end station at Diamond Light Source. Reproduced from [5].

magnified × 100 (blue boxes) and shows the formation of a carbamate peak upon absorption of CO_2.

Figure 5.4. N 1s XPS region recorded at a photon energy of 700 eV for a thin film of [P_{66614}][benzim] as presented, exposed to 10^{-6} mbar CO_2, 1 mbar CO_2, 5 mbar CO_2, and after CO_2 pump out.

Figure 5.5. P 2p region recorded at a photon energy of 430 eV for multilayer [P_{66614}][benzim] as presented, while exposed to various pressures of CO_2, and after CO_2 pump out.

Figure 5.6. Ti 2p region for multilayer [P_{66614}][benzim] as presented, exposed to 10^{-6} mbar CO_2, 1 mbar CO_2, 5 mbar CO_2, and after CO_2 pump out.

Figure 5.7. O 1s region recorded at a photon energy of 830 eV for multilayer [P_{66614}][benzim] as presented, while exposed to various pressures of CO2, and after CO_2 pump out.

Figure 5.8. C 1s normal emission (NE) and grazing emission (GE) XPS spectra of [P_{66614}][benzim].

Figure 5.9. N 1s spectra of multilayer [P_{66614}][benzim] (as presented) recorded at a photon energy of 700 eV at normal and grazing emissions.

Figure 5.10. P 2p spectra of multilayer [P_{66614}][benzim] (as presented) recorded at a photon energy of 430 eV at normal and grazing emissions.

Figure 5.11. O 1s normal and grazing emission of [P_{66614}][benzim]. This is compared to clean TiO_2 (110) at normal emission.

Figure 5.12. C K edge NEXAFS of [P_{66614}][benzim] exposed to 1 mbar CO_2. The experimental data (red) was divided by the background gas-phase CO_2 signal (black), resulting in a CO_2-corrected spectrum (blue).

Figure 5.13: AEY N K edge NEXAFS of [P_{66614}][benzim] exposed to 1 mbar CO_2 with a removed TiO_2 background signal. The experimental data (gold) was divided by the clean TiO_2 substrate signal (black), resulting in a background-corrected IL + CO_2 spectrum (red).

LUMO+1 and LUMO+2 are assigned to the $1\pi^*$, $2\pi^*$, and $1\sigma^*$ antibonding orbitals, respectively.

Figure 5.21. Simulated C K edge NEXAFS spectrum for $[P_{66614}][benzim]$ + COOH. The final DFT spectrum (black) is the sum of the eight spectra from atoms $C^1 - C^8$.

Figure 5.22. Simulated N K edge NEXAFS spectrum for $[P_{66614}][benzim]$. The final DFT spectrum (black) is the sum of the two spectra from atoms N^1 and N^2 (red).

Figure 5.23. Simulated N K edge NEXAFS spectrum for $[P_{66614}][benzim]$ + CO_2. The final DFT spectrum (black) is the sum of the two spectra from atoms $N^{1,r}$ (red) and $N^{2,r}$ (blue).

Figure 5.24. Experimental and simulated (DFT) N K edge NEXAFS of $[P_{66614}][benzim]$ as presented and when exposed to 1 mbar of CO_2. The grey dashed lines highlight features of the DFT spectra for comparison with the experimental spectra. The experimental spectra were taken 70° from the IL surface.

Figure 6.1. Chemical structure of the $[P_{66614}]^+$ cation with C_{hetero} atoms highlighted in magenta and $C_{aliphatic}$ in black (a). The reaction scheme for $[124Triz]^-$ with CO_2 (b) and H_2O (c). Atoms N^1 and N^2 (blue) are equivalent due to resonance effects. Reaction with CO_2 at N^1 results in the formation of carbamate. Reaction with H_2O forms triazole and a hydroxide ion. $N^{1,r}$ (red) and $N^{2,r}$ (green) denote the N atoms following reaction of the anion with CO_2 or H_2O. The gas exposure stages for NAP-XPS measurements are also shown (d).

Figure 6.2. XPS survey spectra of $[P_{66614}][124Triz]$ subject to various exposures of CO_2 and H_2O. Highlighted are the peaks associated with atoms in the rutile TiO_2 (110) crystal substrate (O 1s, Ti 2p), absorbed gases (O 1s) and the IL (N 1s, C 1s, P 2p).

Figure 6.3. C 1s region of an electrosprayed thin film of $[P_{66614}][124Triz]$ for various exposure regimes of CO_2 and H_2O at 1 mbar. (a) shows how the carbamate peak at 288.3 eV varies in intensity throughout these stages. (b) shows how the $C^{3,5}$ component shifts downwards in binding energy throughout the exposure stages.

Figure 6.10. Simulated N K edge NEXAFS spectrum for $[P_{66614}][124Triz]$. The final DFT spectrum (black) is the sum of the spectra from atoms N^1 and N^3 (blue) and N^2 (green).

Figure 6.11. Simulated N K edge NEXAFS spectrum for $[P_{66614}][benzim]$ + CO_2 + H_2O. The final DFT spectrum (black) is the sum of the IL + CO_2 (green) and IL + H_2O (blue) spectra. Nitrogen atom labels are based on those used in Figure 6.1.

Figure 6.12. Lowest unoccupied molecular orbitals (LUMOs) of the isolated $[124Triz]^-$ anion (top row), $[124Triz]^-$ + H_2O (middle row) and $[124Triz]^-$ + CO_2 (bottom row). The LUMOs are arranged in order of increasing energy (left to right).

Figure 7.1. Multisite physical absorption of CO_2 with an isolated $[Tetz]^-$ anion. The distances between nitrogen atoms in the anion and carbon atoms in CO_2 are shown in units of Å. Reproduced from [3].

Figure 7.2. Chemical structure of the isolated $[P_{66614}]^+$ cation and $[Tetz]^-$ anion. In $[P_{66614}]^+$, C_{hetero} atoms are highlighted in green and $C_{aliphatic}$ in black. Various reactions schemes of $[Tetz]^-$ with CO_2 and/or NO are also shown. The colours of the nitrogen atoms in $[Tetz]^-$ denote four different chemical environments: N^1 and N^4 (light blue); $N^{2,3}$ (dark blue); $N^{1,r}$ and $N^{4,r}$ (red); NONO (purple).

Figure 7.3. Exposure scheme for NAP-XPS measurements of $[P_{66614}][Tetz]$ exposed to CO_2 and NO gas. The pressures of the gases and gas mixture are approximately 3 mbar.

Figure 7.4. C 1s XPS of $[P_{66614}][Tetz]$ recorded at a photon energy of 390 eV. Measurements were taken at normal emission (NE), 15° from NE and 27° from NE. These correspond to sampling depths of 1.34, 1.29 and 1.19 nm, respectively. (a) shows the overlayed spectra and (b) shows their fitted components.

Figure 7.5. C 1s XPS of $[P_{66614}][Tetz]$ taken over 4 exposure stages: IL (1), IL + NO (2), IL + CO_2 (4), IL + NO + CO_2 (6). Measurements were recorded at a photon energy of 390 eV and 890 eV, corresponding to surface (1.3 nm) and bulk (4.0 nm) sampling depths, respectively.

Figure 7.6. C 1s XPS of [P_{66614}][Tetz] during the gas exposure and pump out stages. Measurements were recorded at a photon energy of 390 eV and 890 eV, corresponding to surface (1.3 nm) and bulk (4.0 nm) sampling depths, respectively.

Figure 7.7. N 1s XPS of [P_{66614}][Tetz] over 4 exposure stages: IL, IL + NO, IL + CO_2, IL + NO + CO_2 (a). Fitted components over a narrower BE range are shown for the same stages (b). Measurements were recorded at a photon energy of 1000 eV, corresponding to a bulk sampling depth (4.0 nm).

Figure 7.8. Comparison of N 1s XPS spectra of [P_{66614}][Tetz] taken during the gas pump out and exposure stages (a). Fitted components are shown for the pump out stages (b). Measurements were recorded at a photon energy of 1000 eV, corresponding to a bulk sampling depth (4.0 nm).

Figure 7.9. AEY C K edge NEXAFS of [P_{66614}][Tetz] taken at three X-ray angles of incidence (θ) from the surface. Vertical dashed lines highlight common peaks in the experimental spectra. These are compared to the theoretical NEXAFS spectrum labelled DFT.

Figure 7.10. Lowest unoccupied molecular orbitals (LUMOs) of the isolated [Tetz]$^-$ anion, [Tetz]$^-$ + NO and [Tetz]$^-$ + CO_2. The LUMOs are either π^* or σ^* antibonding unoccupied molecular orbitals.

Figure 7.11. AEY N K edge [P_{66614}][Tetz] taken at three X-ray angles of incidence (θ) from the surface. The electrosprayed film appears to be too thin to produce a significant signal.

Figure 7.12. AEY C K edge NEXAFS of [P_{66614}][Tetz] + 3 mbar NO taken at three X-ray angles of incidence (θ) from the surface. Vertical dashed lines highlight common peaks in the experimental spectra. These are compared to theoretical NEXAFS spectra in two absorption regimes, [Tetz]$^-$–NONO and [Tetz]$^-$–2–NONO.

Figure 7.13. AEY C K edge NEXAFS of [P_{66614}][Tetz] + 3 mbar CO_2 taken at three X-ray angles of incidence (θ) from the surface. Vertical dashed lines highlight common peaks in the experimental spectra. These are compared to a theoretical NEXAFS spectrum labelled DFT.

Figure 7.14. Simulated C K edge NEXAFS spectrum for the isolated [Tetz]$^-$ anion reacted with CO_2 to form carbamate. The spectra for C^1 in the anion and C^2 in carbamate are summed to give the final combined DFT spectrum.

Figure 7.15. AEY C K edge NEXAFS of [P$_{66614}$][Tetz] + 3 mbar of a NO + CO_2 mixture taken at three X-ray angles of incidence (θ) from the surface. Vertical dashed lines highlight common peaks in the experimental spectra. These are compared to a theoretical NEXAFS spectrum labelled DFT.

List of Tables

depth due to the reversible absorption of CO_2 and irreversible absorption of the NO + CO_2 mixture.

Table 8.1. The orientation of the plane of the ring of [benzim]$^-$ and [Tetz]$^-$ anions in [P$_{66614}$]$^+$-based SBILs. Orientations are measured with respect to the rutile TiO_2 (110) surface normal and are given for the IL as presented, and when the IL is exposed to CO_2 and NO.

List of Abbreviations

AEY	Auger electron yield
AIL	Aprotic ionic liquid
BE	Binding energy
CCS	Carbon capture and sequestration
DFT	Density functional theory
DSSC	Dye-sensitised solar cell
ESD	Electrospray deposition
ESE	Electronic Schrödinger equation
EXAFS	Extended X-ray absorption fine structure
FWHM	Full width at half maximum
GE	Grazing emission
HF	Hartree-Fock
HOMO	Highest occupied molecular orbital
IL	Ionic liquid
IMFP	Inelastic mean free path
IP	Ionisation potential
LUMO	Lowest unoccupied molecular orbital
MEA	Monoethanolamine
MOF	Metal-organic frameworks
NAP	Near-ambient pressure
NE	Normal emission
NEXAFS	Near-edge X-ray absorption fine structure
PEY	Partial electron yield
PIL	Protic ionic liquid
RTIL	Room temperature ionic liquid
SBIL	Superbasic ionic liquid
SCILL	Solid catalyst with ionic liquid layer
SILP	Supported ionic liquid phase
SR	Synchrotron radiation
TEY	Total electron yield
TSIL	Task-specific ionic liquid
UHV	Ultra-high vacuum
XAS	X-ray absorption spectroscopy
XPS	X-ray photoelectron spectroscopy

List of Publications

Cole J, Henderson Z, Thomas A G, Compeán-González C L, Greer A J, Hardacre C, Venturini F, Garzon W Q, Ferrer P, Grinter D C, Held G and Syres K L 2021 *Near-Ambient Pressure XPS and NEXAFS Study of a Superbasic Ionic Liquid with CO_2* J. Phys. Chem. C **125** 22778–85.
(This paper was published using results from Chapter 5)

Cole J, Henderson Z, Thomas A G, Castle C, Greer A J, Hardacre C, Scardamaglia M, Shavorskiy A and Syres K L 2023 *In situ XPS of competitive CO_2/H_2O absorption in an ionic liquid* J. Phys. Mater. **6** 045012.
(This paper was published using results from Chapter 6)

Cole J and Syres K L 2022 *Ionic liquids on oxide surfaces* J. Phys. Condens. Matter **34** 213002

Compeán-González C L, Thomas A G, Syres K L, Cole J and Li Z 2022 *4-Mercaptobenzoic Acid Adsorption on TiO2 Anatase (101) and TiO2 Rutile (110) Surfaces* Surfaces **5** 238–50

Chapter 1. Introduction

1.1 Context of This Work

Ionic liquids (ILs) are liquid salts consisting of pairs of bulky anions and cations held together by strong Coulombic forces [1]. Inorganic salts have high melting points, for example, 803 °C for NaCl. By definition, ILs are described as having melting points less than 100 °C. Their low melting points are due to their large, asymmetric ions that do not pack easily into crystals [1]. There are millions of possible combinations of ions, allowing the physical and chemical properties of an IL to be fine-tuned [2]. ILs are non-flammable, non-volatile, and have ultra-low vapour pressures, excellent thermal stability, wide liquid ranges, and wide electrochemical windows. Due to their numerous and varied properties, it is no surprise that ILs are being studied across a wide range of fields for applications including catalysis, carbon capture, photovoltaics, lubricants, batteries, and more. A report published in January 2023 (Ionic Liquids: Global Strategic Business Report) predicted that that the worldwide ionic liquids market will grow by US$25.1 Million by 2030 [3]. This strong market growth is led by expanding applications and unique characteristics of ILs.

In recent years, there has been a global drive to make new and existing technologies green and environmentally friendly. Carbon capture and sequestration has become an important method of reducing CO_2 emissions in fossil fuel-burning power plants. Current carbon capture solvents such as monoethanolamine (MEA), also called amine scrubbers, can successfully capture over 90% of CO_2 from industrial flue streams. However, these organic solvents present problems of their own. Due to the high temperatures required to regenerate the solvent after CO_2 capture, amine scrubbers are very energy intensive and costly. Amine scrubbers also tend to be toxic, volatile, and are prone to degradation from acidic gases [4]. Flue streams contain a complex mixture of gases alongside CO_2 including H_2O, NO_x, and SO_2, which can inhibit CO_2 absorption or chemically degrade the solvent.

ILs have drawn attention as promising green alternatives to amine scrubbers thanks to their negligible vapour pressures, high thermal stability, and low volatility. ILs have comparable CO_2 capacities to MEA (if not greater) and have the added benefit of requiring lower regeneration temperatures. This would make ILs more cost effective in an industrial setting, but this is somewhat offset by their high synthesis costs. The main challenges facing ILs for carbon capture is their increased viscosity upon absorption of CO_2, which hinders further CO_2 absorption. An emerging subclass of ILs called superbasic ILs (SBILs) have high CO_2 capacities and exhibit very little viscosity increase upon exposure to CO_2. There is a lack of fundamental studies probing interfacial and intermolecular interactions of ILs with CO_2 and other gases. This is in part due to the infancy of IL research (particularly for the promising new class of SBILs) as well as the overwhelming number of cation/anion combinations.

ILs are of particular interest within the surface science community because they can be studied using ultra-high vacuum (UHV) surface-sensitive techniques. ILs have ultra-low vapour pressures so no not evaporate in UHV (10^{-9} mbar), unlike most molecular liquids. ILs have been studied in UHV using a variety of techniques, including X-ray photoelectron spectroscopy (XPS) and near-edge X-ray absorption fine structure (NEXAFS). These techniques provide information on the elemental and electronic characteristics of materials and can provide information about the bonding and ordering of molecules at surfaces. Recent technological advancements now allow these techniques to be carried out at near-ambient pressures (tens of mbar). This means that the IL/gas interface can be studied *in situ* using XPS and NEXAFS. These techniques are typically found at synchrotron facilities (although lab-based XPS is commonly used). Synchrotrons are large particle accelerators capable of producing incredibly intense X-rays many orders of magnitude brighter than lab-based X-ray sources. When studying ILs it is useful to combine experimental measurements with computational studies. Quantum chemical simulations can provide unique insights into these complex molecular systems.

ILs are highly structured compared to most molecular liquids, particularly when deposited as thin films. The aim of this thesis is to understand how thin films of SBILs react with CO_2 and other flue stream gases, and how the presence of these gases

affects the highly structured ordering of SBIL molecules. SBILs were studied using *in situ* surface-sensitive synchrotron techniques, near-ambient pressure XPS (NAP-XPS) and NEXAFS. Experimental NEXAFS spectra were compared with theoretical spectra calculated using density functional theory simulations. The work detailed, herein, provides new insights into the fundamental interactions and behaviour of SBIL thin films with CO_2 and other flue gases.

1.2 Summary of Aims and Results

The aim of this work is to investigate CO_2 uptake in ILs using cutting-edge *in situ* synchrotron techniques and computational studies. Results give new fundamental insights into the uptake of gas, reversibility of chemical reactions and reordering of ions upon exposure to gas. We push the limits of these techniques to study the absorption of CO_2 in ultrathin films and discover how other gases compete with CO_2 at different depths in the film. Three superbasic ILs with a common cation but different anions are studied, with each anion having an increasing number of nitrogen atoms ([benzim]$^-$: 2, [124Triz]$^-$: 3, [Tetz]$^-$: 4). Chemical and physical interactions between the IL and gas become more complex with an increasing number of chemisorption (nitrogen) sites. The effects of an increasing number of bonding sites on gas uptake, ordering of ILs at interfaces, and competitive gas absorption are explored. Following is a summary of each chapter presented in this thesis.

Chapter 2 provides a background and brief history of ILs, starting from their early discovery in 1914 to their recent spike in popularity as powerful and versatile solvents. Common properties of ILs are discussed alongside the many ways in which the characteristics of an IL can be fine-tuned. Examples of IL applications are also detailed, with a focus on gas capture and its importance as a method for reducing industrial CO_2 emissions. Our current understanding and limitations on CO_2 capture in ILs will also be discussed.

Details on the theory and instrumentation underpinning this work are provided in Chapter 3. Techniques discussed include XPS and NAP-XPS which allow us to study the IL/gas interface at mbar pressures. This chapter also explains how

NEXAFS can be used to determine the orientation of molecules on surfaces. The experiments presented in this thesis were conducted at synchrotron facilities, therefore, the generation of synchrotron radiation for surface science studies is also discussed.

Chapter 4 introduces quantum chemical models that form the basis of the simulations carried out in this thesis. This chapter outlines density functional theory (DFT) and how DFT calculations are used to generate theoretical NEXAFS spectra for comparison with experimental results. The procedure for generating and visualising molecular orbitals is also discussed. These aid in the assignment of NEXAFS peaks.

Chapter 5 is a study into the behaviour of IL molecules upon absorption of CO_2 at various pressures ranging from 10^{-6} to 5 mbar. A multilayer thin film of the SBIL trihexyltetradecylphosphonium benzimidazolide ([P_{66614}][benzim]) was deposited on rutile TiO_2 (110) by drop casting. TiO_2 was chosen as a substrate due to its widespread use alongside ILs in a number of applications. *In situ* NAP-XPS was used to characterise the IL + CO_2 reaction and its reversibility. Angle-resolved NEXAFS measurements were combined with DFT simulations in order to probe the reorientation of IL molecules upon exposure to CO_2. It was found that [benzim]$^-$ anions experience a change in orientation at the TiO_2 surface upon exposure to CO_2. The results from this chapter have been published [5].

Chapter 6 contains an *in situ* study on the competitive absorption of CO_2 and H_2O in thin films of the SBIL trihexyltetradecylphosphonium 1,2,4-triazolide ([P_{66614}][124Triz]). The IL was deposited onto rutile TiO_2 (110) using electrospray deposition. To the best of our knowledge, [P_{66614}][124Triz] is the largest IL molecule to be successfully deposited using electrospray. A depth profiling NAP-XPS study was carried out in order to understand how the IL reacts with CO_2 and H_2O at surface and bulk layers of the IL film. Results indicate that competitive absorption between CO_2 and H_2O films varies with sampling depth.

The study in Chapter 7 builds upon the methods used in Chapters 5 and 6. Here, the competitive absorption between CO_2 and NO was investigated using depth

profiling NAP-XPS and angle-resolved NEXAFS. This is an important study as the presence of NO is known to inhibit CO_2 absorption in some ILs. Thin films of the SBIL trihexyltetradecylphosphonium tetrazole ([P_{66614}][Tetz]) were deposited via electrospray and characterised upon exposure to CO_2, NO, and a CO_2/NO mixture. NEXAFS measurements showed that [Tetz]$^-$ anions reoriented from their positions at UHV to different angles depending on whether the IL is exposed to CO_2 or NO. These results corroborate with those found in Chapter 5 and show common behaviour between these SBILs.

Chapter 8 provides a conclusion and discussion of the results presented in this thesis, as well as thoughts on future work and prospects. Since these results may have an impact on the use of IL thin films in applications and devices, there is scope for expanding these studies with a focus on applications such as catalysis or photovoltaics.

1.3 References

[1]   Welton T 2018 Ionic liquids: a brief history *Biophys. Rev.* **10** 691–706

[2]   Guo F, Zhang S, Wang J, Teng B, Zhang T and Fan M 2015 Synthesis and applications of ionic liquids in clean energy and environment: A review *Curr. Org. Chem.* **19** 455–68

[3]   Verified Market Reports 2023 *Ionic Liquids: Global Strategic Business Report* (Global Industry Analysts Inc.)

[4]   Greer A J, Taylor S F R, Daly H, Quesne M, Catlow C R A, Jacquemin J and Hardacre C 2019 Investigating the Effect of NO on the Capture of CO_2 Using Superbase Ionic Liquids for Flue Gas Applications *ACS Sustain. Chem. Eng.* **7** 3567–74

[5]   Cole J, Henderson Z, Thomas A G, Compeán-González C L, Greer A J, Hardacre C, Venturini F, Garzon W Q, Ferrer P, Grinter D C, Held G and Syres K L 2021 Near-Ambient Pressure XPS and NEXAFS Study of a Superbasic Ionic Liquid with CO_2 *J. Phys. Chem. C* **125** 22778–85

Chapter 2. Background

This chapter will provide a brief background on the history, properties, and applications of ionic liquids (ILs). Current carbon capture methods and materials are discussed. The advantages and limitations of current carbon capture agents will be compared to those of ILs as green alternatives. The absorption of CO_2 in ILs will be discussed, as well as how other flue gases compete for absorption in the IL.

2.1 Ionic Liquids (ILs)

2.1.1 Brief History and Background

The first recorded IL in literature is ethylammonium nitrate, $[EtNH_3][NO_3]$, reported by Walden in 1914, an IL that is still commonly used to this day [1]. This was the first reported case of ions forming a liquid at room temperature without needing to be diluted in a molecular solvent [2]. This new liquid salt was found to have similar behaviour and properties to water [1,2]. What was most interesting about $[EtNH_3][NO_3]$, however, was its high electrical conductivity due to its free moving ions, one of the characteristic properties of ILs.

A famous example of a cation that is still extensively used to this day is alkyl pyridinium, first reported in 1951 by Hurley and Weir [3,4]. Another significant milestone in IL history came in 1982 with the synthesis of 1,3-dialkylimidazolium chlorides [5]. Imidazolium-based cations are responsible for many of the signature properties we now associate with modern-day ILs: high thermal stability, ionic conductivity, wide electrochemical windows, highly tuneable structures, and low melting points due to ineffective packing of the bulky asymmetric cations [6,7]. Common imidazolium-based cations having the $[C_nC_1Im]^+$ (1-alkyl-3-methylimidazolium) structure are shown in Figure 2.1, as well as an example of a common pyridinium-based cation $[C_4C_1Pyrr]^+$ (1-butyl-1-methylpyrrolidinium).
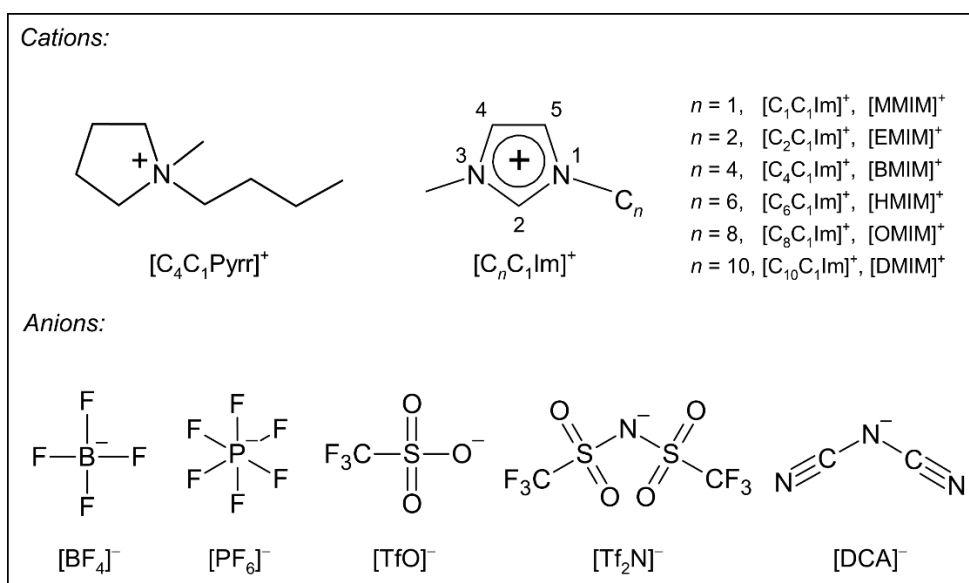
Figure 2.1. Structure of common ionic liquid cations and anions.

However, these breakthrough ILs were not without problems. In 1992, Wilkes tackled the poor stability of ILs in air and water by replacing moisture-sensitive $[Cl]^-$ anions with water-stable fluorinated ions such as tetrafluoroborate, $[BF_4]^-$ [8]. This, alongside hexafluorophosphate ($[PF_6]^-$), remain some of the most commonly used anions to this day. This ushered in the second generation of ILs: air and water stable ILs.

Despite their early discovery, ILs only saw a dramatic rise in research by the mid-1990s, with imidazolium-based ILs dominating the literature at this time. This spike in research is often attributed to groups such as Grätzel who foresaw the potential of ILs in applied chemistry [9]. They exploited the low vapor pressure, low volatility and high conductivity of ILs for use as electrolytes for solar cells [4]. From this point onwards the study and applications of ILs quickly became an interdisciplinary topic spanning many fields such as chemistry, physics, material science, biochemistry, chemical engineering, and more [10]. The number of publications about ILs has steadily increased year after year since the 1990s, rising to a peak number of nearly 9500 articles published in the year 2020 as shown in Figure 2.2.
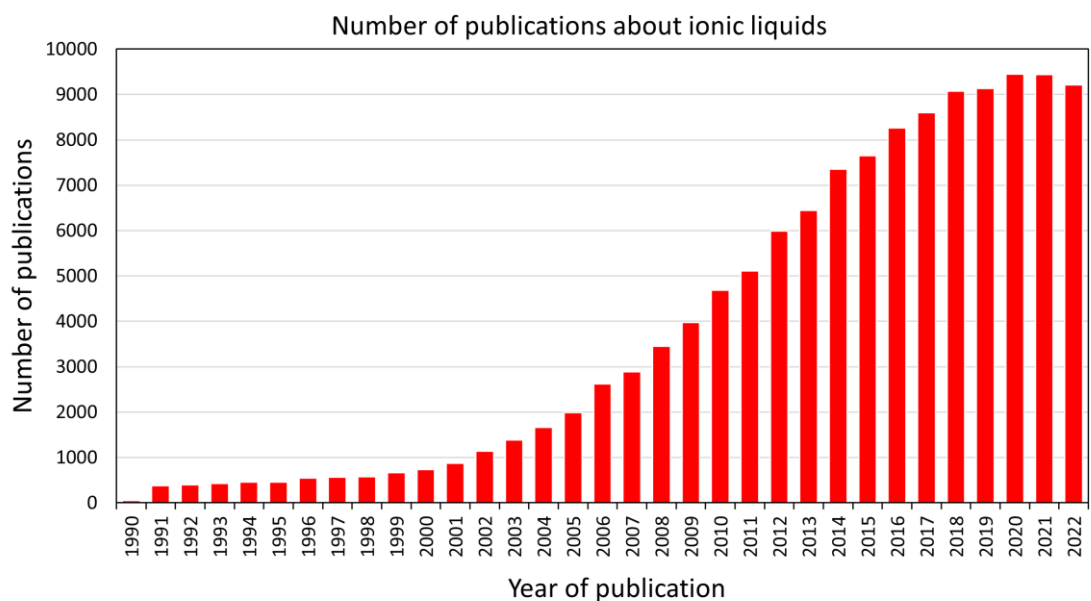
Figure 2.2. Number of publications containing the keyword "ionic liquids" from 1990 to 2022. Data accessed from the Web of Science database on 31/07/2023.

Nowadays, ILs can be categorised into a multitude of subclasses, each distinguished by different properties and characteristics. The first reported IL, [EtNH$_3$][NO$_3$], as discussed above, is an example of what we now call protic ILs (PILs), produced via an equimolar combination of a Brønsted acid with a Brønsted base [11]. This involves the transfer of a proton from the acid to the base. A characteristic property of PILs is an ion with a proton available for hydrogen bonding, oftentimes covalently bound to the charged atom of the cation [1,12]. There have been far fewer reports and applications of PILs compared to their popular counterparts aprotic ILs (AILs).

Aprotic ILs (AILs) are considered "conventional" ILs today. AILs consist of an organic molecular cation and a weakly coordinating organic/inorganic anion [13]. Imidazolium-based cations are some of the most commonly used cations in AILs. They consist of a pentagonal ring structure containing two nitrogen atoms, one of which is positively charged. Commonly, alkyl chains are bonded to the two nitrogen atoms as shown in Figure 2.1. Imidazolium-based cations are very versatile, allowing tuneable properties by changing the length of the alkyl side chains or by substituting these chains for functional groups. Pairing imidazolium-based cations with a chosen anion (examples of anions shown in Figure 2.1) allows the properties of the IL to be further tuned.

With the onset of ILs being researched for an increasing number of applications, a third generation of ILs emerged called task-specific ILs (TSILs). TSILs, also known as functionalised ILs, have ions modified with functional groups in order to enhance and customise specific properties of the IL for a given application. Some of the first recorded cases of TSILs were those used for catalytic applications [14]. The discovery of TSILs also led to an increase in CO_2 capture studies using ILs. It was found that ILs functionalised with amine groups enabled the TSIL to chemically absorb CO_2 in a similar way, and to the same capacity, as conventional solvents. This will be discussed further below.

There is often some confusion in the literature surrounding the naming of ILs, therefore, it is worth noting the many different names used for ILs over the years. These include "molten salts", "melts", "neoteric solvents", "designer solvents", owing to their tunability, and "room temperature ILs" (RTILs). ILs have been commonly mistaken for deep eutectic solvents (DESs), and vice versa, due to their very similar physical properties. Similar to ILs, DESs have ionic constituents, negligible vapour pressures, low flammability and high tunability [15]. Some have argued that DESs are a subclass of ILs while others acknowledge DESs as independent alternatives to ILs [16]. It is now generally accepted that, despite their similar physical properties, these are two distinct groups of solvents due to their different chemical nature. The main difference is that DESs contain a variety of anionic/cationic structures while ILs contain one distinct type of anion and cation [17].

2.1.2 Bulk IL Properties

There have been many studies dedicated to exploring and understanding the physicochemical properties of bulk ILs. The interesting properties of ILs are often determined by the chemical structure of the constituent ions. Below is a summary of the most important IL properties.

Ions and their interactions

Interionic forces and interactions are ubiquitous in ILs and are responsible for most of their signature properties. Due to their completely ionic nature, the strongest interactions in ILs are Coulombic interactions. In an IL, charged constituents of the

ions (of magnitude q_1, q_2) separated by distance r experience an electrostatic force, F, (repulsive or attractive) as governed by Coulomb's Law,

$$F = k_e \frac{q_1\, q_2}{r^2} \tag{2.1}$$

where k_e is Coulomb's constant (8.99 N m^2 C^{-2}). Considering the strong attractive forces between cations and anions, some believe that IL ions can form ion pairs in the bulk liquid phase. There has been some theoretical, computational, and experimental work to support this belief, however, there is little to no evidence showing long-living, stable ion pairs [2,18]. It is generally accepted that ILs can indeed contain ion-ion pairs but only with short lifetimes (less than a few picoseconds) before they disassociate due to their relative motion and the interactions of surrounding ions [2,18].

ILs experience other ion-ion interactions including hydrogen bonding, π-π stacking between aromatic imidazolium rings, and weak van der Waals interactions [7]. The complex balance of these interactions is often governed by the chemical structure of the ions.

<u>Vapour pressure</u>

Perhaps the most compelling property of ILs for green chemistry is their ultra-low vapour pressure. Solvents with low vapour pressures are financially and environmentally desirable as they experience fewer losses from evaporation [19]. ILs do not readily evaporate at room temperature and are therefore considered non-volatile, green, and eco-friendly alternatives to volatile organic solvents used in many applications today. It is thanks to their low vapour pressures that, unlike most other molecular liquids, ILs can be studied using ultra-high vacuum techniques such as X-ray photoelectron spectroscopy (XPS) and near-edge X-ray absorption fine structure (NEXAFS) spectroscopy.

There is little data on the vapour pressures of ILs, and some of that data has been found to be contradictory due to different approaches in measuring or calculating the vapour pressure [19]. At room temperature, the vapour pressure of 1-butyl-3-methylimidazolium hexafluorophosphate, [C$_4$C$_1$Im][PF$_6$], was measured to be 100

pPa compared to 3 kPa for water [20]. IL vapour pressures have been found to increase significantly when heated to temperatures over 100 °C [19,20].

It was thought that the negligible vapour pressure of ILs was exclusively due to strong Coulomb interactions between the ions [21]. It has since been argued that the low vapour pressures exhibited in ILs are also influenced by their low melting points [20]. The evaporation rate, and therefore vapour pressure, of imidazolium-based ILs has been found to decrease with increasing alkyl chain length on the cation [22]. As a result of their negligible vapour pressures ILs also have very low flammability. This makes them excellent solvents in high temperature systems such as lubrication and carbon capture where other liquids fail under the extreme conditions.

Thermal stability and liquid range

Other characteristic properties of ILs are their high thermal stability and a wide liquid range. Some ILs are stable to temperatures over 400 °C [23]. Compare this, for example, to conventional carbon capture agents such as monoethanolamine which begins thermal decomposition at 90 °C [24]. Cation/anion interactions are known to affect the thermal stability of ILs. Stronger interionic interactions lead to easier thermal decomposition, thereby reducing thermal stability limits. On the other hand, weaker interionic interactions result in an increase in thermal stability limits [25]. Babucci *et al.* investigated the thermal stability of 33 imidazolium ILs [26]. They found that systematic changes such as the size of the cation/anion, methylation on the carbon at position 2 of the imidazolium ring, and substitution of alkyl groups on the imidazolium ring with functional groups all have significant effects on thermal stability limits.

The liquid range is the temperature range over which the IL is stable in its liquid phase. The upper limit of an IL's stability range is usually its decomposition temperature, which tends to be much lower than its boiling point due to the IL's very low vapour pressure. The lower end of an IL's liquid range is either the melting point or glass transition temperature, depending on the IL structure. For some ILs this is well below 0 °C [23].

<u>Melting point</u>

Conventionally, since about the early 2000's, ILs have been defined as liquid salts with melting points (T_m) < 100 °C, while molten salts are those with T_m > 100 °C. However, it is feasible that an IL and a molten salt sat closely either side of this T_m = 100 °C boundary can otherwise have nearly indistinguishable properties. Therefore, researchers are beginning to abandon this somewhat arbitrary definition in favour of describing ILs as liquids composed solely of ions [27]. To add to the confusion surrounding the definition of an IL, the terms RTILs (T_m < 25 °C) and ILs (T_m < 100 °C) have mistakenly become interchangeable, although, it is generally accepted that RTILs are liquid at ambient temperatures [2,28].

The underlying mechanisms controlling the melting points of ILs are not fully understood. It is believed that the low packing efficiency of bulky and asymmetric ions, particularly cations, gives ILs their characteristic low melting points [1,6]. Compare this to inorganic salts such as NaCl whose ions pack very efficiently into cubic unit cells, yielding a much higher T_m of 803 °C [28]. Holbrey and Seddon [29] explored the effect of cation chain length, n, on the melting points of 1-alkyl-3-methylimidazolium tetrafluoroborate ILs, [C_nC_1Im][BF_4], for n = 0 − 18 (Figure 2.3). At room temperature, they found that ILs with short alkyl chains (n = 2 − 10) were liquid while those with long chains (n = 12 − 18) were solid with low melting points T_m < 100 °C. ILs with intermediate chain lengths (3 < n < 10) formed a glassy state as they are cooled below T_m to their glass transition temperature, T_g.
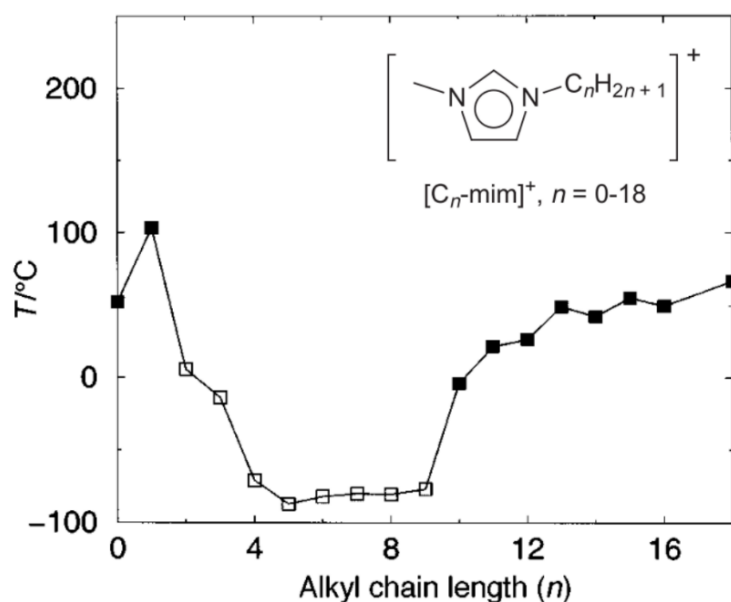
Figure 2.3. Melting (closed squares) and glass (open squares) transition temperatures of 1-alkyl-3-methylimidazolium tetrafluoroborate, $[C_nC_1Im][BF_4]$, ionic liquids for $n = 0 - 18$. Adapted from [29].

Other studies have also found that cooling an IL below T_m can lead to a glassy amorphous solid, with the IL exhibiting an increase in viscosity upon approach to T_g [9,30]. Again, T_g is largely governed by alkyl chain length as well as type (linear, branched, aromatic, etc.) [31]. Other factors that can affect melting point include charge distribution, ion size, and electrostatic intermolecular interactions [23,28]. Increasing the size of the anion size paired with the 1-ethyl-3-methylimidazolium cation, $[C_2C_1Im]^+$, decreases the melting point of the IL due to weaker Coulombic attractions between the ions [32].

Conductivity and electrochemical window

The electrochemical window is an important consideration when selecting ILs for electrochemical applications. The electrochemical window is defined as the electrochemical potential range between which an electrolyte is neither reduced nor oxidised [33]. ILs have wide electrochemical windows making them suitable electrolytes for nanoparticle synthesis and batteries, and useful for the electrodeposition of metals and semiconductors [34]. For example, $[C_4C_1Im][PF_6]$ has an electrochemical window of 4.15 V at a platinum electrode compared to 1.23 V for water [33]. Therefore, when synthesising or selecting ILs for electrochemical

13

applications, it is important to use "pure ILs" with minimal water contamination in order to maximise the IL's electrochemical stability. Quantum chemical calculations can be used to determine the decomposition products of ILs operating at voltages larger than their electrochemical windows [35].

Another important property of ILs for electrochemistry is their ionic conductivity. The conductivity of an IL is largely governed by the number of available charge carriers and their mobility, as well as the viscosity of the IL [1,36]. ILs tend to have reasonably good conductivity, comparable to non-aqueous solvents and electrolytes (~10 mScm^{-1}) [37]. The low mobility of large and bulky ions in an IL limits its ionic conductivity. The formation of short-living and neutral ion pairs can also inhibit conductivity by limiting the number of available charge carriers [32].

By far, viscosity has the largest impact on conductivity as this directly affects ion mobility. The dependence of conductivity, κ, on viscosity, η, is given by Walden's rule,

$$\frac{\kappa M \eta}{\rho} = constant \qquad (2.2)$$

where M is the molecular weight and ρ is density of the IL. Figure 2.4 shows a graph of conductivity against viscosity for a range of room temperature, imidazolium-based and binary haloaluminate ILs [32]. Walden's rule highlights the interesting interplay between an IL's electrochemical characteristics and its physical properties such as viscosity and density.
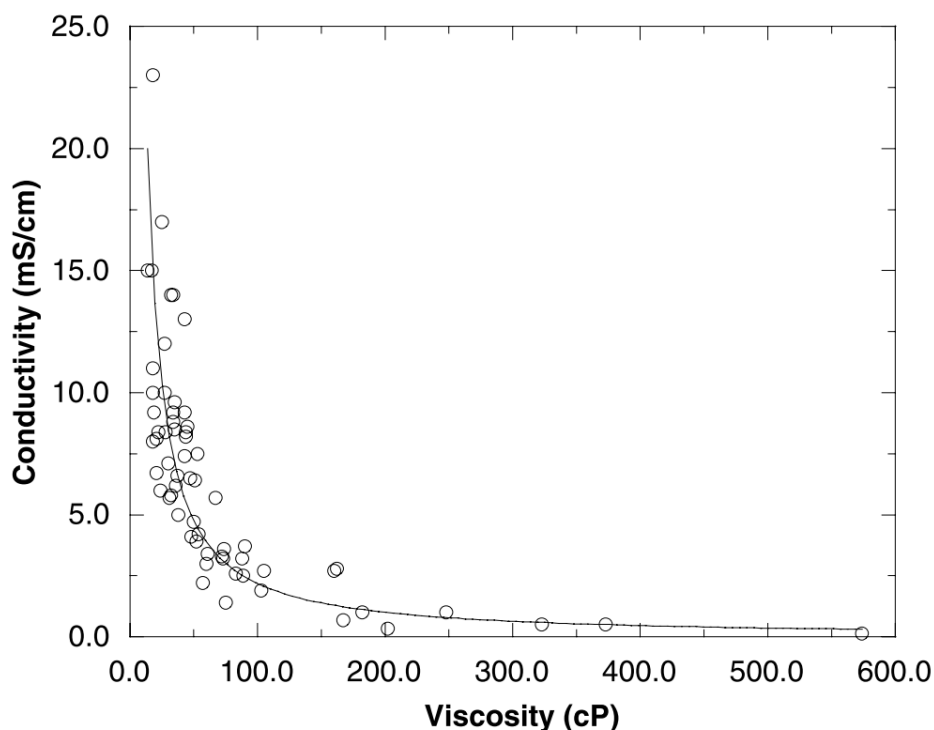
Figure 2.4. Experimental Conductivity of ionic liquids as a function of their viscosity. Reproduced from [38].

Viscosity

ILs tend to be much more viscous than other common molecular solvents. As discussed above, high viscosity can be a significant disadvantage for ionic mobility, as well as mass transfer. On the other hand, viscous ILs are favourable as lubricants because they can form a stable liquid film between the two contacts, preventing friction and wear [39].

The temperature dependence of viscosity is given as

$$\eta = Ae^{\varepsilon/RT} \tag{2.3}$$

where ε is the activation energy for viscous flow, R is the gas constant, and A is a constant [9]. A number of other factors also affect the viscosity of an IL. Van der Waals interactions and hydrogen bonding are believed to be the main influences on viscosity in an IL. For example, increased alkyl side chain length and branching, and increased fluorination of imidazolium cations all result in stronger van der Waals interactions and higher viscosity of the IL [9,40]. Viscosity is also affected by anion

15

structure. The viscosities of imidazolium-based ILs can be lowered by delocalising negative charge, reducing symmetry of the anion, or increasing flexibility of the anion [40]. Size and fluorination of the anion have somewhat positive correlations to viscosity but do not follow a consistent or reliable trend due to the complex relationship of hydrogen bonding and van der Waals interactions [32].

Viscosity of an IL is a crucial consideration for gas capture applications, as solvents with high viscosities are linked with having slower CO_2 absorption rates (this will be discussed in more detail below) [41].

2.1.3 IL Thin Films and Interfaces

ILs are highly structured compared to most other molecular liquids, showing interesting structural and orientational behaviour at interfaces. The performance of many IL-based applications is determined by fundamental interactions of ILs at solid, liquid, and gas interfaces. Improving our understanding of this interfacial behaviour is crucial for designing and commercialising efficient, eco-friendly, high-performance, and stable devices.

<u>IL/solid interface</u>

When an IL is deposited as a thin film, a greater number of structured layers can be observed due to the influence of the substrate surface on the IL ions. Studies of IL thin films on solid surfaces can reveal vital information pertaining to the layering, stacking, and orientational behaviour of these ILs. It is also important to understand how these behaviours change with IL coverage on the surface. Monolayer/multilayer behaviour of conventional imidazolium-based ILs has been investigated on a number of substrates in vacuo, including glass [42], mica [43], gold [44], and nickel [45].

Studies at IL/metal interfaces have shown that the structure of IL thin films is coverage dependent. For example, Cremer *et al.* studied ultrathin films of 1,3-dimethylimidazolium bis(trifluoromethanesulfonyl)imide, $[C_1C_1Im][Tf_2N]$, on Ni(111) single crystal surfaces using angle-resolved X-ray photoelectron spectroscopy [45]. Their results indicated that on clean Ni(111) at submonolayer coverages, the cations arrange at the surface and the anions lie above (similar to the first layer of the double

layer structure shown in Figure 2.5). This transitions to a checkerboard-type structure at higher coverages, with the anions and cations next to each other. Others have found similar checkerboard and double layer arrangements as shown in Figure 2.5 [46].
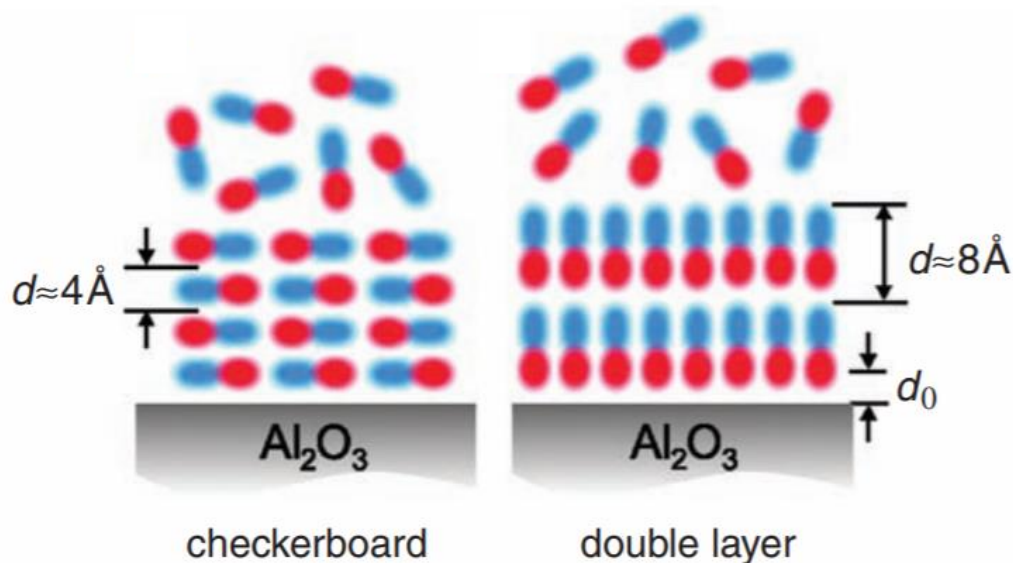
Figure 2.5. Two possible layering arrangements of cations (red) and anions (blue) at an Al_2O_3 surface with checkerboard-type stacking (a) and double-layer stacking (b). Reproduced from [46].

Studies on the IL/metal oxide interface are comparatively sparser due to the complex interaction between ILs and oxide surfaces, with defects in the oxide surface playing a key role in the adsorption behaviour and resulting electronic properties of the system. TiO_2 surfaces have been a popular choice of substrate in the study of ILs at oxide surfaces as many technological applications utilise TiO_2. For example, the anatase TiO_2 (101) surface is thought to be the dominant surface in TiO_2 nanoparticles because it has the lowest surface energy [47]. The rutile TiO_2 (110) surface in its (1 x 1) termination is considered a model metal oxide surface for surface science studies since the surface shares the same configuration of atoms as the bulk TiO_2 crystal structure. It is for this reason that we use TiO_2 substrates in our experiments. The rutile TiO_2 (110) surface is discussed in greater detail in Section 2.1.4.

17

Weber *et al.* studied the adsorption behaviour of 1,3-dimethylimidazolium thiocyanate, [C_1C_1Im][SCN], and 1,3-dimethylimidazolium tetracyanoborate, [C_1C_1Im][TBC], on anatase TiO_2 (101) [48]. They discovered that the surface titanium atoms are predominantly in contact with the nitrogen atoms of the anion. The surface oxygen atoms interact via hydrogen-bond-like structures with the hydrogen atoms in the imidazolium cation, as well as electrostatic and dispersive interactions.

Wagstaffe *et al.* used X-ray photoelectron spectroscopy (XPS) and near-edge X-ray absorption fine structure (NEXAFS) spectroscopy to show how the film thickness of [C_4C_1Im][BF_4] on a single crystal anatase TiO_2 (101) surface affects the ordering of IL ions [49]. At low coverages, they found the IL orders on the surface via electrostatic attraction, with the imidazolium ring oriented at about 32° ± 4° from the surface as shown in Figure 2.6. As they increased the coverage, they found the ordering of the IL was lost, as the IL layers become less influenced by the presence of the surface. Cremer *et al.* reported a similar dependence on coverage using [C_1C_1Im][Tf_2N] on Au (111) with the addition that submonolayer increases in film thickness (i.e., < 7.3 Å increase in coverage for this IL) were sufficient enough to induce chemical shifts in XPS spectra [44]. Thin films of the IL exhibited lower binding energy peaks than the bulk film, with binding energy increasing as coverage increased from 0.3 to 4.5 monolayers.
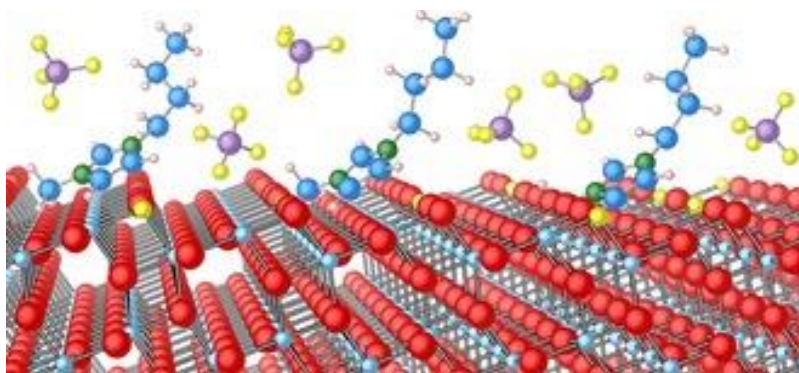
Figure 2.6. Schematic representation of [C_4C_1Im][BF_4] ordering at the anatase TiO_2 (101) surface. Reproduced from [49].

The interaction of surfaces with ILs can also affect their thermal stability. Supported ILs typically have a lower thermal stability than the bulk ILs. Babucci *et al.* studied interactions between [C_4C_1Im][BF_4] and a wide range of high surface area metal

oxides including SiO_2, TiO_2, Fe_2O_3, ZnO, γ-Al_2O_3, CeO_2, MgO, and La_2O_3 [50]. They found that as the point of zero charge of the metal oxide increases, IL/metal oxide surface interactions dominate over interionic interactions, and thermal stability limits decrease. This reveals that the choice of metal oxide support plays an important role in the measured thermal stability limits of the IL. These are important considerations when choosing suitable ILs to withstand the operating conditions in applications such as catalysis.

IL/gas interface

ILs can be studied in ultra-high vacuum (UHV) due to their ultra-low vapour pressures. The IL/vacuum interface has been studied using a variety of UHV techniques including XPS, NEXAFS, ultraviolet photoemission spectroscopy (UPS) and metastable atom electron spectroscopy (MAES) [51,52]. The IL/vacuum interface has also been studied computationally [53]. For imidazolium-based ILs, the surface of the liquid contains the alkyl chains of the imidazolium ion facing outwards towards the vacuum in an ordered fashion, with a charged underlayer just beneath containing the anion and the charged part of the imidazolium cation [51]. It is understood that this behaviour is due to charged moieties being driven into the bulk in order to reduce nearest neighbour interactions, leaving uncharged alkyl chains pointing out towards the vacuum [54].

Using near-ambient pressure beamlines at synchrotron facilities it is now possible to conduct XPS and NEXAFS measurements of liquid/gas interfaces. *In situ* XPS was employed by Henderson *et al.* to study a thin layer of $[C_4C_1Im][BF_4]$ on the rutile TiO_2 (110) surface when exposed to water vapour [55]. They observed a reordering of the IL as water adsorbed to the IL layers. ILs are prone to absorb water and it is likely to be present in many of their potential applications. Rivera-Rubero and Baldelli [56] used surface-sensitive sum frequency generation (SFG) to study the reorientation of $[C_4C_1Im]^+$ cations at the IL/water vapour interface for a variety of ILs. The miscibility of the ILs is determined by the anion. When dry, the $[C_4C_1Im]^+$ cations orient with the imidazolium ring parallel to the substrate surface. Upon addition of water vapour, the cation remains parallel to the surface for water miscible ILs and reorients for water immiscible ILs.

ILs are capable of physically and/or chemically absorbing CO_2 and other gases present in industrial flue streams. Therefore, ILs have become promising gas capture candidates for pre- and post-combustion power plants. More details on ILs for CO_2 capture are given in Section 2.2.3.

<u>IL/liquid interface</u>

Miscibility of ILs with liquid water is important to study as water is present in many applications and can hinder the useful properties of ILs. It has been found that the miscibility of ILs with water depends on the hydrophobicity of the IL. Hydrophobic ILs are immiscible with water, forming liquid-liquid separated biphasic systems. They tend to contain fluorinated and charge-delocalised anions, for example $[Tf_2N]^-$ and $[PF_6]^-$ [57,58]. Meanwhile, hydrophilic ILs, commonly containing halide anions ($[Cl]^-$, $[Br]^-$), are miscible with water [57]. The choice of cation has also been found to affect the miscibility of ILs with water. Imidazolium-based cations show a reduction in miscibility as alkyl chain length is increased [29].

The miscibility of IL-IL mixtures has been investigated and found to be governed by the similarity of the ion structures across the ILs [59]. IL−IL mixtures have been researched for batteries, solar cells, liquid−liquid extraction, and more [59]. ILs have also been mixed with other gas capture solvents such as monoethanolamine (MEA) in order to improve the CO_2 capacity of the solvent [60].

2.1.4 ILs on Rutile TiO_2 (110)

The unit cell structure of rutile TiO_2 is shown in Figure 2.7 alongside other common TiO_2 polymorphs anatase and brookite. Experimentally, oxide surfaces can be challenging to prepare, particularly in the preparation of model single crystal surfaces or thin oxide films for surface science experiments. Single crystal metal oxide surfaces are usually prepared in ultra-high vacuum by sputter/anneal cycles. Ar^+ ions are accelerated into the sample which sputters off the top layer of material and removes surface contamination with it. Subsequent annealing is required, sometimes in the presence of oxygen, to restore the surface crystallography and to remove embedded argon atoms. Several sputter/anneal cycles are required to prepare a well-ordered atomically clean surface. Even then, the surface will have

lattice defects, such as oxygen vacancies and step edges. Defects often determine the electronic and optical properties of the material and provide potential bonding sites for adsorbed atoms and molecules such as water and CO_2 [61]. In turn, the adsorption of molecules on the surface can shift the electronic bands in the oxide material. The interaction of molecules with oxide surfaces is therefore rather complex. Several theoretical models have been developed to model the properties of oxide surfaces and their interaction with adsorbates [62].
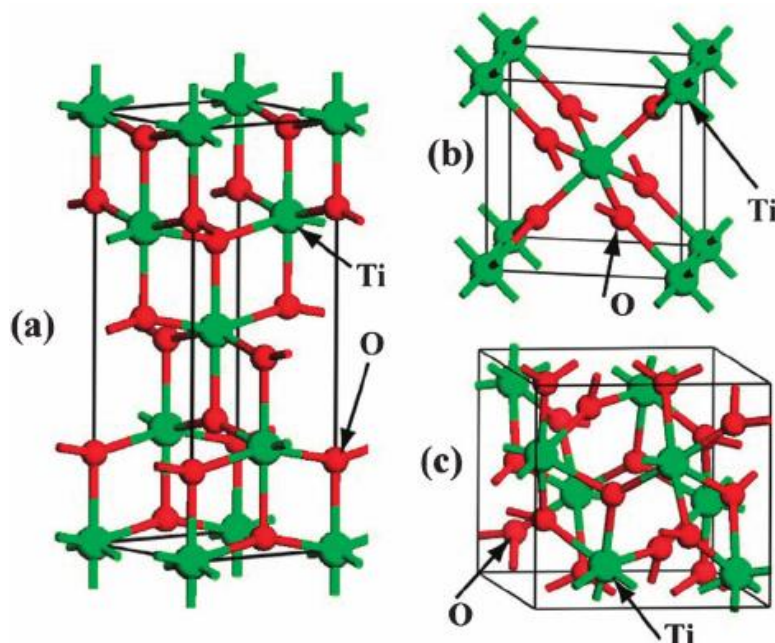
Figure 2.7. Schematic unit cells for (a) anatase, (b) rutile and (c) brookite TiO_2. The large green spheres represent Ti atoms and the small red spheres represent O atoms. Reproduced from [63].

Interactions between ILs and the rutile TiO_2 (110) surface have been studied using a variety of computational [64,65] and experimental [55,66] techniques. However, the influence of substrates such as rutile TiO_2 (110) on the ordering and subsequent gas capture characteristics of ILs has not been explored in detail. It is of interest from a fundamental perspective to explore how this ordering affects interactions with the gas in order to learn more about the IL/gas interface. In this thesis, we are aiming to explore how the uptake of gas will be affected by the highly structured layers, whether this will affect the availability of chemisorption sites or the IL's availability for physisorption. The use of IL thin films and surface sensitive techniques in the studies

21

presented in this thesis allow us to probe the interactions at the IL/gas and IL/TiO$_2$ interfaces.

2.1.5 IL Applications

The unique properties of ILs show great potential for transforming industrial processes, including CO$_2$ absorption [14,67–69], catalysis [70,71], batteries [72–74], lubrication [75,76], nanostructure growth [77,78], corrosion inhibitors [76], and photovoltaic devices [79–81].

Early studies of ILs for catalysis used the IL to immobilise homogeneous catalytic material [82]. Chemical reactivity was found to be controllable by tuning the IL structure. Early implementation of ILs into homogeneous catalysts used a biphasic IL/organic solvent media [83]. These showed low mass transfer and slow diffusion rates due to the high viscosity of the IL and poor contact with the support. These issues can be circumvented by using thin films of ILs with better coverage with the support and shorter diffusion pathways [71]. The use of IL thin films also reduces the financial costs associated with large quantities of IL, therefore making them much more suitable to scaling up for industrial applications.

Two common concepts exist, the first being "solid catalyst with ionic liquid layer" (SCILL) which uses a solid heterogeneous catalyst coated with a thin layer of IL to tune the selectivity of the catalyst [84]. ILs are also used in "supported ionic liquid phase" (SILP) catalysts, where a thin layer of IL containing the catalyst is spread over a high-surface-area support. For SCILL and SILP catalysis, the IL film is dispersed on a high-surface-area oxide support, for example alumina or silica. The underlying mechanisms of these catalysts are largely driven by small scale IL/solid and IL/gas interfacial interactions that are not yet fully understood [84]. Therefore, it is necessary to carry out more fundamental studies on ILs at these interfaces before the effect of the IL can be fully understood and exploited for these technologies. This is also true for TiO$_2$ which has been recently studied as an alternative support material for heterogeneous catalysts [85] and as a support for SILP catalysis [86]. Probing interactions at the IL/TiO$_2$ interface is therefore important in furthering these technologies.

One widely studied potential application of ILs is as electrolytes in batteries, capacitors, transistors, and other electrochemical applications [59]. ILs can be used directly as electrolytes in many electrochemical systems due to their ionic conductivity. In some electrochemical applications, ILs are mixed with conventional electrolytes. The combination can improve properties such as viscosity and conductivity. ILs have been used as solvents, reactants or templates in the synthesis of nanomaterials such as nanoparticles and quantum dots, or more complex nanostructures such as nanotubes, nanowires, nanoflowers, nanorods, and nanosheets [77,78,87]. The use of an IL allows for highly controllable morphologies and properties.

ILs have been incorporated into dye-sensitised solar cells (DSSCs) and perovskite solar cells to improve their long-term stability and efficiency [80,88]. $[C_4C_1Im][BF_4]$ has been used to increase the power conversion efficiency of a perovskite solar cell by improving surface smoothness of the ZnO electron transport layer and $MAPbI_3$ perovskite layer [89]. Zhang *et al.* used the passivation effect of 1-ethyl-3-methylimidazolium hexafluorophosphate, $[C_2C_1Im][PF_6]$, on ZnO to improve the long-term stability of a perovskite solar cell in air [90]. TiO_2 is another common electron transport material in solar cells. It has been found that depositing a layer of IL at the interface between the perovskite and TiO_2 in perovskite solar cells results in more efficient electron transport and has been linked to an improvement in stability of the devices [91,92].

2.2 Carbon Capture and Storage (CCS)

Carbon dioxide (CO_2) capture and separation has become an important process in reducing CO_2 emissions in fossil fuel-fired power plants. Below is a summary of current carbon capture methods and their comparison with ILs as promising new alternative gas capture agents.

2.2.1 Global Motivation

CO_2 and other greenhouse gases are responsible for the recent increase in average global temperatures. Therefore, there is a global drive to reduce CO_2 emissions in our atmosphere. The Paris Agreement established a target of reaching net zero

carbon emissions by 2050 in order to limit the global temperature increase to 1.5°C above pre-industrial times [93]. As a long-term strategy, this can be done in part by phasing out fossil-fuel burning powerplants in favour of renewable energy technologies. However, as of 2020, fossil fuel-based power plants still account for over 60% of global energy production [94]. Therefore, since a vast number of fossil fuel-based technologies are still in use, there is a pressing need to reduce our current CO_2 emissions.

One of the most economic and practical ways of reducing CO_2 emissions is through carbon capture and storage (CCS). This involves the capture and separation of CO_2 from flue gas emitted from power plants. The CO_2 is then transported and stored in underground geological formations where it can remain safely trapped for millions of years [95]. The following contains a summary of CCS methods and materials currently used today.

2.2.2 Current Methods and Solvents
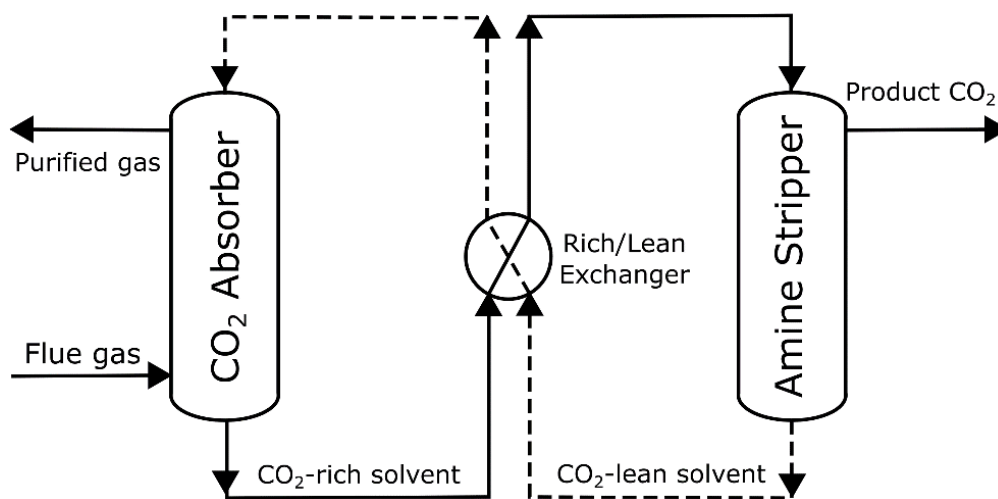
Figure 2.8. Simplified schematic of an absorber-stripper system for separating CO_2 from exhaust (flue) gas in post-combustion power plants. Based on [96,97].

The exhaust gas, or flue gas, emitted from fossil fuel-burning power plants contains a mixture of gases alongside CO_2. Therefore, a crucial step in CO_2 capture is the selective absorption of CO_2 over other gases present. The current method of CO_2 separation uses "amine scrubbers", typically monoethanolamine (MEA), to selectively absorb CO_2 from the flue stream. Conventional post-combustion amine

scrubbing comprises of an absorber-stripper system, shown schematically in Figure 2.8 [96,97]. The first step occurs in the absorber column. Flue gas is pumped through the MEA absorber at approximately 40 °C where MEA chemically reacts with the CO_2 to form carbamate (reaction shown in Figure 2.9) [98]. CO_2-saturated MEA is then transferred to the stripping tower and heated over 100 °C (regulated by the reboiler). CO_2 is released from the MEA and captured for transportation and storage. MEA is regenerated in this process and recycled back into the absorber column for further CO_2 capture. These post-combustion technologies are economically favourable because they can be retrofitted onto existing power plants without the need of widescale redesign.
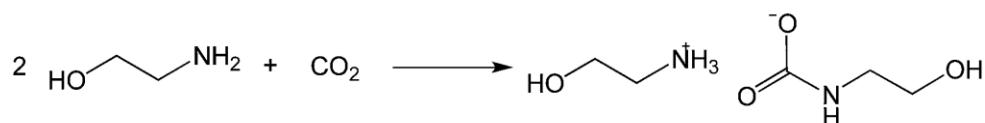
Figure 2.9. Reaction scheme of 2 monoethanolamine (MEA) molecules with CO_2. One MEA forms a carbamate group ($N–COO^-$) while the other MEA is protonated. Adapted from [99].

Post-combustion carbon capture faces a number of challenges. As discussed, the scrubber must be selective for CO_2 absorption in the presence of many other gases. Some of these are acidic gases such as NO and SO_2 which can chemically degrade the solvent, so a chemically robust and resistant solvent is required. Despite reducing a power plant's CO_2 emissions by as much as 90% [100], these conventional amine scrubber methods can increase the energy requirements of a power plant by 25-40% due to the high regeneration temperatures required [98,101]. The volatility and toxicity of amine scrubbers also pose issues to their long-term suitability [102]. As such, a number of alternative carbon capture technologies and materials have been explored. These include pre-combustion, oxyfuel combustion, and direct air capture [103]. Emerging separation materials for carbon capture include ILs, physical absorbents, membranes, activated carbon, and many more. Of these materials, physical absorbents are some of the most widely researched alternatives to amine scrubbers in post-combustion carbon capture.

Zeolites have received much attention as physical CO_2 absorbents. Zeolites are microporous crystalline materials (aluminosilicates) that have already seen widespread industrial and commercial use across many fields. They act as molecular sieves to separate gas molecules by tuning their pore size [104]. However, Zeolites have been found to be sensitive to temperature and humidity, both hindering CO_2 capacity [104,105]. Metal-organic frameworks (MOFs) are a more recent physical absorbent, consisting of metal ion nodes connected into a uniform 3D network via organic bridging ligands. MOFs are promising carbon capture candidates thanks to their ultrahigh porosity, chemical tunability, and high surface area [106]. In MOFs, CO_2 can be selectively captured (via physisorption) in the presence of water by tuning the pore size [98]. However, MOFs are still prone to contamination from other gases in the flue stream, and this remains a challenge for MOFs in post-combustion carbon capture [107]. The weak interactions between CO_2 and physisorbent materials leads to lower selectivity and capacity for CO_2 compared to chemically absorbing materials such as MEA [108]. Therefore, other chemical absorbers such as ILs may prove to be promising alternatives to conventional solvents.

2.2.3 Ionic Liquids for CCS

ILs have a number of advantages over MEA, including high thermal stability, high CO_2 capacity, and lower regeneration temperatures [109–111]. The financial benefit of using ILs over MEA has been verified computationally; it has been reported that ILs can reduce energy consumption costs by as much as 30% compared to typical MEA processes [95]. ILs still face some economic challenges, however, such as high synthesis costs [112]. In some of their earliest CO_2 capture studies, it was found that conventional imidazolium-based ILs physically absorb CO_2 and the anion was found to be largely responsible for the solubility of the gas [101,113]. Alternatives to conventional physically absorbing ILs came in the way of anime-functionalised task-specific ILs which chemically absorb CO_2, leading to higher CO_2 capacities [111,114]. Task-specific ILs, however, were found to suffer increased viscosity upon absorption of CO_2, which consequently hinders further CO_2 absorption and limits their applicability [103,115]. To combat this, an emerging class of ILs called superbasic ILs (SBILs) have been developed which show higher CO_2 capacities and lower viscosity increases compared to task-specific ILs [116].
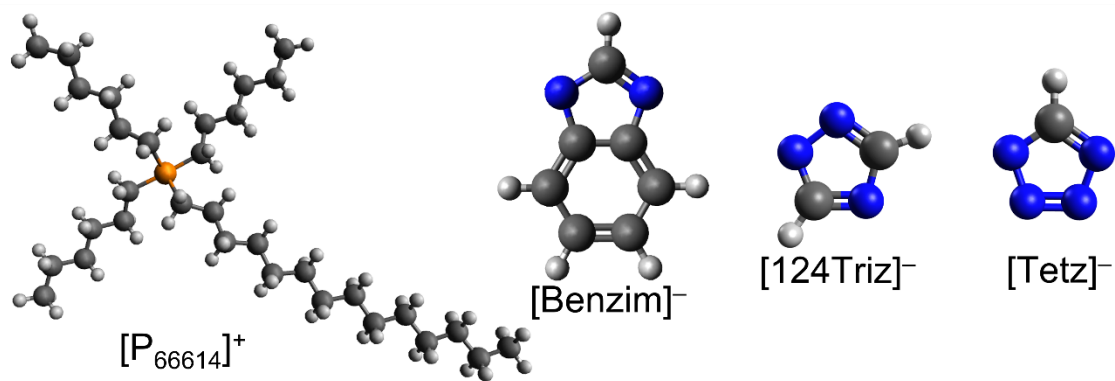
Figure 2.10. Molecular structures of the [P$_{66614}$]$^+$ cation and [Benzim]$^-$, [124Triz]$^-$, and [Tetz]$^-$ anions that comprise three common superbasic ionic liquids.

Commonly, SBILs consist of quaternary phosphonium/ammonium-based cations paired with a superbasic anion such as imidazolide, triazolide or phenoxide [117,118]. In SBILs, the anion chemically reacts with CO_2 [117] the same way as MEA, forming a carbamate species [114]. While it does not contribute to any chemical absorption, the cation has been found to reduce the energy for reaction [119]. Some SBILs, such as [P$_{66614}$][124Triz], have been found to both chemically and physically absorb CO_2 [120]. Anions such as [benzim]$^-$ and [124Triz]$^-$ have been found to yield the highest CO_2 capacities and solubilities [60,118]. Taylor *et al.* reported a CO_2 uptake of 1.20:1 ($n_{CO_2}:n_{IL}$) in the dry state for the SBIL trihexyltetradecylphosphonium benzimidazolide, [P$_{66614}$][benzim] [118]. SBILs are a rather new subclass of ILs, therefore, more fundamental experimental and computational studies are needed before they are likely to see widescale industrial use. In particular, ordering at the solid and gas interface and the competitive absorption between CO_2 and other flue gases in SBILs require further studies and understanding. The work presented in this thesis focuses on the SBILs [P$_{66614}$][benzim], [P$_{66614}$][124Triz] and [P$_{66614}$][Tetz] (molecular structures shown in Figure 2.10). These SBILs share a common cation but have different anions, each with an increasing number of nitrogen atoms ([benzim]$^-$: 2, [124Triz]$^-$: 3, [Tetz]$^-$: 4). Chemical and physical interactions between the IL and gas become more complex with an increasing number of chemisorption (nitrogen) sites. This allows us to investigate the effects of an increasing number of bonding sites on gas uptake

(multiple site bonding), ordering of SBILs at interfaces, and competitive gas absorption.

2.2.4 Competitive Absorption

The majority of early CO_2 capture studies expose the IL to CO_2 alone. While this provides invaluable information about the absorption mechanisms and properties of ILs upon exposure to CO_2, this is not a realistic representation of the environment in which carbon capture occurs in an industrial system. Industrial flue gas contains a complex mixture of gases such as CO_2, H_2O, O_2, N_2, CO, SO_x and NO_x [121,122]. Therefore, an important property of ILs for CO_2 capture is their selectivity for CO_2. It is necessary that other gases present do not inhibit CO_2 absorption or chemically degrade the IL. It is therefore vital to understand the effect of a mixture of gases on the IL and how they compete with CO_2 for absorption. With this in mind, recent steps have been made to study the absorption of CO_2 with another gas, such as H_2O, SO_2, or NO. Current fundamental studies are usually limited to two gases due to the complexity of the system/analysis.

SBILs have been found to only experience minor reductions in CO_2 capacity in the presence of water [118], SO_2 [123], and NO [117]. Henderson *et al.* found that the presence of H_2O did not significantly inhibit CO_2 absorption in thin films of [P$_{66614}$][benzim] at near-ambient pressures [124]. It has been shown that [P$_{66614}$][124Triz] reversibly absorbs CO_2 by heating the SBIL, even in the presence of water [118].

Taylor *et al.* highlighted the negative effects of SO_2 on CO_2 absorption in the SBILs [P$_{66614}$][benzim] and [P$_{66614}$][124Triz]. In their experiment both SO_2 and CO_2 irreversibly react at the same nitrogen sites on the anions. They found that SO_2 could displace previously bound CO_2 while CO_2 was unable to displace previously bound SO_2. The lifetime of the CO_2 scrubbing IL can be extended by using a combined SBIL approach to separate SO_2 from CO_2 [125]. The presence of NO_x in the flue stream degrades amine scrubbers which increases their corrosivity and decreases their lifetime for CO_2 capture [117]. Furthermore, NO_x emissions need to be regulated because they can react in the atmosphere to form acid rain. Greer *et al.* investigated the competitive absorption of CO_2 and NO in [P$_{66614}$][benzim] [117].

Although the absorption of NO resulted in irreversible bonding of NONOate species to the [benzim]$^-$ anion, the presence of NO had little effect on the reversibility of CO_2 absorption and the CO_2 capacity of the IL.

The work in this thesis focusses on CO_2 capture in thin films of SBILs. An interesting question to explore is whether IL thin films show different CO_2 capture behaviour compared to bulk ILs because of their complex ordering at surfaces and interfaces. There is little knowledge on how the ordering of molecules changes upon exposure to gases. Before ILs see widescale industrial use, it is vital to first understand their fundamental interactions with CO_2. In the same vein it is also important to study how the presence of other gases compete with CO_2 for absorption in the IL. Studies in this thesis therefore aim to gain insights into the chemical interaction and reordering of IL molecules upon exposure to CO_2 and other flue stream gases. Surface sensitive techniques NAP-XPS and NEXAFS are used alongside simulations to characterise this behaviour. Understanding interactions of IL thin films with gases is important for other applications including SCILL/SILP catalysis and lubricants.

2.3 References

[1]   Greaves T L and Drummond C J 2008 Protic ionic liquids: Properties and applications *Chem. Rev.* **108** 206–37

[2]   Hayes R, Warr G G and Atkin R 2015 Structure and Nanostructure in Ionic Liquids *Chem. Rev.* **115** 6357–426

[3]   Hurley F H and Wier T P 1951 Electrodeposition of Metals from Fused Quaternary Ammonium Salts *J. Electrochem. Soc.* **98** 203

[4]   Austen Angell C, Ansari Y and Zhao Z 2012 Ionic Liquids: Past, present and future *Faraday Discuss.* **154** 9–27

[5]   Wilkes J S, Levisky J A, Wilson R A and Hussey C L 1982 Dialkylimidazolium Chloroaluminate Melts: A New Class of Room-Temperature Ionic Liquids for Electrochemistry, Spectroscopy, and Synthesis *Inorg. Chem.* **21** 1263–4

[6]   Larsen A S, Holbrey J D, Tham F S and Reed C A 2000 Designing ionic liquids: Imidazolium melts with inert carborane anions *J. Am. Chem. Soc.* **122** 7264–72

[7]   Green M D and Long T E 2009 Designing imidazole-based ionic liquids and ionic liquid monomers for emerging technologies *Polym. Rev.* **49** 291–314

[8]   Wilkes J S and Zaworotko M J 1992 Air and water stable 1-ethyl-3-methylimidazolium based ionic liquids *J. Chem. Soc. Chem. Commun.* **04** 965

[9]   Bonhôte P, Dias A P, Papageorgiou N, Kalyanasundaram K and Grätzel M 1996 Hydrophobic, Highly Conductive Ambient-Temperature Molten Salts *Inorg. Chem.* **35** 1168–78

[10]   Lei Z, Chen B, Koo Y M and Macfarlane D R 2017 Introduction: Ionic Liquids *Chem. Rev.* **117** 6633–5

[11]   Nuthakki B, Greaves T L, Krodkiewska I, Weerawardena A, Burgar M I, Mulder R J and Drummond C J 2007 Protic ionic liquids and ionicity *Aust. J. Chem.* **60** 21–8

[12]   Hunt P A, Ashworth C R and Matthews R P 2015 Hydrogen bonding in ionic liquids *Chem. Soc. Rev.* **44** 1257–88

[13]   Singh V V., Batra A, Boopathi M, Vijayaraghavan R, Singh B and Nigam A K 2012 Applications of Ionic Liquids in Electrochemical Sensors and Biosensors *Int. J. Electrochem.* **2012** 1–19

[14]   Giernoth R 2010 Task-specific ionic liquids *Angew. Chemie - Int. Ed.* **49** 2834–9

[15]   Smith E L, Abbott A P and Ryder K S 2014 Deep Eutectic Solvents (DESs) and Their Applications *Chem. Rev.* **114** 11060–82

[16]   Płotka-Wasylka J, de la Guardia M, Andruch V and Vilková M 2020 Deep eutectic solvents vs ionic liquids: Similarities and differences *Microchem. J.* **159**

[17]   Richter J and Ruck M 2019 Synthesis and Dissolution of Metal Oxides in Ionic Liquids and Deep Eutectic Solvents *Molecules* **25** 78

[18]   Zhao W, Leroy F, Heggen B, Zahn S, Kirchner B, Balasubramanian S and Müller-Plathe F 2009 Are there stable ion-pairs in room-temperature ionic liquids? Molecular dynamics simulations of 1-n-butyl-3-methylimidazolium hexafluorophosphate *J. Am. Chem. Soc.* **131** 15825–33

[19]   Aschenbrenner O, Supasitmongkol S, Taylor M and Styring P 2009 Measurement of vapour pressures of ionic liquids and other low vapour pressure solvents *Green Chem.* **11** 1217–21

[20]   Bier M and Dietrich S 2010 Vapour pressure of ionic liquids *Mol. Phys.* **108** 211–4

[21]   Yoshizawa M, Xu W and Angell C A 2003 Ionic Liquids by Proton Transfer: Vapor Pressure, Conductivity, and the Relevance of ΔpKa from Aqueous Solutions *J. Am. Chem. Soc.* **125** 15411–9

[22]   Earle M J, Esperança J M S S, Gilea M A, Lopes J N C, Rebelo L P N, Magee J W, Seddon K R and Widegren J A 2006 The distillation and volatility of ionic liquids *Nature* **439** 831–4

[23]   Del Sesto R E, Corley C, Robertson A and Wilkes J S 2005 Tetraalkylphosphonium-based ionic liquids *J. Organomet. Chem.* **690** 2536–42

[24]   Wei M, Huang A C, Shu C M and Zhang L 2019 Thermal Decomposition and Nonisothermal Kinetics of Monoethanolamine Mixed with Various Metal Ions *Sci. Rep.* **9** 1–9

[25]   Akçay A, Balci V and Uzun A 2014 Structural factors controlling thermal stability of imidazolium ionic liquids with 1-n-butyl-3-methylimidazolium cation on γ-Al_2O_3 *Thermochim. Acta* **589** 131–6

[26]   Babucci M, Akçay A, Balci V and Uzun A 2015 Thermal Stability Limits of Imidazolium Ionic Liquids Immobilized on Metal-Oxides *Langmuir* **31** 9163–76

[27]   Welton T 2018 Ionic liquids: a brief history *Biophys. Rev.* **10** 691–706

[28]   Marsh K N, Boxall J A and Lichtenthaler R 2004 Room temperature ionic liquids and their mixtures - A review *Fluid Phase Equilib.* **219** 93–8

[29]   Holbrey J D and Seddon K R 1999 The phase behaviour of 1-alkyl-3-methylimidazolium Tetrafluoroborates ; Ionic Liquids and Ionic Liquid Crystals *J. Chem. Soc. Dalt. Trans.* **13** 2133–40

[30]   Fannin A A, Floreani D A, King L A, Landers J S, Piersma B J, Stech D J, Vaughn R L, Wilkes J S and Williams J L 1984 Properties of 1,3-dialkylimidazolium chloride-aluminum chloride ionic liquids. 2. Phase transitions, densities, electrical conductivities, and viscosities *J. Phys. Chem.* **88** 2614–21

[31]   Ivanov M Y, Surovtsev N V. and Fedin M V. 2022 Ionic liquid glasses: properties and applications *Russ. Chem. Rev.* **91** RCR5031

[32]   Mantz R A and Trulove P C 2008 *Ionic Liquids in Synthesis. Chapter 3.* vol 1, ed P Wasserscheid and T Welton

[33]   Tshemese Z, Masikane S C, Mlowe S and Revaprasadu N 2018 Progress in Green Solvents for the Stabilisation of Nanomaterials: Imidazolium Based Ionic Liquids *Recent Advances in Ionic Liquids* (InTech)

[34]   Endres F 2002 Ionic liquids: Solvents for the electrodeposition of metals and semiconductors *ChemPhysChem* **3** 144–54

[35]   Kroon M C, Buijs W, Peters C J and Witkamp G-J 2006 Decomposition of ionic liquids in electrochemical processing *Green Chem.* **8** 241–5

[36]   Hagiwara R and Ito Y 2000 Room temperature ionic liquids of alkylimidazolium cations and fluoroanions *J. Fluor. Chem.* **105** 221–7

[37]   Galiński M, Lewandowski A and Stepniak I 2006 Ionic liquids as electrolytes *Electrochim. Acta* **51** 5567–80

[38]   Mantz R A and Trulove P C 2008 Physicochemical Properties of Ionic Liquids *Ionic Liquids in Synthesis.* vol 1, ed P Wasserscheid and T Welton pp 863–4

[39]   Minami I 2009 Ionic liquids in tribology *Molecules* **14** 2286–305

[40]   Jiang S, Hu Y, Wang Y and Wang X 2019 Viscosity of Typical Room-Temperature Ionic Liquids: A Critical Review *J. Phys. Chem. Ref. Data* **48**

[41]   Babamohammadi S, Shamiri A and Aroua M K 2015 A review of CO_2 capture by absorption in ionic liquid-based solvents *Rev. Chem. Eng.* **31** 383–412

[42]   Cremer T, Killian M, Gottfried J M, Paape N, Wasserscheid P, Maier F and Steinrück H P 2008 Physical vapor deposition of [EMIM][Tf2N]: A new approach to the modification of surface properties with ultrathin ionic liquid films *ChemPhysChem* **9** 2185–90

[43]   Deyko A, Cremer T, Rietzler F, Perkin S, Crowhurst L, Welton T, Steinrück H P and Maier F 2013 Interfacial behavior of thin ionic liquid films on mica *J. Phys. Chem. C* **117** 5101–11

[44]   Cremer T, Stark M, Deyko A, Steinrück H-P and Maier F 2011 Liquid/Solid Interface of Ultrathin Ionic Liquid Films: $[C_1C_1Im][Tf2N]$ and $[C_8C_1Im][Tf2N]$ on Au(111) *Langmuir* **27** 3662–71

[45]   Cremer T, Wibmer L, Calderón S K, Deyko A, Maier F and Steinrück H P 2012 Interfaces of ionic liquids and transition metal surfaces - Adsorption, growth, and thermal reactions of ultrathin $[C_1C_1Im]$ [Tf2N] films on metallic and oxidised Ni(111) surfaces *Phys. Chem. Chem. Phys.* **14** 5153–63

[46]   Mezger M, Schröder H, Reichert H, Schramm S, Okasinski J S, Schöder S, Honkimäki V, Deutsch M, Ocko B M, Ralston J, Rohwerder M, Stratmann M and Dosch H 2008 Molecular Layering of Fluorinated Ionic Liquids at a Charged Sapphire (0001) Surface *Science (80-.).* **322** 424–8

[47]   Lazzeri M, Vittadini A and Selloni A 2001 Structure and energetics of stoichiometric TiO_2 anatase surfaces *Phys. Rev. B* **63** 1554091–9

[48]   Weber H, Bredow T and Kirchner B 2015 Adsorption Behavior of the 1,3-Dimethylimidazolium Thiocyanate and Tetracyanoborate Ionic Liquids at Anatase (101) Surface *J. Phys. Chem. C* **119** 15137–49

[49]   Wagstaffe M, Jackman M J, Syres K L, Generalov A and Thomas A G 2016 Ionic Liquid Ordering at an Oxide Surface *ChemPhysChem* **17** 3430–4

[50]   Babucci M, Balci V, Akçay A and Uzun A 2016 Interactions of $[BMIM][BF_4]$ with Metal Oxides and Their Consequences on Stability Limits *J. Phys. Chem. C* **120** 20089–102

[51]   Lockett V, Sedev R, Bassell C and Ralston J 2008 Angle-resolved X-ray photoelectron spectroscopy of the surface of imidazolium ionic liquids *Phys. Chem. Chem. Phys.* **10** 1330–5

[52]   Iwahashi T, Nishi T, Yamane H, Miyamae T, Kanai K, Seki K, Kim D and Ouchi Y 2009 Surface structural study on ionic liquids using metastable atom electron spectroscopy *J. Phys. Chem. C* **113** 19237–43

[53]   Yan T, Li S, Jiang W, Gao X, Xiang B and Voth G A 2006 Structure of the liquid-vacuum interface of room-temperature ionic liquids: A molecular dynamics study *J. Phys. Chem. B* **110** 1800–6

[54]   Lovelock K R J 2012 Influence of the ionic liquid/gas surface on ionic liquid chemistry *Phys. Chem. Chem. Phys.* **14** 5071–89

[55]   Henderson Z, Walton A S, Thomas A G and Syres K L 2018 Water-induced reordering in ultrathin ionic liquid films *J. Phys. Condens. Matter* **30** 334003

[56]   Rivera-Rubero S and Baldelli S 2004 Influence of water on the surface of hydrophilic and hydrophobic room-temperature ionic liquids *J. Am. Chem. Soc.* **126** 11788–9

[57]   Kohno Y and Ohno H 2012 Ionic liquid/water mixtures: From hostility to conciliation *Chem. Commun.* **48** 7119–30

[58]   Gutowski K E, Broker G A, Willauer H D, Huddleston J G, Swatloski R P, Holbrey J D and Rogers R D 2003 Controlling the aqueous miscibility of ionic liquids: Aqueous biphasic systems of water-miscible ionic liquids and water-structuring salts for recycle, metathesis, and separations *J. Am. Chem. Soc.* **125** 6632–3

[59]   Omar S, Lemus J, Ruiz E, Ferro V R, Ortega J and Palomar J 2014 Ionic liquid mixtures - An analysis of their mutual miscibility *J. Phys. Chem. B* **118** 2442–50

[60]   McCrellis C, Taylor S F R, Jacquemin J and Hardacre C 2016 Effect of the Presence of MEA on the CO_2 Capture Ability of Superbase Ionic Liquids *J. Chem. Eng. Data* **61** 1092–100

[61]   Grinter D C, Graciani J, Palomino R M, Xu F, Waluyo I, Sanz J F, Senanayake S D and Rodriguez J A 2021 Adsorption and activation of CO_2 on $Pt/CeO_x/TiO_2(110)$: Role of the $Pt-CeO_x$ interface *Surf. Sci.* **710** 1–8

[62]   Freund H-J, Kuhlenbeck H and Staemmler V 1996 Oxide surfaces *Reports Prog. Phys.* **59** 283–347

[63]   Zhang J, Zhou P, Liu J and Yu J 2014 New understanding of the difference of photocatalytic activity among anatase, rutile and brookite TiO_2 *Phys. Chem. Chem. Phys.* **16** 20382–6

[64]   Malali S and Foroutan M 2017 Study of Wetting Behavior of $BMIM^+/PF_6^-$ Ionic Liquid on TiO_2 (110) Surface by Molecular Dynamics Simulation *J. Phys. Chem. C* **121** 11226–33

[65]   Liu L, Li S, Cao Z, Peng Y, Li G, Yan T and Gao X P 2007 Well-ordered structure at ionic liquid/rutile (110) interface *J. Phys. Chem. C* **111** 12161–4

[66]   Uhl B, Hekmatfar M, Buchner F and Behm R J 2016 Interaction of the ionic liquid [BMP][TFSA] with rutile TiO_2 (110) and coadsorbed lithium *Phys. Chem. Chem. Phys.* **18** 6618–36

[67]   Li C, Lu D and Wu C 2018 The role of cations in the interactions between anionic N-heterocycles and SO_2 *Sci. Rep.* **8** 1–9

[68]   Greer A J, Jacquemin J and Hardacre C 2020 Industrial applications of ionic liquids *Molecules* **25** 1–31

[69]   Huang J and Rüther T 2009 Why are ionic liquids attractive for CO_2 absorption? An overview *Aust. J. Chem.* **62** 298–308

[70]   Welton T 2004 Ionic liquids in catalysis *Coord. Chem. Rev.* **248** 2459–77

[71]   Steinrück H P and Wasserscheid P 2015 Ionic liquids in catalysis *Catal. Letters* **145** 380–97

[72]   Lewandowski A and Świderska-Mocek A 2009 Ionic liquids as electrolytes for Li-ion batteries-An overview of electrochemical studies *J. Power Sources* **194** 601–9

[73]   Eftekhari A, Liu Y and Chen P 2016 Different roles of ionic liquids in lithium batteries *J. Power Sources* **334** 221–39

[74]   Macfarlane D R, Tachikawa N, Forsyth M, Pringle J M, Howlett P C, Elliott G D, Davis J H, Watanabe M, Simon P and Angell C A 2014 Energy applications of ionic liquids *Energy Environ. Sci.* **7** 232–50

[75]   Somers A E, Howlett P C, MacFarlane D R and Forsyth M 2013 A review of ionic liquid lubricants *Lubricants* **1** 3–21

[76]   Zhou F, Liang Y and Liu W 2009 Ionic liquid lubricants: Designed chemistry for engineering applications *Chem. Soc. Rev.* **38** 2590–9

[77]   Li H, Qu J, Cui Q, Xu H, Luo H, Chi M, Meisner R A, Wang W and Dai S 2011 TiO_2 nanotube arrays grown in ionic liquids: high-efficiency in photocatalysis and pore-widening *J. Mater. Chem.* **21** 9487

[78]   Li X, Zhao Z and Pan C 2016 Ionic liquid-assisted electrochemical exfoliation of carbon dots of different size for fluorescent imaging of bacteria by tuning the water fraction in electrolyte *Microchim. Acta* **183** 2525–32

[79]   Abu Talip R A, Yahya W Z N and Bustam M A 2020 Ionic Liquids Roles and Perspectives in Electrolyte for Dye-Sensitized Solar Cells *Sustainability* **12** 7598

[80]   Zhao Y and Bostrom T 2015 Application of Ionic Liquids in Solar Cells and Batteries: A Review *Curr. Org. Chem.* **19** 556–66

[81]   Roy P, Kim D, Lee K, Spiecker E and Schmuki P 2010 TiO_2 nanotubes and their application in dye-sensitized solar cells *Nanoscale* **2** 45–59

[82]   Bartlewicz O, Dąbek I, Szymańska A and Maciejewski H 2020 Heterogeneous catalysis with the participation of ionic liquids *Catalysts* **10** 1–16

[83]   Zhang G R and Etzold B J M 2021 Emerging Applications of Solid Catalysts with Ionic Liquid Layer Concept in Electrocatalysis *Adv. Funct. Mater.* **31**

[84]   Steinrück H P, Libuda J, Wasserscheid P, Cremer T, Kolbeck C, Laurin M, Maier F, Sobota M, Schulz P S and Stark M 2011 Surface science and model catalysis with ionic liquid-modified materials *Adv. Mater.* **23** 2571–87

[85]   Bagheri S, Muhd Julkapli N and Bee Abd Hamid S 2014 Titanium dioxide as a catalyst support in heterogeneous catalysis *Sci. World J.* **2014**

[86]   Lemus J, Palomar J, Gilarranz M A and Rodriguez J J 2011 Characterization of Supported Ionic Liquid Phase (SILP) materials prepared from different supports *Adsorption* **17** 561–71

[87]   Liu X, Ma J and Zheng W 2011 Applications of ionic liquids (ILs) in the convenient synthesis of nanomaterials *Rev. Adv. Mater. Sci.* **27** 43–51

[88]   Zhu X, Du M, Feng J, Wang H, Xu Z, Wang L, Zuo S, Wang C, Wang Z, Zhang C, Ren X, Priya S, Yang D and Liu S 2021 High-Efficiency Perovskite Solar Cells with Imidazolium-Based Ionic Liquid for Surface Passivation and Charge Transport *Angew. Chemie - Int. Ed.* **60** 4238–44

[89]   Chu W, Yang J, Jiang Q, Li X and Xin J 2018 Enhancement of photovoltaic performance of flexible perovskite solar cells by means of ionic liquid interface modification in a low temperature all solution process *Appl. Surf. Sci.* **440** 1116–22

[90]   Zhang W, Ren Z, Guo Y, He X and Li X 2018 Improved the long-term air stability of ZnO-based perovskite solar cells prepared under ambient conditions via surface modification of the electron transport layer using an ionic liquid *Electrochim. Acta* **268** 539–45

[91]   Yang D, Zhou X, Yang R, Yang Z, Yu W, Wang X, Li C, Liu S and Chang R P H 2016 Surface optimization to eliminate hysteresis for record efficiency planar perovskite solar cells *Energy Environ. Sci.* **9** 3071–8

[92]   Bai S, Da P, Li C, Wang Z, Yuan Z, Fu F, Kawecki M, Liu X, Sakai N, Wang J T W, Huettner S, Buecheler S, Fahlman M, Gao F and Snaith H J 2019 Planar perovskite solar cells with long-term stability using ionic liquid additives *Nature* **571** 245–50

[93]   Jewell J, Vinichenko V, Nacke L and Cherp A 2019 Prospects for powering past coal *Nat. Clim. Chang.* **9** 592–7

[94]   Kabeyi M J B and Olanrewaju O A 2022 Sustainable Energy Transition for Renewable and Low Carbon Grid Electricity Generation and Supply *Front. Energy Res.* **9** 1–45

[95]   Ma Y, Gao J, Wang Y, Hu J and Cui P 2018 Ionic liquid-based CO_2 capture in power plants for low carbon emissions *Int. J. Greenh. Gas Control* **75** 134–9

[96]   Øi L E 2012 Comparison of aspen HYSYS and aspen plus simulation of CO_2 absorption into MEA from atmospheric gas *Energy Procedia* **23** 360–9

[97]   Salvinder K M S, Zabiri H, Taqvi S A, Ramasamy M, Isa F, Rozali N E M, Suleman H, Maulud A and Shariff A M 2019 An overview on control strategies for CO_2 capture using absorption/stripping system *Chem. Eng. Res. Des.* **147** 319–37

[98]   D'Alessandro D M, Smit B and Long J R 2010 Carbon dioxide capture: Prospects for new materials *Angew. Chemie - Int. Ed.* **49** 6058–82

[99]   Yang J, Tan H Y, Low Q X, Binks B P and Chin J M 2015 CO_2 capture by dry alkanolamines and an efficient microwave regeneration process *J. Mater. Chem. A* **3** 6440–6

[100]   Rao A B and Rubin E S 2006 Identifying cost-effective CO_2 control levels for amine-based CO_2 capture systems *Ind. Eng. Chem. Res.* **45** 2421–9

[101]   Boot-Handford M E, Abanades J C, Anthony E J, Blunt M J, Brandani S, Mac Dowell N, Fernández J R, Ferrari M C, Gross R, Hallett J P, Haszeldine R S, Heptonstall P, Lyngfelt A, Makuch Z, Mangano E, Porter R T J, Pourkashanian M, Rochelle G T, Shah N, Yao J G and Fennell P S 2014 Carbon capture and storage update *Energy Environ. Sci.* **7** 130–89

[102]   Cuéllar-Franca R M and Azapagic A 2015 Carbon capture, storage and utilisation technologies: A critical analysis and comparison of their life cycle environmental impacts *J. CO_2 Util.* **9** 82–102

[103]   Liang Z, Rongwong W, Liu H, Fu K, Gao H, Cao F, Zhang R, Sema T, Henni A, Sumon K, Nath D, Gelowitz D, Srisang W, Saiwan C, Benamor A, Al-Marri M, Shi H, Supap T, Chan C, Zhou Q, Abu-Zahra M, Wilson M, Olson W, Idem R and Tontiwachwuthikul P 2015 Recent progress and new developments in post-combustion carbon-capture technology with amine based solvents *Int. J. Greenh. Gas Control* **40** 26–54

[104]   Samanta A, Zhao A, Shimizu G K H, Sarkar P and Gupta R 2012 Post-Combustion CO_2 Capture Using Solid Sorbents: A Review *Ind. Eng. Chem. Res.* **51** 1438–63

[105]   Kumar S, Srivastava R and Koh J 2020 Utilization of zeolites as CO2capturing agents: Advances and future perspectives *J. CO_2 Util.* **41** 101251

[106]   Hu Z, Wang Y, Shah B B and Zhao D 2019 CO_2 Capture in Metal-Organic Framework Adsorbents: An Engineering Perspective *Adv. Sustain. Syst.* **3** 1800080

[107]   Trickett C A, Helal A, Al-Maythalony B A, Yamani Z H, Cordova K E and Yaghi O M 2017 The chemistry of metal-organic frameworks for CO_2 capture, regeneration and conversion *Nat. Rev. Mater.* **2** 1–16

[108]   Ozkan M and Custelcean R 2022 The status and prospects of materials for carbon capture technologies *MRS Bull.* **47** 390–4

[109]   Yu C H, Huang C H and Tan C S 2012 A review of CO_2 capture by absorption and adsorption *Aerosol Air Qual. Res.* **12** 745–69

[110]   Cuéllar-Franca R M, García-Gutiérrez P, Taylor S F R, Hardacre C and Azapagic A 2016 A novel methodology for assessing the environmental sustainability of ionic liquids used for CO_2 capture *Faraday Discuss.* **192** 283–301

[111]   Bates E D, Mayton R D, Ntai I and Davis J H 2002 CO_2 capture by a task-specific ionic liquid *J. Am. Chem. Soc.* **124** 926–7

[112]   Aghaie M, Rezaei N and Zendehboudi S 2018 A systematic review on CO_2 capture with ionic liquids: Current status and future prospects *Renew. Sustain. Energy Rev.* **96** 502–25

[113]   Lei Z, Dai C and Chen B 2014 Gas solubility in ionic liquids *Chem. Rev.* **114** 1289–326

[114]   Zhang X, Zhang X, Dong H, Zhao Z, Zhang S and Huang Y 2012 Carbon capture with ionic liquids: Overview and progress *Energy Environ. Sci.* **5** 6668–81

[115]   Babamohammadi S, Shamiri A and Aroua M K 2015 A review of CO_2 capture by absorption in ionic liquid-based solvents *Rev. Chem. Eng.* **31** 383–412

[116]   Wang C, Luo X, Luo H, Jiang D, Li H and Dai S 2011 Tuning the basicity of ionic liquids for equimolar CO_2 capture *Angew. Chemie* **123** 5020–4

[117]   Greer A J, Taylor S F R, Daly H, Quesne M, Catlow C R A, Jacquemin J and Hardacre C 2019 Investigating the effect of NO on the capture of CO_2 using superbase ionic liquids for flue gas applications *ACS Sustain. Chem. Eng.* **7** 3567–74

[118]   Taylor S F R, McCrellis C, McStay C, Jacquemin J, Hardacre C, Mercy M, Bell R G and De Leeuw N H 2015 CO2 capture in wet and dry superbase ionic liquids *J. Solution Chem.* **44** 511–27

[119]   Mercy M, Rebecca Taylor S F, Jacquemin J, Hardacre C, Bell R G and De Leeuw N H 2015 The addition of CO_2 to four superbase ionic liquids: a DFT study *Phys. Chem. Chem. Phys.* **17** 28674–82

[120]   Hollingsworth N, Taylor S F R, Galante M T, Jacquemin J, Longo C, Holt K B, De Leeuw N H and Hardacre C 2015 CO_2 capture and electrochemical conversion using superbasic [P_{66614}][124Triz] *Faraday Discuss.* **183** 389–400

[121]   Porter R T J, Fairweather M, Pourkashanian M and Woolley R M 2015 The range and level of impurities in CO_2 streams from different carbon capture sources *Int. J. Greenh. Gas Control* **36** 161–74

[122]   Xu X, Song C, Wincek R, Andresen J M, Miller B G and Scaroni A W 2003 Separation of CO_2 from Power Plant Flue Gas Using a Novel CO_2 "Molecular Basket" Adsorbent *ACS Div. Fuel Chem. Prepr.* **48** 162–3

[123]   Taylor S F R, McClung M, McReynolds C, Daly H, Greer A J, Jacquemin J and Hardacre C 2018 Understanding the Competitive Gas Absorption of CO_2 and SO_2 in Superbase Ionic Liquids *Ind. Eng. Chem. Res.* **57** 17033–42

[124]   Henderson Z, Thomas A G, Wagstaffe M, Taylor S F R, Hardacre C and Syres K L 2019 Reversible reaction of CO_2 with superbasic ionic liquid [P_{66614}][benzim] studied with in situ photoelectron spectroscopy *J. Phys. Chem. C* **123** 7134–41

[125]   Greer A J, Taylor S F R, Daly H, Jacquemin J and Hardacre C 2022 Combined Superbase Ionic Liquid Approach to Separate CO_2 from Flue Gas *ACS Sustain. Chem. Eng.* **10** 9453–9

Chapter 3. Surface Science Techniques and Theory

This chapter contains a summary of the theory and instrumentation of two surface-sensitive techniques used in this thesis: X-ray photoelectron spectroscopy and near-edge X-ray absorption fine structure.

3.1 X-ray Photoelectron Spectroscopy (XPS)

X-ray photoelectron spectroscopy is a non-destructive, surface-sensitive technique that utilises the photoemission of core level electrons using soft X-rays. XPS is routinely used to investigate the elemental composition, electronic states, and surface chemistry of a wide range of materials. These include but are not limited to organic and inorganic compounds, semiconductors, biomolecules, thin films and adsorbates, and nanostructures.

3.1.1 Theory

Core level photoemission

X-ray Photoemission
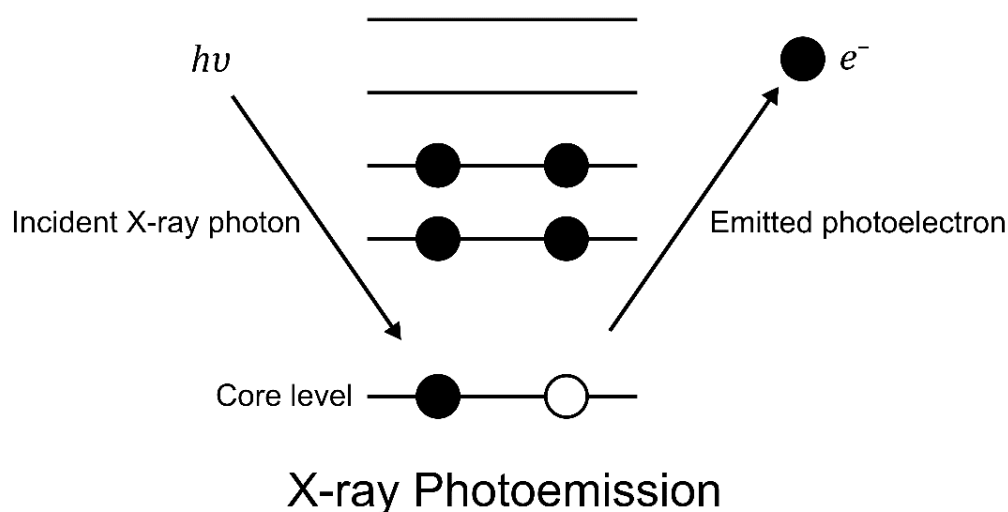
Figure 3.1. Energy level diagram showing the emission of a photoelectron via the excitation of a core level electron by an X-ray photon.

Photoemission can be described as the excitation and subsequent ejection of electrons from their atoms by the absorption of incoming photons as shown in Figure 3.1. In XPS the absorption of soft X-rays (ranging from about 100 to a few thousand eV in energy) results in the photoemission of core level electrons. The kinetic energy, E_K, of the emitted photoelectron is a function of its binding energy (BE) in the atom it was ejected from. The BE of an electron is characteristic of both the electronic state it occupies and the atom in which it resides. BE can be calculated by using Einstein's photoelectric effect equation,

$$BE = h\nu - E_K - \varphi_{spec} \tag{3.1}$$

where $h\nu$ is the X-ray photon energy and φ_{spec} is the work function of the spectrometer. The work function is defined as the energy required to remove an electron from the Fermi level to the vacuum level (see Figure 3.2). The sample is in electrical contact with the spectrometer, so in practice the work function of the spectrometer is measured, not the work function of the sample. BE is typically referenced to the Fermi level for electrons in solids [1].
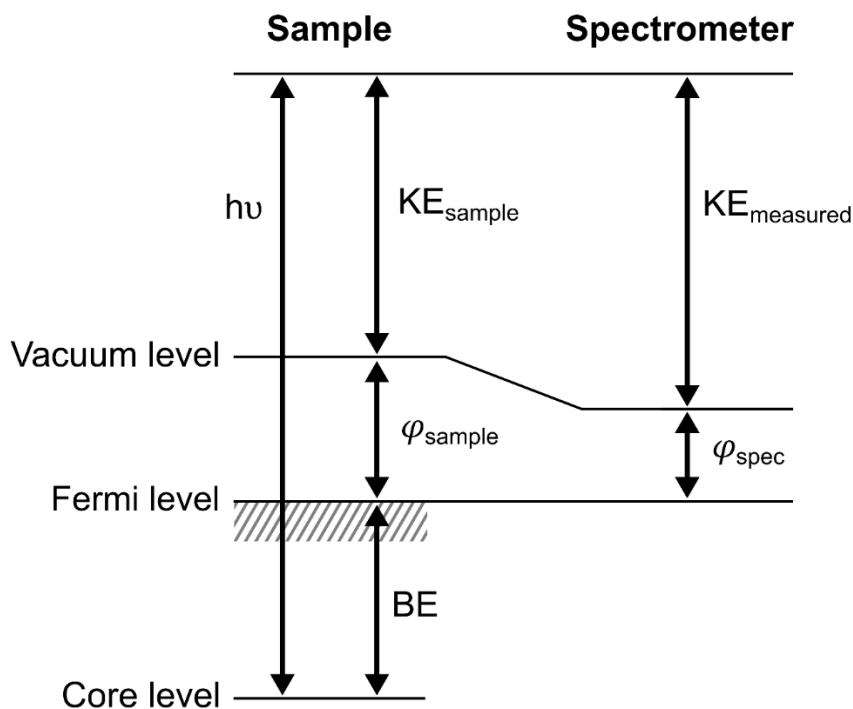
Figure 3.2. Energy level diagram of a core level electron in a sample that is in electrical contact with an electron energy analyser. Adapted from [2].

X-ray sources for lab based XPS include Al Kα and Mg Kα which have fixed photon energies, hv, of 1486.6 eV and 1254.6 eV, respectively. This distinguishes XPS from other photoemission techniques such as ultraviolet photoelectron spectroscopy (UPS) which uses lower energy light to probe valence electrons. Synchrotron facilities allow the X-ray energy to be varied as described in Section 3.3.3.

Sampling depth and depth profiling
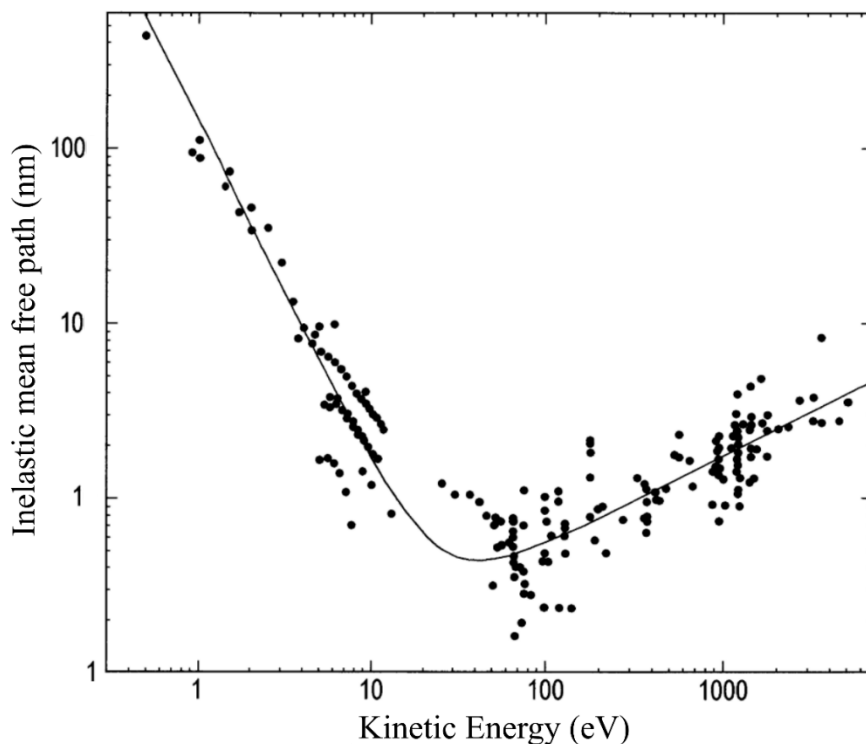
Figure 3.3. Experimental data of the inelastic mean free path of electrons as a function of their kinetic energy for various materials. Reproduced from [3].

XPS is described as a surface sensitive technique due to its small sampling depth (~ 1 – 10 nm). Photoelectrons can be created a few microns into the sample surface but experience large energy losses due to inelastic scattering. This scattering can be quantified as the inelastic mean free path (IMPF), λ, defined as the average distance an electron travels between two successive inelastic collisions as a function of E_K. The IMFP curve is shown in Figure 3.3. The IMFP is at a minimum (less than 1 nm) when E_K is approximately 20 – 200 eV. Photoelectrons have small mean free paths in solids and only those generated within a few nanometres of the surface can

41

escape without significant energy loss. 95% of XPS signal intensity comes from a depth 3λ.

Sampling depth, d, is given by.

$$d = 3\lambda \sin \theta \qquad (3.2)$$

where θ is the angle at which the photoelectron is emitted with respect to the sample surface, as shown in Figure 3.4. For most materials bombarded with Al Kα X-rays, λ = 1 – 3 nm. Therefore, the maximum sampling depth of conventional XPS is typically ~ 10 nm (at θ = 90°). As electrons can only escape through 3λ of material, smaller angles of θ results in a smaller vertical sampling depth d as shown in Figure 3.4. The sample can be oriented such that the electron energy analyser detects these surface sensitive electrons at what is called grazing emission (GE). Electrons escaping perpendicular to the surface have the largest possible sampling depth and are detected at normal emission (NE). Comparison of GE and NE measurements provides insights into the different chemical and elemental states found at the surface compared to the deeper layers of the sample, respectively. These depth profiling measurements are useful for characterising surface contaminants, ab/adsorbates and oxidation of the sample surface.
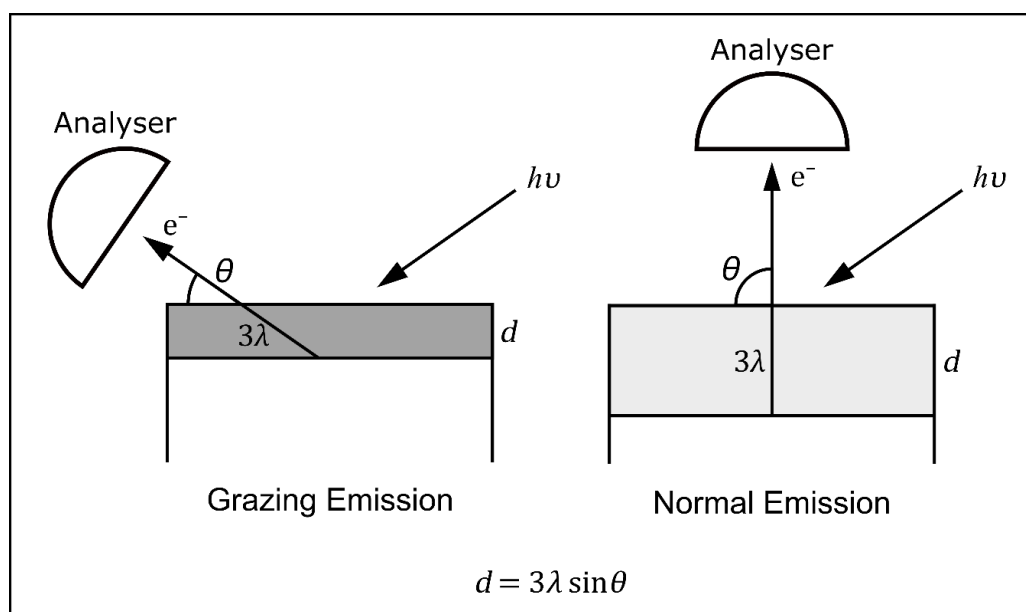
Figure 3.4. Sampling depth, d, changing with emission angle, θ, of the photoelectron for grazing and normal emission. Adapted from [4].

42

Sampling depth can also be altered by changing the photon energy at synchrotron facilities. Synchrotron beamlines used for XPS have tuneable photon energies and typically operate in a soft X-ray photon energy range of approximately 45 - 2800 eV [5]. For example, increasing the photon energy increases the E_K of electrons emitted from a particular orbital. Electrons with higher E_K have a larger λ, resulting in a larger sampling depth.

The attenuation of electrons in a material can be described by the Beer-Lambert Law,

$$I = I_0 \exp\left(\frac{-x}{\lambda \sin\theta}\right)$$

(3.3)

where I_0 is the original intensity and I is the measured intensity after travelling distance x through the material. Another important parameter describing the intensity of an XPS signal is the photoelectric cross section, σ. This is the probability that a core level electron originating from a specific element is excited by a photon of specific energy. Cross sections vary with atomic number Z and the electron orbital being excited (i.e., 1s, 2s, 2p, etc). The excitation cross section is highest when the photon energy is approximately equal to the core level BE.

<u>Electron detection</u>

In XPS the number and kinetic energy of the photoelectrons is measured using a hemispherical electron energy analyser, shown schematically in Figure 3.5. Electrons escape the sample in many directions with a range of kinetic energies. Electrons emitted from the sample are first focused by an electrostatic lens system into a beam smaller than the size of the entrance slits of the analyser. E_K of the electrons is also reduced to a value called the pass energy before entering the analyser. The role of the analyser is to only allow electrons of a specific E_K to reach the detector.

The hemispherical analyser consists of two concentric hemispherical electrodes with different radii. The outer hemisphere has a negative potential while the inner hemisphere has a positive potential. Electrons travel in the space between the electrodes, and the degree to which the electrons are deflected by the potential

difference depends on their E_K. Electrons with E_K higher than the pass energy will not be sufficiently deflected and will hit the outer hemisphere. Electrons with E_K lower than the pass energy will hit the inner hemisphere. Therefore, only electrons with E_K similar to the pass energy will reach the detector. Electrons are typically detected by a channeltron or a microchannel plate and their signal is amplified using secondary electron emission in order to produce a measurable current.
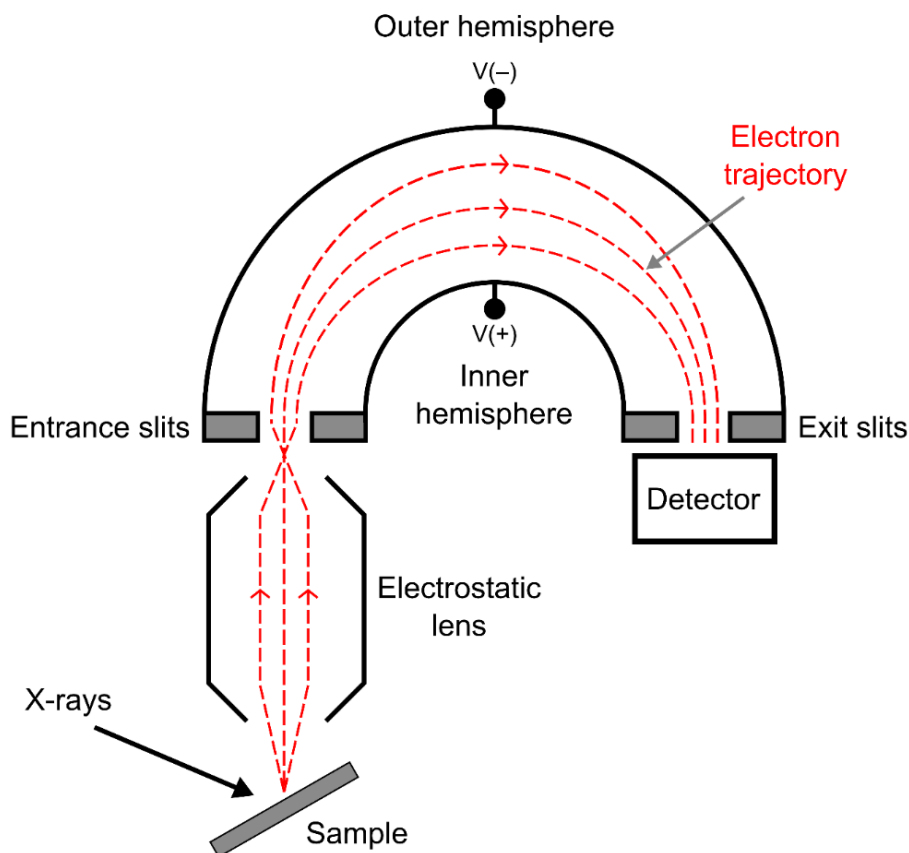
Figure 3.5. Schematic cross section of a hemispherical electron energy analyser. Electrons collected from the sample are focused using an electrostatic lens. Dotted lines show the trajectory of electrons deflected by the potential difference between the two hemispherical electrodes before reaching the detector. Adapted from [3].

Spin orbit splitting

Core level electrons detected in XPS originate from s, p, d and f atomic orbitals. A core level can be described by a set of four quantum numbers. The principal quantum number, n, takes integer values starting from 1 and denotes the shell from

which the electron was ejected. The total angular momentum quantum number, j, is given as $j = l \pm s$ and takes integer values between $|l - s| \leq j \leq |l + s|$. The angular momentum quantum number, l, relates to the orbital, taking values of 0, 1, 2, 3 for orbitals s, p, d, f, respectively. The spin angular momentum number, s, is equal to $\pm 1/2$ depending on whether the electron spin is parallel or antiparallel to the orbital angular momentum.
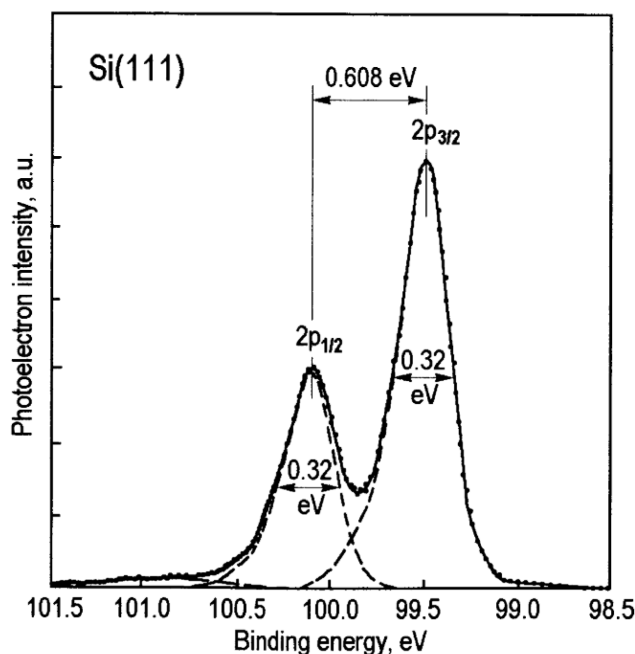
Figure 3.6. XPS Si 2p doublet of a Si(111) surface. The two peaks $2p_{1/2}$ and $2p_{3/2}$ have the same full width at half maximum (0.32 eV), a spin orbit separation of 0.608 eV and an area ratio of 1:2. Reproduced from [3].

For the s orbital, $j = 1/2$ and results in a single peak in XPS spectra. Spin orbit splitting occurs when electrons are excited from higher orbitals for which $l > 0$, resulting in two sublevels with degeneracy $2j + 1$. This manifests as a split peak, or a doublet (shown in Figure 3.6). For example, in p orbitals $j = 1/2$ or $3/2$ (see Table 3.1 for further examples). Therefore, the two spin orbit peaks in a p doublet are assigned as $p_{1/2}$ and $p_{3/2}$, where the $p_{1/2}$ peak occurs at a higher BE. The BE separation of spin orbit peaks is fixed and is specific to the orbital and element. The area ratio of these peaks is given as $(2j^- + 1)/(2j^+ + 1)$. For p orbitals, $j^- = 1/2$ and $j^+ = 3/2$ and, therefore, $p_{1/2}$ and $p_{3/2}$ peaks have an area ratio of 1:2. An example of spin orbit splitting of the Si 2p peak is shown in Figure 3.6. Note that peaks in XPS are labelled

45

by their element, n, orbital, and j. For example, a Si $2p_{3/2}$ peak indicates electrons that are excited from the 2p orbital of a silicon atom with $j = 3/2$.

Orbital	j values: (j^-, j^+)	Area Ratio: $(j^- : j^+)$
s $(l = 0)$	1/2 (singlet)	–
p $(l = 1)$	1/2, 3/2	1: 2
d $(l = 2)$	3/2, 5/2	2: 3
f $(l = 3)$	5/2, 7/2	3: 4

Table 3.1. Spin orbit splitting j values and doublet peak area ratios for s, p, d, and f orbitals.

3.1.2 Near-Ambient Pressure XPS (NAP-XPS)

Electrons have short mean free paths, approximately 68 nm in air at ambient conditions. XPS is conventionally carried out at ultra-high vacuum (UHV), approximately 10^{-9} mbar, in order to limit the attenuation of electrons. Recent advancements in electron optics have driven development of XPS to near-ambient pressures (up to about 20 mbar). NAP-XPS can be carried out using lab- and synchrotron-based X-ray sources. In this technique the sample is either placed in an analysis chamber backfilled with gas or is housed within a NAP cell into which gases can be introduced. The use of a NAP cell ensures that UHV is maintained in the rest of the analysis chamber. X-rays enter the NAP cell through an X-ray window coated with a thin film of silicon nitride. This film can range from nm – μm in thickness and is designed to limit X-ray absorption by the window material. To overcome the attenuation of electrons through the gas the distance between the sample surface and analyser cone aperture, z, is small (see Figure 3.7(a)). Depending on the equipment, z is typically a similar distance as the aperture diameter (less than 1 mm). Greater than 1 bar of pressure has been achieved by state-of-the-art beamlines such as P22 at PETRAIII synchrotron (DESY, Hamburg) by using hard X-ray photoelectron spectroscopy (HAXPES) and an analyser cone working distance of only a few μm [6,7].

As the cone aperture is under a few mbar of pressure while the analyser is held at UHV, the pressure between must be reduced using a differential pumping system as shown in Figure 3.7(b). Each pumping stage successively reduces the pressure. A series of electrostatic lenses focus the electrons through small apertures separating each pumping stage in order to minimise signal loss.
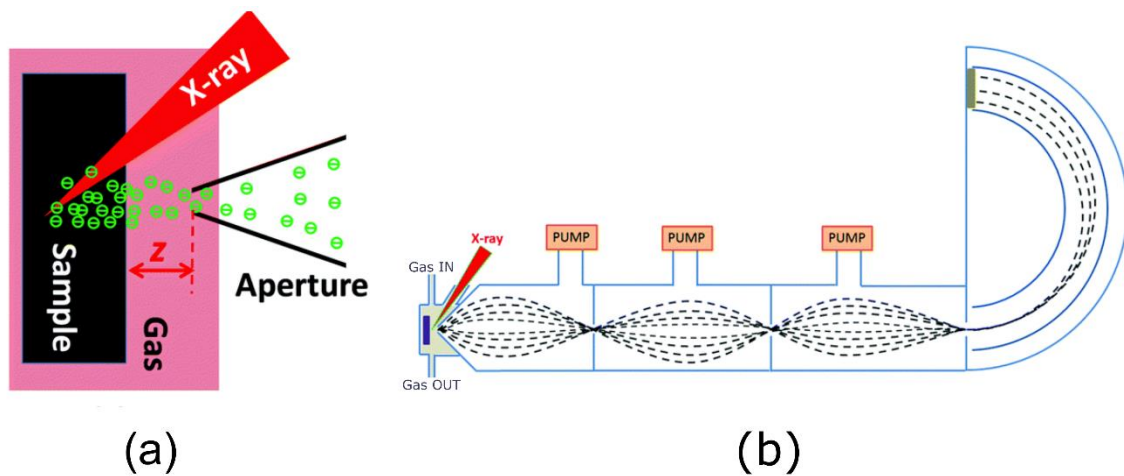
(a)   (b)

Figure 3.7. Illustration (not to scale) of a NAP-cell containing the sample and gas (a) and a schematic cross section of a NAP analyser (b). The aperture of the analyser cone is a small distance, z, away from the sample surface. A series of pumps reduce the pressure from mbar at the aperture to ultra-high vacuum in the analyser. Dotted lines show electron trajectories as they are focused between each pumping stage. Adapted from [8].

Many gases have been studied in NAP-XPS including H_2O, CO_2, CO, NO, N_2, H_2, O_2. Although there has been great effort put into minimising the attenuation of photoelectrons through the gas, NAP-XPS tends to yield lower counts than conventional XPS. This can lead to a poorer signal to noise ratio. Signals from the gas phase are also measured in NAP-XPS, typically manifesting as sharp peaks higher in BE than usual peaks in the same region.

3.1.3 Introduction to XPS Analysis

Although the number and E_K of photoemitted core level electrons are measured by the analyser, XPS spectra are conventionally shown as counts per second against BE. A spectrum in terms of BE is far more useful for the chemical and elemental analysis of the sample. BE is typically plotted in reverse, increasing from right to left, so that the measured photoelectron kinetic energy increases from left to right. An

XPS spectrum consists of sharp peaks corresponding to different core level photoemission. These peaks sit upon a background generated by the detection of inelastically scattered electrons. This is called a survey scan, or wide scan, and an example is shown in Figure 3.8(a).
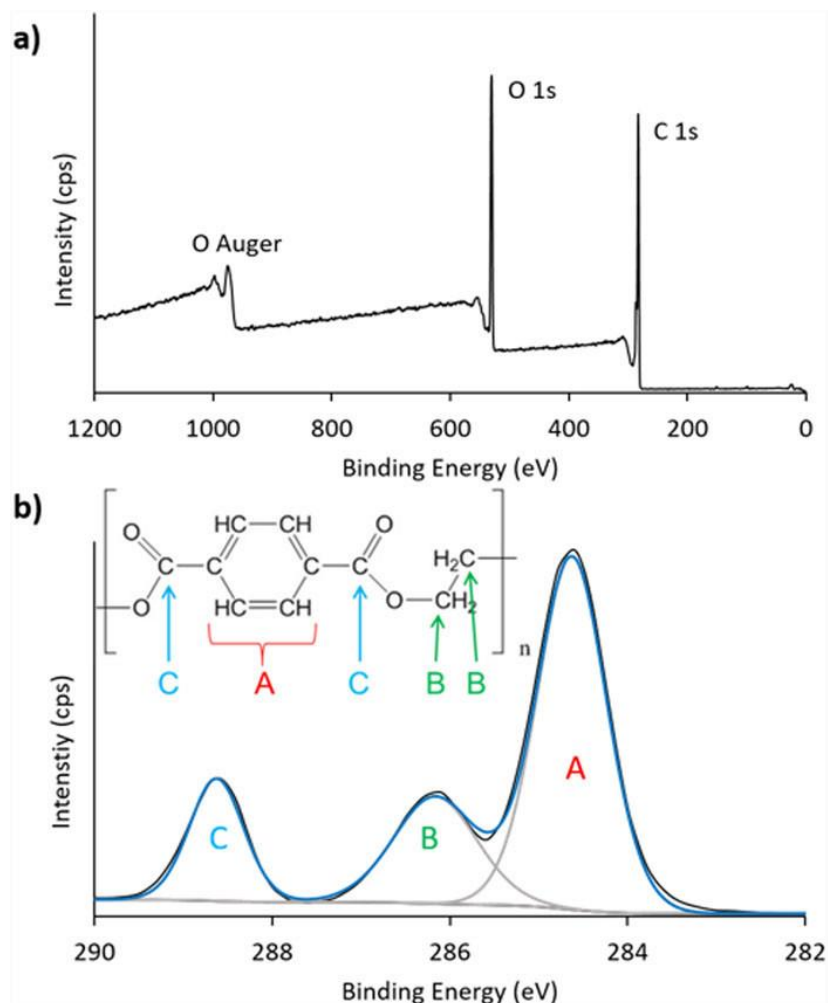
Figure 3.8. Survey scan (a) and a high-resolution C 1s spectrum (b) of polyethylene terephthalate (PET). Chemical assignment of the three C 1s components is also shown. Reproduced from [2].

The sharp peaks in an XPS survey scan occur at characteristic BEs corresponding to specific core level excitations. For example, C 1s denotes excitations from the 1s level of a carbon atom. Subsequent high-resolution scans (taken at finer energy step sizes) are taken over narrow BE regions around the desired peaks (i.e., over the C 1s region). Narrow scans typically contain one or more peaks attributed to specific chemical species. XPS is sensitive to small changes in chemical environment (called

chemical shifts). Each environment has a characteristic BE, giving rise to specific peaks or features in the region. Analysis of XPS spectra involves fitting peaks (or components) to the spectra and assigning each component to a chemical environment in the sample. This peak fitting procedure will be discussed in greater detail below. An example of the chemical assignment of C 1s peaks for polyethylene terephthalate (PET) is shown in Figure 3.8(b).

Peak fitting

XPS spectra are analysed by fitting peaks (which we will call components) to the experimental data. First the background signal must be subtracted from the spectra in the narrow scans. The background signal arises from inelastic scattering of electrons in the material. Inelastic scattering lowers the E_K of electrons, resulting in a background that is more intense on the high BE (low E_K) side of the peak. Common background corrections include linear, Shirley, and Tougaard, as shown in Figure 3.9. All three are commonly used and present their own advantages and disadvantages.
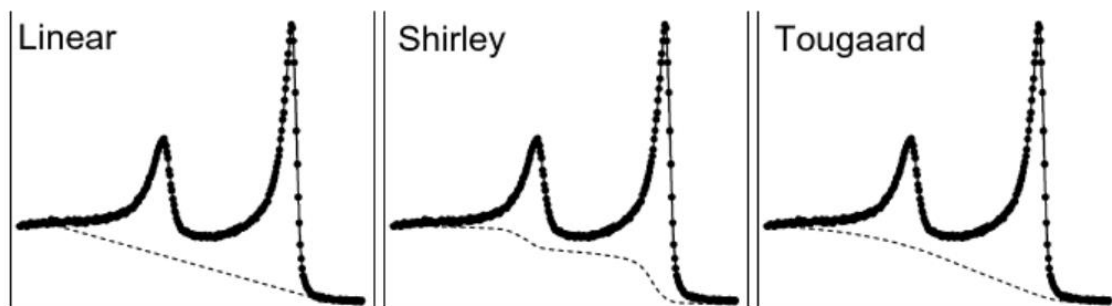
Figure 3.9. Examples of the Linear, Shirley and Tougaard background subtraction for a Fe 2p XPS peak. Reproduced from [1].

Once the background signal is subtracted, components are fitted to the peaks in the narrow scans. These tend to have a symmetrical Gaussian-Lorentzian shape, although some metallic regions can have complex asymmetric peaks with long tails at high BE, such as Fe 2p shown in Figure 3.9. The most common line shapes for fitting components are Gaussian-Lorentzian products, typically with a 30:70 Lorentzian:Gaussian contribution. Peaks can be fitted with one or more components. The sum of the fitted components produces an envelope that is compared to the

experimental peak. Components are fitted until there is good agreement between the envelope and experimental data (so long as each component can still be chemically assigned). An example of a fitted C 1s spectrum is shown in Figure 3.8(b).

An important parameter of the fitted components is their BE as this relates to a distinct chemical state. Therefore, for the fitting to be meaningful, all components must be assigned to a chemical species or environment present in the sample. The BE of common chemical species is well documented in the literature. They are typically known to a narrow range of values as shown in Figure 3.10. Chemical shifts in XPS are changes in BE depending on the chemical bonding of the atom. Atoms bonded to more electronegative atoms appear at higher BEs in XPS spectra. For example, in C–F bonds, electron density is withdrawn from the carbon atom by the electron withdrawing fluorine atom. Core electrons in the carbon atom are therefore more tightly bound to the nucleus due to less screening effects from other electrons. Photoelectrons ejected from the carbon atom in C–F will appear at higher BEs than those from C–C, for example (as shown in Figure 3.10).
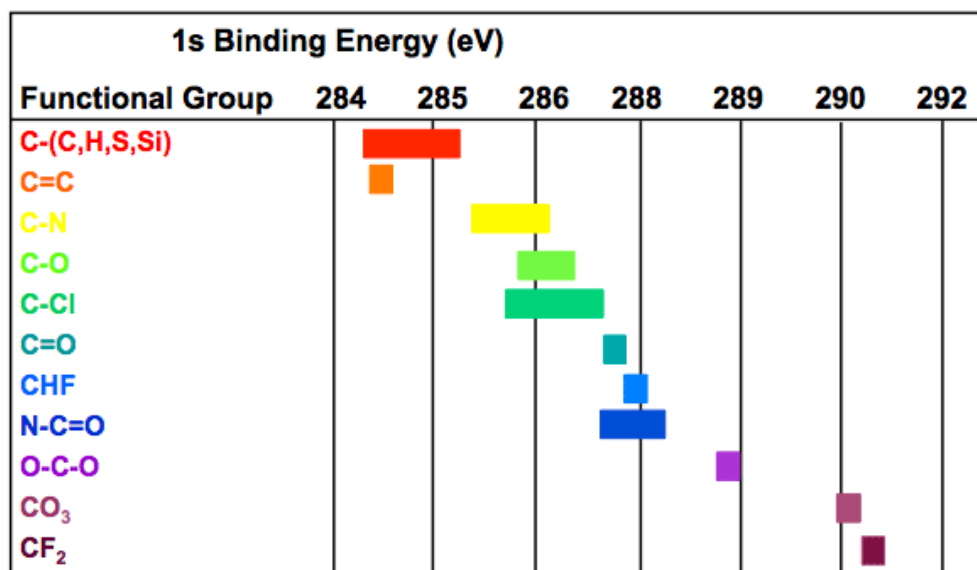
Figure 3.10. XPS binding energy values of common chemical species are known within a narrow energy range. Reproduced from [9].

XPS measurements taken on different samples and/or using different equipment will have small discrepancies in the measured BE of their peaks. This can be due to

changes in surface charge accumulation (as discussed below) and differences in the work functions of the samples and spectrometers. Therefore, XPS spectra must be calibrated by aligning a strong signal found in all of the spectra to a known BE. C 1s is historically the most common peak to calibrate to, where C–C bonds tend to occur at 284.8 – 285.0 eV. A metal peak arising from a substrate can also be used for calibration, for example Ti 2p for TiO_2 substrates. Alternatively, spectra can be calibrated by determining the zero point of the BE scale. The Fermi levels of a sample and the spectrometer align when they are in electrical contact, as shown earlier in Figure 3.2. A Fermi edge spectrum can be measured from the metal sample plate (the spectrum shows a step-like drop of signal at the highest occupied state) and this edge is calibrated to BE = 0 eV.

The full width at half maximum (FHWM) of an XPS peak is a combination of natural width of the signal (Lorentzian line shape) and experimental resolution (Gaussian). The natural width is governed by the lifetime of the core hole excited state while experimental broadening is determined by the width of the X-ray line and analyser resolution. It is common that components within the same narrow scan will have the same FWHM so this can be constrained to the same value.

The area of a narrow region is proportional to the concentration of atoms of that element. For the comparison of areas to be meaningful, they must be normalised by their relative sensitivity factor (RSF). These empirically defined RSFs depend on the element of the narrow region. They ensure that the ratio of the areas of different regions accurately describes their relative elemental concentration [10]. For example, the ratio of a C 1s region area to the areas of all other regions gives the relative atomic concentration of carbon in the sample. As such XPS is a powerful analytical technique for determining the elemental composition of a sample.

Other XPS peaks and losses

Photoexcitation of a core level electron leaves behind a core hole that can be filled by an outer shell electron. The energy released in this process can result in the emission of an Auger electron. These electrons can be detected and manifest as

Auger peaks in XPS spectra. A characteristic property of Auger electrons is that they have a fixed E_k regardless of the X-ray source.

Features called shake-up and called shake-off satellites can also appear in XPS spectra. Here, an outgoing photoelectron interacts with valence electrons, reducing the kinetic energy of the photoelectron. The energy lost to the system can either excite a valence electron to a higher unfilled energy level or remove it from the system entirely [11]. These photoelectrons with reduced E_k result in features at higher BE than the core level.

Electrically insulating samples are susceptible to charging effects. When electrons are excited and ejected from the sample, a region of positive charge accumulates at the surface. As this accumulation of positive charge builds, the E_K of the photoelectrons will be reduced. This produces distorted peaks that are higher in BE than expected. The surface can be neutralised by externally supplying low-energy electrons and positive ions to the sample, leading to fast redistribution of charges [12]. Prolonged exposure to the X-ray beam can also cause damage to the sample surface, known as beam damage. Beam damage is capable of distorting peak shapes and introducing degradation species. This can often be avoided by moving the position of the beam on the sample between scans.

3.2 Near-Edge X-ray Absorption Fine Structure (NEXAFS)

Near-edge X-ray absorption fine structure (NEXAFS), also called X-ray absorption near edge structure (XANES), is a complementary technique to XPS. Unlike XPS which probes occupied core level states, NEXAFS provides information on the electronic structure of unoccupied molecular orbitals. NEXAFS can also be used to characterise bonding and determine the orientation of molecules on surfaces.

3.2.1 Theory

X-ray absorption

X-ray absorption spectroscopies (XAS) involve the excitation of core level electrons using X-rays. When passing through an absorber, X-rays are attenuated according to the Beer-Lambert law,

$$I = I_0 e^{-\mu t} \tag{3.4}$$

where I_0 is the original X-ray intensity, I is the intensity after passing through the material of thickness t, and μ is the absorption coefficient.

In XAS, a sudden increase in X-ray absorption occurs when the photon energy is roughly equal to the BE of the inner shell of the atom (commonly denoted using X-ray notation K, L, M, etc.). This strong absorption edge occurs at different photon energies depending on the element (for example, 285 eV for carbon K-edge). For low Z elements such as carbon, oxygen, and nitrogen, NEXAFS probes the K-edge, X-rays absorbed in the innermost K shell of the atom. For metals the K-edges are not accessible by soft X-rays so require hard X-rays (> 10 keV in energy). NEXAFS focusses on the fine structure roughly 30 eV above the X-ray absorption edge. This region has many sharp resonance peaks that are sensitive to bonding and electronic states. The region even higher in energy is called the extended X-ray absorption fine structure (EXAFS). Figure 3.11(b) shows the absorption edge of an XAS spectrum with the NEXAFS and EXAFS regions highlighted. When an X-ray is absorbed, the excited electron can be ejected into to the continuum of free states above the vacuum level (EXAFS) or an unoccupied molecular orbital (NEXAFS) as shown in Figure 3.11(a).
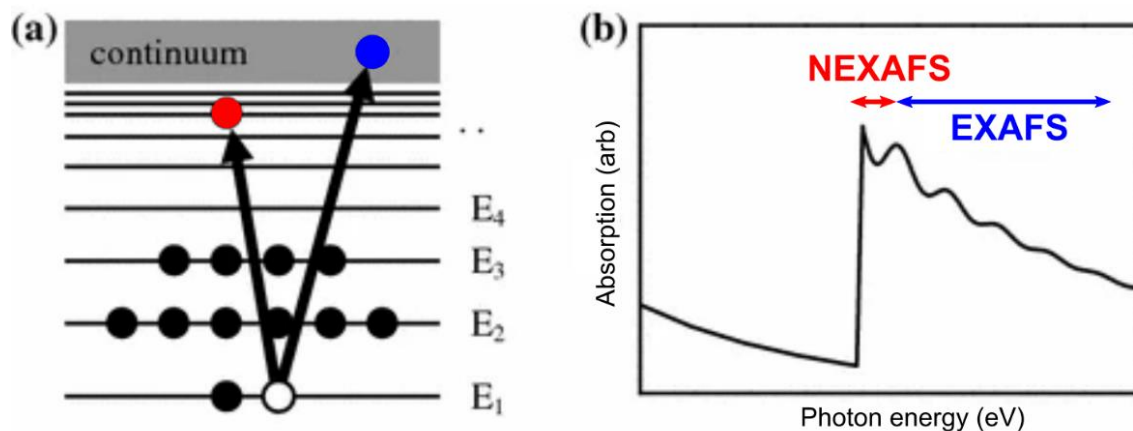
Figure 3.11. Energy level diagram depicting the excitation of a core level electron into an unoccupied molecular orbital (NEXAFS) or into the continuum of free states (EXAFS) (a). NEXAFS and EXAFS regions near the absorption edge (b). Adapted from [13].

Molecular orbitals

Molecular orbitals (MOs) in diatomic molecules can be described as interactions of atomic orbitals. The interaction of adjacent atomic orbitals with in-phase orbital amplitudes form bonding molecular orbitals while those with out-of-phase orbital amplitudes form antibonding molecular orbitals (denoted by an asterisk). Bonding orbitals have lower energy than the constituent atomic orbitals while antibonding orbitals have higher energy. For example, π orbitals (or π bonding) involves the interaction of p_x-p_x or p_y-p_y atomic orbitals wile σ orbitals consist of s-s or p_z-p_z atomic orbital interactions (subscripts denote axis of symmetry). Figure 3.12 shows an example of the formation of π and σ bonding and antibonding molecular orbitals from the interaction of 2p atomic orbitals.
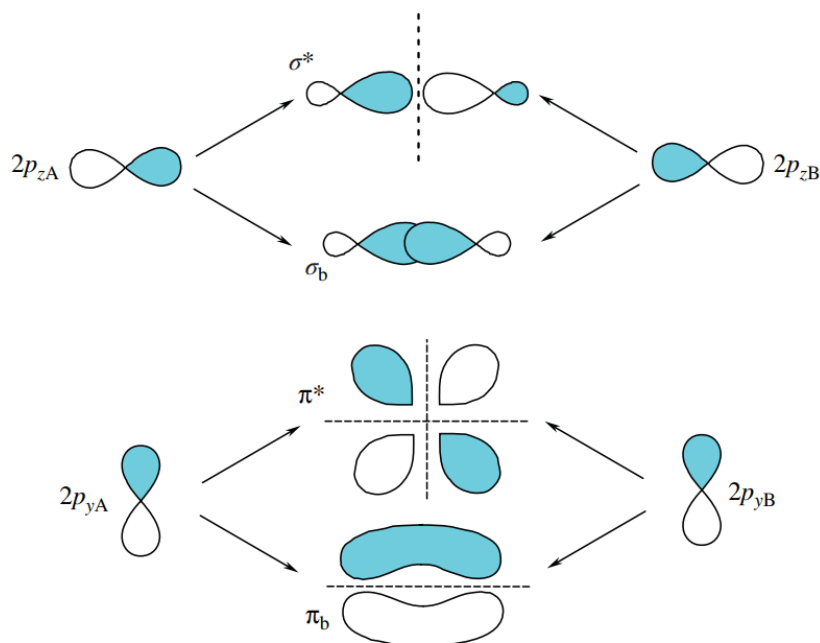
Figure 3.12. σ and π bonding and antibonding (*) molecular orbitals made by interactions of 2p atomic orbitals in a diatomic molecule. Reproduced from [15].

In NEXAFS, the allowable transitions of K shell electrons to unoccupied MOs are governed by the dipole selection rules. For a transition to be allowed it must satisfy the condition

$$\Delta l = \pm 1 \tag{3.5}$$

54

where l is the orbital angular momentum [14]. This means that an electron originating from the 1s initial state with $l = 0$ can only transition into a final state with an atomic p orbital component. Since all bonding orbitals are occupied, electrons from the 1s level are excited into antibonding π^* and σ^* MOs in NEXAFS.

The π^* antibonding MO is the lowest unoccupied molecular orbital (LUMO) while σ^* MOs appear at higher energies. Although NEXAFS probes unoccupied states, these transitions still provide useful information on the electronic structure of a molecule. 1s $\rightarrow$ π^* transitions are only valid for materials in which π-bonding is present. Therefore, π^* resonances indicate the presence of double/triple bonds or aromatic structures in the molecule [16].

NEXAFS spectra

A schematic of a typical K-shell NEXAFS spectrum is shown in Figure 3.13(a). This consists of a sharp resonance peak at low energy attributed to 1s $\rightarrow$ π^* transitions. This peak can be followed by a series of smaller sharp resonances attributed to transitions into Rydberg states (high energy states that lie closely under the vacuum energy as shown in Figure 3.13(b)). Rydberg states merge into a step-like feature approximately 2 eV below the vacuum level, also called the ionisation potential (IP). The small step feature at the IP can be seen in NEXAFS spectra as shown in Figure 3.13(a). The IP is the energy required to excite a core level electron into the continuum of free states (above the vacuum level). Above the IP there is a broad high energy peak attributed to σ^* transitions.

The width of NEXAFS resonances is governed by the lifetime of the excited state. In 1s $\rightarrow$ π^* transitions, the core hole has a long lifetime before it decays via the de-excitation of the excited electron, leading to sharp, narrow π^* resonances. An electron travelling through the continuum of free states experiences an increasing decay probability, resulting in broadening of σ^* peaks with increasing energy. As σ^* bonds lie along the internuclear axis between two atoms, the positions of σ^* peaks are very sensitive to the internuclear distance. Consequently, σ^* peaks are also broadened by vibrational motion of the molecule. In general, the energy width of a NEXAFS peak increases with increasing photon energy.
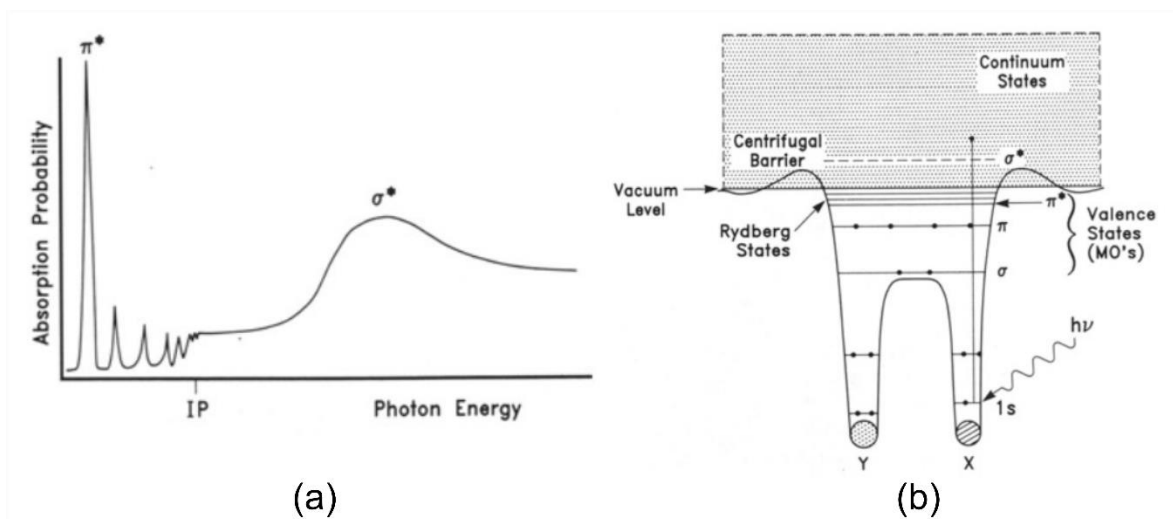
Figure 3.13. A schematic K-shell NEXAFS spectrum (a) and the potential well of a diatomic molecule (b). 1s electrons are excited into π* or Rydberg states below the vacuum level (ionisation potential), or into the continuum of free states above the vacuum level. Adapted from [17].

Before photoexcitation both the π* and σ* MOs would lie above the vacuum level. However, the creation of a core hole increases the Coulomb potential between the nucleus and remaining electrons. This increases the binding energy of the outermost levels, effectively lowering the 1s → π* transition energy below that of the vacuum level as shown in Figure 3.13(b).

The background on which these resonances sit can arise from a number of sources including signals from the substrate, experimental losses and interferences, and sample surface impurities. Some of these can be accounted for by carrying out background corrections. These are typically done by dividing the experimental spectrum by a clean substrate signal or by the X-ray photon flux taken from a reference grid over the same region.

3.2.2 Electron Detection

The core hole generated after the excitation of a core level electron can be filled by an electron from a higher level, losing energy either in the form of an X-ray photon or an Auger electron. These recombination processes are shown in Figure 3.14.

56

Both fluorescence photons and Auger electrons can be detected in NEXAFS. Auger decay is dominant for low atomic number elements such as C, N, and O. It is also dominant in the soft X-ray region compared to X-ray fluorescence; therefore, electron yield detection tends to be a more favourable choice [17].
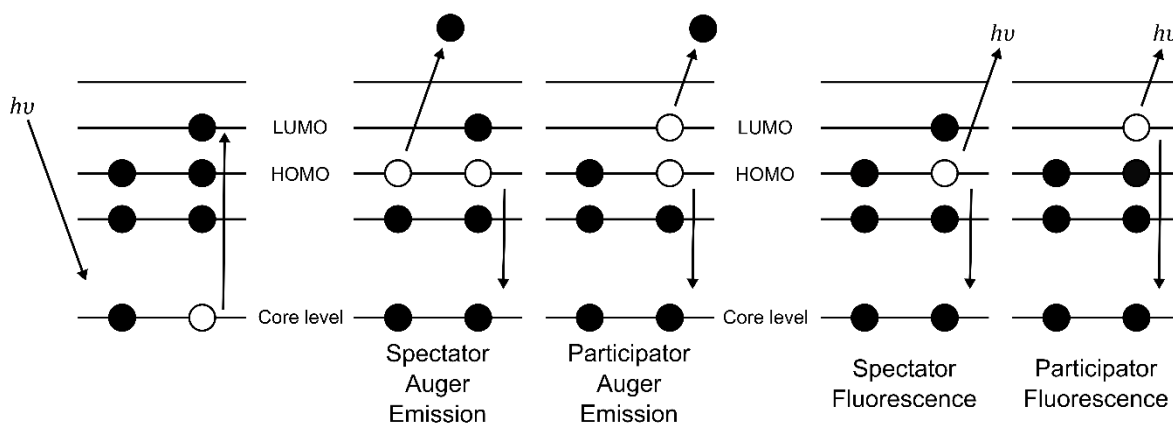
Figure 3.14. Energy level diagram showing the creation of an Auger electron or fluorescence photon after the decay of a core hole. The Auger decay process can involve either the originally excited electron (participator method) or another electron (spectator method).

There are three ways in which the electron yield can be measured: auger electron yield (AEY), partial electron yield (PEY), and total electron yield (TEY). These methods are often used simultaneously. In TEY all electrons are detected by measuring the drain current from the sample as a function of photon energy. As such, the TEY signal is strong but dominated by the inelastic background. This background originates from the inelastic scattering of electrons, resulting in the detection of secondary electrons with a range of energies. PEY introduces a minimum pass energy, E_p, to prevent low kinetic energy electrons from reaching the detector. This results in a higher signal-to-background ratio compared to TEY. In AEY the detector window is closely set around the energy of the Auger peak. This aims to detect only the elastically scattered Auger electrons and produces higher surface sensitivity. These yield window settings are shown in Figure 3.15. The main discrepancy between the three methods are differences in signal-to-background and signal-to-noise ratios, and surface sensitivity. In this thesis our NEXAFS spectra are recorded using AEY in order to gain the highest surface sensitivity.
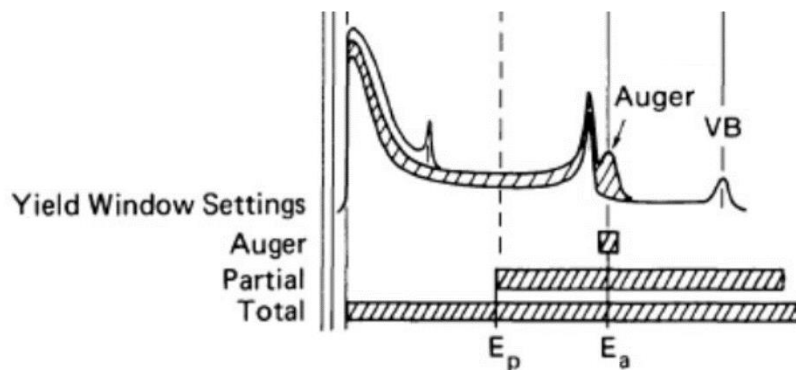
Figure 3.15. Yield window settings showing the energy ranges used in Auger, partial and total electron yield detection. E_a is the energy of the Auger peak while E_p is the user-controlled pass energy. Photoemission spectra are shown above, where VB is a valence band peak. Reproduced from [17].

3.2.3 Angle-Resolved NEXAFS

NEXAFS can be used to determine the orientation of molecules on substrate surfaces. This makes use of the highly directional nature of bonds and their corresponding MOs. The spatial orientation of an orbital can be described as a vector pointing in the direction of maximum orbital amplitude, $\vec{O}$ [17]. If the X-ray beam is polarised (such as synchrotron light), 1s $\rightarrow$ π^* and 1s $\rightarrow$ σ^* transition intensities, I, depend on the orientation of the electric field vector, $\vec{E}$, with respect to $\vec{O}$ according to Equation 3.6,

$$I = A[PI^{\parallel} + (1 - P)I^{\perp}] \tag{3.6}$$

where A is a constant dependent on the system and P is the polarisation factor of the beam, commonly given a value of 0.85 [17]. The transition intensity has $I^{\parallel}$ and $I^{\perp}$ components originating from the parallel and perpendicular components of the electric field vector of the X-ray beam, respectively (shown as $\vec{E^{\parallel}}$ and $\vec{E^{\perp}}$ in Figure 3.16):

$$I^{\parallel} = \cos^2 \theta \cos^2 \alpha + \sin^2 \theta \sin^2 \alpha \cos^2 \phi \tag{3.7}$$

$$I^{\perp} = \sin^2 \alpha \sin^2 \phi \tag{3.8}$$

where θ is the X-ray incidence angle (also equal to the polar angle of $\vec{E}^{\parallel}$), ϕ is the azimuthal angle of $\vec{O}$, and α is the polar angle of $\vec{O}$. These angles and vectors are shown schematically in Figure 3.16.
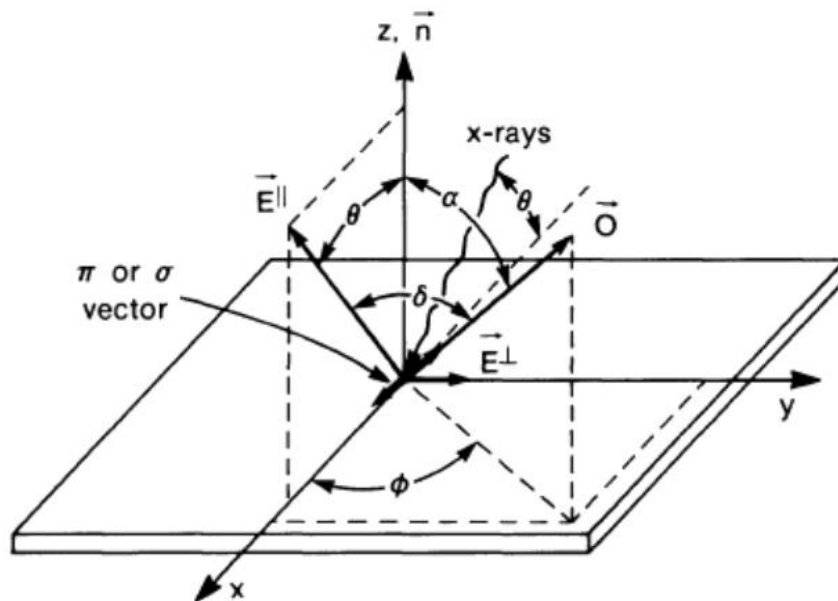
Figure 3.16. Coordinate system showing the geometry of a π^* or σ^* MO on a surface. $\vec{O}$ is the direction of the MO vector described by a polar angle α and azimuthal angle ϕ. X-rays are incident at an angle θ from the surface, equal to the polar angle of the $\vec{E}^{\parallel}$ vector. Reproduced from [17].

From Equations 3.6 – 3.8 it is found that resonances are maximised when $\vec{E}$ is parallel to $\vec{O}$. As $\vec{E}$ is perpendicular to the direction of propagation of the X-ray beam, resonances are maximised when the incident X-rays are perpendicular to $\vec{O}$. This is shown in Figure 3.17 and can be used to qualitatively describe the orientation of a molecule on the surface.
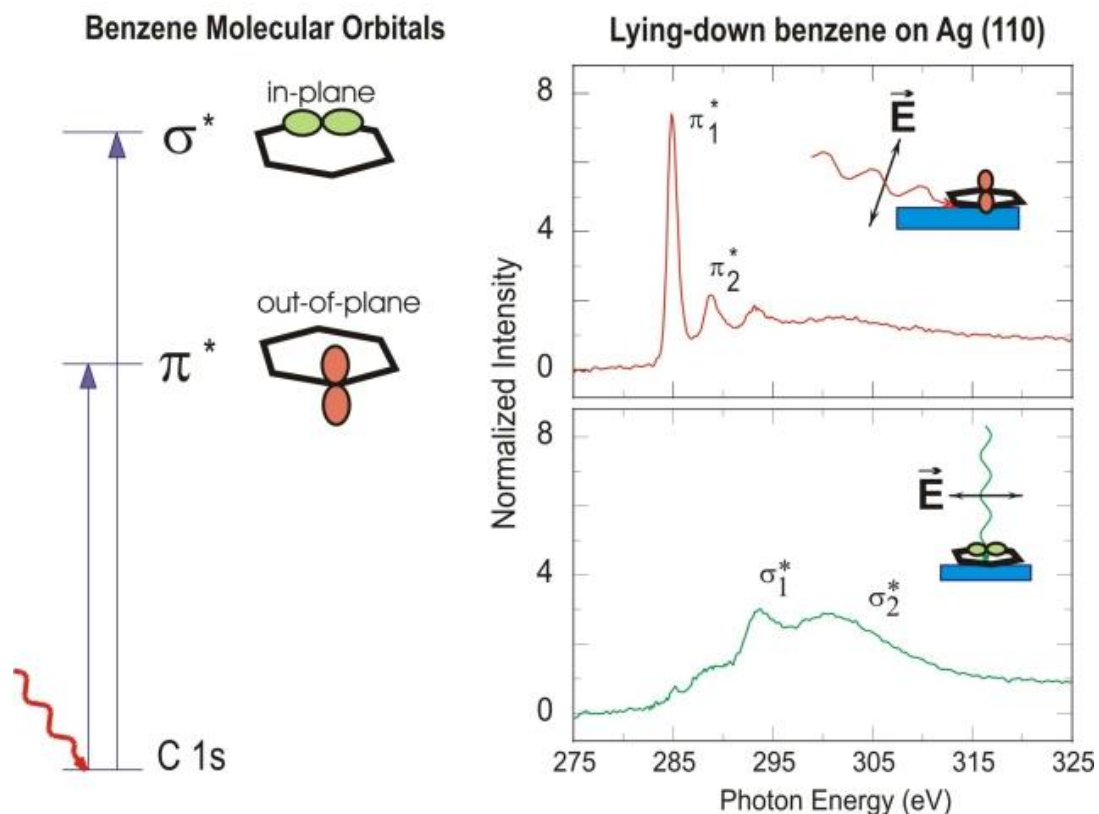
Figure 3.17. Angle-resolved NEXAFS showing the angular dependence of π* and σ* peaks with X-ray incidence angle for benzene. π* orbitals point out-of-plane while σ* orbitals are in-plane. Overlap of the electric field vector with the direction of the orbital changes the intensity of the resonance. Reproduced from [18].

The orientation of molecules can be determined in a more quantitative approach by calculating the polar angle of $\vec{O}$, α. For this to be done, measurements are taken at a large and small angle of θ (X-ray incidence angle). Taking measurements at multiple different angles allows a closer fit to Equation 3.6. The relative intensity of π* peaks at different values of θ can be compared to the theoretical intensity ratio calculated as a function of α using Equation 3.7, as shown in Figure 3.18. This provides an angle of α. In aromatic ring structures, π* orbitals point out of the plane of the ring, and in such an example, the orientation of the plane of the ring with respect to the surface normal would be calculated as 90 − α °.
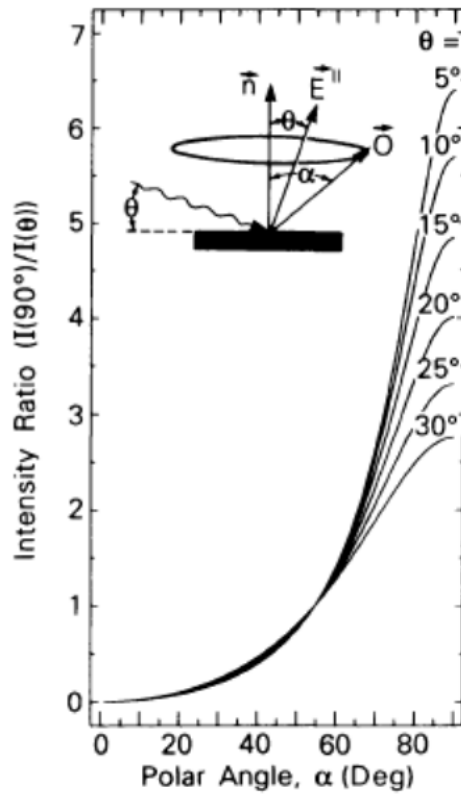
Figure 3.18. Ratio of resonance intensities taken at normal incidence and grazing incidence (5 – 30°) as a function of orbital polar angle α. If an experimental intensity ratio is known, it can be compared to the theoretical intensity ratio using Equation 3.7 to obtain a value of α. Reproduced from [17].

3.3 Synchrotron Radiation (SR)

Synchrotron radiation (SR) is electromagnetic (EM) radiation generated by accelerating high energy charged particles around curved paths close to the speed of light (c). SR is very intense, has high collimation, and tuneable polarisation. SR has a wide and continuous spectral range spanning from the infrared to hard X-ray region [19]. In particular, SR is much more intense in the soft X-ray region compared to lab-based sources such as Al Kα. X-rays generated from synchrotron sources are useful for XPS due to their high intensity and tuneable photon energy for depth profiling studies. NEXAFS requires the photon energy to be swept during measurements, which cannot be done with a fixed X-ray source. Below is a summary of the theory and instrumentation behind the generation of SR.

3.3.1 Properties of SR

When a charged particle moves in an external magnetic field, $\vec{\mathbf{B}}$, and electric field, $\vec{\mathbf{E}}$, it experiences a Lorentz force, given by

$$\frac{d\vec{\mathbf{p}}}{dt} = q\left(\vec{\mathbf{E}} + \frac{\vec{\mathbf{v}} \times \vec{\mathbf{B}}}{c}\right) \tag{3.9}$$

for a particle with momentum $\vec{\mathbf{p}}$, velocity $\vec{\mathbf{v}}$ and charge q. When $\vec{\mathbf{B}}$ is perpendicular to the velocity of the particle, $\vec{\mathbf{v}}$, the Lorentz force is a centripetal magnetic force perpendicular to both $\vec{\mathbf{B}}$ and $\vec{\mathbf{v}}$ and causes the particle to travel in a circular orbit. Charged particles moving in a circular orbit emit EM radiation, called synchrotron radiation. The shape of the SR pattern depends on the speed of the particle as shown in Figure 3.19. Nonrelativistic particles moving at speeds much less than the speed of light ($v \ll c$) emit SR radiation in a doughnut-like shape called a dipole pattern. When travelling at relativistic speeds ($v \approx c$), the radiation pattern distorts into a cone pointing in the direction of travel, tangential to the electron orbit. This beam of SR radiation is highly directional and collimated. SR therefore has a very high flux over a small area. The collimation of the SR is described by the emission angle ψ,

$$\psi = 1/\gamma = \sqrt{1 - \frac{v^2}{c^2}} \tag{3.10}$$

where γ is the Lorentz factor.
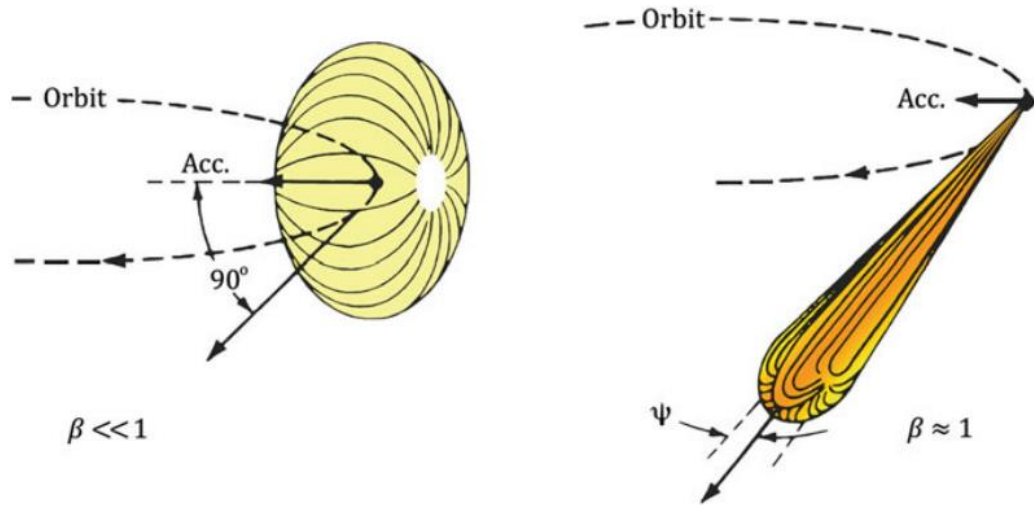
Figure 3.19. Radiation patterns of synchrotron light emitted from an electron travelling in a circular orbit at non-relativistic ($\beta = v/c << 1$) and relativistic ($\beta = v/c \approx 1$) speeds. Acc. denotes the direction of centripetal acceleration. Reproduced from [20].

The total energy of the orbiting electron, E, is given by.

$$E = \gamma m_0 c^2 \tag{3.11}$$

where $m_0 c^2$ is the electron rest mass energy equal to 0.511 MeV. Here we can see that as E increases the emission angle of the SR ($1/\gamma$) decreases. Current day synchrotron facilities routinely accelerate electrons to energies in the order of GeV, resulting in highly collimated SR with an angular spread typically less than 1 mrad [21]. The power, P, of SR radiated by a relativistic electron is given as

$$P = \frac{2}{3} \frac{e^2 c}{R^2} \left[\frac{E}{m_0 c^2} \right]^4 \tag{3.12}$$

where R is the radius of curvature of electrons and e is the charge of an electron [20]. As P is proportional to $1/m_0^4$, electrons emit more powerful SR compared to protons due to their smaller rest mass m_0. This is why electrons are favoured over protons for SR generation. P can also be increased by decreasing the radius of the storage ring of the synchrotron.

3.3.2 Generating SR

A schematic layout of a typical synchrotron facility is shown in Figure 3.20. The production of SR begins with the generation of an electron beam. Electrons with energies in the order of keV are generated by heating a cathode. These electrons are accelerated to relativistic speeds (energy ~ 0.1 GeV) using a linear accelerator (linac). They are then injected into a booster ring to further increase their energy to the required operational energy (for example, 3 GeV for Diamond Light Source) using radio frequency electric fields and bending magnets [21]. The high energy electrons are injected into the main storage ring where they will travel in a circular orbit and emit SR.
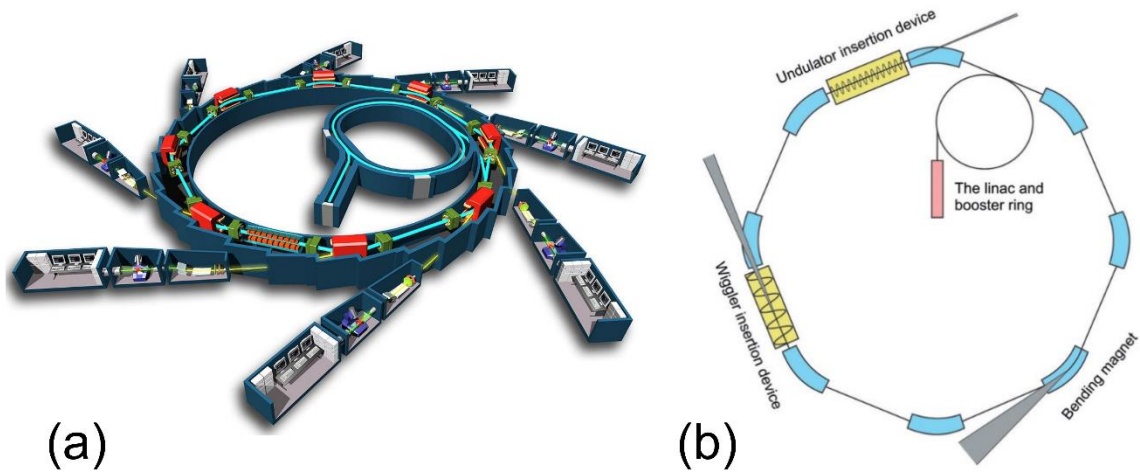
Figure 3.20. Illustration of the SOLEIL synchrotron facility (a) where electrons (blue) travelling around the outer storage ring emit synchrotron light (yellow) down beamlines. Scheme showing a simplified configuration of a synchrotron storage ring (b). The grey cones depict the emission of synchrotron radiation from bending magnets, wiggler and undulator insertion devices. Reproduced from [21,22].

In practice, storage rings are not a perfect circle but consist of a large number of straight sections connected by dipole bending magnets which bend the electron beam between each straight section. Every time the electron trajectory is bent by a bending magnet they emit SR tangential to the plane of the storage ring. The SR is directed along beamlines where it is used for experiments. The storage ring is held at ultra-high vacuum (~ 10^{-9} mbar) in order to limit the scattering and energy loss of electrons [19]. However, electrons still lose energy at each bending magnet in the

form of SR. This energy loss is compensated by radio frequency (RF) cavities. These contain RF electric fields that provide electrons a surge of energy. Coulomb repulsion between electrons is counteracted using by quadrupole magnets to focus the electron beam. Insertion devices are positioned along the straight sections of the storage ring in order to increase the intensity and brightness of the SR.

Insertion devices

The two most common insertion devices are wigglers and undulators. Wigglers consist of a series of alternating dipole magnets with $\vec{B}$ pointing vertically ($\pm$ z direction) as shown in Figure 3.21. The alternating magnets cause the electron beam to follow a sinusoidal-like curved path in the horizontal (x-y) plane. During each "wiggle" the electron beam releases SR at an emission angle of, $1/\gamma$. The electron trajectory shown in Figure 3.22 is characterised by the maximum deflection angle of the electrons, α, and the period of oscillation, λ_u.
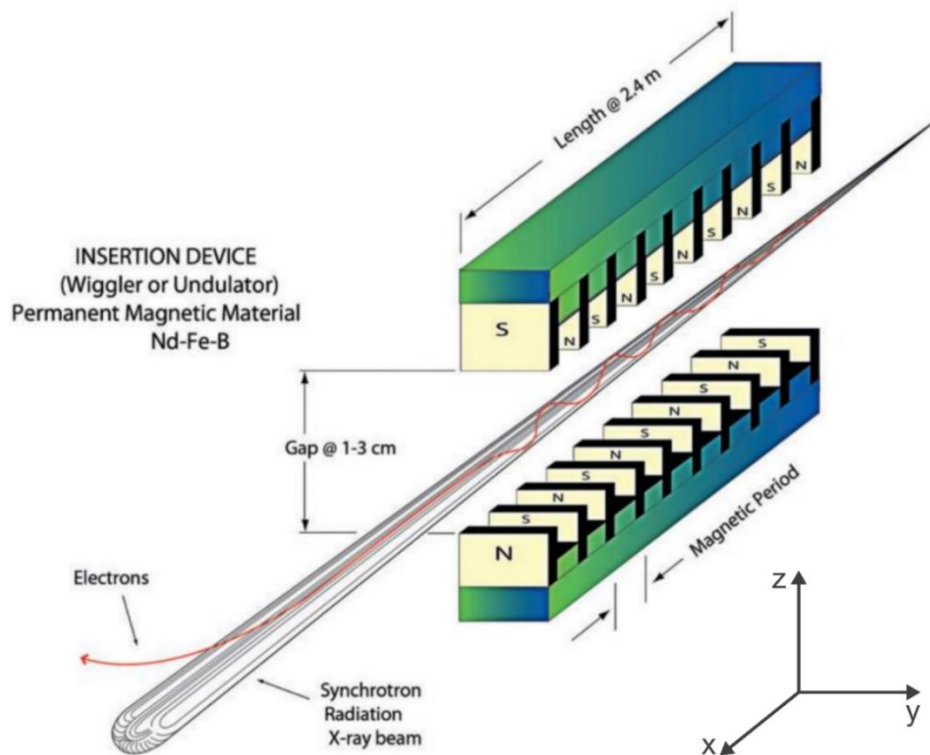
Figure 3.21. Experimental setup of a wiggler insertion device. Alternating dipole magnets cause the electrons to oscillate and produce more intense synchrotron radiation. Adapted from [21].

65
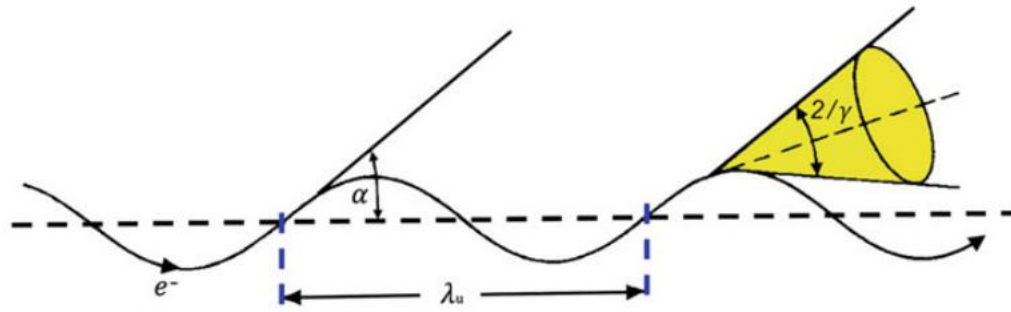
Figure 3.22. Schematic illustration of the electron trajectory through a wiggler and the emission angle of the SR $1/\gamma$. Reproduced from [20].

Undulators are very similar to wigglers but can be distinguished by a dimensionless quantity known as the K value [23].

$$K = \alpha\gamma \qquad\qquad (3.13)$$

Undulators have a small K value < 1 while wigglers tend to have K > 3. The distance between successive magnetic poles in undulators is shorter than in wigglers, resulting in a wiggling angle α that is smaller than $1/\gamma$ (i.e., K < 1). In undulators SR constructively interferes at successive magnetic poles (or crests in the electron trajectory), resulting in SR with a smaller emission angle and higher photon flux compared to those generated by wigglers. For an array of N dipole magnets, wigglers enhance the intensity by a factor of N while undulators enhance the intensity by a factor of N^2 [20].

The polarization of SR can be changed by modifying the arrangement of magnets in an insertion device. Electrons undergoing a transverse oscillation (such as those shown in Figure 3.22) emit SR that is linearly polarised in the plane of the electron orbit. If instead the electrons are given a helical trajectory, then the SR is circularly polarised [24].

3.3.3 Monochromators

SR has a continuous energy distribution meaning a particular photon energy must be selected by using a monochromator. A monochromator consists of a concave quartz crystal that diffracts incident X-rays according to Bragg's Law,

$$n\lambda = d \sin\theta \qquad\qquad (3.14)$$

where λ is the wavelength of light, n is the order of diffraction, d is the lattice spacing of the crystal and θ is the incident angle of the SR with respect to the crystal lattice planes. By rotating the crystal and changing θ, the transmitted light emerges with a wavelength in a narrow bandwidth around λ. The entrance and exit slits of the instrument both lie on a Rowland circle as shown in Figure 3.23. This circle has a diameter equal to the radius of curvature of the quartz crystal and ensures that the diffracted beam is refocussed before reaching the sample.
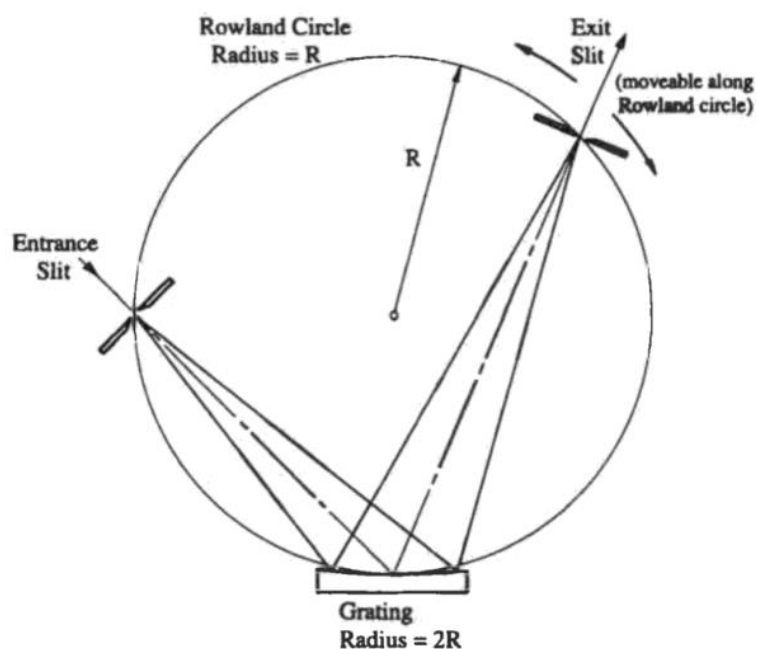
Figure 3.23. Schematic of a monochromator used to select the photon energy of synchrotron light. A curved quartz crystal diffracts the light, which is refocused on a point on the Rowland circle. Reproduced from [25].

3.4 Instrumentation

3.4.1 Achieving Ultra-High Vacuum

A number of surface science techniques including XPS and NEXAFS use ultra-high vacuum (UHV), typically characterised as pressures less than 10^{-9} mbar. UHV is required in order to maximise the mean free paths of electrons and allows atomically clean surfaces to be prepared *in situ*. In order to achieve UHV, a series of pumps

are required to remove the gas in the chamber. Water vapour and other absorbed gases can sit on the inside walls of the spectrometer and contaminate the vacuum. These contaminants are removed by a bakeout process in which the chamber is heated to over 100 °C for 24 hours while under vacuum. Gases are desorbed from the walls of the chamber and are pumped out of the system.

The pressure in an UHV system must be brought down from atmospheric pressure to UHV in a series of stages. The first step requires a roughing or fore pump to bring the pressure down to approximately 10^{-3} mbar. These are commonly scroll pumps or rotary pumps. Following this, a turbomolecular pump is used to bring the pressure down to 10^{-9} mbar. Turbomolecular pumps consist of alternating stacks of rotating and stationary angled blades (rotors and stators, respectively, as shown in Figure 3.24). The blades have a turbine-like design and rotate at very high speeds such that molecules hitting the blades are given a downward bias to their direction, driving them down to the next blade. This process repeats until the gas molecules reach a backing pump. The backing pump is typically a scroll pump or rotary pump and removes the exhaust gases from the turbomolecular pump.
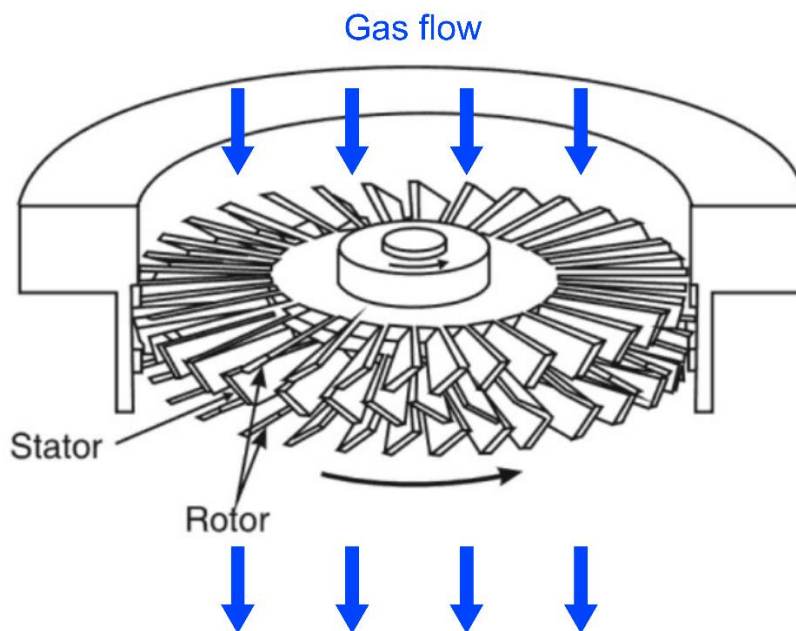
Figure 3.24. Schematic illustration of the rotors and stators used in a turbomolecular pump. Adapted from [26].

Once UHV is attained, it is maintained through the use of pumps and airtight seals. UHV instruments consist of various chambers that can be isolated from one another using gate valves. The components of an UHV system are connected by flanges. Two flanges are held together by bolts and sealed using a gasket. The gasket is made of a soft metal such as copper and is sandwiched between the flanges. When the flanges are bolted together, sharp knife-edges machined into the flanges bite into the soft metal gasket, forming an airtight seal.

3.4.2 Sample Preparation

<u>TiO$_2$ sputtering and annealing</u>

In the studies presented in this thesis, ILs were deposited onto rutile TiO$_2$ (110) crystals. Before deposition and characterisation of the IL, it is important that the substrate surface is atomically clean. TiO$_2$ crystals were prepared in UHV by multiple sputter/anneal cycles. In sputtering, Ar$^+$ ions are bombarded into the substrate surface at grazing angles with energies in the order of keV. This sputters off the top layer of material and removes surface contamination with it. Following this, the crystal is heated and left to slowly cool, a process called annealing. This restores the surface crystallography and removes embedded argon atoms. TiO$_2$ transitions from the anatase (101) to the rutile (110) structure when heated in the range of 600 – 700 °C [27]. The rutile TiO$_2$ crystal was sputtered at 1 keV for 10 minutes and annealed at approximately 700 °C for 10 minutes. Several sputter/anneal cycles are required to prepare a well-ordered atomically clean surface. XPS survey scans are used to confirm whether surface contaminants have been removed.

<u>Electrospray deposition</u>

ILs can be deposited onto substrate surfaces using a range of deposition techniques including physical vapour deposition (PVD) [28–30], dip-coating [31,32] and electrospray deposition (ESD) [33]. These are capable of yielding bulk deposits, uniform thin films, and submonolayer coverages of ILs. In our studies discussed in Chapters 6 and 7 we used ESD to obtain thin films of [P$_{66614}$][124Triz] and [P$_{66614}$][Tetz]. The working mechanisms of ESD are shown in Figure 3.25.
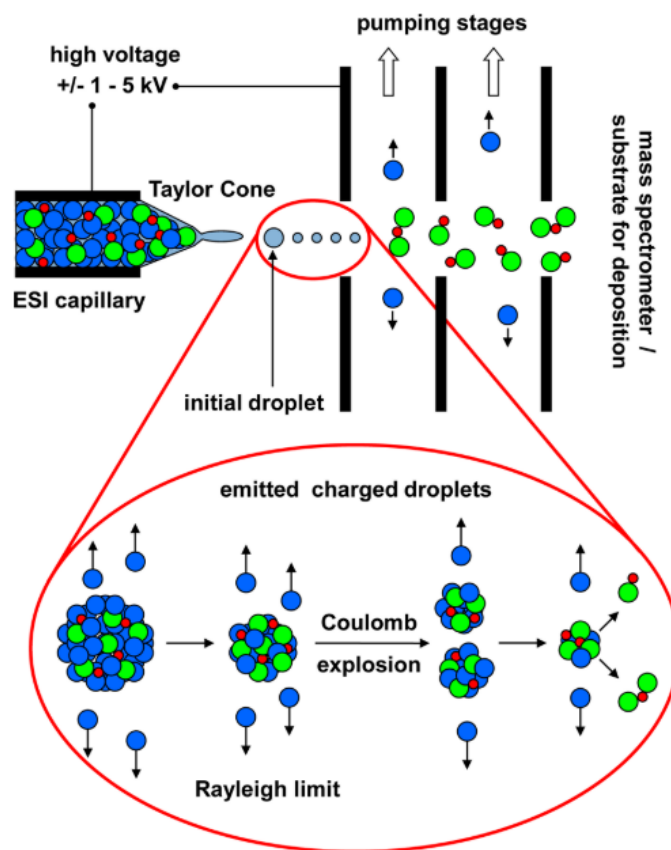
Figure 3.25. Illustration of the electrospray ionisation deposition process. The solution for deposition escapes the capillary in the form of a Taylor cone jet. A scheme shows Coulomb explosion of droplets into small molecular clusters. Reproduced from [33].

In ESD an electrically conducting solution containing dissolved target molecules is pumped through an emitter needle using a syringe. The flow rate of the liquid, typically around 0.3 mL/h, can be controlled using a syringe pump. The needle is held at high voltage (1 – 5 kV) with respect to the grounded entrance capillary (shown in Figure 3.26). The liquid is charged as it emerges from the needle tip. When the applied voltage is sufficiently large, the electric field at the tip dominates over the surface tension of the liquid and causes it to form a cone of small, charged droplets, called a Taylor cone-jet. The strong electric field drives the charged droplets towards the substrate surface. During this journey, the solvent evaporates. The surface tension of the droplets therefore decreases and can no longer compensate for Coulomb repulsion of the ions. This is known as the Rayleigh limit and causes droplets to separate into progressively smaller constituents. This process continues until an aerosol of solvent-free small molecular clusters or ion pairs is achieved [33].

70

This Coulomb fission is called Coulomb explosion and is shown in Figure 3.25. It results in the deposition of a uniform thin film of the target material on the substrate surface.
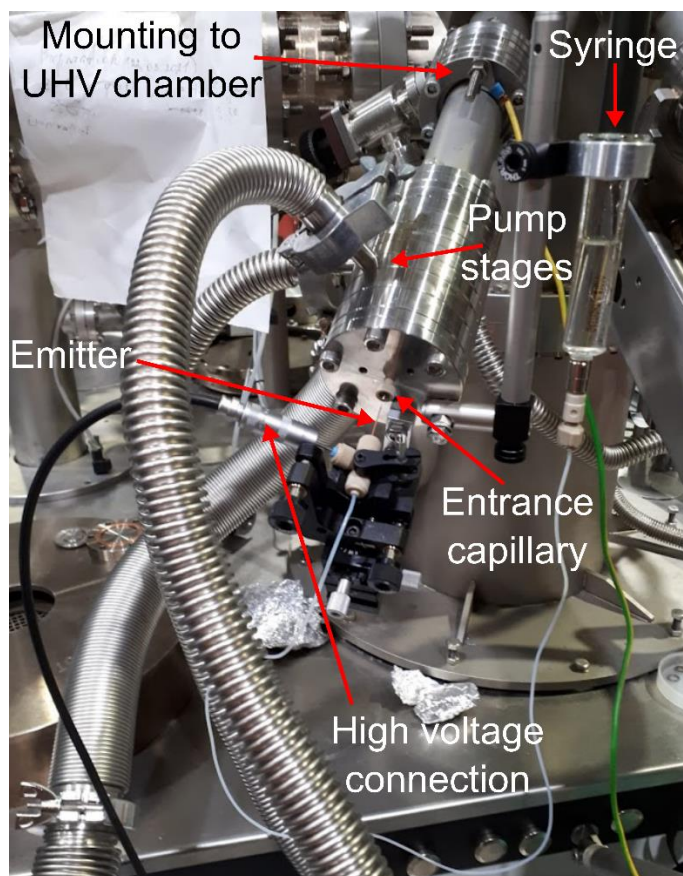
Figure 3.26. Photograph of a Molecularspray UHV4 electrospray system mounted to a UHV chamber.

ESD systems are fitted with multiple differential pumping stages allowing *in situ* deposition at UHV conditions. The emitter is at atmospheric pressure and the jet of the solution enters the differential pumping stages through the entrance capillary. The first two pumping stages require roughing pumps to reduce the pressure from atmospheric pressure to 0.1 mbar. The final high vacuum stage requires a turbomolecular pump to bring the pressure down to ~ 10^{-4} mbar. This ensures that the pressure in the preparation chamber remains close to UHV (~10^{-8} mbar) during deposition. Each stage is separated by electrostatic lenses to focus the ions [34]. A photograph of an ESD system mounted to a UHV chamber is shown in Figure 3.26.

ESD has advantages over other deposition methods such as PVD. For example, PVD can only be used to deposit thermally stable molecules whereas ESD can be used to deposit large labile molecules. In this thesis, ESD allows thin films of large ILs to be deposited *in situ* in ultra-high vacuum [34]. A disadvantage of electrosprayed IL thin films is that they can have an unequal concentration of cations and anions compared to PVD due to the increased diffusion of cations and anions with positive and negative tip biases, respectively [33]. ESD of ILs is comparatively underutilised, and prior to the studies in this thesis has not been used to deposit large IL molecules such as $[P_{66614}]^+$ or used alongside NAP-XPS to study ILs, to the best of our knowledge.

Thin film thickness calculations

The thicknesses of electrosprayed thin films, t_{IL}, was calculated using the Beer-Lambert Law (Equation 3.18). First the IMFP λ of electrons in the IL must be determined using calculations developed by Seah for organic materials [35]. The IMFP of organic materials is given as

$$\lambda = \frac{\left(4 + 0.44Z_{IL}^{0.5} + 0.104E_{K,max}^{0.872}\right)a_{IL}^{1.7}}{Z_{IL}^{0.3}} \text{ (nm)} \tag{3.15}$$

where Z_{IL} is the average number of protons in one IL pair, $E_{K,max}$ is the maximum photoelectron kinetic energy and a_{IL} is the cube root of the atomic volume of one IL pair. Z_{IL} is given as

$$Z_{IL} = \frac{cZ_c + nZ_n + pZ_p}{c + n + p} \tag{3.16}$$

where Z_c, Z_n and Z_p are the number of protons in one carbon, nitrogen, and phosphorous atom, respectively. The atomic volume, a_{IL}^3, of one IL pair is calculated as

$$a_{IL}^3 = \frac{10^{21}M_{IL}}{\rho_{IL}N_A(c + n + p + h)} \text{ (nm}^3) \tag{3.17}$$

where c, n, p and h are the number of carbon, nitrogen, phosphorous and hydrogen atoms in one IL pair, respectively, N_A is Avogadro's constant, M_{IL} is the molecular mass of the IL, and ρ_{IL} is the density of the IL.

Once λ is determined, the IL film thickness, t_{IL}, can be calculated by rearranging the Beer-Lambert Law (Equation 3.3) for t_{IL}.

$$t_{IL} = -\lambda \ln\left(\frac{I}{I_0}\right) \ \text{(nm)} \tag{3.18}$$

When an overlayer is deposited on a substrate surface, the signal from the substrate is attenuated by the overlayer material. This results in a less intense substrate signal (I) compared the clean substrate signal (I_0). I_0 and I can be taken as the areas of a substrate peak (e.g., Ti 2p or O 1s peak area for a TiO_2 substrate) before and after deposition of the IL onto the substrate, respectively.

3.4.3 Diamond Lightsource B07 VerSoX Beamline

Diamond light source is a third generation synchrotron located in the UK operating at an energy of 3 GeV and maximum beam current of 300 mA. The storage ring is a 50-sided polygon with a circumference of 561 m. It uses bending magnets and insertion devices to generate high intensity SR for 32 beamlines. Experiments in Chapters 5 and 7 were carried out at the versatile soft X-ray beamline, VerSoX, also called B07. The B07 beamline has two branches, B and C, that operate at energy ranges of 45–2200 eV and 130–2800 eV, respectively [5,36]. Experiments presented in Chapters 5 and 7 studied ILs on rutile TiO_2 (110) single crystals and were carried out at branch C. This branch allows NAP-XPS and NEXAFS measurements to be taken at pressures up to tens of mbar. The B07-C end station consists of a preparation chamber, radial distribution chamber, analysis chamber (called Tea Pot in Figure 3.27) and an electron energy analyser. The X-ray beam has a spot size of 90 μm (horizontal) $\times$ 60-100 μm (vertical) and a photon flux of 10^{10} photons/s.
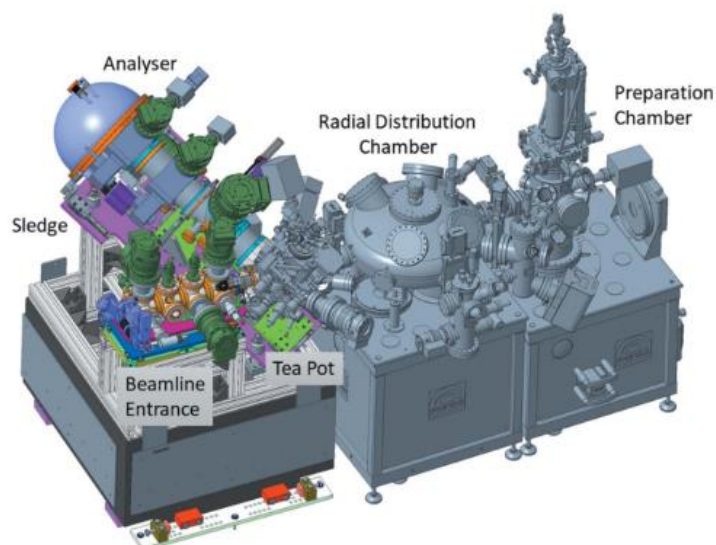
Figure 3.27. Schematic diagram of the B07 end station at Diamond Light Source. Reproduced from [5].

A rutile TiO_2 (110) single crystal (1 cm $\times$ 1 cm) was secured onto a sample holder by three tantalum strips as shown in Figure 3.28. The sample holders allow the sample to be transferred across the various chambers using wobble sticks. A resistive heater and K-type thermocouple are also integrated within the sample holder to heat and monitor the sample temperature. Figure 3.28 shows photographs of the TiO_2 crystal mounted in a sample holder before cleaning, during sputtering/annealing in the preparation chamber, and after ESD.
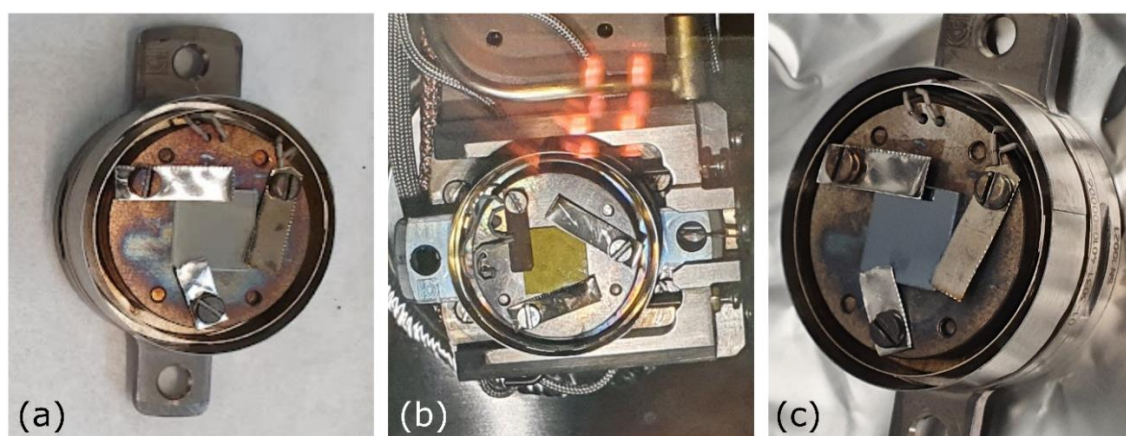
Figure 3.28. Rutile TiO_2 (110) single crystal secured onto a sample holder using tantalum strips. A change in colour of the TiO_2 is seen before (a), during cleaning via sputter/anneal cycles (b), and after electrospray deposition (c).

A load lock is used to introduce samples into the system. The load lock is vented to atmospheric pressure, the TiO_2 substrate is inserted, and the load lock returned to vacuum. The radial distribution chamber is used to store multiple samples *in vacuo* and transfer them to the preparation chamber. A manipulator is used to adjust the position of the sample in the preparation chamber. The TiO_2 crystal was cleaned in the preparation chamber via multiple sputter/anneal cycles. The crystal changed colour during cleaning due to the creation of oxygen vacancies in the sputter/anneal process (Figure 3.28(b)). An electrospray system was mounted to the preparation chamber for *in situ* deposition of ILs (photographed in Figure 3.29). During one of the experiments at B07, the preparation chamber was in a different room to the analysis chamber (due to construction work on the beamline) so the sample was transported from the preparation chamber to the end station in a vacuum suitcase held at UHV. The vacuum suitcase can be mounted to a load lock and the sample loaded into the analysis system without contamination with air.
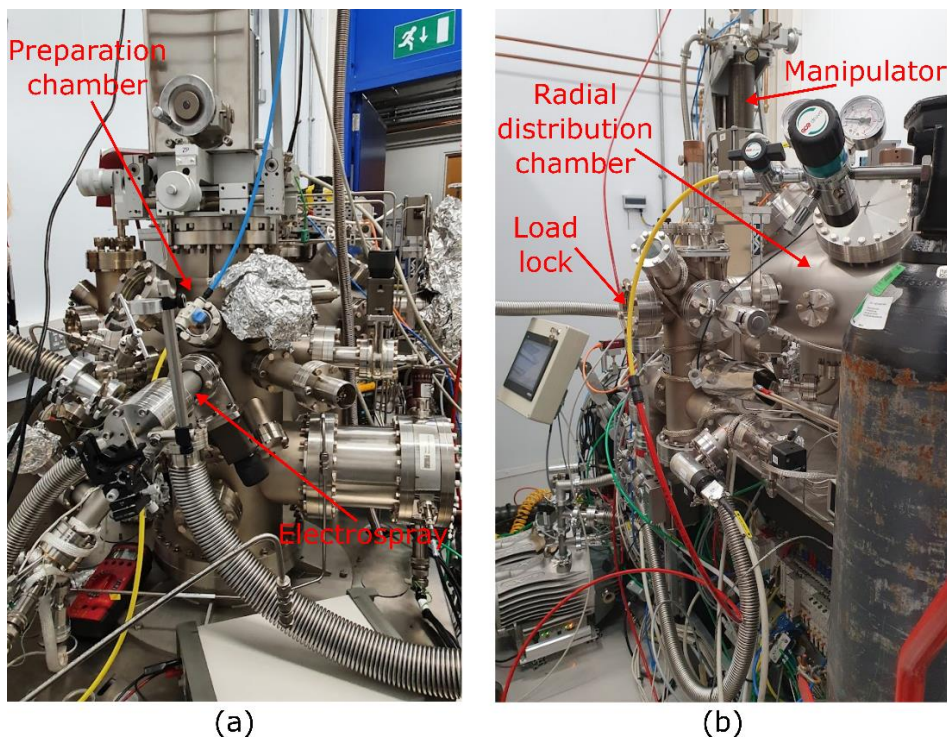
Figure 3.29. Photographs of the sample preparation system taken from two different perspectives. This consists of a load lock, radial distribution chamber for storing and transferring samples, and a preparation chamber. An electrospray system was mounted to the preparation chamber in order to deposit thin films of ionic liquids.

Measurements are carried out in the analysis chamber which is backfilled with gas during NAP measurements. The end station (Figure 3.30) has a hemispherical PHOIBOS 150 NAP electron energy analyser with a 0.3 mm cone aperture. This is similar to the working distance between the analyser cone and sample surface. The sample holder is mounted to a manipulator, allowing remote control of the position and orientation of the sample with respect to the analyser. Angle-resolved XPS and NEXAFS measurements can therefore be carried out at near-ambient pressures.
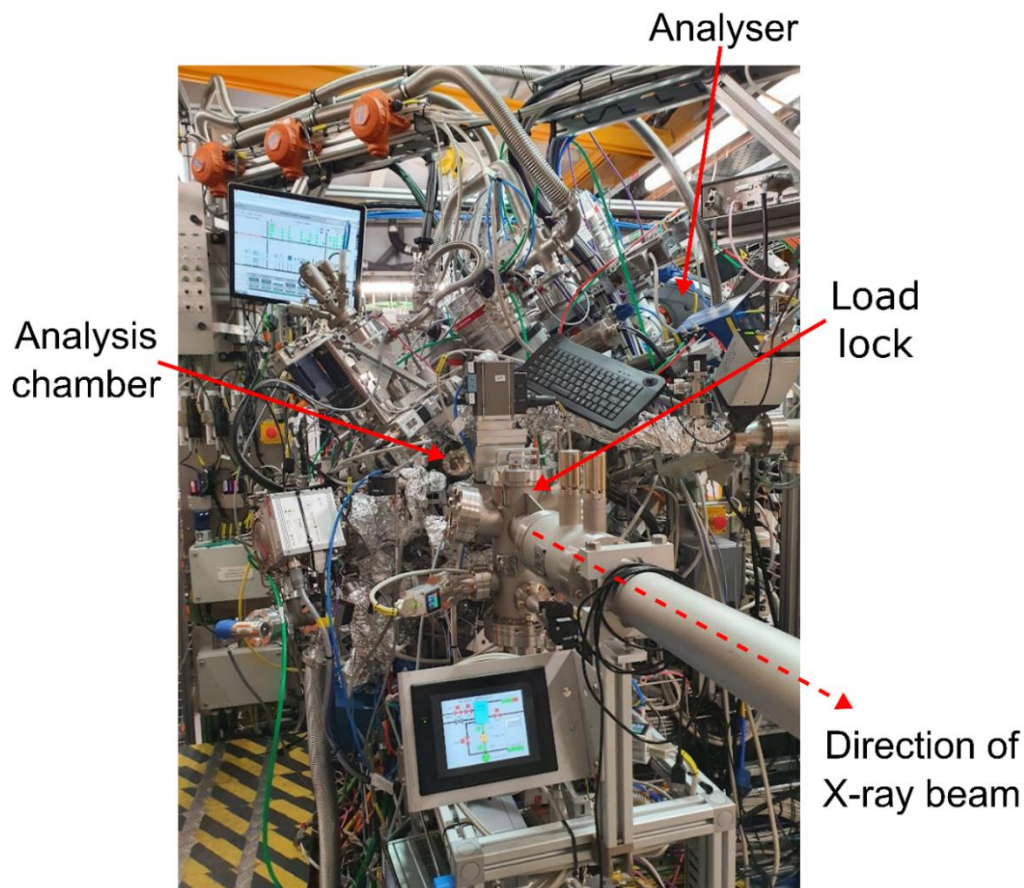
Figure 3.30. VerSoX B07-C end station at Diamond Light Source.

3.4.4 MAX-IV LAB HIPPIE Beamline

MAX-IV laboratory is a Swedish synchrotron facility, producing SR with a broad spectral range by using two storage rings. The larger ring has a circumference of 528 m and is capable of accelerating electrons to an energy of 3 GeV. This storage ring specialises in the production of high-intensity X-rays. The smaller storage ring (1.5 GeV, 96 m circumference) produces UV light. A schematic overview of the two

storage rings is shown in Figure 3.31. The storage rings at MAX-IV are designed using a novel multi-bend achromat lattice. In the 3 GeV storage ring there are 20 achromats, each consisting of 7 bending magnets. The achromats are connected by 19 long straight sections for the inclusion of insertion devices and a further 40 short straights for RF cavities [37]. This configuration results in a beam current of 500 mA and very low electron beam emittance, meaning electrons are confined to a small area in six-dimensional phase space (position and momentum).
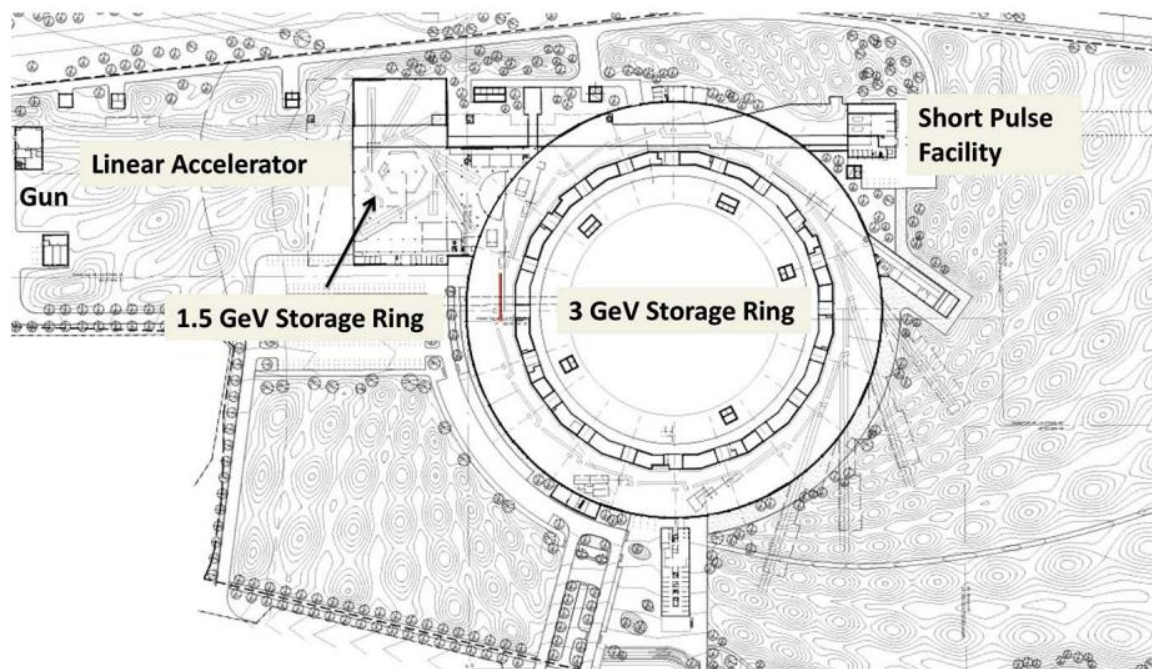
Figure 3.31. Schematic overview of the 1.5 and 3 GeV storage rings at MAX-IV laboratory. Reproduced from [38].

The 3 GeV storage ring hosts 11 beamlines. The study presented in Chapter 6 was carried out at the HIPPIE beamline [39]. This soft X-ray beamline has a photon energy range of 250 – 2200 eV. The X-ray beam has a 60 μm (horizontal) $\times$ 25 μm (vertical) spot size and a maximum photon flux > 10^{12} photons/s. XPS and NEXAFS measurements can be carried out at UHV or NAP up 30 mbar.

The HIPPIE end station consists of an analysis chamber, electron energy analyser, radial distribution chamber, load lock, preparation chamber, and an ambient pressure cell chamber (where the NAP cell is stored), as shown in Figure 3.32. When carrying out NAP-XPS, the NAP cell is docked to the hemispherical Scienta-Omicron

HiPP-3 electron energy analyser. Angle-resolved measurements therefore cannot be taken during NAP. The X-ray beam enters the NAP cell through an X-ray window coated with a 200 nm thick silicon nitride film to transmit the X-rays. The analyser cone has a 0.3 mm diameter aperture. The end station has 8 gases available including CO_2, CO, O_2, and H_2.
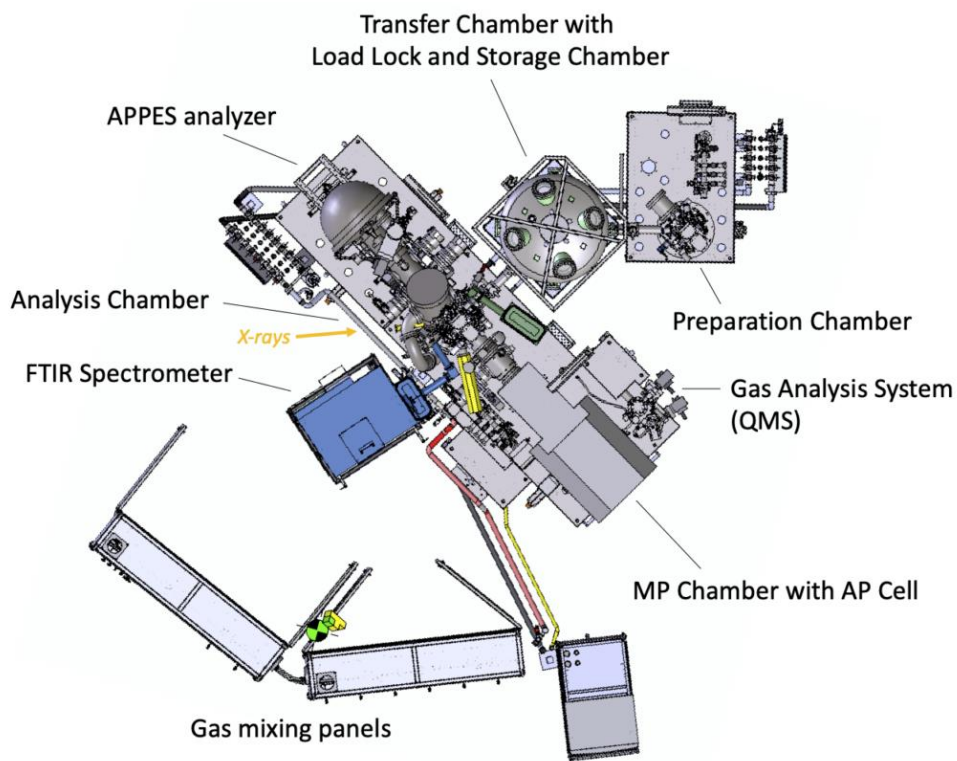
Figure 3.32. Overview of the HIPPIE beamline at MAX-IV laboratory. Reproduced from [39].

3.5 References

[1]   van der Heide P 2011 *X-Ray Photoelectron Spectroscopy: An Introduction to Principles and Practices* (John Wiley & Sons, Incorporated)

[2]   Stevie F A and Donley C L 2020 Introduction to x-ray photoelectron spectroscopy *J. Vac. Sci. Technol. A* **38** 063204

[3]   Oura K, Lifshits V G, Zotov A V., Katayama M and Saranin A A 2003 Surface Analysis II. Electron Spectroscopy Methods *Surface Science : An Introduction* (Springer Berlin / Heidelberg)

[4]   Wagner J M 2011 *X-ray photoelectron spectroscopy* (Nova Science Publishers)

[5]   Held G, Venturini F, Grinter D C, Ferrer P, Arrigo R, Deacon L, Garzon W Q, Roy K, Large A, Stephens C, Watts A, Larkin P, Hand M, Wang H, Pratt L, Mudd J J, Richardson T, Patel S, Hillman M and Scott S 2020 Ambient-pressure endstation of the Versatile Soft X-ray (VerSoX) beamline at Diamond Light Source *J. Synchrotron Radiat.* **27** 1153–66

[6]   Schlueter C, Gloskovskii A, Ederer K, Schostak I, Piec S, Sarkar I, Matveyev Y, Lömker P, Sing M, Claessen R, Wiemann C, Schneider C M, Medjanik K, Schönhense G, Amann P, Nilsson A and Drube W 2019 The new dedicated HAXPES beamline P22 at PETRAIII *AIP Conf. Proc.* **2054** 040010

[7]   Flavell W R 2022 Spiers Memorial Lecture : prospects for photoelectron spectroscopy *Faraday Discuss.* **236** 9–57

[8]   Tao F and Nguyen L 2018 Interactions of gaseous molecules with X-ray photons and photoelectrons in AP-XPS study of solid surface in gas phase *Phys. Chem. Chem. Phys.* **20** 9812–23

[9]   EAG Laboratories *XPS provides chemical bond information*, https://www.eag.com/app-note/xps-provides-chemical-bond-information/ [date accessed 02/03/2023]

[10]   Shallenberger J R, Smith N J and Banerjee J 2021 Derivation of empirical XPS relative sensitivity factors from silicate glasses *Surf. Interface Anal.* **53** 569–79

[11]   Persson P, Lunell S, Szöke A, Ziaja B and Hajdu J 2009 Shake-up and shake-off excitations with associated electron losses in X-ray studies of proteins *Protein Sci.* **10** 2480–4

[12]   Baer D R, Artyushkova K, Cohen H, Easton C D, Engelhard M, Gengenbach T R, Greczynski G, Mack P, Morgan D J and Roberts A 2020 XPS guide: Charge neutralization and binding energy referencing for insulating samples *J. Vac. Sci. Technol. A* **38** 031204

[13]   Schnohr C S and Ridgway M C 2015 Introduction to X-Ray Absorption Spectroscopy *X-Ray Absorption Spectroscopy of Semiconductors* (Springer, Berlin, Heidelberg) pp 1–26

[14]   Thorne A, Litzen U and Johansson S 1999 *Spectrophysics. Principles and applications* (Springer)

[15]   Pfennig B W 2015 Covalent Bonding *Principles of Inorganic Chemistry* (John Wiley & Sons, Incorporated)

[16]   Nefedov A and Wöll C 2013 Advanced applications of NEXAFS spectroscopy for functionalized surfaces *Springer Ser. Surf. Sci.* **51** 277–303

[17]   Stöhr J 2003 *NEXAFS Spectroscopy* (Berlin: Springer)

[18]   Stöhr J NEXAFS Spectroscopy https://www-ssrl.slac.stanford.edu/stohr/nexafs.htm [date accessed 02/03/2023]

[19]   Winick H 1994 Introduction and Overview *Synchrotron Radiation Sources: A Primer* (World Scientific) pp 1–29

[20]   Mobilio S, Boscherini F and Meneghini C 2015 *Synchrotron Radiation* ed S Mobilio, F Boscherini and C Meneghini (Berlin, Heidelberg: Springer Berlin Heidelberg)

[21]   L'Annunziata M F 2016 *Radioactivity: Introduction and History, From the Quantum to Quarks* (Elsevier Science)

[22]   SOLEIL Synchrotron *SOLEIL in 3 Questions* https://www.synchrotron-soleil.fr/en/about-us/what-soleil/soleil-3-questions [date accessed 02/03/2023]

[23]   Elleaume P 1992 Insertion devices for the new generation of synchrotron sources: A review *Rev. Sci. Instrum.* **63** 321–6

[24]   Asakura K, Niimi H and Kato M 2010 Energy Filtered X-Ray Photoemission Electron Microscopy *Advances in Imaging and Electron Physics* vol 162 (Elsevier Inc.) pp 1–43

[25]   Peatman W B 2018 *Gratings, Mirrors and Slits: Beamline Design for Soft X-Ray Synchrotron Radiation Sources* (CRC Press)

[26]   Avadhanulu M N, Kshirsagar P G and Arun Murthy T 2008 *A Textbook of Engineering Physics* (S. Chand Publishing)

[27]   Byrne C, Fagan R, Hinder S, McCormack D E and Pillai S C 2016 New approach of modifying the anatase to rutile transition temperature in TiO_2 photocatalysts *RSC Adv.* **6** 95232–8

[28]   Cremer T, Killian M, Gottfried J M, Paape N, Wasserscheid P, Maier F and Steinrück H P 2008 Physical vapor deposition of [EMIM][Tf2N]: A new approach to the modification of surface properties with ultrathin ionic liquid films *ChemPhysChem* **9** 2185–90

[29]   Henderson Z, Walton A S, Thomas A G and Syres K L 2018 Water-induced reordering in ultrathin ionic liquid films *J. Phys. Condens. Matter* **30** 334003

[30]   Wagstaffe M, Jackman M J, Syres K L, Generalov A and Thomas A G 2016 Ionic Liquid Ordering at an Oxide Surface *ChemPhysChem* **17** 3430–4

[31]   Zhao W, Zhu M, Mo Y and Bai M 2009 Effect of anion on micro/nano-tribological properties of ultra-thin imidazolium ionic liquid films on silicon wafer *Colloids Surfaces A Physicochem. Eng. Asp.* **332** 78–83

[32]   Palacio M and Bhushan B 2008 Ultrathin wear-resistant ionic liquid films for novel MEMS/NEMS applications *Adv. Mater.* **20** 1194–8

[33]   Rietzler F, Piermaier M, Deyko A, Steinrück H P and Maier F 2014 Electrospray ionization deposition of ultrathin ionic liquid films: $[C_8C_1Im]Cl$ and $[C_8C_1Im][Tf2N]$ on Au(111) *Langmuir* **30** 1063–71

[34]   Swarbrick J C, Taylor J Ben and O'Shea J N 2006 Electrospray deposition in vacuum *Appl. Surf. Sci.* **252** 5622–6

[35]   Seah M P 2012 An accurate and simple universal curve for the energy-dependent electron inelastic mean free path *Surf. Interface Anal.* **44** 497–503

[36]   Grinter D C, Venturini F, Ferrer P, van Spronsen M A, Arrigo R, Quevedo Garzon W, Roy K, Large A I, Kumar S and Held G 2022 The Versatile Soft X-Ray (VerSoX) Beamline at Diamond Light Source *Synchrotron Radiat. News* **35** 39–47

[37]   Eriksson M, Al-Dmour E, Andersson, Johansson M, Leemann S C, Malmgren L, Tavares P F and Thorin S 2016 Commissioning of the MAX IV light source *IPAC 2016 - Proc. 7th Int. Part. Accel. Conf.* 11–5

[38]   Tavares P F, Al-Dmour E, Andersson Å, Cullinan F, Jensen B N, Olsson D, Olsson D K, Sjöström M, Tarawneh H, Thorin S and Vorozhtsov A 2018 Commissioning and first-year operational results of the MAX IV 3 GeV ring *J. Synchrotron Radiat.* **25** 1291–316

[39]   Zhu S, Scardamaglia M, Kundsen J, Sankari R, Tarawneh H, Temperton R, Pickworth L, Cavalca F, Wang C, Tissot H, Weissenrieder J, Hagman B, Gustafson J, Kaya S, Lindgren F, Kallquist I, Maibach J, Hahlin M, Boix V, Gallo T, Rehman F, D'Acunto G, Schnadta J and Shavorskiy A 2021 HIPPIE: A new platform for ambient-pressure X-ray photoelectron spectroscopy at the MAX IV Laboratory *J. Synchrotron Radiat.* **28** 624–36

Chapter 4. Simulating molecular systems

Combinations of experimental and computational studies are often required to understand a molecular system in detail. The chemical and electronic behaviour of molecules requires a quantum mechanical understanding of their constituent electrons and nuclei. This often means calculating the ground state and excited state energies of the system by solving the Schrödinger equation. Since the Schrödinger equation has no exact solution for a many-electron system such as an IL ion, a number of approximations have been developed. This chapter will summarise the most common approximations used in molecular modelling and their applications in software. There are a number of approaches one can take to study ILs computationally. Molecular dynamics (MD) and Monte Carlo (MC) simulations offer insights into the properties and structure of ILs, as well as the long-range ordering of ions and interionic interactions [1]. For comparison with experimental X-ray absorption measurements such as X-ray photoelectron spectroscopy (XPS) and near-edge X-ray absorption fine structure (NEXAFS), density functional theory (DFT) is by far the most common model of choice [2]. Unlike classical MD, DFT accounts for the quantum mechanical nature of the system and allows us to probe the electronic structure of ILs. Each of these models (and subsequently software) have their own advantages and disadvantages and should be chosen with consideration of computational resources and the system at hand [3]. In this thesis, the software StoBe-deMon was used to calculate excited states and obtain theoretical NEXAFS spectra of ILs for comparison with experimental results. ORCA and Avogadro were used to generate and visualise molecular orbitals, respectively. These simulations are all carried out for isolated IL ions before and upon chemical reaction with gases such as CO_2 and NO.

4.1 The Schrödinger Equation

The Schrödinger equation (SE) forms the basis of computational quantum chemistry by describing the energy and position of interacting nonrelativistic electrons and

nuclei. The lowest energy configuration of electrons in a system is called the ground state energy (E_0). The SE of a system of N interacting electrons is given by

$$\hat{H}\Psi = E\Psi \tag{4.1}$$

where $\hat{H}$ is the Hamiltonian operator, E is the energy of the system, and Ψ is a many-body wavefunction dependant on the spatial coordinates of electrons and nuclei ($\vec{r}$), and electron spin coordinates [4,5]. $\hat{H}$ (and therefore E) has components describing the kinetic energy of the electrons ($\hat{T}_e$), kinetic energy of the nuclei ($\hat{T}_n$), potential energy due to electron-nuclei Coulomb attraction ($\hat{V}_{en}$), electron-electron Coulomb repulsions ($\hat{V}_{ee}$), and nucleus-nucleus Coulomb repulsions ($\hat{V}_{nn}$). A more detailed version of the SE is given as

$$\hat{H}\Psi = \left[\hat{T}_e + \hat{T}_n + \hat{V}_{en} + \hat{V}_{ee} + \hat{V}_{nn}\right]\Psi \tag{4.2}$$

$$\hat{H}\Psi = \left[-\frac{\hbar^2}{2m_i}\sum_i^N \nabla_i^2 - \frac{\hbar^2}{2m_k}\sum_k^M \nabla_k^2 - \sum_i^N\sum_k^M \frac{e^2 Z_k}{r_{ik}} + \sum_i^N\sum_{i<j}^N \frac{e^2}{r_{ij}} + \sum_k^M\sum_{k<l}^M \frac{e^2 Z_k Z_l}{r_{kl}}\right]\Psi \tag{4.3}$$

where $\hbar$ is the reduced Planck constant, m is the mass of the particle, ∇^2 is the Laplacian operator $\left(\frac{\partial^2}{\partial x^2} + \frac{\partial^2}{\partial y^2} + \frac{\partial^2}{\partial z^2}\right)$, e is the charge of an electron, Z is atomic number, r is the distance between particles, i and j count over the number of electrons N, and k and l count over M nuclei [4].

In its current form, Equation 4.3 is impossible to solve analytically for a many-body system because of the interelectronic repulsion term ($\hat{V}_{ee}$). The solution to the SE grows exponentially more complex with increasing number of interacting electron pairs. Therefore, a number of approximations have been established in order to solve Equation 4.3.

4.1.1 The Born-Oppenheimer Approximation

The first simplification to Equation 4.3 is found by accounting for the motion of electrons and atomic nuclei in molecules. Electron mass is many orders of magnitude smaller than nuclear mass, meaning that electrons travel at much faster timescales than nuclei. In molecules we can therefore assume that the positions of

nuclei are fixed in space while electrons remain dynamic. This is called the Born-Oppenheimer approximation. The kinetic energy term of the stationary nuclei $\hat{T}_n$ can be removed from Equation 4.3 and the Coulomb interactions between nuclei $\hat{V}_{nn}$ can be treated as a constant. Nuclear coordinates are considered external parameters in the SE and Ψ considered a function of only electronic coordinates. This yields the electronic SE (ESE)

$$\hat{H}\Psi = \left[-\frac{\hbar^2}{2m_i}\sum_i^N \nabla_i^2 - \sum_i^N\sum_k^M \frac{e^2 Z_k}{r_{ik}} + \sum_i^N\sum_{i<j}^N \frac{e^2}{r_{ij}} \right]\Psi \tag{4.4}$$

The ESE has $4N$ degrees of freedom ($3N$ spatial coordinates, N spin coordinates) compared to $4(N+M)$ for the SE. While the Born-Oppenheimer approximation reduces the number of calculations it does not account for the computationally expensive $\hat{V}_{ee}$ term. Further assumptions are therefore required, with the Born-Oppenheimer approximation forming their basis.

4.2 Hartree-Fock Theory

The Hartree-Fock (HF) method finds the ground state energy of a many-body system of interacting electrons using a single-electron approach. The ESE is solved by assuming a system of non-interacting electrons that "feel" an effective average potential generated by the other electrons. In a system of non-interacting electrons, the ESE does not include the computationally costly $\hat{V}_{ee}$ term. By neglecting interelectronic interactions, the Hamiltonian of an N electron and M nuclei system can be given as

$$\hat{H} = \sum_i^N \hat{h}_i \tag{4.5}$$

where $\hat{h}_i$ is the one-electron Hamiltonian of electron i, given by

$$\hat{h}_i = -\frac{1}{2}\nabla_i^2 - \sum_k^M \frac{Z_k}{r_{ik}} \tag{4.6}$$

The many-body wavefunction describing the non-interacting electron system is known as the Hartree product and is given by

$$\Psi(\vec{x}_1, \dots, \vec{x}_N) = \chi_1(\vec{x}_1) \dots \chi_N(\vec{x}_N) \tag{4.7}$$

where the vector $\vec{x}_i$ describes the position and spin state of electron i in the spin orbital χ_i. All fermions, including electrons, must follow the Pauli exclusion principle which states that any two fermions in a quantum system cannot exist in the same electronic state. By extension, switching the spatial and spin coordinates $\vec{x}_i$ between a pair of electrons (where $\chi_1 \neq \chi_2$) must result in a change in sign of the many-body wavefunction:

$$\Psi(\vec{x}_1, \vec{x}_2) = -\Psi(\vec{x}_2, \vec{x}_1) \tag{4.8}$$

This condition is not met by the symmetric Hartree product in Equation 4.7, but is satisfied by an antisymmetric wavefunction:

$$\Psi(\vec{x}_1, \vec{x}_2) = \frac{1}{\sqrt{2}} [\chi_1(\vec{x}_1)\chi_2(\vec{x}_2) - \chi_1(\vec{x}_2)\chi_2(\vec{x}_1)] \tag{4.9}$$

Equation 4.9 can be written in the form of a matrix determinant known as the Slater determinant,

$$\Psi(\vec{x}_1, \vec{x}_2) = \frac{1}{\sqrt{2}} \begin{vmatrix} \chi_1(\vec{x}_1) & \chi_2(\vec{x}_1) \\ \chi_1(\vec{x}_2) & \chi_2(\vec{x}_2) \end{vmatrix} \tag{4.10}$$

This wavefunction satisfies the conditions of the Pauli exclusion principle because electrons in the same electronic state ($\chi_1 = \chi_2$) result in a wavefunction $\Psi(\vec{x}_1, \vec{x}_2) = 0$. The Slater determinant can be generalised for N electrons,

$$\Psi(\vec{x}_1, \vec{x}_2) = \frac{1}{\sqrt{N!}} \begin{bmatrix} \chi_1(\vec{x}_1) & \chi_2(\vec{x}_1) & \cdots & \chi_N(\vec{x}_1) \\ \chi_1(\vec{x}_2) & \chi_2(\vec{x}_2) & & \chi_N(\vec{x}_2) \\ \vdots & & \ddots & \vdots \\ \chi_1(\vec{x}_N) & \chi_2(\vec{x}_N) & \cdots & \chi_N(\vec{x}_N) \end{bmatrix} \tag{4.11}$$

This is now a suitable wavefunction to describe our system.

The HF method provides a solution to the many-body ESE by using the Slater determinant, a matrix of N single-electron spin orbitals, as the wavefunction. In the

HF method the electrons do not interact but instead interact with an external effective potential called the Hartree potential, V_H, generated by the stationary nuclei and other electrons in the system. It is worth noting that the Slater determinant also mathematically describes this interaction. The single-electron Hamiltonian used in the HF method is given as

$$\hat{h}_i = -\frac{1}{2}\nabla_i^2 - \sum_k^M \frac{Z_k}{r_{ik}} + V_H \tag{4.12}$$

where the Hartree potential is

$$V_H = \sum_{j \neq i}^N e^2 \int \frac{\rho_j}{r_{ij}} dr \tag{4.13}$$

where ρ_j is the electron density associated with electron j, given by

$$\rho_j(\vec{r}) = \sum_i^N |\chi_i(\vec{r})|^2 \tag{4.14}$$

and is equal to the probability of finding an electron in each occupied state i. Note that the one-electron Hamiltonian $\hat{h}_i$ in Equation 4.12 is similar to that in Equation 4.6 but with an added V_H term. Summing $\hat{h}_i$ according to Equation 4.5 gives $\hat{H}$ of the many-electron system. $\hat{H}$ can be substituted into the ESE in Equation 4.4, using the Slater determinant as the wavefunction, in order to find the ground state energy of the system.

The HF method is an example of a self-consistent field (SCF) method. An initial guess for the wavefunctions of all of the occupied spin orbitals is used to generate $\hat{h}_i$. Parameters of the spin orbitals are altered iteratively until the system is self-consistent. This means that χ_i obtained as a solution from Equation 4.12, when used to calculate V_H in Equations 4.13 and 4.14, should result in the same solutions χ_i when the resulting V_H is inserted back into Equation 4.12 [4].

The set of single-electron spin orbitals χ in the Slater determinant (Equation 4.11) can be found for the ground state using a process called minimisation of the energy

expectation value. The expectation value of energy, $\langle E \rangle = \langle \Psi | \hat{H} | \Psi \rangle$, is the average energy of the system weighted by the probability of measuring each energy value. $\langle E \rangle$ is always larger than the ground state energy E_0 except when in the ground state, at which point it takes its lowest value $\langle E \rangle = E_0$. The set of ground state spin orbitals is obtained when small iterative changes in the spin orbital parameters result in negligible changes in $\langle E \rangle = E_0$.

Spin orbitals can be described by basis sets. A basis set containing a finite number (K) of functions ϕ_i describing the spin orbital χ_j is given as

$$\chi_j = \sum_{i=1}^{K} \alpha_{j,i} \, \phi_i(\vec{x}_i) \tag{4.15}$$

where $\alpha_{j,i}$ is an expansion coefficient. To obtain the set of spin orbitals necessary to solve the ESE, only the expansion coefficients for $i = 1, \ldots K$ and $j = 1, \ldots N$ are needed [6]. Larger basis sets more accurately calculate the spin orbitals of the system but increase the number of calculations.

4.3 Density Functional Theory (DFT)

Density functional theory (DFT) is based on the concept that the ground state energy of a many-electron system can be expressed as a functional of electron density $\rho(\vec{r})$, denoted $E_0[\rho(\vec{r})]$ [4]. A functional is a function whose argument is also a function. In this case, E_0 is a function of ρ which is a function of three spatial coordinates $\vec{r}$. E_0 can therefore be found using $\rho(\vec{r})$ with only three spatial dimensions, instead of the many-body wavefunction with $3N$ spatial dimensions. Finding E_0 using the electron density dramatically reduces the number of calculations required.

Electron density provides all the information required to construct the Hamiltonian operator $\hat{h}_i$. The total number of electrons N is found by integrating the electron density over all space. It follows that electron density can be used to determine the many-electron wavefunction, positions of nuclei and their nuclear atomic numbers from local maxima, and external potentials (as shown in Equation 4.13) [5]. The form of the ground state energy functional is found using the Kohn-Sham method.

4.3.1 Kohn-Sham Equations

In the Kohn-Sham method, an interacting system of *N* electrons is approximated by a fictitious system of *N* non-interacting electrons with the same ground state electron density as the real interacting system. The ground state electron density is calculated from a set of non-physical orbitals ϕ_i according to Equation 4.14 (using ϕ_i in place of spin orbitals χ_i). Electrons in this system move within a local effective potential called the Kohn-Sham potential. The total energy functional of the fictitious system is split into multiple components:

$$E[\rho(\vec{r})] = T_{ni}[\rho(\vec{r})] + V_{en}[\rho(\vec{r})] + V_H[\rho(\vec{r})] + \Delta T[\rho(\vec{r})] + \Delta V_{ee}[\rho(\vec{r})] \tag{4.16}$$

where $T_{ni}[\rho(\vec{r})]$ is the kinetic energy of the non-interacting electrons, $V_{en}[\rho(\vec{r})]$ is the electron-nuclear interaction, $V_H[\rho(\vec{r})]$ is the Hartree potential, $\Delta T[\rho(\vec{r})]$ is a kinetic energy correction term, and $\Delta V_{ee}[\rho(\vec{r})]$ is a non-classical interelectronic repulsion correction term. The exchange-correlation energy $E_{XC}[\rho(\vec{r})]$ encompasses the $\Delta T[\rho(\vec{r})]$ and $\Delta V_{ee}[\rho(\vec{r})]$ correction terms. $E_{XC}[\rho(\vec{r})]$ accounts for the difference in kinetic energy between the fictitious non-interacting system and the real interacting system, and the difference between classical and quantum mechanical interelectronic repulsion. The exchange-correlation energy has an associated exchange-correlation potential, V_{XC}. Importantly, $E_{XC}[\rho(\vec{r})]$ is unknown and must be approximated as discussed below.

The ESE describing the fictitious system of *N* non-interacting electrons takes the form of the single-electron ESE, given as

$$\hat{h}_i \phi_i(\vec{r}) = \varepsilon_i \phi_i(\vec{r}) \tag{4.17}$$

where ε_i is the orbital energy eigenvalue ($E = \sum_i^N \varepsilon_i$) of orbital ϕ_i. Using the electron density to construct $\hat{h}_i$, this equation is given as

$$\left[-\frac{\hbar^2}{2m_i} \nabla_i^2 + V_{en}(\vec{r}) + V_H(\vec{r}) + V_{XC}(\vec{r}) \right] \phi_i(\vec{r}) = \varepsilon_i \phi_i(\vec{r}) \tag{4.18}$$

where V_{en} is the Coulomb potential between an electron and the nuclei, V_H is the Hartree potential given in Equation 4.13, and V_{XC} is the exchange-correlation

potential. Equations 4.18 are known as the Kohn-Sham (KS) equations. Similar to the HF equations, the solutions to the KS equations are self-consistent. KS equations are solved iteratively by first defining a trial electron density $\rho(\vec{r})$. The KS equations are then solved using $\rho(\vec{r})$, outputting single-electron wave functions ψ_i. These wavefunctions are used to calculate a new electron density $\rho_{KS}(\vec{r})$ and compared to $\rho(\vec{r})$. The electron density is iteratively altered until $\rho(\vec{r}) \approx \rho_{KS}(\vec{r})$ within some small tolerance. This convergence occurs at the ground state electron density. The ground state energy E_0 can be determined once a value for the exchange-correlation functional $E_{XC}[\rho(\vec{r})]$ is approximated.

A number of methods have been developed to approximate $E_{XC}[\rho(\vec{r})]$, the simplest of which is the local density approximation (LDA). The LDA assumes a constant electron density at all points in space. The exchange-correlation energy density ε_{XC} can be calculated from the value of ρ at position $\vec{r}$. A constant electron density is not strictly accurate for structurally complex materials or systems. The exchange-correlation functional can be improved by considering the local electron density and the gradient in electron density at the same point $\vec{r}$. This is known as the generalized gradient approximation (GGA). Dozens of GGA functionals have been developed for different configurations of isolated atoms or atoms in solids to give accurate $E_{XC}[\rho(\vec{r})]$ values.

4.4 Visualising Molecular Orbitals

4.4.1 Geometry Optimisation

In this thesis the occupied and unoccupied molecular orbitals (MOs) of IL ions were visualised. The first step in generating the MOs of a molecule is to optimise its geometry into the lowest energy state (i.e., the ground state energy). For the work in this thesis, IL ions were geometry optimised using the software Avogadro [7]. The IL molecules were first constructed by connecting the correct atoms and bonds. Avogadro was then allowed to optimise the atom positions, bond lengths and bond angles. The coordinates and atomic information of the geometry optimised molecule were exported as a text file and imported into other software for further analysis.

The energy of a molecule varies with the position of atoms and can be described by a potential energy surface (PES). This surface maps the energy of the molecule in a given state as a function of nuclear coordinates as shown in Figure 4.1. The PES makes use of the Born-Oppenheimer approximation in which the nuclei have fixed positions. The energy of the molecule can therefore be determined as a function of any set of nuclear positions [8]. The global minimum in the PES signifies the lowest energy state and therefore the optimal geometry of the molecule.
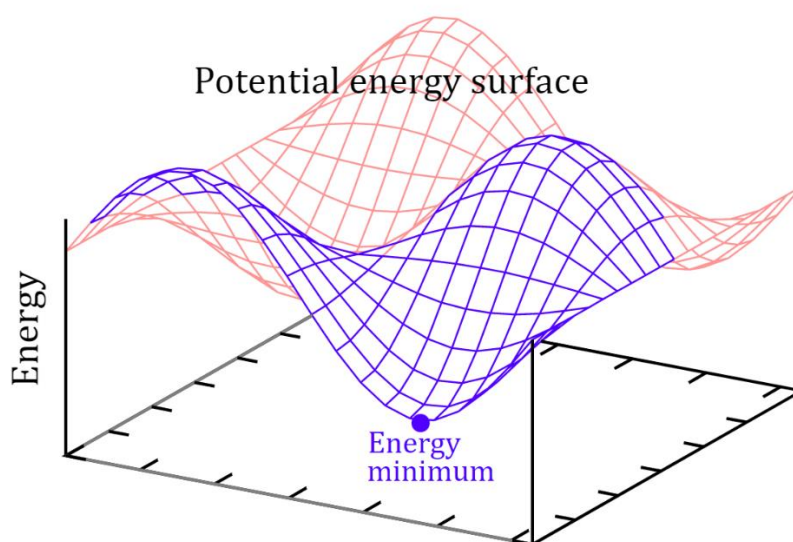
Figure 4.1. Potential energy surface used for molecular geometry optimisation. The point highlighted is the global energy minimum and corresponds to the optimal geometry. Reproduced from [9].

4.4.2 Molecular Orbitals

Occupied and unoccupied MOs of IL ions were generated using ORCA [10,11] and visualised using Avogadro. Examples of MOs that can be visualised include the highest occupied molecular orbital (HOMO) and lowest unoccupied molecular orbital (LUMO). The HOMO and LUMO of the benzimidazolide anion are shown in Figure 4.2. LUMOs are called virtual orbitals since they are unoccupied in the ground state. Visualisation of MOs is important for understanding how changes in chemical structure and bonding affect the distribution of electrons in the molecule.

A MO is represented by an isosurface for which all points on the surface have the same value of the wavefunction describing the MO, i.e., regions in the molecule where electrons are likely to be found. The red and blue colours indicate positive and negative phases of the wavefunction, respectively. A variant on the HF method called the reduced Hartree-Fock (RHF) method was used to calculate the MOs within ORCA. In the RHF method two electrons with opposite spin orbitals are confined to the same spatial orbital.

<center>HOMO   LUMO</center>
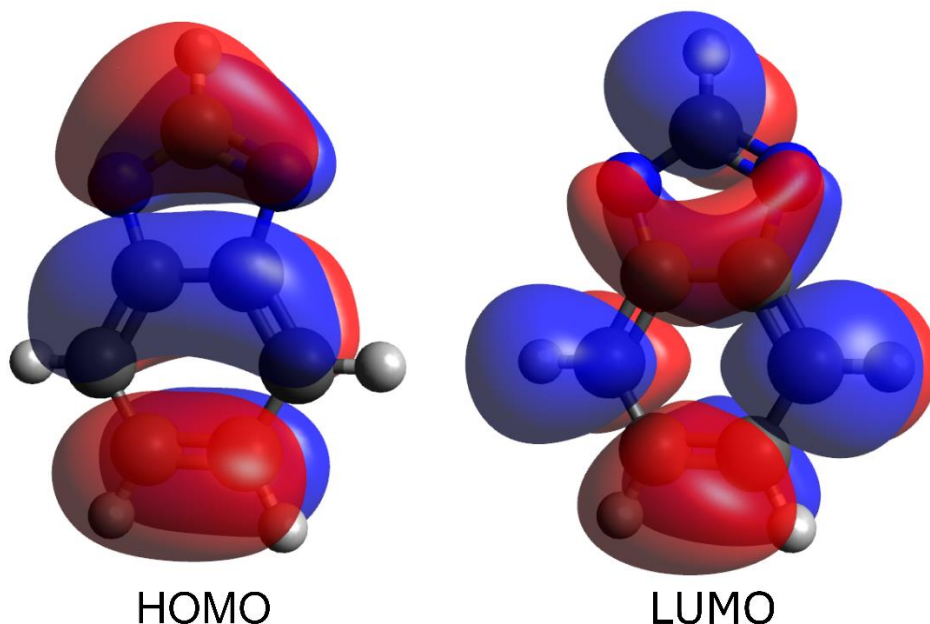
Figure 4.2. Highest occupied molecular orbital (HOMO) of the ionic liquid anion benzimidazolide. The HOMO was generated using ORCA and visualised using Avogadro.

4.5 Simulating NEXAFS Spectra

DFT calculations can be used to calculate the ground state of a molecule and its excited state upon photoionization. This makes it particularly useful for generating theoretical X-ray absorption spectra. In this thesis, theoretical NEXAFS spectra of ILs were calculated using the DFT software StoBe-deMon [12].

4.5.1 StoBe-deMon

The software StoBe-deMon uses transition potential density functional theory (TP-DFT) calculations to generate theoretical NEXAFS spectra. TP-DFT is a single-particle approach based on the Kohn-Sham method [13,14]. A single excitation site

(for example a carbon atom for the C K edge) is used to represent all electronic excitations from core orbitals to unoccupied orbitals [13]. Therefore, all transition energies within the excitation site can be determined with a single calculation. This is achieved by giving the core level of the excited transition state a fractional occupancy of 0.5 [15]. Leaving half an electron in the core hole and placing the other half into the excited state allows the TP-DFT method to account for electronic relaxation effects [16]. Theoretical NEXAFS spectra are plots of total absorption cross-section for each excitation centre as a function of photon energy. The total cross-section corresponds to an angular average. i.e., as if obtained from molecules that are randomly orientated with respect to the incoming electric field vector. The procedure for generating theoretical NEXAFS spectra of the IL is as follows.

StoBe procedure

The IL anions were first geometry optimised in Avogadro. Only the anions of the ILs were considered in this work because $1s \rightarrow \pi^*$ transitions are only valid for structures in which π-bonding is present. The $[P_{66614}]^+$ cation has no ring structures or double/triple bonds so it does not contribute to the experimental NEXAFS spectra. The optimised coordinates of the anion were inserted into a StoBe input file. Examples of StoBe input files and broadening files are given in Appendix A. StoBe input files recognise a wide range of keywords that allow the user to control the parameters of the calculations and their system. This includes information on charge of the system, a suitable exchange-correlation potential (a GGA functional was used here), basis sets, and more. Basis sets contain a set of Gaussian type orbitals, functions that describe a molecular orbital as discussed earlier. Split valence basis sets are commonly used. One basis function describes core orbitals while multiple basis functions describe valence orbitals since they are more susceptible to changes due to chemical bonding.

To generate a NEXAFS spectrum for a whole IL anion, each carbon (for the C K edge) or nitrogen (for the N K edge) atom was simulated separately, energy calibrated, and then added together to produce the total NEXAFS spectrum. Energy calibration requires the lowest energy transition to be known, calculated as the difference in energy between the ground state and the first core-excited state (not to

be confused with the half-core-hole state discussed above). The calculated transition energies were Gaussian-broadened to simulate the increase in full width at half maximum (FWHM) with increasing photon energy of the experimental data. To Gaussian broaden the data, a value of FWHM is chosen for datapoints below the ionisation potential. For photon energies above the ionisation potential the FWHM increases linearly with energy to a maximum FWHM value. The FWHM values can be tuned to match the experimental data.

4.6 References

[1]   Maginn E J 2009 Molecular simulation of ionic liquids: Current status and future opportunities *J. Phys. Condens. Matter* **21**

[2]   Saielli G 2018 Computational Spectroscopy of Ionic Liquids for Bulk Structure Elucidation *Adv. Theory Simulations* **1** 1–18

[3]   Kirchner B, Hollóczki O, Canongia Lopes J N and Pádua A A H 2015 Multiresolution calculation of ionic liquids *Wiley Interdiscip. Rev. Comput. Mol. Sci.* **5** 202–14

[4]   Giustino F 2014 *Materials Modelling Using Density Functional Theory : Properties and Predictions* (Oxford University Press)

[5]   Parr R G and Weitao Y Y 1994 *Density-Functional Theory of Atoms and Molecules* (Oxford University Press)

[6]   Sholl D S and Steckel J A 2009 *Density Functional Theory : A Practical Introduction* (John Wiley & Sons, Incorporated)

[7]   Hanwell M D, Curtis D E, Lonie D C, Vandermeerschd T, Zurek E and Hutchison G R 2012 Avogadro: An advanced semantic chemical editor, visualization, and analysis platform *J. Cheminform.* **4** 17

[8]   Schlegel H B 2011 Geometry optimization *Wiley Interdiscip. Rev. Comput. Mol. Sci.* **1** 790–809

[9]   FamaLab *FamaLab tutorial: ORCA using DFT* https://www.molphys.org/orca_tutorial_2020/en/geom_opt.html [date accessed: 01/03/2023]

[10]   Neese F 2012 The ORCA program system *Wiley Interdiscip. Rev. Comput. Mol. Sci.* **2** 73–8

[11]   Neese F 2018 Software update: the ORCA program system, version 4.0 *Wiley Interdiscip. Rev. Comput. Mol. Sci.* **8** 4–9

[12]   Hermann K, Pettersson L G M, Casida M E, Daul C, Goursot A, Koester A, Proynov E, St-Amant A, Salahub D R, Carravetta V, Duarte H, Friedrich C, Godbout

N, Gruber M, Guan J, Jamorski C, Leboeuf M, Leetmaa M, Nyberg M, Patchkovskii S, Pedocchi L, Sim F, Triguero L and Vela A 2014 StoBe-deMon version 3.3

[13]   Ehlert C, Holzweber M, Lippitz A, Unger W E S and Saalfrank P 2016 A detailed assignment of NEXAFS resonances of imidazolium based ionic liquids *Phys. Chem. Chem. Phys.* **18** 8654–61

[14]   Triguero L, Pettersson L and Ågren H 1998 Calculations of near-edge X-ray-absorption spectra of gas-phase and chemisorbed molecules by means of density-functional and transition-potential theory *Phys. Rev. B - Condens. Matter Mater. Phys.* **58** 8097–110

[15]   Fogarty R M, Matthews R P, Clough M T, Ashworth C R, Brandt-Talbot A, Corbett P J, Palgrave R G, Bourne R A, Chamberlain T W, Vander Hoogerstraete T, Thompson P B J, Hunt P A, Besley N A and Lovelock K R J 2017 NEXAFS spectroscopy of ionic liquids: Experiments versus calculations *Phys. Chem. Chem. Phys.* **19** 31156–67

[16]   Iannuzzi M and Hutter J 2007 Inner-shell spectroscopy by the Gaussian and augmented plane wave method *Phys. Chem. Chem. Phys.* **9** 1599–610

Chapter 5. Near-Ambient Pressure XPS and NEXAFS Study of [P$_{66614}$][benzim] with CO$_2$

The work presented in this chapter was published in the following paper [1]:

Cole J, *et al.*, (2021) "Near-Ambient Pressure XPS and NEXAFS Study of a Superbasic Ionic Liquid with CO$_2$" *J. Phys. Chem. C* **125** 22778–85.

5.1 Introduction

Carbon dioxide (CO$_2$) capture and separation has become an important process in reducing CO$_2$ emissions in fossil fuel-fired power plants. In current industrial applications, alkanolamine solvents such as monoethanolamine (MEA) are typically used for CO$_2$ capture but incur unwanted long-term costs due to the energy required to regenerate them [2]. In recent years, ionic liquids (ILs) have been researched as potential green alternatives for CO$_2$ capture in post-combustion power plants owing to their high CO$_2$ capacity, very low volatility, high thermal stability and lower regeneration temperatures compared to MEA [3–5]. A recent sub-group of ILs called superbasic ILs (SBILs) are being researched for gas capture applications due to their higher CO$_2$ capacities and low viscosity increases compared to conventional ILs [6]. SBILs consist of quaternary phosphonium/ammonium-based cations paired with a superbasic anion such as imidazolide, triazolide or phenoxide [7,8]. SBILs chemically react with CO$_2$ to form carbamate in the same way as MEA.

Unlike conventional imidazolium-based ILs, there is little information available in the literature about monolayer and multilayer behaviour of SBILs. ILs are more highly structured than most molecular liquids, and these studies have all revealed vital information pertaining to the layering and stacking behaviour of these ILs. However, there is little available literature involving the use of X-ray absorption techniques, specifically near edge X-ray absorption fine structure (NEXAFS) spectroscopy. NEXAFS can be used to quantitatively determine the orientation of aromatic IL ions at submonolayer, monolayer, and multilayer coverages [9]. Using near-ambient

pressure synchrotron facilities it is now possible to conduct XPS and NEXAFS measurements of liquid-gas interfaces. It is also helpful to pair experimental NEXAFS with density functional theory (DFT) simulations due to a lack of comparable experimental spectra. No literature currently exists in the way of NEXAFS investigations of IL/gas systems under near-ambient pressure conditions, so simulated NEXAFS spectra will be used in our study to provide further insight into our experimental results.

This chapter reports a combined *in situ* XPS and NEXAFS study into the ordering and interactions of a multilayer thin film deposition of the SBIL trihexyltetradecylphosphonium benzimidazolide ([P$_{66614}$][benzim]) on rutile TiO$_2$ (110) before, during, and after exposure to CO$_2$. NEXAFS measurements are compared to simulated NEXAFS spectra calculated using DFT and quantum chemical simulations are used to visualise the unoccupied antibonding molecular orbitals. This combined approach identifies chemical reactions at the ionic liquid/gas interface and reordering of the IL upon exposure to gas. These results give a new perspective on CO$_2$ uptake in ILs and fundamental interactions at the liquid/gas interface. Understanding this interfacial behaviour is important for developing ILs for gas capture applications and may influence the performance of other IL-based technologies.

5.2 Experimental and Theoretical Methods

Experimental measurements of [P$_{66614}$][benzim] were carried out at beamline VerSoX (B07) at Diamond Light Source in the UK (photon energy range 250 - 2800 eV) [10,11]. The [P$_{66614}$]$^+$ cation was synthesised by collaborators (Christopher Hardacre, Adam Greer) using a trihexylphosphine precursor as detailed in ref. [12]. The VerSoX endstation has a hemispherical PHOIBOS 150 NAP electron energy analyser and the analysis chamber is backfilled with gas to carry out near-ambient pressure measurements. The angle of the sample can be rotated with respect to the analyser whilst at near-ambient pressure which allows angle-resolved NEXAFS measurements. A rutile TiO$_2$ (110) single crystal (PI-KEM) was cleaned via Ar$^+$ sputter/anneal cycles (sputtering at 1 keV for 10 minutes and annealing at 700°C for 10 minutes) until XPS spectra showed no contamination. The cleaning process

introduces defects on the TiO_2 crystal surface in the form of oxygen vacancies. These induce the formation of a small amounts of Ti^{3+} species which can be seen in the Ti 2p region (Figure 5.6) as a low BE peak at approximately 467 eV [13]. Following preparation of the clean TiO_2 surface, a 0.5 M solution of $[P_{66614}][benzim]$ (chemical structure shown in Figure 5.1) in methanol was deposited dropwise via a syringe onto the TiO_2 substrate in the load lock of the end station in ambient laboratory conditions. It was then allowed to degas for several hours under vacuum conditions prior to measurements. We expect the methanol to be fully removed in this time. A small amount of water may remain ad/absorbed after degassing since the IL/methanol solution was exposed to air during deposition (as discussed below).
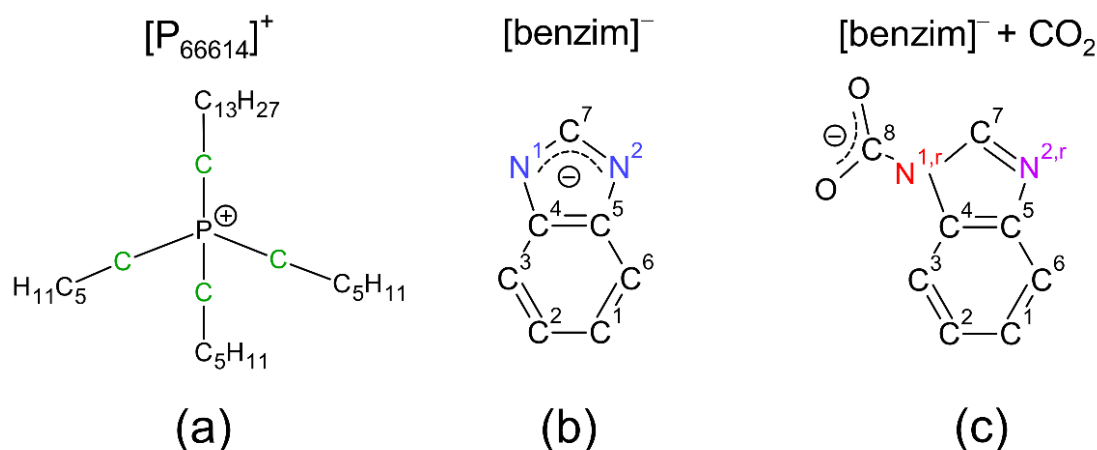
Figure 5.1. (a) Chemical structure of the $[P_{66614}]^+$ cation with C_{hetero} atoms highlighted in green and $C_{aliphatic}$ in black. The $[benzim]^-$ anion is shown (b) as presented and (c) while reacted with CO_2, where $N^{1,r}$ (red) and $N^{2,r}$ (purple) denote the N atoms following reaction with CO_2 at the N^1 site.

Near-ambient pressure XPS (NAP-XPS) measurements of the $[P_{66614}][benzim]$ multilayer thin film were taken at high vacuum (as presented), during exposure to three different pressure regimes of CO_2 (10^{-6} mbar, 1 mbar, and 5 mbar), and after CO_2 gas was pumped out. The reaction of CO_2 with the $[benzim]^-$ anion is shown in Figure 5.1(c). XPS scans across the IL layer showed a film with inhomogeneous thickness, therefore measurements were taken on a very thin part of the film such that the Ti 2p signal from the TiO_2 substrate was still detectable (homogeneous over approximately 2 mm square, approximately 0.5 nm thick on average). The sample

was moved approximately 0.2 mm between scans to avoid degradation and charging of the film (beam size ≤ 200 μm × ≤ 200 μm). All XPS peaks have been fitted using a Gaussian-Lorentzian product line shape (30:70 Lorentzian:Gaussian contribution) and a linear background, using the software CasaXPS [14]. The binding energy (BE) scale for all regions has been calibrated to the alkyl C 1s signal at 285.0 eV and all fitted peaks are quoted to ± 0.1 eV BE [15].

The photoemission measurements were accompanied by *in situ* AEY C K edge and N K edge NEXAFS. C K edge NEXAFS spectra were recorded over the range 280 to 315 eV by monitoring the C Auger peak at a kinetic energy of 260 eV. N K edge NEXAFS spectra were recorded over the range 390 to 430 eV by monitoring the N Auger peak at a kinetic energy of 375 eV. The NEXAFS spectra are intensity-normalised such that the step between 280 eV and 315 eV (for the C K edge), and between 390 eV and 430 eV (for the N K edge), is equal to unity. Background correction procedures were also performed to account for the gas-phase CO_2 and TiO_2 substrate signals.

The experimental NEXAFS spectra are compared to theoretical spectra obtained using DFT simulations performed in the software StoBe-deMon [16]. The isolated [benzim]$^-$ anion was geometry optimised in Avogadro [17] (version 1.2) before excited state calculations were carried out in StoBe-deMon. For the C K edge, theoretical NEXAFS spectra were obtained for each carbon atom in the anion and then combined to produce the total theoretical spectrum for the anion. The same procedure was carried out for the N K edge, using each nitrogen atom in the anion. These simulations represent an angular average in which the anions are considered to be randomly oriented with respect to the incoming electric field vector. The spectra were then broadened using Gaussian functions with linearly increasing Full-Width at Half Maxima (FWHM) from 0.7 eV to 12.0 eV between the photon energies of 290 and 310 eV. This accounts for the reduced lifetime of the σ^* resonances [18]. The theoretical NEXAFS spectra for each individual atom were energy calibrated by calculating the difference in total energy between the ground state and first core-excited state. This gives the energy of the first transition in the NEXAFS spectrum for that atom. The calibrated individual spectra were added together to produce the

total theoretical spectra. The total theoretical spectra were then simply shifted in energy to match the experimental NEXAFS spectra. To complement NEXAFS simulations, unoccupied molecular orbitals were calculated using the software ORCA (version 4.0) and visualised using Avogadro [19,20].

5.3 NAP-XPS of [P$_{66614}$][benzim]
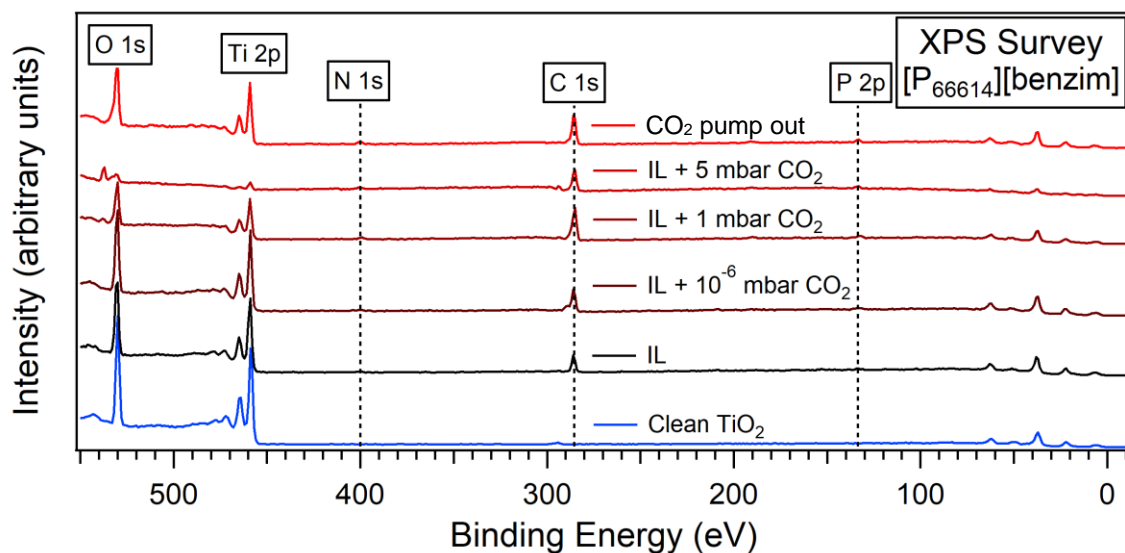
Figure 5.2. XPS survey spectra of clean TiO$_2$ and [P$_{66614}$][benzim] thin films on TiO$_2$ subject to various exposures of CO$_2$. Highlighted are the peaks associated with atoms in the TiO$_2$ (110) crystal substrate (O 1s, Ti 2p) and the IL (N 1s, C 1s, P 2p).

NAP-XPS measurements of multilayer [P$_{66614}$][benzim] were taken upon exposure to increasing pressures of CO$_2$ (10^{-6}, 1 and 5 mbar) in the C 1s, N 1s, O1s, Ti 2p, and P 2p regions (taken at photon energies of 585, 700, 830, 760, and 430 eV, respectively). The fitted components of these regions are summarised in Table 5.1. Figure 5.2 shows survey spectra for each exposure stage and the clean TiO$_2$ (110) crystal prior to deposition of the IL. These were all taken with a photon energy of 1200 eV.

Region	Binding Energy (eV) ± 0.1 eV	Assignment
C 1s	285.0	$C_{aliphatic}$
	285.9	C_{hetero}
	286.8 → 287.1	C_{anion}
	289.0 [a]	Carbamate
	293.3	Gas-Phase CO_2
N 1s	398.6	$N^{1,2}$
	400.0	$N^{2,r}$
	401.1	$N^{1,r}$
O 1s	530.0[a]	TiO_2 lattice O
	531.1	Carbamate
	532.2	$C = O^{b}$
	533.3[a]	$C - OH^{b}$
	537.2	Gas-Phase CO_2
P 2p	130.4	THP $2p_{3/2}$
	131.3	THP $2p_{1/2}$
	132.4 → 132.8	$[P_{66614}]^+$ $2p_{3/2}$
	133.3 → 133.7	$[P_{66614}]^+$ $2p_{1/2}$
	135.6	Phosphine oxide $2p_{3/2}$
	136.5	Phosphine oxide $2p_{1/2}$

Table 5.1. Assignments and BEs of fitted components in the C 1s, N 1s, O 1s and P 2p regions for [P$_{66614}$][benzim] before exposure, while exposed to CO_2 at various pressures, and after pumping out CO_2. These were taken at photon energies of 585, 700, 830, and 430 eV, respectively, for each of the above regions. The arrow (→) denotes a chemical shift due to the absorption of CO_2. [a] BEs differ by ± 0.2 eV. [b] Within the protonated carbamate group.
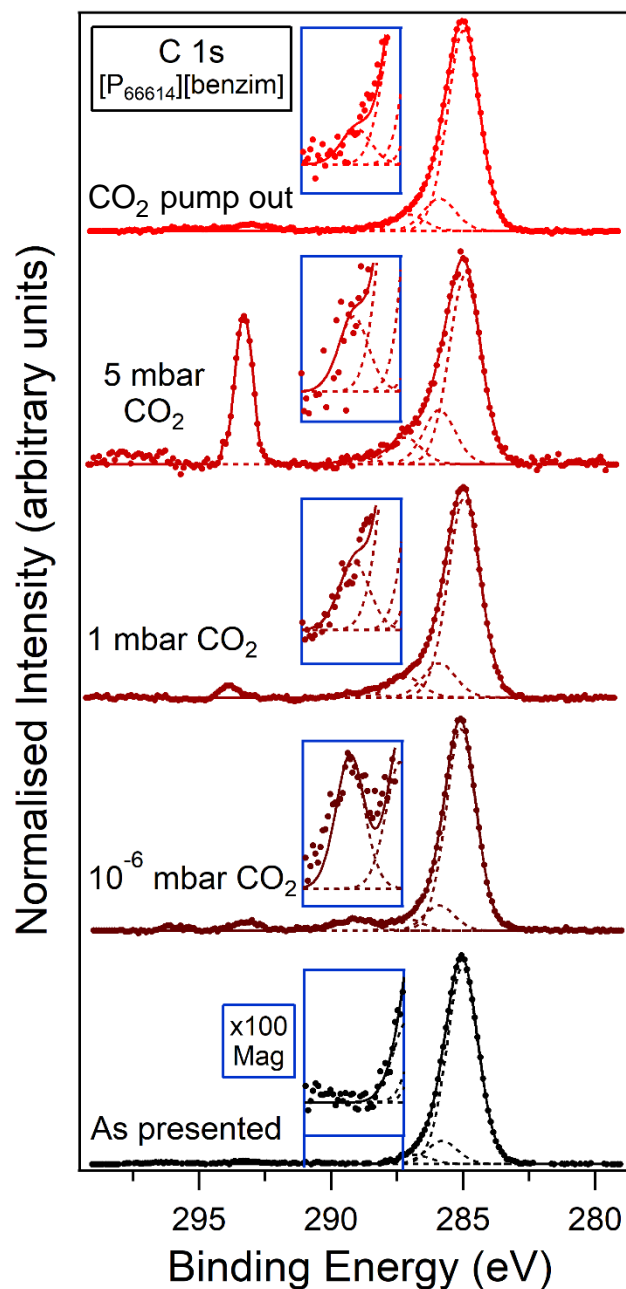
Figure 5.3. C 1s XPS regions recorded at a photon energy of 585 eV for a thin film of [P_{66614}][benzim] as presented, exposed to 10^{-6} mbar CO_2, 1 mbar CO_2, 5 mbar CO_2, and after CO_2 pump out. The binding energy range between 287 to 291 eV is magnified × 100 (blue boxes) and shows the formation of a carbamate peak upon absorption of CO_2.

All the spectra in the C 1s region shown in Figure 5.3 are normalised to the main peak which can be fitted with two components attributed to carbon atoms in the [P_{66614}]$^+$ cation. The component at 285.0 eV is attributed to aliphatic carbon ($C_{aliphatic}$,

see Figure 5.1(a)) and the component at 285.9 eV is attributed to carbon atoms immediately around the phosphorous atom, C_{hetero}. Their positions are consistent with previous reports for phosphonium-based ILs with the same $[P_{66614}]^+$ cation [15]. For the IL as presented, the area ratio of these components ($C_{aliphatic}$:C_{hetero}) is 8.6:1 compared to 7:1 from the stoichiometry of the cation. The slight discrepancy from stoichiometry may be due to aliphatic contamination during deposition of the IL in atmosphere or could be due to photoelectron diffraction effects. It is possible that C−C bonds in the [benzim]⁻ anion provide a small contribution to the main $C_{aliphatic}$ peak which can also affect this $C_{aliphatic}$:C_{hetero} ratio. As discussed in our P 2p analysis below, there will also be aliphatic and hetero contributions from the trihexylphosphine precursor used in the synthesis of the IL at similar BEs. The C 1s peak is asymmetric towards higher BEs and can be fitted with a component at 286.8 eV attributed to C−N bonds in the [benzim]⁻ anion (C_{anion}) [9,15,21].

When the IL is exposed to CO_2, it results in a peak at 293.3 eV attributed to gas-phase CO_2. This is only visible in the 1 mbar and 5 mbar exposure stages. At 10^{-6} mbar, a feature appears at a similar BE but is assigned to K 2p as discussed below in Figure 5.8. Further changes arise when CO_2 is introduced; while the $C_{aliphatic}$ and C_{hetero} components remain unchanged in position, the C_{anion} component experiences an upward chemical shift of 0.3 eV to 287.1 eV, true for each of the pressures tested. Even after removal of CO_2 this component remains shifted to a higher BE. Additionally, the absorption of CO_2 results in another peak at a BE of 289.0 eV, assigned to the formation of carbamate as shown in Figure 5.1(c). The position of this carbamate peak is in line with previous reports of CO_2 absorption in bulk coverages of $[P_{66614}]$[benzim] [22]. For the IL as presented there is no carbamate peak, further confirming that this peak is due to the IL's reaction with CO_2. The region between 287 to 291 eV in Figure 5.3 is magnified (×100) to highlight the relative change in intensity of this carbamate feature with increasing CO_2 pressure. Even at pressures as low as 10^{-6} mbar of CO_2, the formation of carbamate can be observed. In fact, the carbamate peak is more intense for 10^{-6} mbar than for any of the higher pressures. At this low pressure, reactions are likely to occur at the IL/gas interface, causing the intense carbamate peak. The decrease in intensity of the carbamate peak at higher pressures suggests that the saturated anions are reorienting towards

the bulk. Interestingly, this carbamate peak is still present after removal of CO_2, implying that the absorption/desorption of CO_2 is not fully reversible in this experiment. It has been shown that bulk thicknesses of $[P_{66614}][benzim]$ absorb and desorb CO_2 reversibly when the surrounding CO_2 gas is pumped out [22], or when the IL is heated [8], so it is unclear why the reaction is not fully reversible here. The thickness of the IL film is likely to influence the reversibility of reactions, as well as the TiO_2 surface, as discussed further in the chapter.

There is a gradual shift of the carbamate peak from 289.1 eV in the 10^{-6} mbar stage to 288.8 eV after CO_2 pump out. The cause of this BE shift is unknown. However, the N 1s and P 2p spectra below show significant changes throughout the exposure stages and after removal of gas. For example, the P 2p spectra in Figure 5.5 indicate reordering of a number of different species through the sample depth (as discussed further below), all of which can interact with anions. These intermolecular interactions may change when the anions reorientate upon exposure to (or removal of) CO_2 and may cause a BE shift in the carbamate component after CO_2 is pumped out. Note that since the IL film was deposited dropwise, there may be some direct adsorption of CO_2 on the TiO_2 surface. Adsorbed CO_2 commonly occurs at approximately 290.5 – 292.5 eV [23]. However, there is no visible adsorbed CO_2 peak here nor any evidence of reaction with the TiO_2 surface to form CO_3^{2-} (288.5 – 289.0 eV, [23]). Therefore, it appears that the IL fully covers the substrate here and no IL islands have formed.

The N 1s spectra in Figure 5.4 have been normalised to the total area and can be fitted with three components at 398.6, 400.0 and 401.1 eV. These are attributed to the chemically equivalent imidazolide N^1 and N^2 atoms ($N^{1,2}$), $N^{2,r}$ in the CO_2-reacted anion, and $N^{1,r}$ in the CO_2-reacted anion, respectively. N^1 and N^2, shown in Figure 5.1(b), are chemically equivalent due to resonance effects in the anion [22,24]. Imidazole carbamate forms at $N^{1,r}$ and the remaining unreacted N in the anion is labelled $N^{2,r}$. We would expect $N^{1,2}$ to be the only component in the as presented (pre-exposure) stage, however, we still see $N^{1,r}$ and $N^{2,r}$ reaction peaks. These occur from reaction to ambient CO_2 in the atmosphere when the sample was transferred to the UHV chamber.
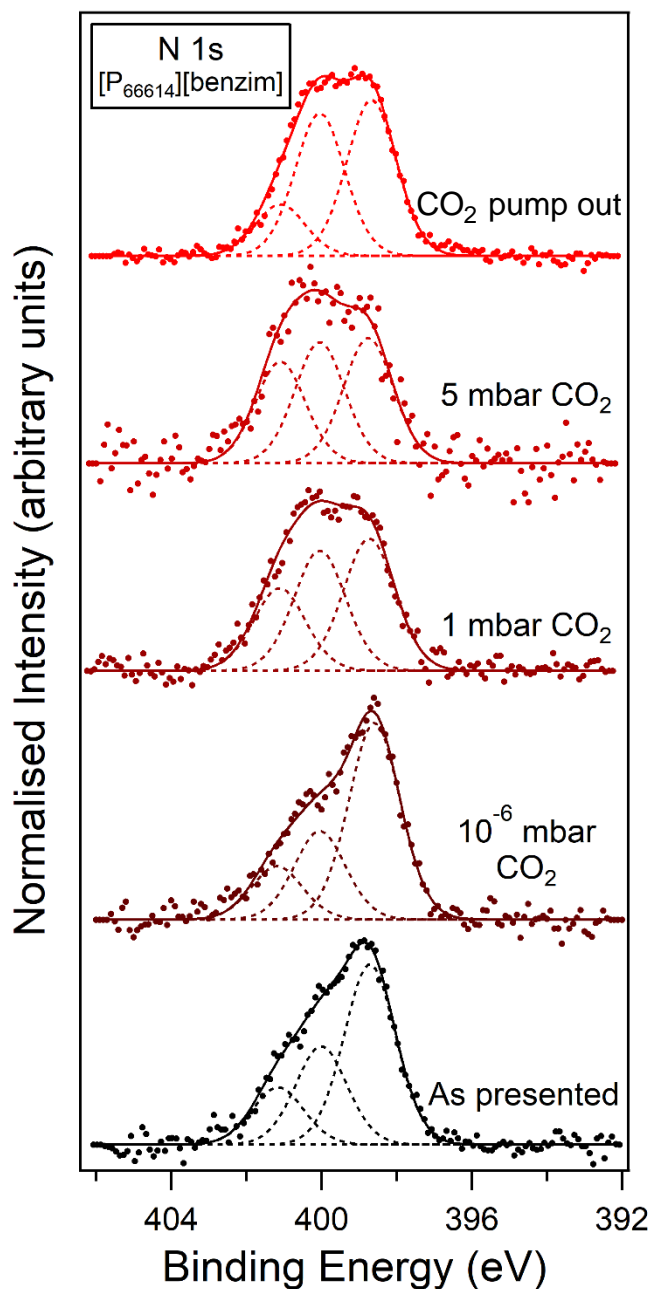
Figure 5.4. N 1s XPS region recorded at a photon energy of 700 eV for a thin film of [P_{66614}][benzim] as presented, exposed to 10^{-6} mbar CO_2, 1 mbar CO_2, 5 mbar CO_2, and after CO_2 pump out.

As the IL is exposed to CO_2, the $N^{1,r}$ and $N^{2,r}$ components in Figure 5.4 increase in intensity with increasing pressure of CO_2 relative to $N^{1,2}$, further suggesting that these components are attributed to the absorption of CO_2. However, the $N^{1,r}$ and $N^{2,r}$ components deviate from the expected 1:1 area ratio. The $N^{2,r}$ component remains

of comparable intensity to $N^{1,2}$, however, the $N^{1,r}$ component reduces in relative intensity compared to $N^{1,2}$. This deviation from a 1:1 area ratio may be due to the weak interaction between unreacted anions and CO_2 trapped between the IL layers. Such an interaction is likely to result in a shift of the $N^{1,2}$ component towards higher BEs, causing an apparent increase in the $N^{2,r}$ component. After pumping out CO_2, the intensities of these components do not return to their pre-exposure intensities (as presented stage), indicating an irreversible reaction. The presence of reacted species both before exposure and after removal of CO_2 indicates that CO_2 cannot be fully removed by pumping down to high vacuum.

The P 2p spectra in Figure 5.5 have been normalized to the total area of the peak. For the as presented spectrum, the lower-energy feature can be fitted with $2p_{3/2}$ and $2p_{1/2}$ components at 130.4 and 131.3 eV and may be attributed to trihexylphosphine (THP). There is no evidence of beam damage-induced degradation of the $[P_{66614}]^+$ cation, therefore, it is likely that THP is present as a precursor impurity from the synthesis of $[P_{66614}]^+$ [12]. The higher-energy feature is fitted with $2p_{3/2}$ and $2p_{1/2}$ components at 132.4 and 133.3 eV, respectively, and is assigned to the $[P_{66614}]^+$ cation [15].

Upon exposure to CO_2, the $[P_{66614}]^+$ components shift by 0.4 eV to higher BEs of 132.8 and 133.7 eV, respectively. In addition, the THP feature reduces in intensity with CO_2 exposure. These changes could be explained by a reversible reaction between phosphine (THP) and CO_2. As CO_2 exposure is increased, there is a reduction in the THP feature and an increase in the THP-CO_2 adduct feature, which is likely to occur at a similar BE to the $[P_{66614}]^+$ feature. Therefore, the $[P_{66614}]^+$ feature at about 133 eV appears to broaden and increase in intensity. The THP peak reduces to zero upon exposure to the highest pressure of 5 mbar CO_2. The THP peak reappears after CO_2 is pumped out but the region is dominated by the $[P_{66614}]^+$ peak. The intensities of these two peaks are flipped compared to the IL pre-exposure peaks and may be indicative of reordering of the depth profile of the ions, or weak interaction between the cation and trapped CO_2 in the IL layers.
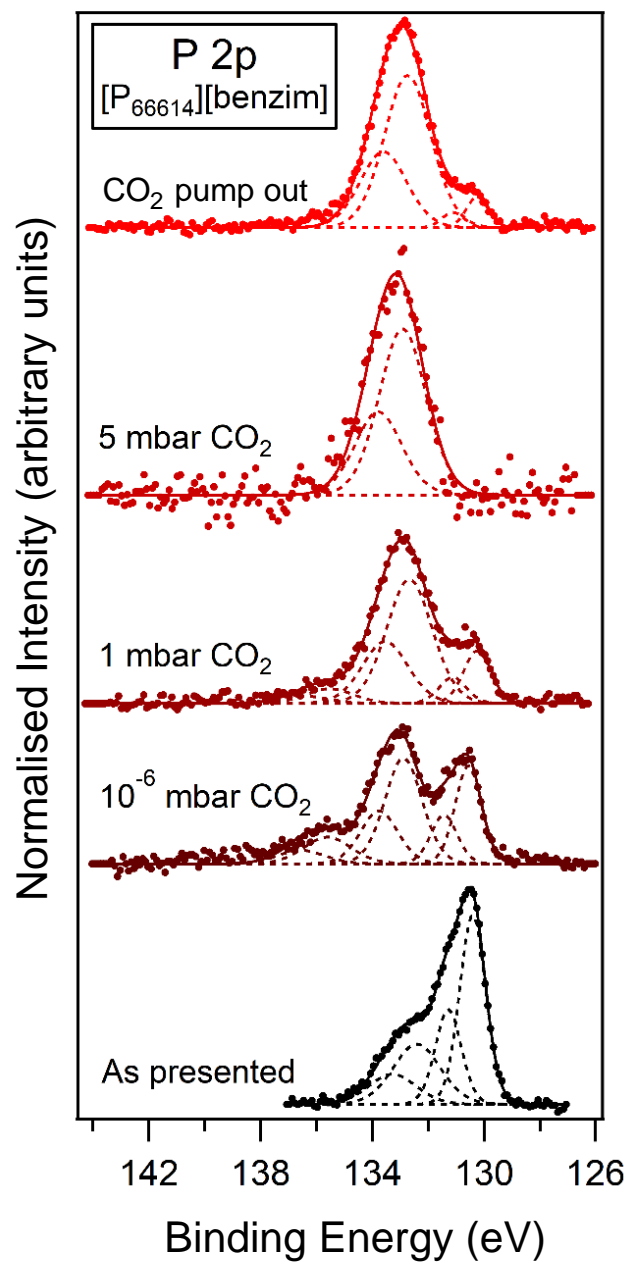
Figure 5.5. P 2p region recorded at a photon energy of 430 eV for multilayer [P_{66614}][benzim] as presented, while exposed to various pressures of CO_2, and after CO_2 pump out.

A shoulder at 136 eV appears when the IL is exposed to low pressures of CO_2 (10^{-6} and 1 mbar), assigned as phosphine oxide, forming from the reaction between phosphine and residual water in the chamber or on the sample surface [25]. As shown in Figure 5.10, this phosphine oxide peak is more pronounced at GE, suggesting it is a surface phenomenon. This may explain why the peak only occurs

106

at low pressures of CO_2, because the residual water is likely to be displaced away from the surface with increasing pressures of CO_2. Phosphine oxide should appear in the O 1s spectra but this has not been specifically assigned due to the complex nature of the O 1s region.
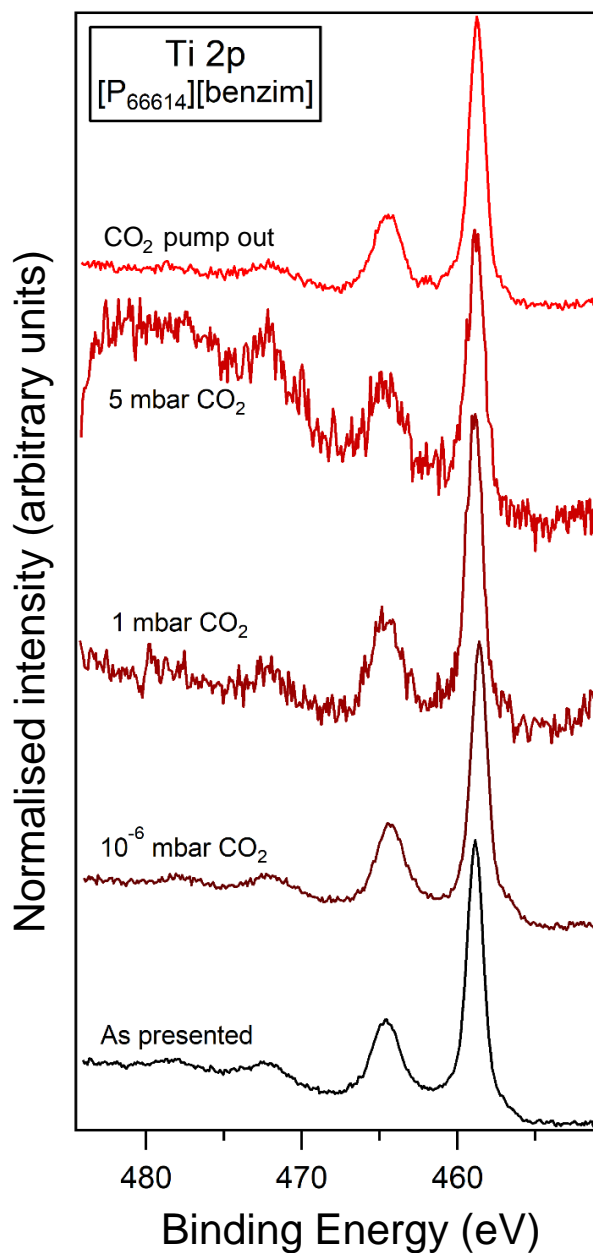
Figure 5.6. Ti 2p region for multilayer [P$_{66614}$][benzim] as presented, exposed to 10^{-6} mbar CO_2, 1 mbar CO_2, 5 mbar CO_2, and after CO_2 pump out.

Narrow scans over the Ti 2p region for [P_{66614}][benzim] are shown in Figure 5.6 before exposure to CO_2; upon exposure to 10^{-6} mbar, 1 mbar and 5 mbar of CO_2; and after pumping out CO_2. The region consists of two peaks at 458.7 and 464.5 eV which occur due to spin-orbit coupling, assigned as $2p_{3/2}$ and $2p_{1/2}$, respectively. These peaks result from Ti^{4+} atoms in the TiO_2 substrate. A small shoulder at approximately 467 eV can be seen, attributed to Ti^{3+} formed due to oxygen vacancies introduced in the sputter/anneal cycles. The spectra show very little change through the exposure stages, except for increasing noise with higher pressures of CO_2 due to increased attenuation of photoelectrons. The high BE features at ~ 472 and 478 eV are energy loss satellite peaks [26,27].

O 1s spectra taken over the same exposure stages are shown in Figure 5.7. For the IL as presented, the O 1s peak is fitted with three peaks at 530.0, 531.1, 532.2 eV. The component at 530.0 eV is attributed to O atoms in the TiO_2 lattice and is detectable because the IL film is sufficiently thin (approximately 0.5 nm) [28]. The two higher BE peaks are attributed to surface defects/hydroxyls at the TiO_2 surface [13]. Since no evidence of CO_2 adsorption at the TiO_2 surface was seen in the C 1s spectra in Figure 5.3, it is likely that the peak at 532.2 eV is instead due to the formation of hydroxyl species upon adsorption of trace amounts of water. When the IL is exposed to higher pressures of CO_2 (1 mbar and 5 mbar), the spectra can be fitted with four components at BE of 530.0, 531.1, 532.2 and 533.3 eV. Note that the intense gas-phase CO_2 peak at 537.2 eV is not shown in Figure 5.7 in order to make the region clearer. We suspect there is a mixture of protonated and unprotonated carbamate species in the sample, therefore, the component at 531.1 eV is attributed to unprotonated carbamate, while the remaining components at 532.2 and 533.3 eV are attributed to $C = O$ and $C – OH$ in the protonated carbamate group, respectively [29–31]. Protonation of the anion is likely to arise due to contamination of water vapour. The TiO_2 lattice O component at 530.0 eV reduces in intensity with increasing CO_2 pressure. Upon exposure to the highest pressure of 5 mbar CO_2, the $C = O$ and $C – OH$ components contribute to a pronounced protonated carbamate feature. After removal of CO_2, the protonated carbamate components are still present (top spectrum of Figure 5.7), however, in the IL as presented and IL + 10^{-6} mbar CO_2 stages the $C – OH$ component is too small to be fitted.
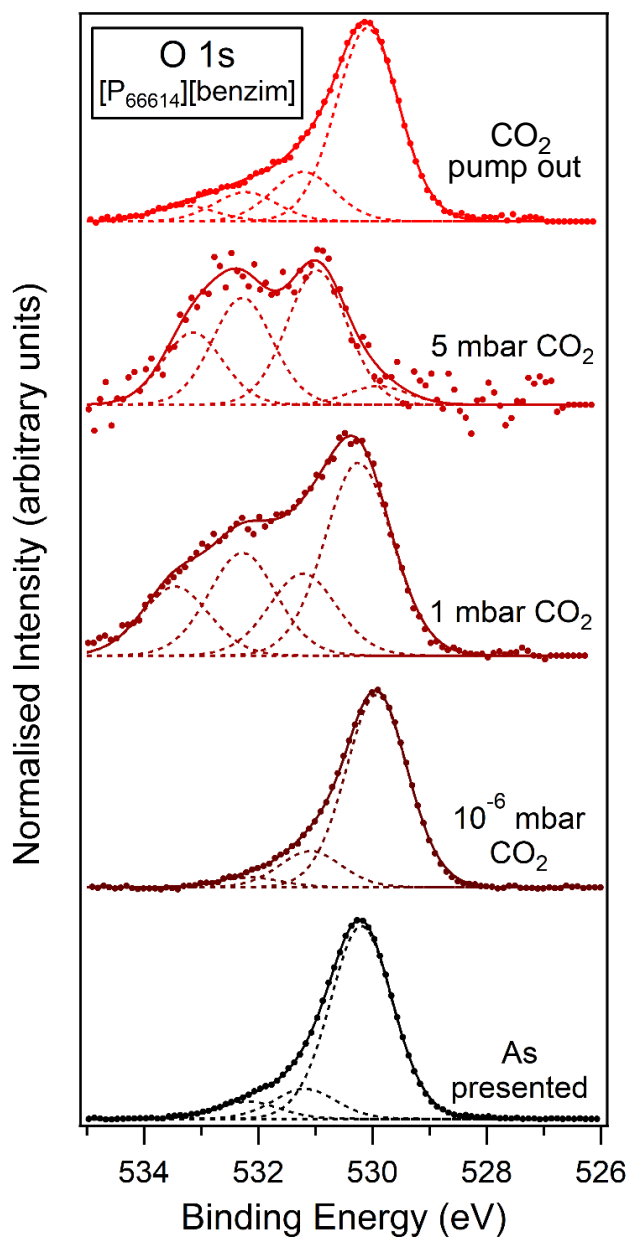
Figure 5.7. O 1s region recorded at a photon energy of 830 eV for multilayer [P_{66614}][benzim] as presented, while exposed to various pressures of CO_2, and after CO_2 pump out.

The O 1s spectra have been normalised to the intensity of the TiO_2 lattice O peak at 530.0 eV. However, there is a dramatic relative decrease in the 530.0 eV component of the IL + 5 mbar CO_2 spectrum as the IL absorbs more CO_2. Therefore, this spectrum was normalised such that the intensities of high BE components at 532.2 and 533.3 eV have the same intensities as those for 1 mbar CO_2.

Alongside the C 1s and N 1s spectra, O 1s spectra in Figure 5.7 also show evidence of irreversible CO_2 absorption occurring in our thin film of [P_{66614}][benzim]. The results presented, herein, suggest that the reversibility of CO_2 absorption is not only dependent on the structure of the IL, but also the thickness of the IL film. The interaction of the substrate and vacuum with our ultra-thin film of an imidazolide-based IL results in highly structured IL layers which have the potential to trap CO_2. This trapped CO_2 may impact the reversibility of CO_2 absorption in thin films with only several layers. Angle-resolved XPS can be used to determine whether the trapped CO_2 is surface-bound or resides in the deeper layers of the IL film.

5.4 Angle-Resolved XPS
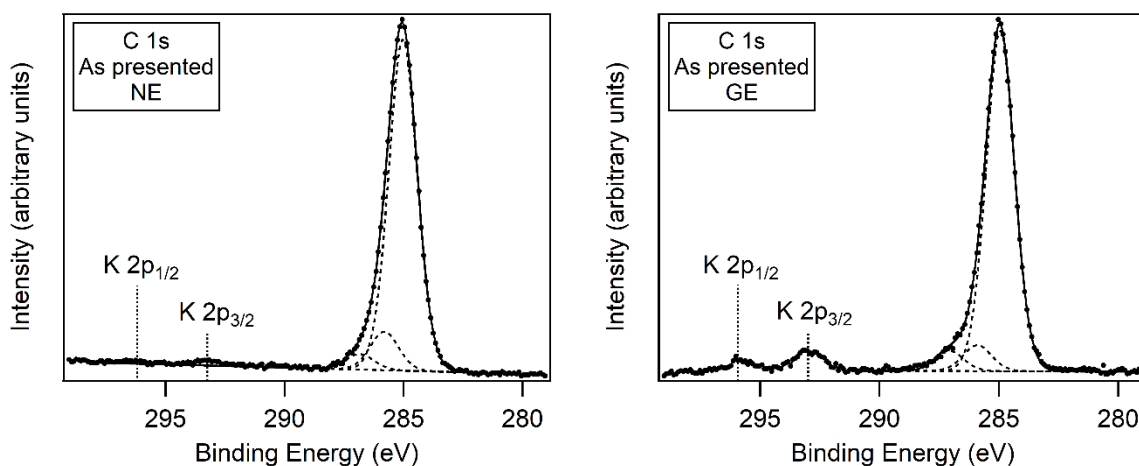
Figure 5.8. C 1s normal emission (NE) and grazing emission (GE) XPS spectra of [P_{66614}][benzim].

XPS spectra of [P_{66614}][benzim] were taken at grazing emission (GE, 40° from normal emission) over the C 1s region as shown in Figure 5.8, providing more surface-sensitive measurements. There is little change in the overall shape of the C 1s peak when taken at GE compared to normal emission (NE) except for a slight reduction in the intensity of the C_{hetero} component at 285.9 eV. From this we can deduce that the concentration of $C_{aliphatic}$, C_{hetero} and C_{anion} species does not vary significantly throughout the sample depth. The peaks at 293 and 296 eV are assigned as K $2p_{3/2}$ and K $2p_{1/2}$, respectively. They become more pronounced for GE, indicating surface contamination with potassium. Shake-up satellites may also manifest at similar BEs

but the presence of a feature at approximately 295 eV in the clean TiO_2 survey spectrum would suggest this is K contamination.

GE and NE measurements of [P_{66614}][benzim] taken over the N 1s region are shown in Figure 5.9. This provides an insight into how the concentration of the $N^{2,r}$ (400.0 eV) and $N^{1,r}$ (401.1 eV) reaction species changes with depth into the sample. Compared to NE, the N 1s peak taken at GE has a more intense $N^{1,2}$ (398.6 eV) component relative to the two reaction-based components. This suggests that there is a greater concentration of unreacted anions ($N^{1,2}$) in the surface layers of the IL, and a greater concentration of reacted anions ($N^{1,r}$ and $N^{2,r}$) in the bulk. Similar behaviour was reported for aqueous MEA solutions treated with CO_2 by Lewis *et al.*, revealing that reacted MEA had a greater concentration in the bulk of the solution while unreacted MEA was more concentrated at the surface [32].
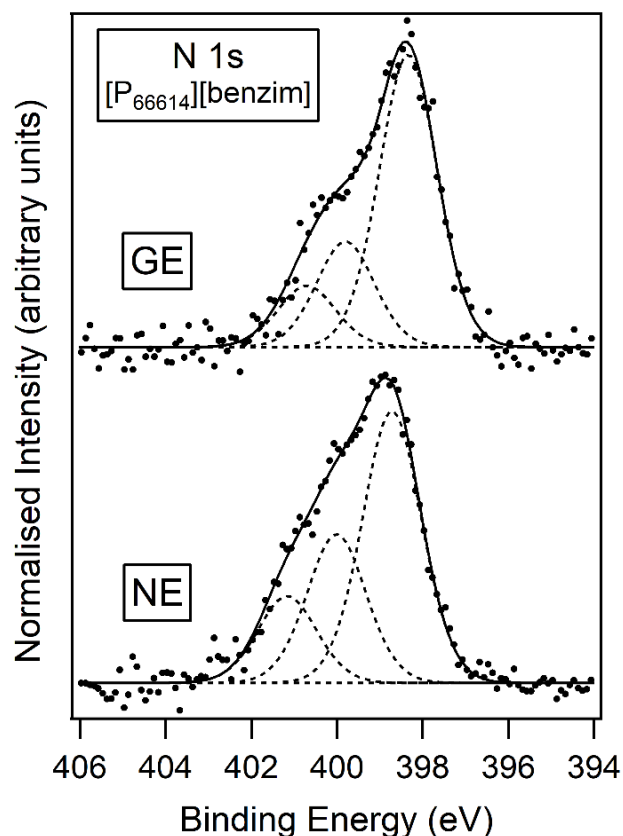
Figure 5.9. N 1s spectra of multilayer [P_{66614}][benzim] (as presented) recorded at a photon energy of 700 eV at normal and grazing emissions.

As discussed by Henderson *et al.*, the anion can also react with ambient water vapour, resulting in $N^{1,2}$, $N^{2,r}$, and $N^{1,r}$ components at BEs of 397.5, 398.5 and 400.0 eV, respectively [22]. Our results in Figures 5.4 and 5.9 show a significant increase in BE for these components in a multilayer thin film compared to those found by Henderson *et al.* for bulk deposition. Wagstaffe *et al.* reported a dependence of peak position on overlayer thickness, finding that components undergo a downward shift in BE when deposited as a thin film compared to bulk deposition [9]. Coverage-dependent chemical shifts have been found for thin films of the IL [C_1C_1Im][Tf_2N] deposited on Au (111) via physical vapour deposition by Cremer *et al.* [33]. They reported a similar dependence to Wagstaffe *et al.* with the addition that the peak positions for thin films of increasing thicknesses did not tend to those of a bulk film but exceeded them by as much as 0.2 eV (4.5 monolayer film). This may explain the higher BEs reported here for our thin film in Figure 5.4 compared to previous reports for bulk thicknesses.
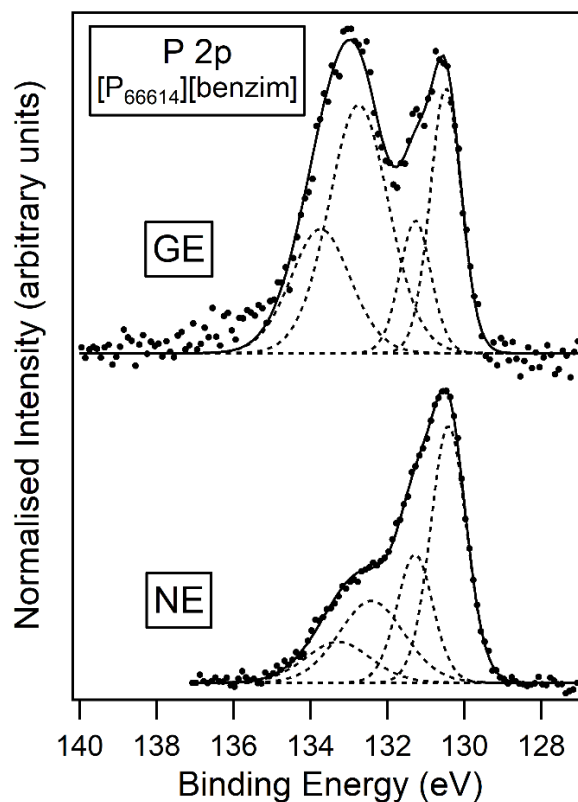
Figure 5.10. P 2p spectra of multilayer [P_{66614}][benzim] (as presented) recorded at a photon energy of 430 eV at normal and grazing emissions.

112

GE measurements over the P 2p region (Figure 5.10) show a more intense 133 eV [P_{66614}]$^+$ peak at GE compared to NE before exposure to CO_2, suggesting there is a greater concentration of [P_{66614}]$^+$ cations at the surface compared to the bulk. Meanwhile there is a higher concentration of THP in the bulk (~130 eV). As discussed earlier, the high BE phosphine oxide shoulder is only visible in the GE measurements here.

GE measurements of the IL were taken over the O 1s region and compared to NE measurements of the IL as well as a clean TiO_2 (110) substrate, shown in Figure 5.11. There is no change in the spectra of the IL thin film when taken at GE compared to NE.
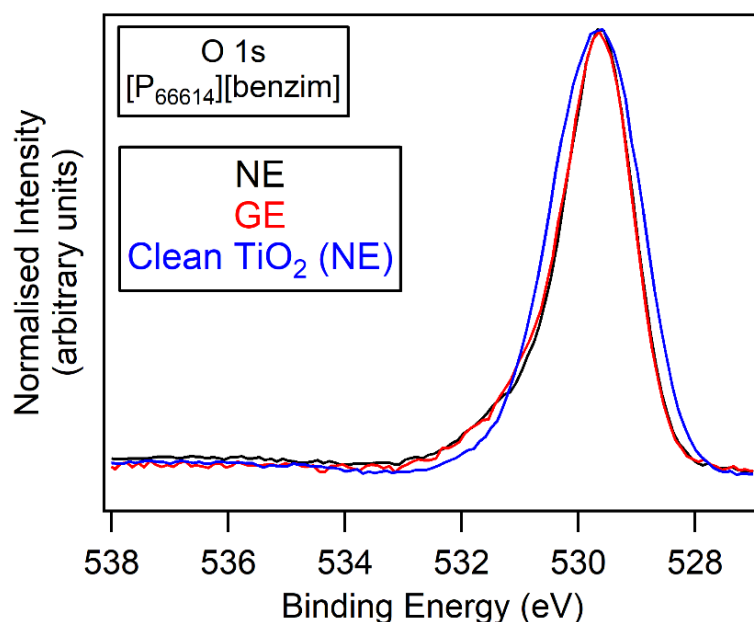
Figure 5.11. O 1s normal and grazing emission of [P_{66614}][benzim]. This is compared to clean TiO_2 (110) at normal emission.

5.5 NEXAFS of [P_{66614}][benzim]

5.5.1 Gas-Phase and Substrate Corrections

The orientational behaviour of the [benzim]$^-$ anion before and upon exposure to CO_2 was investigated using angle-resolved NEXAFS. When CO_2 is introduced, the gas absorbs incoming X-rays at certain energies, introducing dips in the C K edge NEXAFS spectrum for [P_{66614}][benzim] exposed to 1 mbar CO_2 (red line) in Figure

5.12. The IL + CO_2 spectra were therefore divided by a gas-phase CO_2 spectrum recorded over the same photon energy range (black line). This removes the dips in the spectra, however, a slight mismatch between data causes spikes to be introduced into the σ^* region of the background-corrected spectrum (blue line), as shown in Figure 5.12.
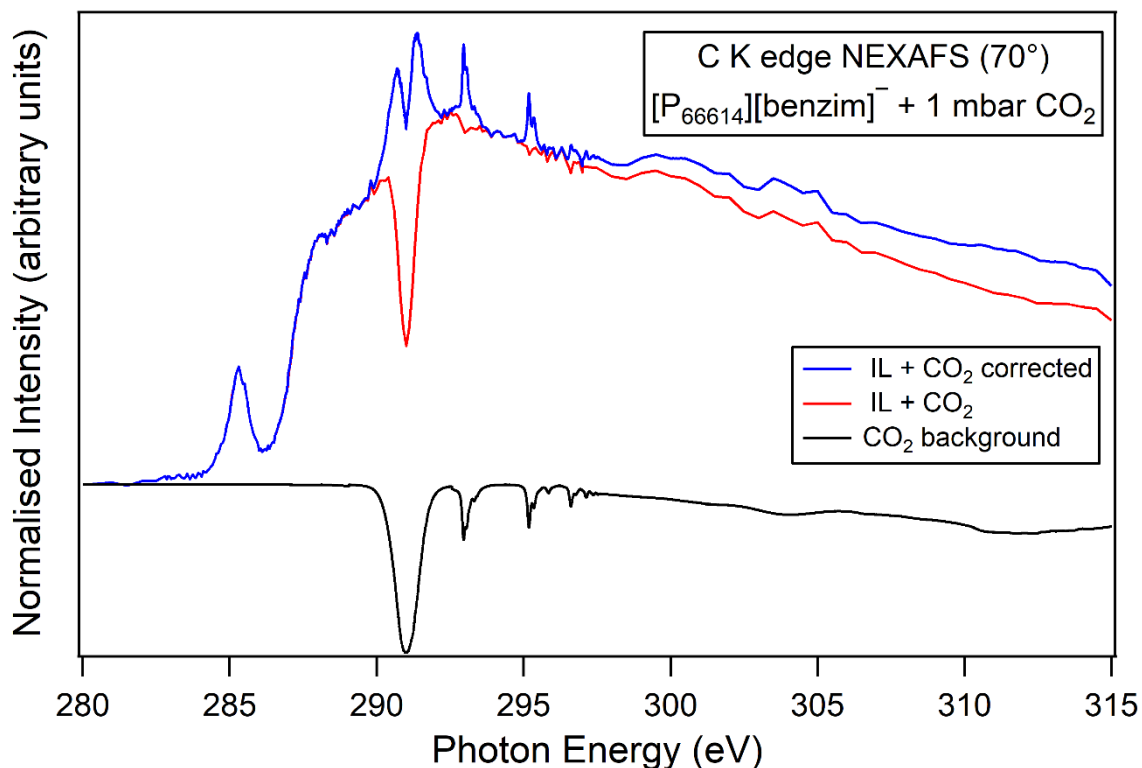
Figure 5.12. C K edge NEXAFS of [P$_{66614}$][benzim] exposed to 1 mbar CO_2. The experimental data (red) was divided by the background gas-phase CO_2 signal (black), resulting in a CO_2-corrected spectrum (blue).

Secondly, NEXAFS measurements must also be corrected for the TiO_2 substrate onto which the IL is deposited. This was done by dividing the scan of the IL by the scan of the clean TiO_2 substrate. The example given in Figure 5.13 shows N K edge measurements of the IL exposed to 1 mbar of CO_2 (gold line), the clean TiO_2 signal (black), and the background-corrected IL + CO_2 signal obtained through division of the TiO_2 spectrum.
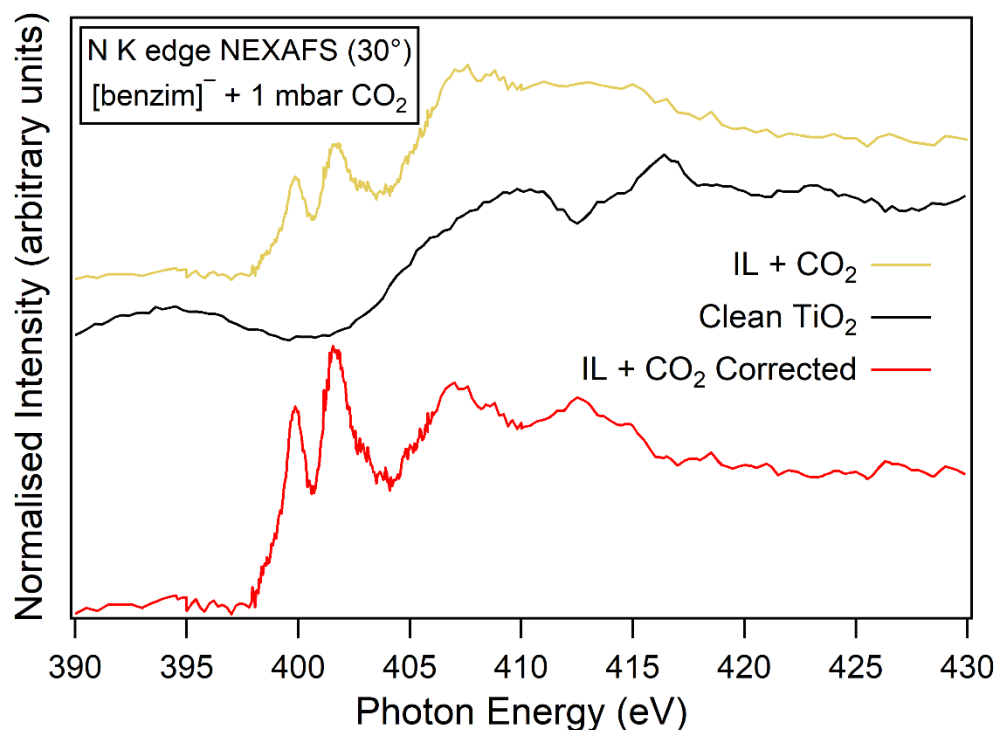
Figure 5.13: AEY N K edge NEXAFS of [P_{66614}][benzim] exposed to 1 mbar CO_2 with a removed TiO_2 background signal. The experimental data (gold) was divided by the clean TiO_2 substrate signal (black), resulting in a background-corrected IL + CO_2 spectrum (red).

5.5.2 C K edge NEXAFS

C K edge NEXAFS of [P_{66614}][benzim] at X-ray incidence angles of 30° and 70° from the substrate surface is shown in Figure 5.14(a). This was carried out for the IL as presented and upon exposure to 1 mbar of CO_2. For the as presented IL, there is a split π^* peak with two features at 285.3 and 287.9 eV, and a σ^* peak at 292.6 eV. Walsh *et al*. found a split π^* peak at similar photon energies over the C K edge for benzimidazole on Cu (100) for multilayer coverage [34]. They also found that the higher-energy π^* peak disappears at submonolayer coverage. Angle-resolved NEXAFS allows us to determine the orientation of the anion on the TiO_2 (110) substrate by comparing the relative intensities of the π^* and σ^* peaks at different X-ray angles of incidence. Relative to the σ^* peak, the lower-energy π^* peak at 285.3 eV is more intense for an X-ray incidence angle of 70° than for 30°. As π^* orbitals point perpendicular out of the plane of the benzimidazolide ring, we can infer that

the ring of the anion preferentially orients towards the surface normal (i.e., upright from the surface, as shown schematically in Figure 5.14(c)).
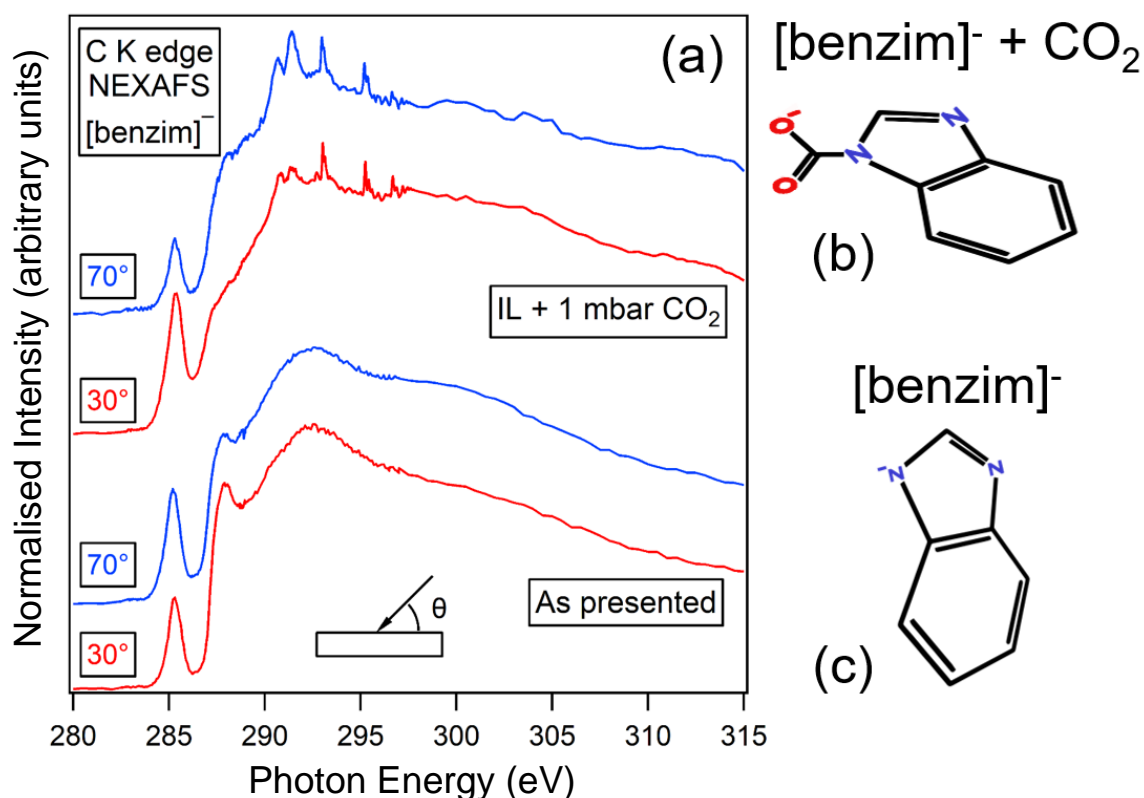
Figure 5.14. (a) AEY C K edge NEXAFS spectra of [P$_{66614}$][benzim] as presented and when exposed to 1 mbar of CO_2, for the X-ray beam incident at angles (θ) of 30° and 70° from the IL surface. Schematic pictures indicating the orientation of the anion (b) while exposed to CO_2 (benzim ring 54° ± 4° from surface normal) and (c) as presented (benzim ring 27° ± 5° from surface normal).

Upon exposure to 1 mbar of CO_2, the lower-energy π^* peak at 285.3 eV is significantly more intense relative to the σ^* peak at approximately 291 eV for X-rays incident at 30° rather than 70°, indicating that benzim ring tends to lie closer to the plane of the substrate when exposed to CO_2. This suggests that the formation of carbamate at the anion induces a realignment of the IL at the TiO_2 surface. We can estimate the tilt of the ring of the anion from the surface normal (before and upon exposure to CO_2) using the Stöhr equations [35]. These provide a theoretical intensity ratio of the lowest-energy π^* peak at both X-ray incidence angles which can

be compared to the experimental intensity ratio. In our calculations we assume a random azimuthal orientation and a value of P = 0.85 for the polarisation factor.
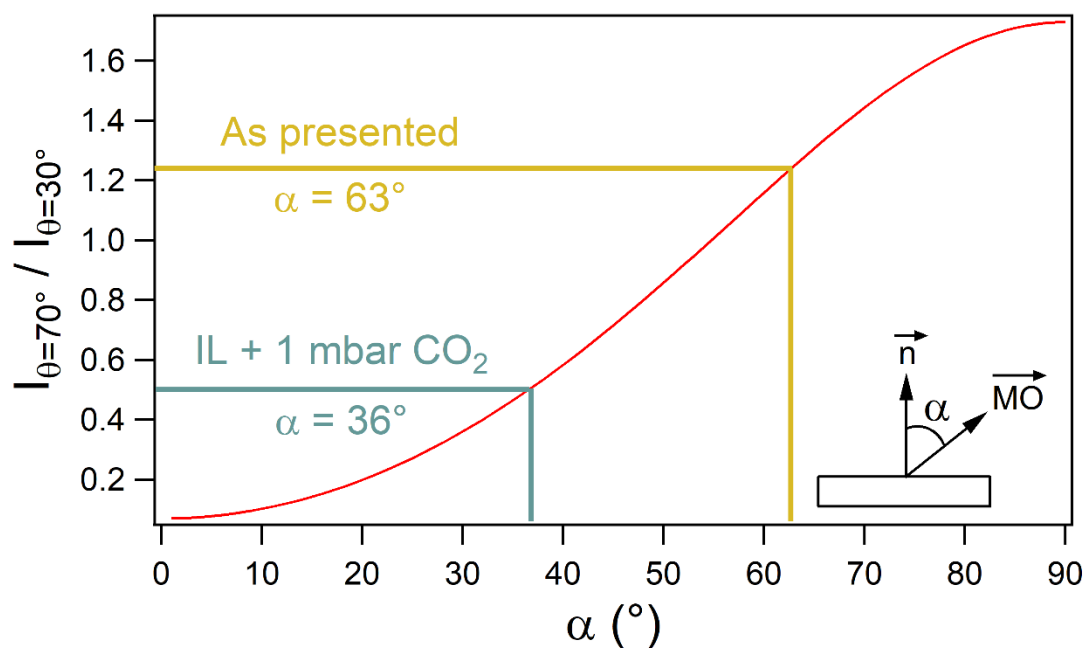
Figure 5.15: Intensity ratios measured at X-ray angles of incidence ($\theta=70°$ and $\theta=30°$) calculated as a function of the angle between the surface normal and the molecular orbital, α, using the Stöhr equations. Comparing these to the experimental intensity ratios gives α = 63° for the as presented stage and α = 36° upon exposure to 1 mbar of CO_2.

The angle between the surface normal and the direction of the π^* molecular orbital is α. The ring of the anion is perpendicular to the π^* molecular orbital, therefore, the tilt of the benzim ring is given by 90° − α. The angle α can be calculated using the intensity ratio of the π^* resonance peak at 285 eV for the two X-ray incidence angles [35]. In the as presented case, the intensities of the 285 eV π^* peaks are 0.97 ± 0.01 and 0.78 ± 0.01 for θ = 70° and θ = 30°, respectively. This results in a resonance intensity ratio ($I_{\theta=70°}/I_{\theta=30°}$) of 1.24 ± 0.16. When exposed to 1 mbar of CO_2, these intensities are 0.59 ± 0.04 and 1.19 ± 0.02, respectively, resulting in an intensity ratio of 0.50 ± 0.09. Comparing these to the theoretical intensity ratio calculated as a function of α using the Stöhr equations (Figure 5.15), we can estimate the tilt of the benzim ring to be 27° ± 5° from the surface normal in the as presented case. Upon exposure to CO_2, the benzim ring reorientates to 54° ± 4° from the surface normal.

To the best of our knowledge, realignment of ions in ultrathin IL films upon absorption of CO_2 has not been previously reported.

5.5.3 N K edge NEXAFS
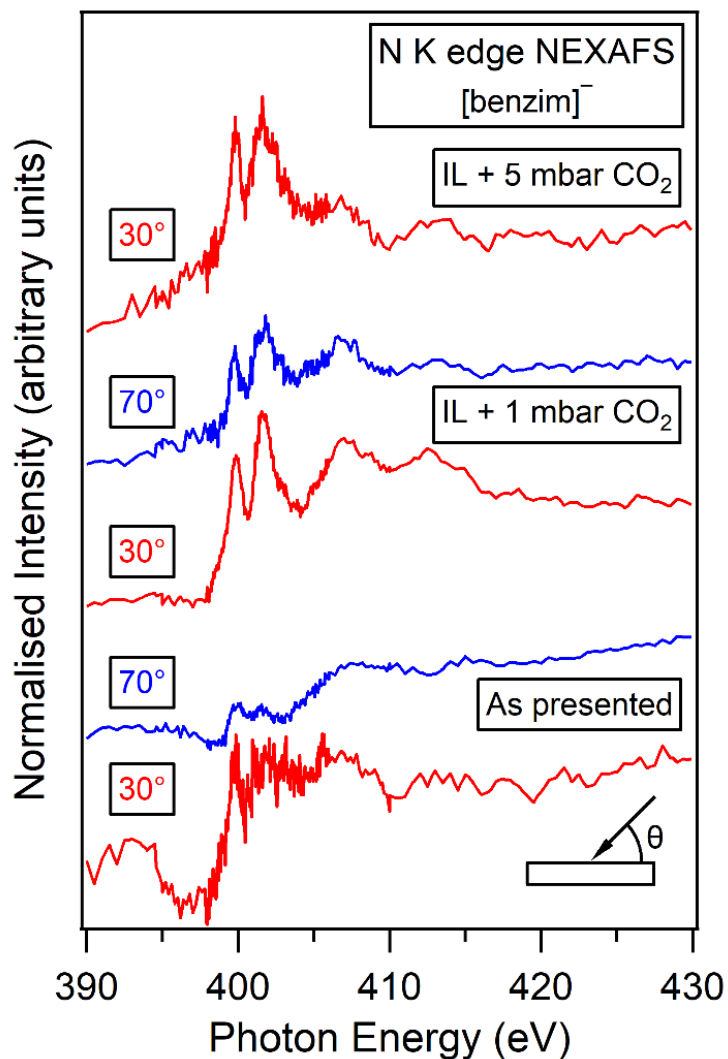
Figure 5.16. AEY N K edge NEXAFS spectra of $[P_{66614}][benzim]$ as presented (bottom), when exposed to 1 mbar of CO_2 (middle) and when exposed to 5 mbar of CO_2 (top), for the X-ray beam incident at angles of 30° and 70° from the IL surface.

N K edge NEXAFS of the IL as presented in Figure 5.16 has a feature at approximately 400 eV consisting of two peaks at photon energies of 399.9 and 401.7 eV. These peaks are attributed to N 1s $\rightarrow$ π^* transitions. There is a broader peak at 408.0 eV attributed to N 1s $\rightarrow$ σ^* transitions. There is no definitive evidence of

realignment of [benzim]⁻ anions in the as presented film in Figure 5.16 due to the noisy nature of the spectra. Walsh *et al.* reported a split π^* peak in multilayer benzimidazole on Cu (100) at similar photon energies, and also for the similarly-structured benzotriazole on Cu (100) [34]. Grillo *et al.* reported a split π^* peak at different positions for benzotriazole on Au (111), revealing that the positions of these split π^* resonances vary depending on the substrate onto which the molecules are deposited [36]. Splitting of the π^* peak is due to initial state effects, arising from chemical shifts between different environments of N atoms in the imidazolide ring [28,37]. The ions in these examples above are not charged and the N atoms would, therefore, be inequivalent, resulting in a split π^* peak. However, our DFT simulations of the isolated [benzim]⁻ anion (Figure 5.22) show that both N atoms contribute to the split π^* peak equally, implying they share the same chemical environment. The origin of the split π^* peak for [benzim]⁻ will be discussed below.

To investigate the realignment of [benzim]⁻ anions upon absorption of CO_2 the IL was subjected to two pressures of CO_2, 1 mbar and 5 mbar, as shown in Figure 5.16. Both the π^* and σ^* features become more prominent than those for the IL as presented, particularly the split π^* peak. However, there is no obvious change in the relative intensity of these π^* and σ^* peaks due to the noisy nature of the data. As found with 1 mbar CO_2, when the IL is exposed to the higher 5 mbar CO_2 pressure we still see a split π^* peak. However, the higher-energy π^* peak at 401.7 eV is less intense relative to the lower-energy peak at 399.9 eV compared to 1 mbar CO_2. The lower-energy peak remains unchanged with CO_2 pressure, while all other features reduce in relative intensity with increased CO_2 pressure. This could be an indication of a change in electronic interaction due to the chemisorption of CO_2. At a 5 mbar pressure the π^* peaks are much more intense relative to the σ^* peak, suggesting that the ring of the anion orients more in-plane than it does when exposed to a lower pressure of 1 mbar (i.e., suggesting further reorientation of the anions towards the surface with increasing CO_2 pressure). We do not have measurements at another angle to verify this, however, from computational results shown in Figure 5.23 below, we find that N^1 provides the greatest contribution to the σ^* peak. This is the site at which carbamate forms, and we would therefore expect a higher intensity σ^* peak upon exposure to higher pressures of CO_2 (5 mbar).

119

5.6 DFT NEXAFS Simulations

5.6.1 C K edge NEXAFS
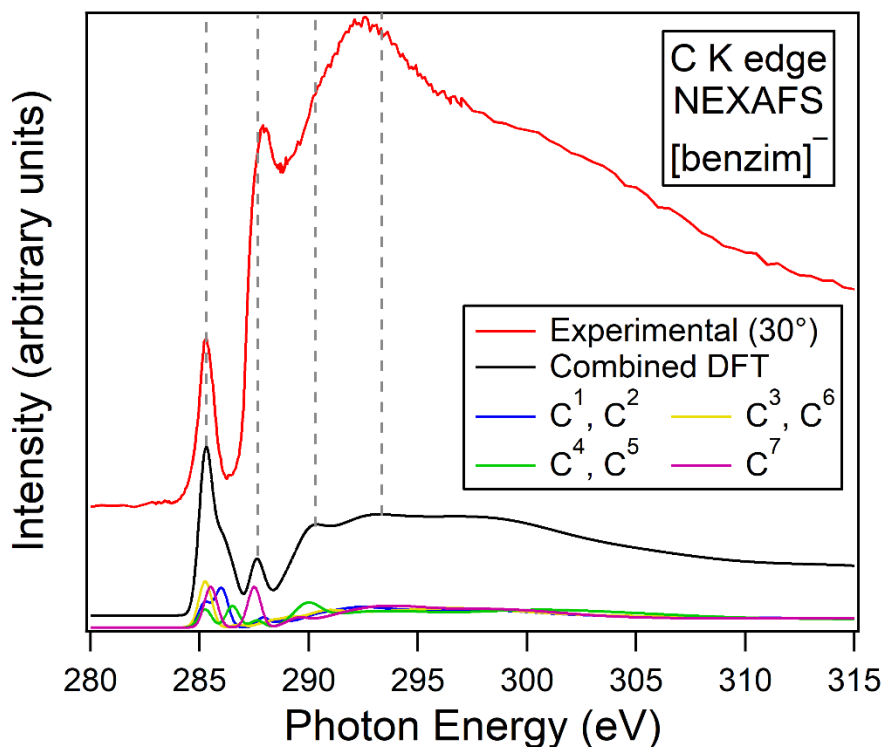
Figure 5.17. Experimental and simulated (DFT) C K edge NEXAFS spectrum for [P_{66614}][benzim]. The final DFT spectrum (black) is the sum of the seven spectra from atoms $C^1 - C^7$. The grey dashed lines highlight features of the DFT spectra for comparison with the experimental spectra. The experimental spectra were taken 30° from the substrate surface.

The DFT simulated C K edge NEXAFS of the IL isolated [benzim]⁻ anion is shown in Figure 5.17. The breakdown of the combined DFT spectrum (black line) indicates that there are four distinct environments of C atoms in the [benzim]⁻ anion: $C^{1,2}$; $C^{3,6}$; $C^{4,5}$; C^7 (see Figure 5.1(b) for assignments). For the IL as presented, the theoretical DFT spectrum has three π^* peaks at 285.3, 287.6 and 290.3 eV, and a σ^* peak at 293.2 eV. These correspond to features in the experimental spectra at 285.3, 287.9, 290.2 (feature is very small) and 292.6 eV, respectively.

The π^* peak at 285.3 eV in the experimental spectrum is largely attributed to transitions from atoms C^3, C^6 and C^7, with a smaller contribution from C^1, C^2, C^4 and

120

C^5. The broadening of the 285.3 eV π^* peak in the DFT spectrum is due to transitions from atoms C^1, C^2, C^4 and C^5 in the [benzim]$^-$ anion. The π^* peak at 287.9 eV in the experimental spectrum is largely attributed to transitions from atom C^7. This peak occurs at higher photon energies because it is located between the two electronegative N atoms, consistent with reports for imidazolium-based ILs by Ehlert *et al.* [37]. Although in their case the splitting of the π^* peak is much narrower, with a split of 0.3 eV, compared to a wider separation of 2.6 eV here for [benzim]$^-$. The π^* peak at 290.2 eV is largely due to transitions from atoms C^4 and C^5, which also have neighbouring N atoms.

To complement the simulated NEXAFS spectra, unoccupied antibonding orbitals of the isolated and CO_2-reacted [benzim]$^-$ anion were computed using ORCA. This allows us to assign features of the experimental NEXAFS spectra to specific atoms in the anion and transitions into specific unoccupied molecular orbitals (MOs). Figure 5.18 shows the lowest unoccupied molecular orbital (LUMO), LUMO+1, and LUMO+2 orbitals for [benzim]$^-$. These are similar to those of imidazole obtained by Thomason *et al.* and can be assigned as $1\pi^*$, $1\sigma^*$ and $2\pi^*$ orbitals, respectively [38]. The $1\pi^*$ orbital shows four distinct environments of C atoms in the anion in Figure 5.18: $C^{1,2}$, $C^{3,6}$, $C^{4,5}$, C^7. This agrees with the simulated NEXAFS spectra of each individual atom in the [benzim]$^-$ anion in Figure 5.17, showing the same four environments. Using results of the DFT and MO simulations we can assign the π^* peaks at 285.3 and 287.9 eV in the IL as presented experimental spectrum as $C^{3,6,7}$ $\rightarrow$ $1\pi^*$ (LUMO) and C^7 $\rightarrow$ $2\pi^*$ (LUMO+2) transitions, respectively. The $C \rightarrow 1\sigma^*$ transition is weak and therefore cannot be resolved in this spectrum.

<div align="center">

1π*
LUMO

1σ*
LUMO +1

2π*
LUMO +2

</div>
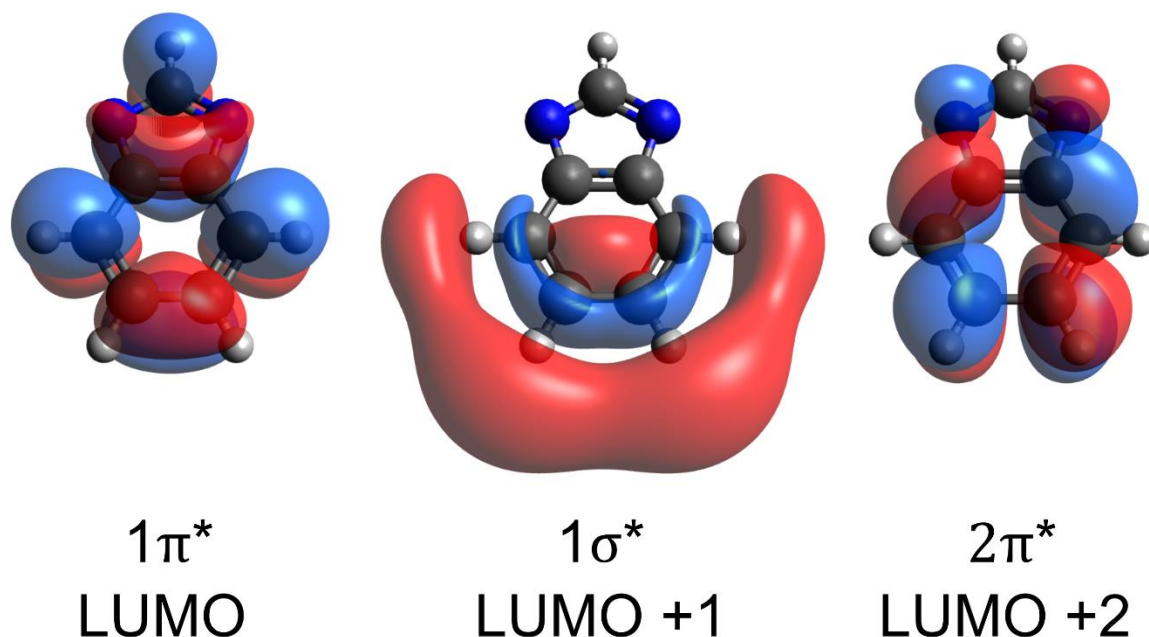
Figure 5.18. Lowest unoccupied molecular orbitals (LUMOs) of the isolated [benzim]$^-$ anion arranged in order of increasing energy (left to right). LUMO, LUMO+1 and LUMO+2 are assigned to the 1π*, 1σ* and 2π* antibonding orbitals, respectively.

When simulating the IL exposed to CO_2, the CO_2 was bonded to atom N^1 to form carbamate as shown in Figure 5.1(c). The negative charge from N^1 was given to the singly-bonded O atom. Figure 5.19 shows DFT and experimental spectra of [benzim]$^-$ + CO_2 over the C K edge. The combined DFT spectrum is the sum of all C atoms in the [benzim]$^-$ anion (C^{1-7}) and the C atom in the carbamate species (C^8). The IL + CO_2 DFT spectrum has three π* peaks at 285.3, 287.2 and 288.4 eV, and a σ* peak at 291.1 eV. These occur at the same energies as their corresponding peaks in the experimental spectra. Note that the resonance at 287.9 eV is strong in the IL as presented stage but shifts to 287.2 eV and significantly reduces in intensity upon exposure to CO_2. This resonance is due to $C^7 \rightarrow$ π* transitions, where C^7 is located between two nitrogen atoms. The shift and change in intensity of this resonance could therefore indicate a change in the strength of bonding around the C^7 atom when the IL reacts with CO_2. This is to be expected considering the atom's proximity to the carbamate group (since C^7 neighbours the chemisorption site N^1). This can be seen, for example, as a change in the 2π* antibonding molecular orbitals around C^7 in Figures 5.18 and 5.20. It is worth noting that in the DFT spectra this resonance does not decrease but instead increases in intensity when CO_2 is

introduced. As stated earlier, the DFT simulated spectra represent an angular average and therefore cannot account for any contributions from the orientation of molecules on the strength of resonances. It is possible that the DFT model cannot fully account for the interactions between C^7 and the carbamate group (particularly because the charge is not delocalised in our model, but fixed to one of the oxygen atoms).
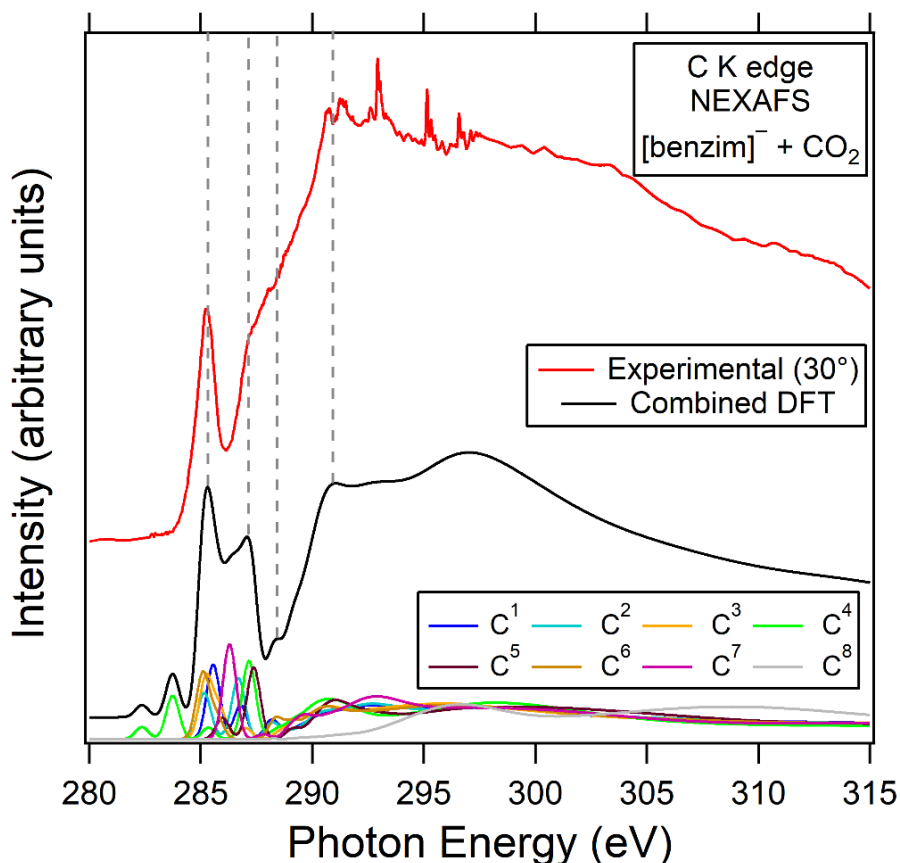
Figure 5.19. Experimental and simulated (DFT) C K edge NEXAFS spectrum for [P$_{66614}$][benzim] + CO$_2$. The final DFT spectrum (black) is the sum of the eight spectra from atoms C^1 – C^8. The grey dashed lines highlight features of the DFT spectra for comparison with the experimental spectra. The experimental spectra were taken 30° from the substrate surface.

Using the individual DFT spectra for each atom, we see that when reacted with CO$_2$, the four environments of C atoms in [benzim]$^-$ expand into eight: C^{1-7} for each C atom in the [benzim]$^-$ anion, and C^8 in the carbamate species. The pre-edge peaks at approximately 282 and 284 eV are attributed to atom C^4 near the carbamate.

These pre-edge features do not appear in the experimental spectra. The reason for this discrepancy is discussed below. The lower-energy π^* peak at 285.3 eV in the experimental spectrum is mostly attributed to transitions from atoms C^1, C^2, C^3 and C^6, those furthest from the azole side of the [benzim]$^-$ anion. Both the broadening of this peak towards higher photon energies and the π^* peak at 287.2 eV can be largely attributed to the remaining atoms nearer the carbamate: C^4, C^5 and C^7 (with smaller contributions from C^1 and C^2). Using the DFT components in Figure 5.19 and MOs in Figure 5.20, we can assign the π^* peaks at 285.3 and 287.2 eV to $C^{1,2,3,6} \rightarrow 1\pi^*$ (LUMO) and $C^{4,5,7} \rightarrow 2\pi^*$ (LUMO+1) transitions, respectively.

In Figure 5.19, we see that C^8 in the carbamate group does not contribute to any of the three π^* peaks or the σ^* peak at 291.1 eV, but rather contributes solely to σ^* resonances greater than 295 eV. This may be because the negative charge was assigned to the singly bonded O atom in the carbamate group (in the software used the negative charge has to be assigned to one atom rather than delocalised).

$1\pi^*$
LUMO

$2\pi^*$
LUMO +1

$1\sigma^*$
LUMO +2
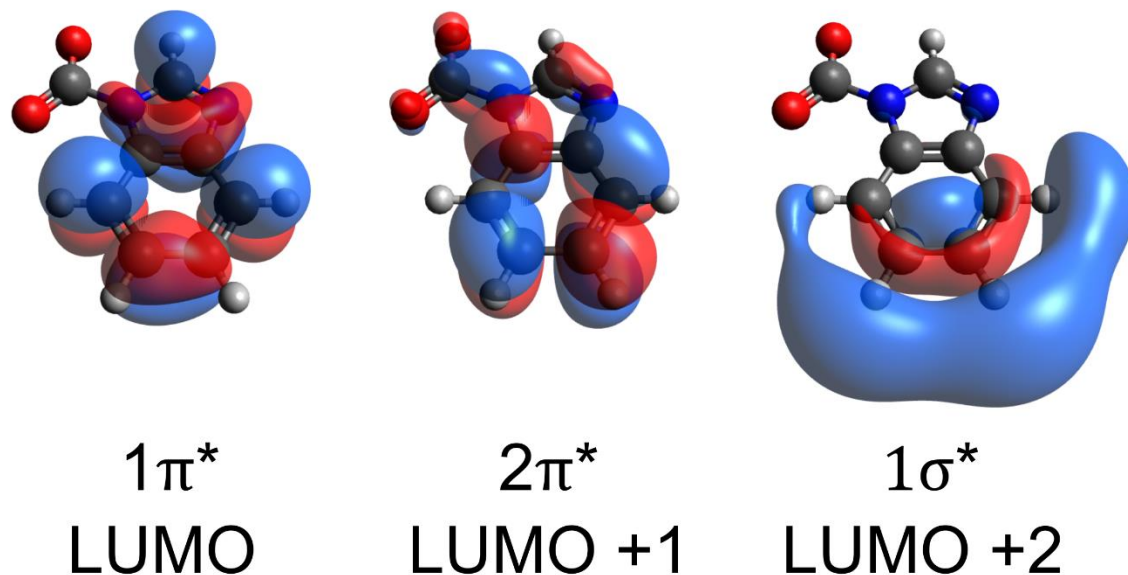
Figure 5.20. Lowest unoccupied molecular orbitals (LUMOs) of the CO_2-reacted [benzim]$^-$ anion arranged in order of increasing energy (left to right). LUMO, LUMO+1 and LUMO+2 are assigned to the $1\pi^*$, $2\pi^*$, and $1\sigma^*$ antibonding orbitals, respectively.

We believe there may be protonated carbamate groups present in the sample, so we have also calculated NEXAFS spectra for IL + COOH, shown in Figure 5.21. The pre-edge features found in the DFT spectrum of Figure 5.19 are not present in the protonated carbamate calculation, so they are most likely a result of the interaction between C^4 and the COO^- moiety.
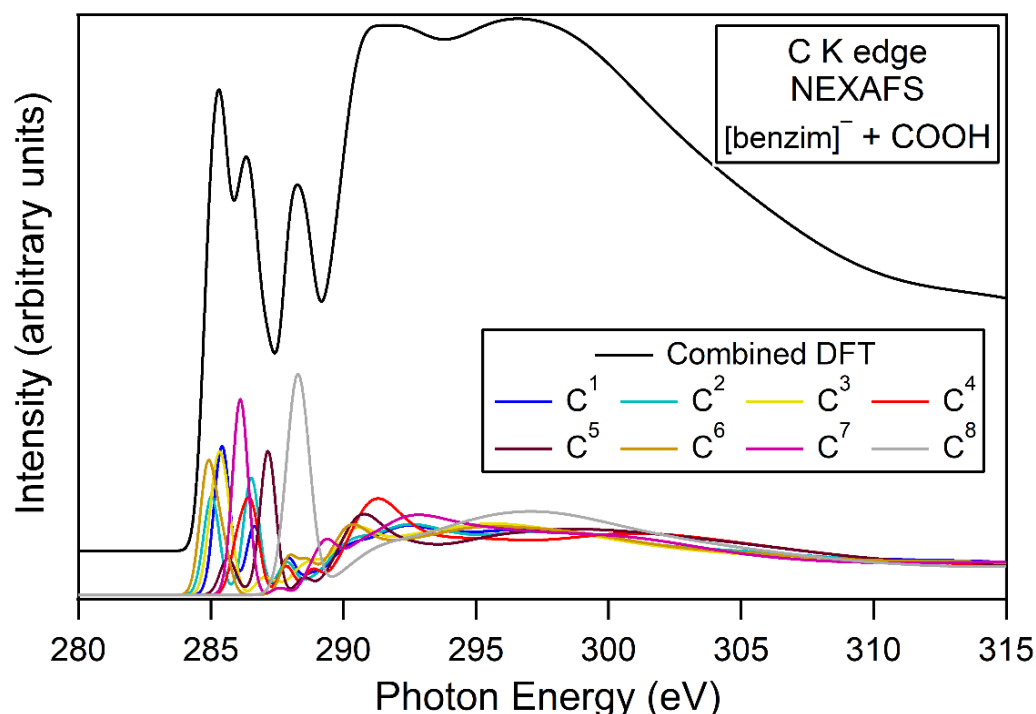
Figure 5.21. Simulated C K edge NEXAFS spectrum for [P$_{66614}$][benzim] + COOH. The final DFT spectrum (black) is the sum of the eight spectra from atoms $C^1 - C^8$.

5.6.2 N K edge NEXAFS

DFT simulations were carried out for [benzim]$^-$ over the N K edge as shown in Figure 5.22. In this case, atoms N^1 and N^2 have the same spectra, contributing to the final DFT spectrum equally. This is because an isolated [benzim]$^-$ anion is simulated (in which N^1 and N^2 are chemically equivalent) and the cation's influence on the anion is not considered. Mercy *et al.* have shown that the interaction between a [P$_{3333}$]$^+$ cation and a [124Triz]$^-$ anion results in preferential reactivity at N^1, before which the reaction enthalpy was equivalent at both N sites [39]. Although it is possible that the influence of the [P$_{66614}$]$^+$ cation may affect the reaction enthalpy and/or chemical bonding of the N atoms, its presence is not expected to significantly change the

simulated NEXAFS spectra. To account for the influence of the TiO_2 surface, a dedicated computational study would be required which is outside the scope of this work.
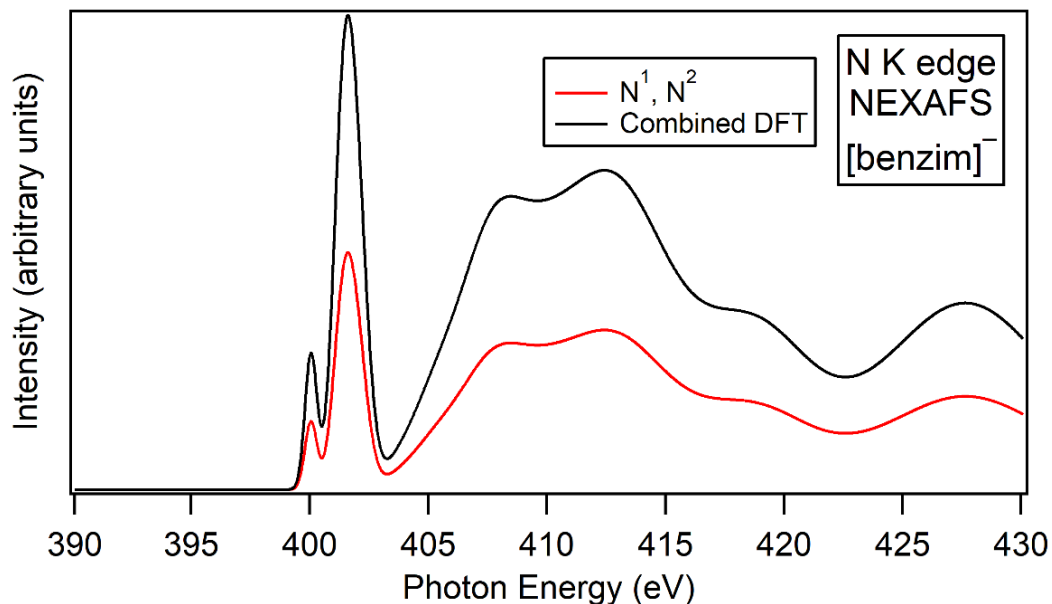
Figure 5.22. Simulated N K edge NEXAFS spectrum for [P_{66614}][benzim]. The final DFT spectrum (black) is the sum of the two spectra from atoms N^1 and N^2 (red).

When the IL absorbs CO_2 (Figure 5.23) we see that the spectra for N^1 and N^2 are no longer equivalent due to the formation of carbamate at $N^{1,r}$. The formation of this carbamate species destroys the $N^1 \rightarrow \pi^*$ resonances. Therefore, in the final DFT spectrum, we see that the π^* peak is solely attributed to transitions from $N^{2,r}$ (N^2 in the CO_2-reacted anion). The spectra for N^2 before exposure (Figure 5.22) and upon exposure to CO_2 (Figure 5.23, $N^{2,r}$) are also different, showing that the formation of carbamate at $N^{1,r}$ influences π^* transitions from $N^{2,r}$.
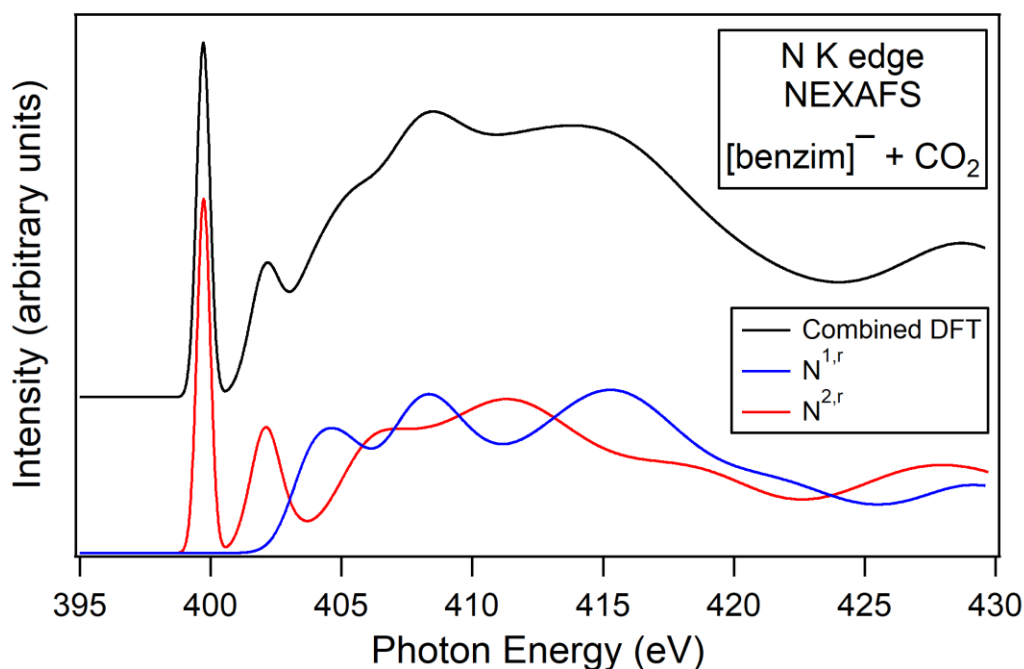
Figure 5.23. Simulated N K edge NEXAFS spectrum for $[P_{66614}][benzim] + CO_2$. The final DFT spectrum (black) is the sum of the two spectra from atoms $N^{1,r}$ (red) and $N^{2,r}$ (blue).

Theoretical DFT spectra were compared to experimental spectra over the N K edge for the IL as presented and when exposed to CO_2, as shown in Figure 5.24. For the IL as presented, the lower- and higher-energy π^* peaks appear at photon energies of 399.9 and 401.4 eV, respectively, similar to those in the experimental spectra (399.9 and 401.7 eV). The σ^* peak of the simulated NEXAFS spectrum occurs at the same energy as that of the experimental spectrum (408.0 eV). Thomason *et al.* studied aqueous imidazole using experimental and theoretical NEXAFS over the N K edge and found a split π^* feature with two peaks at 400.2 and 401.9 eV [38]. This is similar to the π^* peaks of the experimental and simulated NEXAFS of our benzimidazolide-based IL in Figure 5.24. Thomason *et al.* suggest that the lower- and higher-energy π^* peaks are assigned to transitions from atoms N^2 and N^1 in the imidazole, respectively. However, in our case, N^1 and N^2 are found to contribute in equal parts to the simulated NEXAFS spectrum, as shown in Figure 5.22. The difference in results may be due to a number of reasons. The main cause of disparity may be due to differences in the chemical environment of the N atoms (N atoms are chemically equivalent in benzimidazolide but not in imidazole) and charge of the two systems.
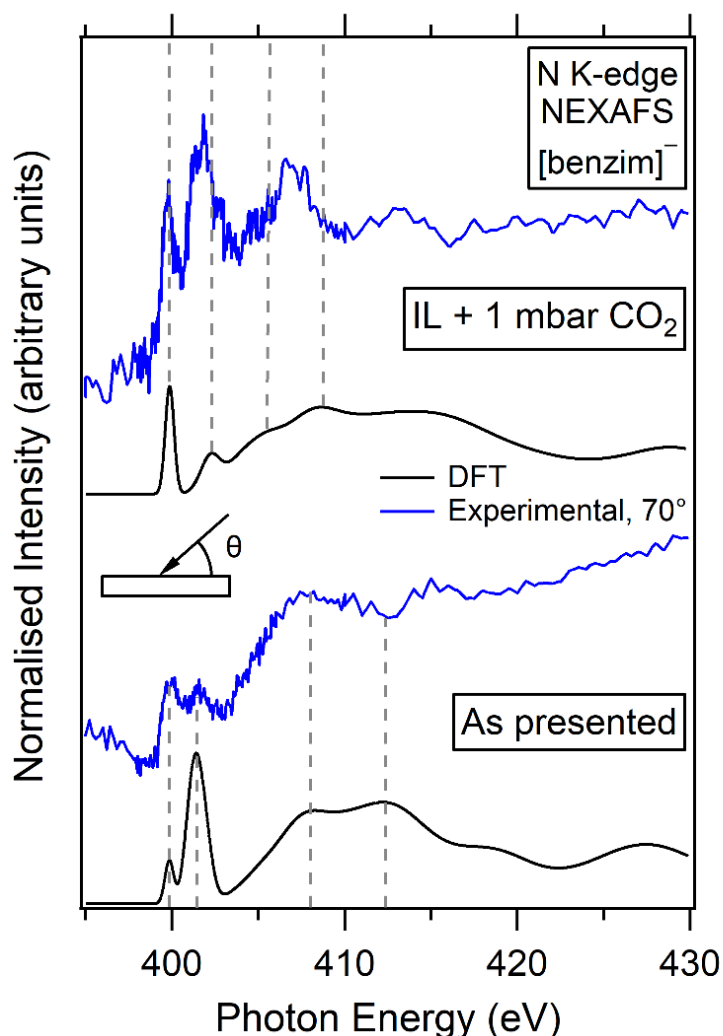
Figure 5.24. Experimental and simulated (DFT) N K edge NEXAFS of $[P_{66614}][benzim]$ as presented and when exposed to 1 mbar of CO_2. The grey dashed lines highlight features of the DFT spectra for comparison with the experimental spectra. The experimental spectra were taken 70° from the IL surface.

The IL + CO_2 simulated N K edge NEXAFS has a split π^* feature with peaks at 399.9 and 402.3 eV, compared to 399.9 and 401.7 eV in the experimental spectra. The σ^* peak occurs at a higher energy in the simulated spectrum (408.7 eV) compared to the experimental spectrum (407.7 eV).

We can compare the theoretical N K edge NEXAFS in Figures 5.22 and 5.23 to the unoccupied antibonding orbitals of $[benzim]^-$ shown in Figures 5.18 and 5.20. From the $1\pi^*$ orbital we can infer that there are an equal number of excitations from N^1 and N^2 into the $1\pi^*$ orbital formed around atoms N^1, C^4, C^5 and N^2. However, the

introduction of CO_2 results in an asymmetry of this orbital compared to the same orbital in [benzim]$^-$ pre-exposure. We can assign the two π^* peaks at 399.9 and 401.7 eV in the IL as presented experimental spectra as $N^{1,2} \rightarrow 1\pi^*$ and $N^{1,2} \rightarrow 2\pi^*$ transitions, respectively. Upon exposure to CO_2, the peak at 399.9 eV is assigned to $N^{2,r} \rightarrow 1\pi^*$ transitions, while the peak at 401.7 eV is assigned to $N^{1,r}$ and $N^{2,r} \rightarrow 2\pi^*$ transitions.

5.7 Discussion and Conclusions

Absorption of CO_2 in a thin film of the IL [P_{66614}][benzim] was studied using *in situ* near-ambient pressure X-ray photoelectron spectroscopy (NAP-XPS) and near edge X-ray absorption fine structure (NEXAFS). Results indicate that reaction with CO_2 leads to the formation of carbamate and causes a reordering of the cations and anions. The [benzim]$^-$ anions orient 27° ± 5° from the surface normal before exposure to CO_2 and approximately 54° ± 4° from the surface normal when they react with CO_2. This change in orientation could be due to a number of factors including interaction with the TiO_2 surface or the pressure of the surrounding gas above the IL 'pushing' the ions down towards the substrate. Investigating this in a dedicated computational study would make for interesting further work.

Angle-resolved XPS shows a greater concentration of CO_2-reacted anions in the deeper layers of the ionic liquid. Additionally, there is evidence that the reaction with CO_2 is not fully reversible in our thin film. Experimental NEXAFS spectra are in good agreement with simulated NEXAFS spectra obtained using density functional theory. Unoccupied antibonding molecular orbitals were calculated and used to assign electron transitions to the spectral features of the experimental NEXAFS.

Surface structure of IL thin and thick films has previously been explored using a variety of different substrates including metals (Au [33,36], Ag [40], Cu [34,41], Pt [42]), metal oxides (TiO_2 [9,43], ZnO [44]), carbon (graphite [45], graphene [46], nanotubes [47]), and many more. We opted to study rutile TiO_2 (110) as our substrate for its relevance in a wide range of IL-based technologies including catalysts, TiO_2 nanotubes, and photovoltaic devices [48–50]. Modification of these

systems using ILs can lead to greener technologies with improved performance and stability [51–53].

Orientational ordering of ILs is typically demonstrated with imidazolium-based ions with long alkyl chains that preferentially orient towards the vacuum and away from the surface due to interactions at the IL/vacuum interface [9,54]. However, reordering of IL thin films upon absorption of CO_2 has not been shown experimentally prior to this study, to the best of our knowledge. CO_2-induced reordering of IL films may impact the performance of IL-based technologies such as photovoltaic devices, IL lubricants, and catalysis. Some groups have carried out molecular dynamics simulations to investigate ordering of IL thin films on various solid surfaces [55–58], and CO_2 absorption in bulk ILs [59]. It is clear that complementary computational and experimental studies are required to gain a deeper insight into the physical and chemical effects of reordering of IL films in realistic environments.

5.8 References

[1]   Cole J, Henderson Z, Thomas A G, Compeán-González C L, Greer A J, Hardacre C, Venturini F, Garzon W Q, Ferrer P, Grinter D C, Held G and Syres K L 2021 Near-Ambient Pressure XPS and NEXAFS Study of a Superbasic Ionic Liquid with CO_2 *J. Phys. Chem. C* **125** 22778–85

[2]   Boot-Handford M E, Abanades J C, Anthony E J, Blunt M J, Brandani S, Mac Dowell N, Fernández J R, Ferrari M C, Gross R, Hallett J P, Haszeldine R S, Heptonstall P, Lyngfelt A, Makuch Z, Mangano E, Porter R T J, Pourkashanian M, Rochelle G T, Shah N, Yao J G and Fennell P S 2014 Carbon capture and storage update *Energy Environ. Sci.* **7** 130–89

[3]   Yu C H, Huang C H and Tan C S 2012 A review of CO_2 capture by absorption and adsorption *Aerosol Air Qual. Res.* **12** 745–69

[4]   Cuéllar-Franca R M, García-Gutiérrez P, Taylor S F R, Hardacre C and Azapagic A 2016 A novel methodology for assessing the environmental sustainability of ionic liquids used for CO_2 capture *Faraday Discuss.* **192** 283–301

[5]   Bates E D, Mayton R D, Ntai I and Davis J H 2002 CO_2 capture by a task-specific ionic liquid *J. Am. Chem. Soc.* **124** 926–7

[6]   Wang C, Luo X, Luo H, Jiang D, Li H and Dai S 2011 Tuning the basicity of ionic liquids for equimolar CO_2 capture *Angew. Chemie* **123** 5020–4

[7]   Greer A J, Taylor S F R, Daly H, Quesne M, Catlow C R A, Jacquemin J and Hardacre C 2019 Investigating the effect of NO on the capture of CO_2 using

superbase ionic liquids for flue gas applications *ACS Sustain. Chem. Eng.* **7** 3567–74

[8]   Taylor S F R, McCrellis C, McStay C, Jacquemin J, Hardacre C, Mercy M, Bell R G and De Leeuw N H 2015 CO_2 capture in wet and dry superbase ionic liquids *J. Solution Chem.* **44** 511–27

[9]   Wagstaffe M, Jackman M J, Syres K L, Generalov A and Thomas A G 2016 Ionic Liquid Ordering at an Oxide Surface *ChemPhysChem* **17** 3430–4

[10]   Held G, Venturini F, Grinter D C, Ferrer P, Arrigo R, Deacon L, Garzon W Q, Roy K, Large A, Stephens C, Watts A, Larkin P, Hand M, Wang H, Pratt L, Mudd J J, Richardson T, Patel S, Hillman M and Scott S 2020 Ambient-pressure endstation of the Versatile Soft X-ray (VerSoX) beamline at Diamond Light Source *J. Synchrotron Radiat.* **27** 1153–66

[11]   Grinter D C, Venturini F, Ferrer P, van Spronsen M A, Arrigo R, Quevedo Garzon W, Roy K, Large A I, Kumar S and Held G 2022 The Versatile Soft X-Ray (VerSoX) Beamline at Diamond Light Source *Synchrotron Radiat. News* **35** 39–47

[12]   Bradaric C J, Downard A, Kennedy C, Robertson A J and Zhou Y 2003 Industrial preparation of phosphonium ionic liquids *Green Chem.* **5** 143–52

[13]   Grinter D C, Graciani J, Palomino R M, Xu F, Waluyo I, Sanz J F, Senanayake S D and Rodriguez J A 2021 Adsorption and activation of CO_2 on Pt/CeO$_x$/TiO$_2$(110): Role of the Pt-CeO$_x$ interface *Surf. Sci.* **710** 1–8

[14]   Fairely N 2009 CasaXPS manual 2.3.15 *Casa Softw. Ltd* 1–177

[15]   Blundell R K and Licence P 2014 Quaternary ammonium and phosphonium based ionic liquids: A comparison of common anions *Phys. Chem. Chem. Phys.* **16** 15278–88

[16]   Hermann K, Pettersson L G M, Casida M E, Daul C, Goursot A, Koester A, Proynov E, St-Amant A, Salahub D R, Carravetta V, Duarte H, Friedrich C, Godbout N, Gruber M, Guan J, Jamorski C, Leboeuf M, Leetmaa M, Nyberg M, Patchkovskii S, Pedocchi L, Sim F, Triguero L and Vela A 2014 StoBe-deMon version 3.3

[17]   Hanwell M D, Curtis D E, Lonie D C, Vandermeerschd T, Zurek E and Hutchison G R 2012 Avogadro: An advanced semantic chemical editor, visualization, and analysis platform *J. Cheminform.* **4** 17

[18]   Diller K, Maurer R J, Müller M and Reuter K 2017 Interpretation of X-ray absorption spectroscopy in the presence of surface hybridization *J. Chem. Phys.* **146** 1–6

[19]   Neese F 2012 The ORCA program system *Wiley Interdiscip. Rev. Comput. Mol. Sci.* **2** 73–8

[20]   Neese F 2018 Software update: the ORCA program system, version 4.0 *Wiley Interdiscip. Rev. Comput. Mol. Sci.* **8** 4–9

[21]   Villar-Garcia I J, Smith E F, Taylor A W, Qiu F, Lovelock K R J, Jones R G and Licence P 2011 Charging of ionic liquid surfaces under X-ray irradiation: The measurement of absolute binding energies by XPS *Phys. Chem. Chem. Phys.* **13** 2797–808

[22]   Henderson Z, Thomas A G, Wagstaffe M, Taylor S F R, Hardacre C and Syres K L 2019 Reversible reaction of CO_2 with superbasic ionic liquid [P_{66614}][benzim] studied with in situ photoelectron spectroscopy *J. Phys. Chem. C* **123** 7134–41

[23]   Tanaka K, Miyahara K and Toyoshima I 1984 Adsorption of CO_2 on TiO_2 and Pt/TiO_2 Studied by X-ray Photoelectron Spectroscopy and Auger Electron Spectroscopy **3534** 3504–8

[24]   Lovelock K R J, Smith E F, Deyko A, Villar-Garcia I J, Licence P and Jones R G 2007 Water adsorption on a liquid surface *Chem. Commun.* 4866–8

[25]   Yerushalmi R, Ho J C, Fan Z and Javey A 2008 Phosphine oxide monolayers on SiO_2 surfaces *Angew. Chemie - Int. Ed.* **47** 4440–2

[26]   Engelhard M H, Baer D R, Herrera-Gomez A and Sherwood P M A 2020 Introductory guide to backgrounds in XPS spectra and their impact on determining peak intensities *J. Vac. Sci. Technol. A Vacuum, Surfaces, Film.* **38**

[27]   Oku M, Matsuta H, Wagatsuma K, Waseda Y and Kohiki S 2002 Removal of inelastic scattering part from Ti2p XPS spectrum of TiO_2 by deconvolution method using O1s as response function *J. Electron Spectros. Relat. Phenomena* **105** 211–8

[28]   Syres K L, Thomas A G, Flavell W R, Spencer B F, Bondino F, Malvestuto M, Preobrajenski A and Grätzel M 2012 Adsorbate-induced modification of surface electronic structure: Pyrocatechol adsorption on the anatase TiO_2 (101) and rutile TiO_2 (110) surfaces *J. Phys. Chem. C* **116** 23515–25

[29]   Taneichi D, Haneda R and Aramaki K 2001 A novel modification of an alkanethiol self-assembled monolayer with alkylisocyanates to prepare protective films against copper corrosion *Corros. Sci.* **43** 1589–600

[30]   Ferraria A M, Boufi S, Battaglini N, Botelho do Rego A M and Reivilar M 2010 Hybrid systems of silver nanoparticles generated on cellulose surfaces *Langmuir* **26** 1996–2001

[31]   Stevens J S, De Luca A C, Pelendritis M, Terenghi G, Downes S and Schroeder S L M 2013 Quantitative analysis of complex amino acids and RGD peptides by X-ray photoelectron spectroscopy (XPS) *Surf. Interface Anal.* **45** 1238–46

[32]   Lewis T, Faubel M, Winter B and Hemminger J C 2011 CO_2 capture in amine-based aqueous solution: Role of the gas-solution interface *Angew. Chemie - Int. Ed.* **50** 10178–81

[33]   Cremer T, Stark M, Deyko A, Steinrück H-P and Maier F 2011 Liquid/Solid Interface of Ultrathin Ionic Liquid Films: $[C_1C_1Im][Tf_2N]$ and $[C_8C_1Im][Tf_2N]$ on Au(111) *Langmuir* **27** 3662–71

[34]   Walsh J F, Dhariwal H S, Gutiérrez-Sosa A, Finetti P, Muryn C A, Brookes N B, Oldman R J and Thornton G 1998 Probing molecular orientation in corrosion inhibition via a NEXAFS study of benzotriazole and related molecules on Cu(100) *Surf. Sci.* **415** 423–32

[35]   Stöhr J 2003 *NEXAFS Spectroscopy* (Berlin: Springer)

[36]   Grillo F, Garrido Torres J A, Treanor M J, Larrea C R, Götze J P, Lacovig P, Früchtl H A, Schaub R and Richardson N V. 2016 Two-dimensional self-assembly of benzotriazole on an inert substrate *Nanoscale* **8** 9167–77

[37]   Ehlert C, Holzweber M, Lippitz A, Unger W E S and Saalfrank P 2016 A detailed assignment of NEXAFS resonances of imidazolium based ionic liquids *Phys. Chem. Chem. Phys.* **18** 8654–61

[38]   Thomason M J, Seabourne C R, Sattelle B M, Hembury G A, Stevens J S, Scott A J, Aziz E F and Schroeder S L M 2015 Self-association of organic solutes in solution: A NEXAFS study of aqueous imidazole *Faraday Discuss.* **179** 269–89

[39]   Mercy M, Rebecca Taylor S F, Jacquemin J, Hardacre C, Bell R G and De Leeuw N H 2015 The addition of CO_2 to four superbase ionic liquids: a DFT study *Phys. Chem. Chem. Phys.* **17** 28674–82

[40]   Buchner F, Forster-Tonigold K, Uhl B, Alwast D, Wagner N, Farkhondeh H, Groß A and Behm R J 2013 Toward the microscopic identification of anions and cations at the ionic liquid|Ag(111) interface: A combined experimental and theoretical investigation *ACS Nano* **7** 7773–84

[41]   Syres K L and Jones R G 2015 Adsorption, desorption, and reaction of 1-octyl-3-methylimidazolium tetrafluoroborate, $[C_8C_1Im][BF_4]$, ionic liquid multilayers on Cu(111) *Langmuir* **31** 9799–808

[42]   Baldelli S 2008 Surface structure at the ionic liquid-electrified metal interface *Acc. Chem. Res.* **41** 421–31

[43]   Henderson Z, Walton A S, Thomas A G and Syres K L 2018 Water-induced reordering in ultrathin ionic liquid films *J. Phys. Condens. Matter* **30** 334003

[44]   Lee B R, Choi H, SunPark J, Lee H J, Kim S O, Kim J Y and Song M H 2011 Surface modification of metal oxide using ionic liquid molecules in hybrid organic–inorganic optoelectronic devices *J. Mater. Chem.* **21** 2051

[45]   Wang S, Li S, Cao Z and Yan T 2010 Molecular dynamic simulations of ionic liquids at graphite surface *J. Phys. Chem. C* **114** 990–5

[46]   Fedorov M V. and Lynden-Bell R M 2012 Probing the neutral graphene-ionic liquid interface: Insights from molecular dynamics simulations *Phys. Chem. Chem. Phys.* **14** 2552–6

[47]   Dong K, Zhou G, Liu X, Yao X, Zhang S and Lyubartsev A 2009 Structural evidence for the ordered crystallites of ionic liquid in confined carbon nanotubes *J. Phys. Chem. C* **113** 10013–20

[48]   Smiglak M, Pringle J M, Lu X, Han L, Zhang S, Gao H, Mac Farlane D R and Rogers R D 2014 Ionic liquids for energy, materials, and medicine *Chem. Commun.* **50** 9228–50

[49]   Paramasivam I, Macak J M, Selvam T and Schmuki P 2008 Electrochemical synthesis of self-organized TiO_2 nanotubular structures using an ionic liquid (BMIM-BF_4) *Electrochim. Acta* **54** 643–8

[50]   Park N G 2015 Perovskite solar cells: An emerging photovoltaic technology *Mater. Today* **18** 65–72

[51]   Gorlov M and Kloo L 2008 Ionic liquid electrolytes for dye-sensitized solar cells *J. Chem. Soc. Dalt. Trans.* 2655–66

[52]   Bai S, Da P, Li C, Wang Z, Yuan Z, Fu F, Kawecki M, Liu X, Sakai N, Wang J T W, Huettner S, Buecheler S, Fahlman M, Gao F and Snaith H J 2019 Planar perovskite solar cells with long-term stability using ionic liquid additives *Nature* **571** 245–50

[53]   Sowmiah S, Srinivasadesikan V, Tseng M C and Chu Y H 2009 On the chemical stabilities of ionic liquids *Molecules* **14** 3780–813

[54]   Lockett V, Sedev R, Bassell C and Ralston J 2008 Angle-resolved X-ray photoelectron spectroscopy of the surface of imidazolium ionic liquids *Phys. Chem. Chem. Phys.* **10** 1330–5

[55]   Shimizu K, Pensado A, Malfreyt P, Pádua A A H and Canongia Lopes J N 2012 2D or not 2D: Structural and charge ordering at the solid-liquid interface of the 1-(2-hydroxyethyl)-3-methylimidazolium tetrafluoroborate ionic liquid *Faraday Discuss.* **154** 155–69

[56]   Dragoni D, Manini N and Ballone P 2012 Interfacial layering of a room-temperature ionic liquid thin film on mica: A computational investigation *ChemPhysChem* **13** 1772–80

[57]   Kislenko S A, Samoylov I S and Amirov R H 2009 Molecular dynamics simulation of the electrochemical interface between a graphite surface and the ionic liquid [BMIM][PF_6] *Phys. Chem. Chem. Phys.* **11** 5584–90

[58]   Liu L, Li S, Cao Z, Peng Y, Li G, Yan T and Gao X P 2007 Well-ordered structure at ionic liquid/rutile (110) interface *J. Phys. Chem. C* **111** 12161–4

[59]   Zhang X, Zhang X, Dong H, Zhao Z, Zhang S and Huang Y 2012 Carbon capture with ionic liquids: Overview and progress *Energy Environ. Sci.* **5** 6668–81

Chapter 6. *In Situ* Depth Profiling Study of Competitive CO$_2$/H$_2$O Absorption in [P$_{66614}$][124Triz]

The work presented in this chapter was published in the following paper [1]:

Cole J, *et al.*, (2023) "*In situ* XPS of competitive CO$_2$/H$_2$O absorption in an ionic liquid" *J. Phys. Mater.* **6** 045012.

6.1 Introduction

Results in Chapter 5 showed the reordering of [P$_{66614}$][benzim] molecules on the rutile TiO$_2$ (110) surface upon exposure to CO$_2$. The aim of this chapter is to understand how the presence of H$_2$O affects CO$_2$ absorption in ILs and the interaction of ILs with surfaces. Water vapour is a common gas present in flue streams as well as many IL-based technologies and devices.

In Chapter 5 a thin film of [P$_{66614}$][benzim] was deposited onto the TiO$_2$ substrate using a drop casting method at atmosphere. In this study, thin films of [P$_{66614}$][124Triz] were deposited in vacuum using electrospray deposition (ESD). This limits contamination of the IL with atmospheric CO$_2$ and H$_2$O. Rietzler *et al.* were the first to deposit conventional ILs ([C$_8$C$_1$Im][Cl] and [C$_8$C$_1$Im][Tf$_2$N]) using ESD [2] but this technique has not yet been used to deposit SBILs. Combining ESD with NAP-XPS allows us to investigate CO$_2$ capture in clean ultrathin IL films (not exposed to atmosphere).

Hollingsworth *et al.* studied CO$_2$ absorption in [P$_{66614}$][124Triz] and found that carbamate forms on the anion (see Figure 6.1 (b)) [3]. Their results showed that the SBIL is capable of both physical and (equimolar) chemical absorption of CO$_2$. Mercy *et al.* used DFT simulations to study CO$_2$ capture in the SBIL [P$_{3333}$][124Triz] [4]. Their computational results also confirmed the formation of covalently bound carbamate on the [124Triz]$^-$ anion. They also found that while the cation plays no

direct role in the chemisorption of CO_2, the presence of the cation increases the negative charge of the N^1 nitrogen site in $[124Triz]^-$ (see Figure 6.1). This increases the reactivity on N^1, which is considered the most favourable reaction site in the anion.

Figure 6.1. Chemical structure of the $[P_{66614}]^+$ cation with C_{hetero} atoms highlighted in magenta and $C_{aliphatic}$ in black (a). The reaction scheme for $[124Triz]^-$ with CO_2 (b) and H_2O (c). Atoms N^1 and N^2 (blue) are equivalent due to resonance effects. Reaction with CO_2 at N^1 results in the formation of carbamate. Reaction with H_2O forms triazole and a hydroxide ion. $N^{1,r}$ (red) and $N^{2,r}$ (green) denote the N atoms following reaction of the anion with CO_2 or H_2O. The gas exposure stages for NAP-XPS measurements are also shown (d).

In this chapter, the competitive absorption between CO_2 and H_2O vapour was studied using *in situ* depth profiling NAP-XPS. The ordering and interactions of electrosprayed thin films of the SBIL $[P_{66614}][124Triz]$ on rutile TiO_2 (110) was investigated before, during, and after exposure to CO_2, H_2O and a CO_2/H_2O mixture. Depth profiling NAP-XPS gives insights into how the competitive absorption of CO_2 and H_2O varies with depth into the IL film. To the best of our knowledge, this is the first use of depth profiling XPS at near ambient pressures to study CO_2 absorption in ILs.

6.2 Experimental Methods

Experimental measurements of the IL trihexyltetradecylphosphonium 1,2,4-triazolide ([P$_{66614}$][124Triz], structure shown in Figure 6.1) were carried out at beamline HIPPIE at MAX-IV synchrotron in Sweden. A rutile TiO$_2$ (110) single crystal (PI-KEM) was cleaned via Ar$^+$ sputter/anneal cycles (sputtering at 1 keV for 10 minutes and annealing at 700°C for 10 minutes) until XPS spectra showed no contamination. [P$_{66614}$][124Triz] was deposited onto the rutile TiO$_2$ (110) substrate via electrospray deposition in vacuum using a Molecularspray UHV4 system. The deposition chamber had a base pressure of 2.0×10^{-10} mbar and a deposition pressure of 7.0×10^{-10} mbar. A 0.02 M [P$_{66614}$][124Triz]/methanol solution was fed into the emitter capillary by a syringe pump delivering a flow rate of 0.3 mL h^{-1}. The emitter, syringe and tubing were cleaned prior to use by flushing with the solvent. 3.0 kV was applied to the emitter with respect to the grounded entrance capillary. Two electrospray thin films were deposited, a 2.3 nm (ESD1) and a 6.2 nm (ESD2) thin film. Film thicknesses were calculated using Equation 3.18 using the molecular weight and density of [P$_{66614}$][124Triz] (552 g/mol and 0.9019 g/cm^3, respectively) [5,6]. A beam damage study showed no degradation of the IL upon prolonged exposure to the beam, but the sample was still moved ~ 0.1 mm (beam size 60 μm × 25 μm) between scans to avoid possible charging and degradation of the IL.

The ESD1 thin film of [P$_{66614}$][124Triz] was characterised using photoemission while exposed to CO$_2$, H$_2$O and finally a CO$_2$/H$_2$O gas mixture, all at approximately 1 mbar. The molar ratio of CO$_2$:H$_2$O in the gas mixture was 1.1:1 ± 0.1, calculated using the areas of the gas-phase peaks in the O 1s spectra. Measurements were taken during exposure and after the gas was pumped out of the NAP cell after each stage in order to study the reversibility of absorption. This exposure procedure is detailed in Figure 6.1(d). A depth profiling XPS study was carried out on the [P$_{66614}$][124Triz] ESD2 thin film by changing the photon energy as summarised in Table 6.1. These photon energies produce photoelectrons with maximum kinetic energies of 150 and 600 eV, corresponding to surface and bulk sampling depths, respectively. The 6.2 nm thin film was probed at sampling depths of 1.6 and 4.0 nm, calculated as $3\lambda \cos(\theta_{em})$ where θ_{em} is the photoelectron emission angle with respect to the surface normal and

λ is the IMFP of [P$_{66614}$][124Triz] calculated using Equation 3.15 in Chapter 3. NAP-XPS measurements were taken before exposure, during exposure to CO_2, and during exposure to H_2O, both at 1 mbar. A summary of the photon energies used for each photoemission region is presented in Table 6.1.

Region	Photon energy (eV)		
	[P$_{66614}$][124Triz] ESD1	[P$_{66614}$][124Triz] ESD2 (surface)	[P$_{66614}$][124Triz] ESD2 (bulk)
Survey	1000	1000	–
C 1s	435	435	885
N 1s	550	550	1000
O 1s	680	680	1130

Table 6.1 Photon energies used for each region. ESD1 and ESD2 correspond to the two electrosprayed thin films of [P$_{66614}$][124Triz], 2.3 and 6.2 nm thick, respectively. Depth profiling measurements of ESD2 were taken at sampling depths near the surface and in the bulk of the film, achieved by changing the photon energy.

All XPS peaks have been fitted using 30:70 (Lorentzian:Gaussian) line shapes and a linear background, using the software CasaXPS [7]. The binding energy (BE) scale for all regions has been calibrated to the alkyl C 1s signal at 285.0 eV and all fitted peaks are quoted to ± 0.1 eV BE [8].

Experimental N K edge NEXAFS measurements were recorded for a [P$_{66614}$][124Triz] thin film made by depositing 2 µL of a 0.14 M IL-ethanol solution dropwise onto a tantalum sample plate. The IL was deposited dropwise because the low coverages achieved from electrospray deposition resulted in a very weak NEXAFS signal and spectra that were too noisy to analyse. Despite this, C K edge spectra were still too noisy to include in the analysis here. N K edge NEXAFS measurements were recorded both for the IL and for the IL exposed to a 1 mbar CO_2 + 1 mbar H_2O mixture. Measurements were taken at one angle, 60° from normal incidence ($\theta = 30°$), as the near-ambient pressure cell limited large changes in angle of the incident X-ray beam. The spectra were normalised in intensity such that the step between 395 and 425 eV is unity.

Unoccupied molecular orbitals were generated in ORCA and visualised in Avogadro to aid in the assignment of NEXAFS spectral features. Prior to calculations the isolated [124Triz]$^-$ anion was geometry optimized in Avogadro. Only transitions from electrons in the anion contribute to the NEXAFS spectra since there is no π bonding in the [P$_{66614}$]$^+$ cation. Experimental NEXAFS spectra were compared to simulated spectra obtained using density functional theory (DFT) simulations in the software StoBe-deMon. These simulations are not angle-resolved, meaning they are representative of anions being randomly oriented with respect to the incident X-ray beam. The final DFT NEXAFS spectrum is the sum of the individual simulated spectra for each target centre in the anion (e.g., each N atom for N K edge simulations).

6.3 NAP-XPS of [P$_{66614}$][124Triz]
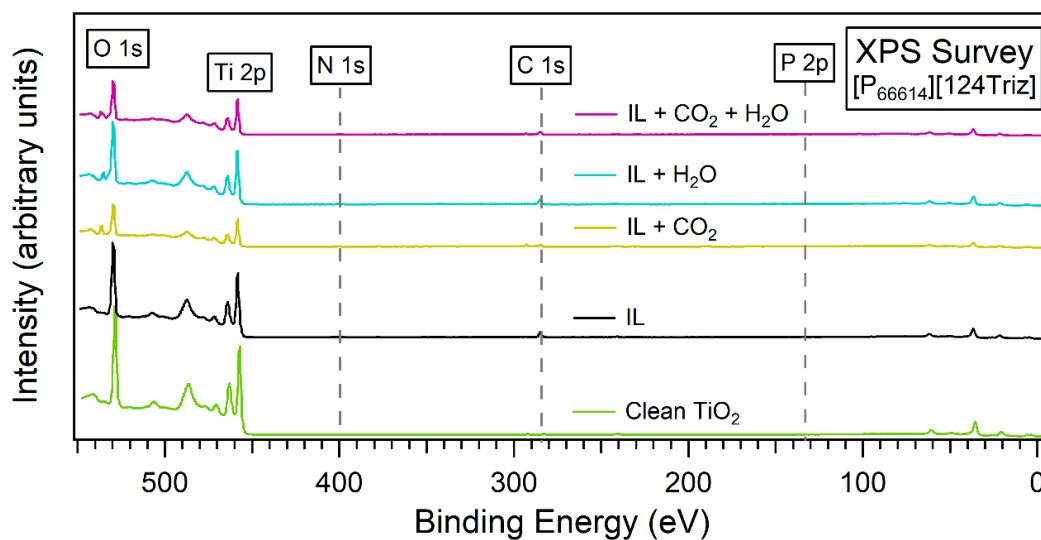
Figure 6.2. XPS survey spectra of [P$_{66614}$][124Triz] subject to various exposures of CO_2 and H_2O. Highlighted are the peaks associated with atoms in the rutile TiO_2 (110) crystal substrate (O 1s, Ti 2p), absorbed gases (O 1s) and the IL (N 1s, C 1s, P 2p).

NAP-XPS measurements were carried out on an electrosprayed 2.3 nm thin film (ESD1) of [P$_{66614}$][124Triz]. Measurements were taken as the IL was exposed to CO_2, H_2O, and finally a CO_2/H_2O mixture, all at 1 mbar. Measurements were also taken prior to exposure and after the gas was removed between each exposure stage, as summarised in Figure 6.1(d), in order to investigate the reversibility of

absorption. Figure 6.2 shows survey scans of the IL before and during the gas exposure stages, as well as the clean TiO_2 (110) crystal prior to deposition.

Region	Binding Energy (eV) $\pm$ 0.1 eV	Assignment
C 1s	285.0	$C_{aliphatic}$
	285.7	C_{hetero}
	$287.1^a \rightarrow 286.9 \rightarrow 286.7 \rightarrow 286.6$	$C^{3,5}$
	288.3	Carbamate
	293.3	Gas-Phase CO_2
N 1s	399.1	N^4
	400.1	$N^{1,2}$
	401.1	$N^{2,r}$
	402.0	$N_{CO_2}^{1,r}$
	402.4	$N_{H_2O}^{1,r}$
O 1s	530.0	TiO_2 lattice O
	531.1	Carbamate[c]
	532.1	$C = O^{b,c}$
	533.2	$C - OH^b$
	535.6	Gas phase H_2O
	537.0	Gas phase CO_2

Table 6.2. Assignments and corresponding BEs of fitted components in the C 1s, N 1s and O 1s regions for [P$_{66614}$][124Triz] for various gas exposure stages. The arrows ($\rightarrow$) denote chemical shifts of the $C^{3,5}$ component between the following exposure stages: IL $\rightarrow$ IL + CO_2 $\rightarrow$ IL + H_2O $\rightarrow$ IL + CO_2 + H_2O. [a] $C^{3,5}$ component returns to this BE during the CO_2 and H_2O pump out stages. [b] Within the protonated carbamate group. [c] These peaks are assigned to hydroxyl species and defects at the TiO_2 surface in Stage 1.

The C 1s region is shown in Figure 6.3(a) for all stages, and the fitted components for each gas exposure stage are shown in Figure 6.3(b). A summary of the fitting for each region is shown in Table 6.2. The C 1s spectra are intensity normalised to the peak at 285.0 eV. The main C 1s peak at 285 eV can be fitted with two components attributed to the [P$_{66614}$]$^+$ cation. These occur at 285.0 and 285.7 eV in all stages and are assigned as $C_{aliphatic}$ and C_{hetero}, respectively (see Figure 6.1(a)). These agree with previous reports on the [P$_{66614}$]$^+$ cation [8]. A third component at 287.1 eV is attributed to carbon atoms in positions 3 and 5 in the [124Triz]$^-$ anion ($C^{3,5}$).
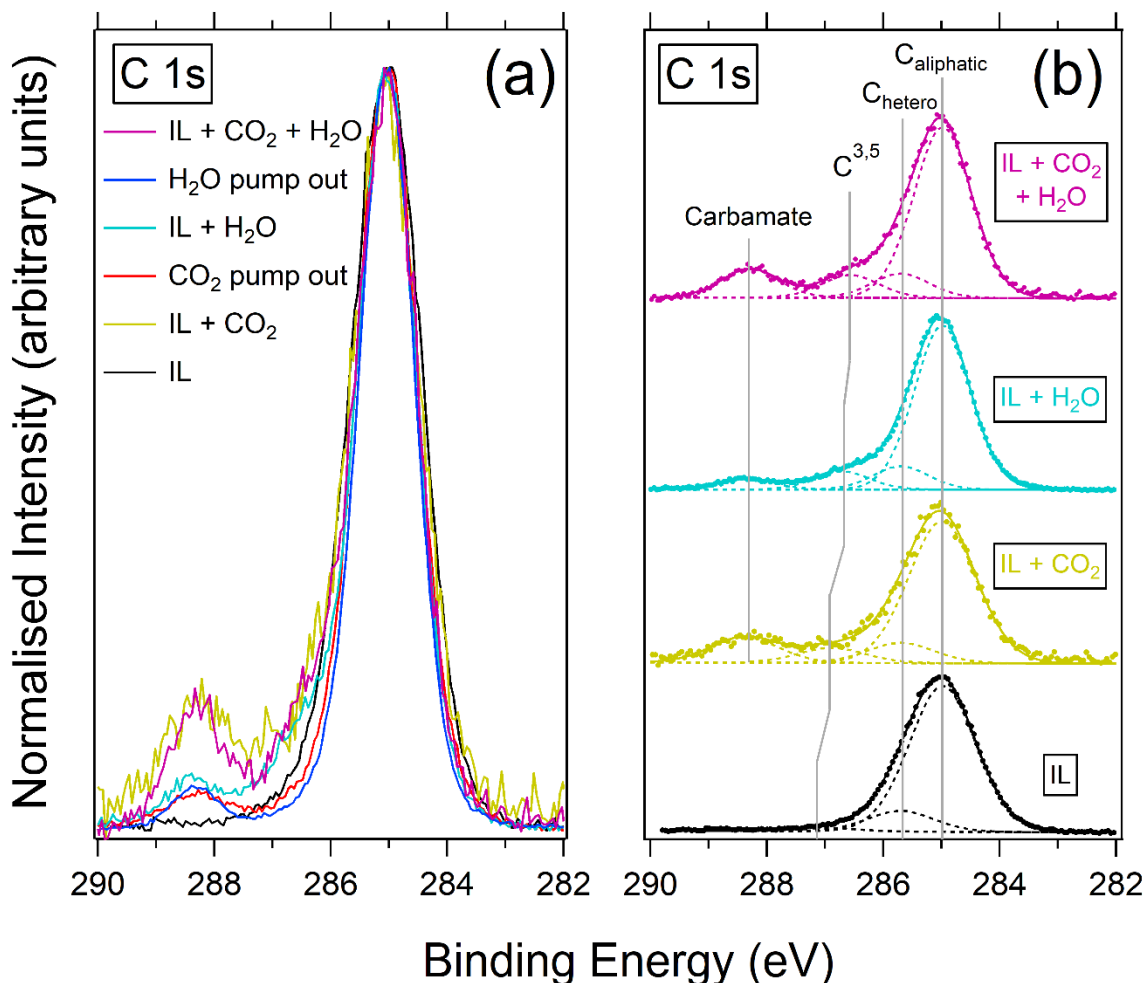
Figure 6.3. C 1s region of an electrosprayed thin film of $[P_{66614}][124Triz]$ for various exposure regimes of CO_2 and H_2O at 1 mbar. (a) shows how the carbamate peak at 288.3 eV varies in intensity throughout these stages. (b) shows how the $C^{3,5}$ component shifts downwards in binding energy throughout the exposure stages.

Exposing the electrosprayed IL to CO_2 in Stage 2 results in a gas-phase CO_2 peak at 293.3 eV (not shown) and a carbamate peak (see Figure 6.1(b)) at 288.3 eV. As expected, there is no carbamate peak present prior to CO_2 exposure in Stage 1. In addition to a chemical shift of -0.2 eV to 286.9 eV, the $C^{3,5}$ component increases in intensity during exposure to CO_2, reverting to its original intensity and BE when the gas is removed in Stage 3. Similarly, the carbamate peak reduces in intensity but does not reduce to zero when CO_2 is removed, indicating that the reaction with CO_2 is not fully reversible. Hereinafter, this will be referred to as residual carbamate. It has been shown that bulk depositions of $[124Triz]^-$ ILs reversibly absorb CO_2 by

141

heating the IL, even in the presence of water [6]. A thick film of a similar SBIL has been shown to reversibly absorb and desorb CO_2 by pumping out the gas [9]. However, as shown here, our thin films of [P_{66614}][124Triz] cannot be regenerated through removing the surrounding gas. This could be due interactions at the IL/vacuum and IL/TiO_2 interfaces which are likely to have a greater influence in our thin films than they do in bulk ILs. This is explored in more detail in the discussion section below.

When the IL is exposed to H_2O in Stage 4 there is no significant change in intensity of the residual carbamate peak. This would suggest that the absorption of H_2O, which reacts at the same N^1 site as CO_2, does not remove the irreversibly absorbed CO_2. The $C^{3,5}$ component also shifts down to 286.7 eV and increases in intensity, similar behaviour to that found in Stage 2 (IL + CO_2). When the H_2O is removed in Stage 5, the residual carbamate peak persists, suggesting that the absorption and desorption of H_2O has little effect on the absorbed residual carbamate. Overall, the H_2O pump out spectrum closely resembles that of the CO_2 pump out stage, with the $C^{3,5}$ components showing similar intensities and BEs (287.1 eV). This suggests that the IL's reaction with H_2O is reversible.

When the electrosprayed IL is exposed to the CO_2/H_2O mixture in Stage 6, the carbamate peak increases again to a similar intensity to that of Stage 2 (IL + CO_2). This further suggests that the presence of H_2O does not inhibit the absorption of CO_2 and formation of carbamate, which is in agreement with other reports for [124Triz]$^-$-based ILs [6]. The $C^{3,5}$ component (which shifts again to 286.6 eV) also increases to a similar intensity as that in Stages 2 and 4, when the IL is exposed to CO_2 and H_2O, respectively. The change in BE and intensity of the $C^{3,5}$ component during gas exposure Stages 2, 4 and 6 is not fully understood. The small BE shifts may be due a change in chemical environment of $C^{3,5}$ upon chemical reaction or physical interaction between the anion and gas. The change in intensity could be explained by a reordering of anions upon exposure to gas. Note that for the CO_2/H_2O mixture, reaction between the two gases may form carbonic acid (H_2CO_3) [10]. It is possible this may interact with the IL thin film, though we find no evidence of carbonic acid in our spectra.
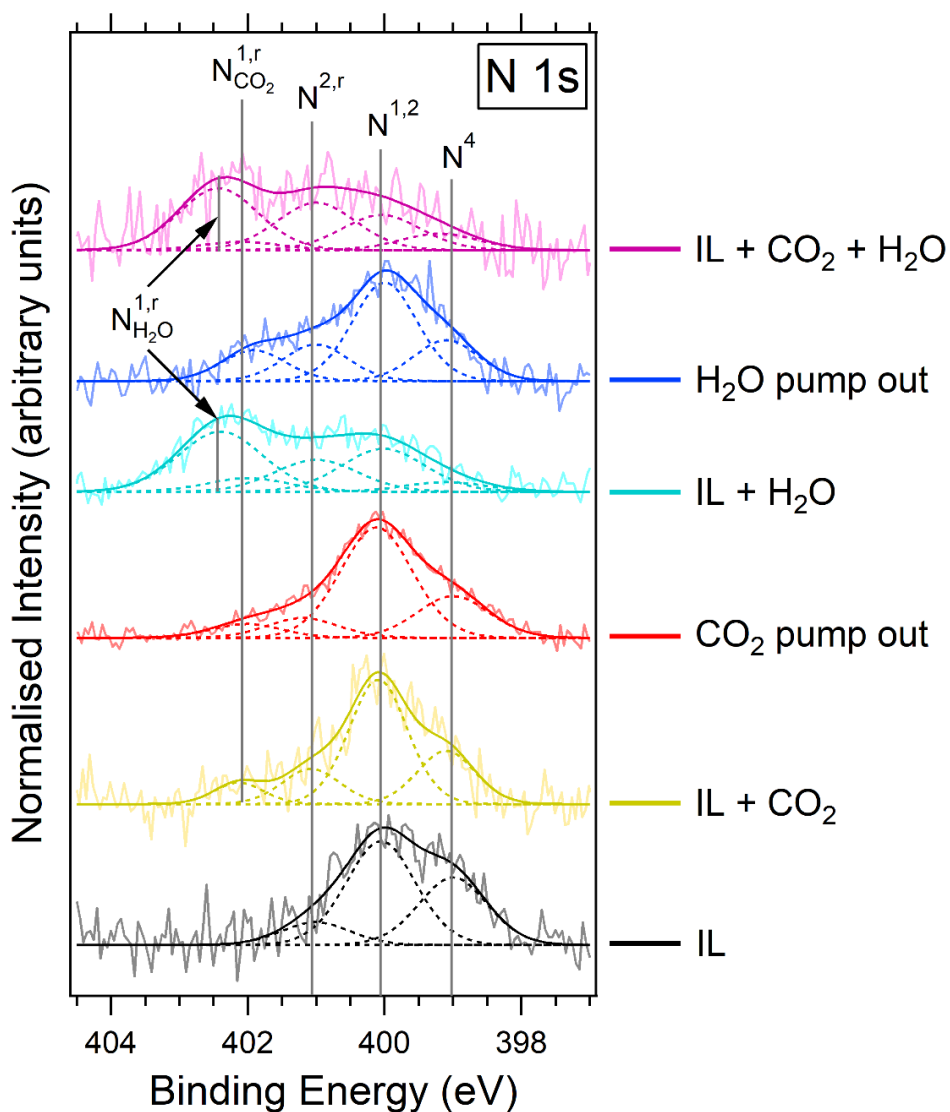
Figure 6.4. N 1s region of an electrosprayed thin film of [P$_{66614}$][124Triz] for various exposure regimes of CO_2 and H_2O at 1 mbar. The grey lines show common components fitted through each stage of exposure.

Figure 6.4 shows the N 1s region for all six stages. The N 1s peak can be fitted with three components, the first two of which at 399.1 and 400.1 eV are assigned to nitrogen species inherent to the [124Triz]$^-$ anion. The component at 399.1 eV is attributed to N^4 (C−N−C) while the component at 400.1 eV is assigned to the chemically equivalent N^1 and N^2 atoms (N^{1,2}, see Figure 6.1 for assignments). N^1 and N^2 are chemically equivalent due to resonance effects [11], confirmed by molecular orbital calculations using the software ORCA (LUMOs of the anion are also shown in Figure 6.12 in Section 6.4). The IL film was prepared by electrospray

in vacuum so we would not expect any significant higher BE peaks attributed to reaction with gas. However, there is a small peak at 401.1 eV which may be due to reactions with trace amounts of gas remaining in the UHV chamber. This peak is assigned to atom $N^{2,r}$ in the reacted anion. We would expect another peak at higher BE attributed to $N^{1,r}$ (atom at which gas reacts), but this cannot be resolved here. It is unclear whether the IL has absorbed CO_2, H_2O, or both in this case because the $N^{2,r}$ component remains at this same BE throughout each of the following exposure stages (the same is also true for the N^4 and $N^{1,2}$ components).

Upon exposure to CO_2 in Stage 2, a peak appears at 402.0 eV. We can assign this to atom $N^{1,r}$, the atom at which carbamate forms ($N^{1,r}_{CO_2}$). Similar to the C 1s region in Figure 6.3, this carbamate peak reduces in intensity, but not to zero, when the CO_2 is removed in Stage 3, indicating irreversible CO_2 absorption. This residual carbamate peak appears in all following stages, consistent with the C 1s spectra in Figure 6.3. Note that the carbamate peak is higher in BE than it is for [P66614][benzim] in Chapter 5 (401.1 eV). This is likely due to the different structure of the anions.

When the IL is exposed to H_2O in Stage 4, a strong peak occurs at 402.4 eV attributed to protonated $N^{1,r}$ in H_2O-reacted [124Triz]$^-$ ($N^{1,r}_{H_2O}$). In our group's previous work on [P66614][benzim], $N^{1,r}_{CO_2}$ and $N^{1,r}_{H_2O}$ occurred at the same or very similar BEs and could not be individually resolved [9]. This difference is most likely due to the different chemical environments of nitrogen atoms in the [124Triz]$^-$ anion compared to [benzim]$^-$. When H_2O is removed in Stage 5, the $N^{1,r}_{H_2O}$ peak at 402.4 eV disappears completely while the residual carbamate peak ($N^{1,r}_{CO_2}$) remains, further indicating that this peak is due to a reversible reaction with H_2O. This supports previous evidence of reversible H_2O absorption discussed above (Figure 6.3).

Finally, when the IL is exposed to the CO_2/H_2O mixture in Stage 6 the spectrum closely resembles that of Stage 4 (IL + H_2O) except for a more intense $N^{2,r}$ component at 401.1 eV. The pressure in Stage 6 rose slightly higher than 1 mbar (1.3 mbar), therefore resulting in a stronger $N^{2,r}$ component due to a higher relative concentration of reacted anions. Despite an approximately equal CO_2:H_2O molecular ratio in the mixture, the $N^{1,r}_{H_2O}$ component at 402.4 eV is much more intense than the

$N_{CO_2}^{1,r}$ component at 402.0 eV. The reason why H_2O absorption appears to dominate over CO_2 absorption in Stage 6 can be explained with depth profiling XPS and will be discussed in detail below (see discussion for Figure 6.6). Another explanation may be that the timescale over which measurements were taken plays an important role. It has been shown that for the IL [BMIM][OAc] the uptake of water into the bulk takes many hours, yet is much quicker at the IL-gas interfacial layers [12]. Conversely, it has been found by Wang *et al*. that bulk thicknesses of SBILs (similar to those used in this study) absorbed CO_2 very quickly, on the order of minutes [13,14]. Admittedly these timescales are likely to change at the mbar pressures used in our study compared to atmospheric pressures used by Wang *et al*. Our measurements were taken over a 30 minute timeframe at a surface sensitive sampling depth. Therefore, if [P_{66614}][124Triz] behaves similar to these ILs, then the reason that H_2O absorption dominates over CO_2 absorption may be that there is an abundance of H_2O at the surface due to a slower uptake of the gas into the bulk layers of the IL compared to CO_2.

In the O 1s region in Figure 6.5(a) there is a common peak at 530.0 eV for all stages, attributed to O atoms in the TiO_2 substrate lattice [15]. The electrosprayed IL (black line) can be fitted with two more components at 531.1 and 532.1 eV. Since there are no oxygen atoms in the IL and we do not see any carbamate species in the C 1s region in Stage 1, these are assigned to hydroxyls/defects at the TiO_2 surface [16].

When the electrosprayed IL is exposed to CO_2 (gold line) peaks are fitted at 530.1, 531.1, 532.1, 533.2, and 535.6 eV. These are assigned to TiO_2, carbamate, C=O in protonated carbamate, C–OH in protonated carbamate, and gas-phase CO_2 (not shown), respectively. Carbamate species formed upon reaction with CO_2 can be protonated and it is likely that there is a mixture of protonated and unprotonated carbamate species present here [17]. The 531.1 and 532.1 eV peaks in Stages 2 – 6 will also contain contributions from the hydroxyl species/defects at the TiO_2 surface. It is likely the film is not completely homogeneous and it is possible the IL could form islands on the surface rather than forming layers. However, we are unable to verify the growth mode from our data. If islands have formed then direct absoprtion of CO_2 on the rutile TiO_2 (110) surface is possible. It has been shown experimentally

and verified using DFT that frozen CO_2 at -196 °C preferentially binds at oxygen defect sites but can also react at Ti^{4+} sites, either through one of the O atoms or the C atom in CO_2 [18]. However, Grinter *et al.* found using NAP-XPS that 100 mTorr (~133 mbar) of gas-phase CO_2 at 200 °C barely binds at the rutile TiO_2 (110) surface (i.e. does not form stable carbonates) but instead weakly physisorbs [19]. Since their substrate was prepared using similar sputter/anneal cycles and exposed to approximately mbar pressures of CO_2, is likely there is also no strong chemical reaction between CO_2 and the TiO_2 surface in our experiment.
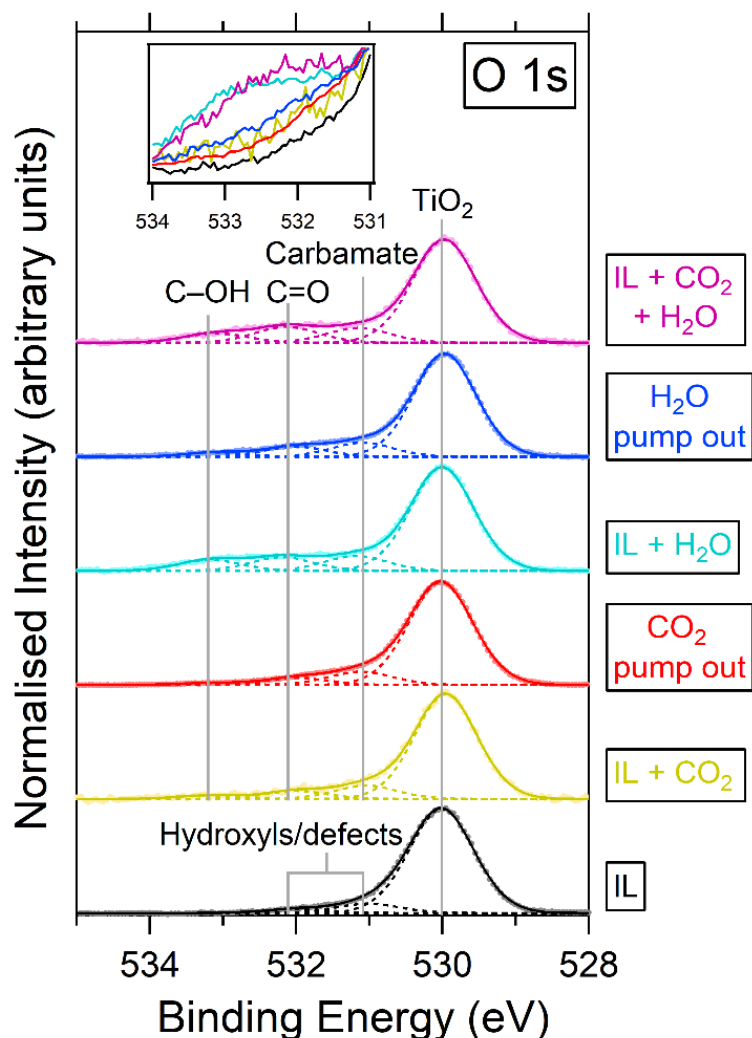
Figure 6.5. O 1s region of an electrosprayed thin film of [P$_{66614}$][124Triz] for various exposure regimes of CO_2 and H_2O at 1 mbar. (a) shows how the broad reaction peak at ~533 eV varies in intensity throughout these stages. (b) shows peak fitting for the gas exposure stages.

When the CO_2 gas is removed in Stage 3 the broad reaction shoulder reduces in intensity but does not return to the original intensity from Stage 1. This provides further evidence of irreversible CO_2 absorption and reordering in the IL, shown previously in the C 1s and N 1s regions in Figures 6.3 and 6.4, respectively.

When the IL is exposed to H_2O in Stage 4, we see a significant increase in intensity of the reaction components. This would support our assumption that components at 532.1 and 533.2 eV are attributed to interactions with water vapour (C=O and C–OH in protonated carbamate species). Upon exposure to the CO_2/H_2O mixture in the final stage, the broad reaction peak returns to a similar intensity to that when exposed to H_2O alone. This suggests that the presence of CO_2 does not inhibit the ad/absorption of H_2O. The reason why H_2O absorption appears to dominate over CO_2 absorption in Figure 6.5 can be explained using depth profiling XPS.

6.4 Depth Profiling NAP-XPS of [P$_{66614}$][124Triz]

Depth profiling XPS was carried out on an electrosprayed 6.2 nm thin film of [P$_{66614}$][124Triz] (ESD2) by probing two sampling depths: 4.0 nm to probe the bulk layers of the IL, and 1.6 nm to probe the surface layers. Photoemission measurements were taken for the electrosprayed IL, the IL exposed to 1 mbar CO_2, and the IL exposed to 1 mbar H_2O, for both bulk and surface sampling depths. Note that these sampling depths are expected to alter slightly during gas exposure stages due to attenuation of electrons through the gas.

Figure 6.6 shows depth profiling measurements in the C 1s region, with spectra normalised to the peak at 285.0 eV. For the electrosprayed IL, even before exposure to CO_2 there is a small carbamate feature at 288.3 eV for the surface sampling depth (grey line) which may be due to trace amounts of residual CO_2 in the chamber. Alternatively, it could indicate irreversibly absorbed CO_2 from previous exposures (since the ESD2 film was deposited over ESD1), which would further suggest that irreversibly absorbed CO_2 moves to the surface. In Chapter 5 there was evidence of irreversible CO_2 absorption in multilayer thin films of the similar SBIL [P$_{66614}$][benzim].
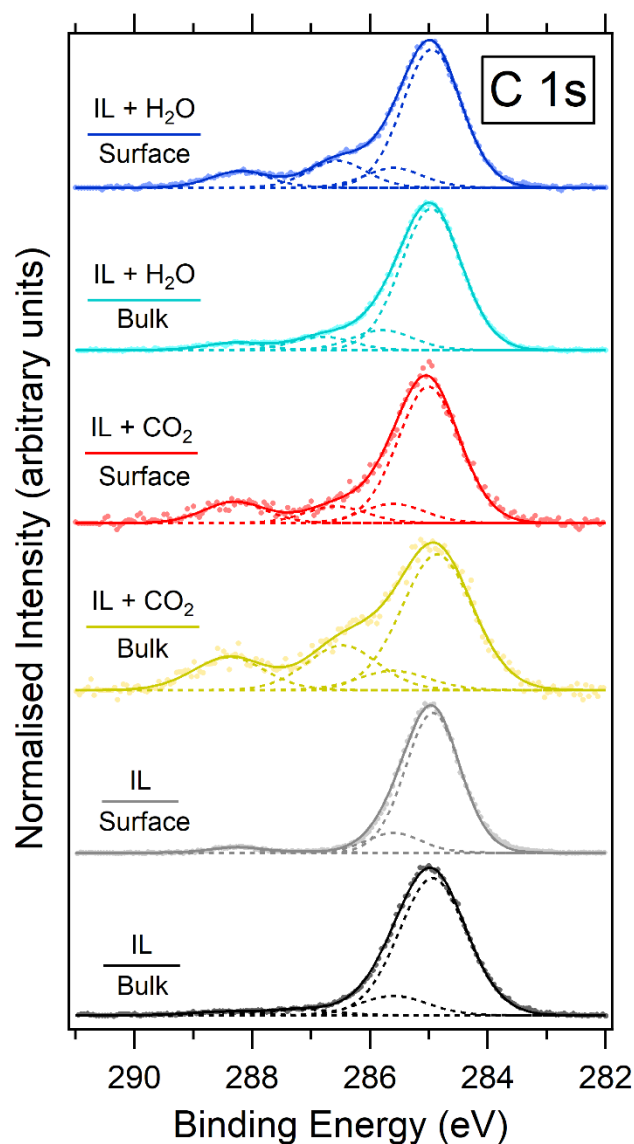
Figure 6.6. Depth profiling XPS of the C 1s region for an electrosprayed [P$_{66614}$][124Triz] thin film. The 6.2 nm thick sample was probed at two sampling depths: 4.0 nm to sample the bulk layers (denoted "Bulk") and 1.6 nm to sample the surface layers (denoted "Surface").

When the IL is exposed to CO_2, the resulting carbamate peak at 288.3 eV is more intense for the bulk sampling depth (gold line) compared to the surface (red line). This implies that a greater concentration of carbamate species occurs in the bulk compared to the surface. Lewis *et al.* have reported similar behaviour for aqueous MEA solutions treated with CO_2 [20]. Greater concentrations of CO_2-reacted MEA were found in the bulk of the solution while unreacted MEA was more concentrated at the surface.

When CO_2 is removed and the IL is exposed to H_2O alone, a smaller residual carbamate peak remains in the IL + H_2O spectra (blue lines) at 288.3 eV in Figure 6.6. Similar evidence of irreversible CO_2 absorption was seen earlier in Figure 6.3. The residual carbamate peak here is stronger when probed at the surface sampling depth (dark blue line) rather than in the bulk (light blue line), suggesting that more residual carbamate resides at the IL surface than in its bulk layers. In fact, the residual carbamate peak at the surface (dark blue line) is a similar intensity to the carbamate peak at the surface when exposed to CO_2 (red line). This implies that most of the CO_2 that absorbs within the surface layers of the IL does so irreversibly, remaining absorbed when the surrounding gas is pumped out. However, carbamate formed in the bulk (gold line) dramatically reduces in concentration when CO_2 is removed and H_2O introduced (light blue line). This suggests that the irreversible nature of CO_2 absorption in this IL is largely attributed to reactions at the surface.

To summarise Figure 6.6, more CO_2 absorption appears to occur in the bulk of the IL, and this absorption is largely reversible. Less CO_2 ad/absorbs at the surface and this is irreversible. These results show that both the concentration of carbamate and the level of reversibility varies with depth into the sample.

Depth profiling measurements taken in the N 1s region are shown in Figure 6.7. The spectra have been normalised by peak area between 396 and 404 eV. For the electrosprayed IL, the N 1s peaks are similar at the two sampling depths. As discussed in Figure 6.4, $N^{1,2}$ atoms in the unreacted anion are largely responsible for the main peak centred on 400 eV, implying that the concentration of unreacted anions does not vary significantly through the IL layers prior to exposure.

Upon absorption of CO_2, a carbamate peak appears at approximately 402 eV for the bulk sampling depth (gold line). For the surface sampling depth (red line) there is no discernible N 1s peak or evidence of carbamate formation. Comparing the two is tenuous given the very noisy nature of the surface sampling depth spectrum. This is most likely due to attenuation of photoelectrons through the CO_2 gas, considering they have low kinetic energies (maximum of 150 eV).
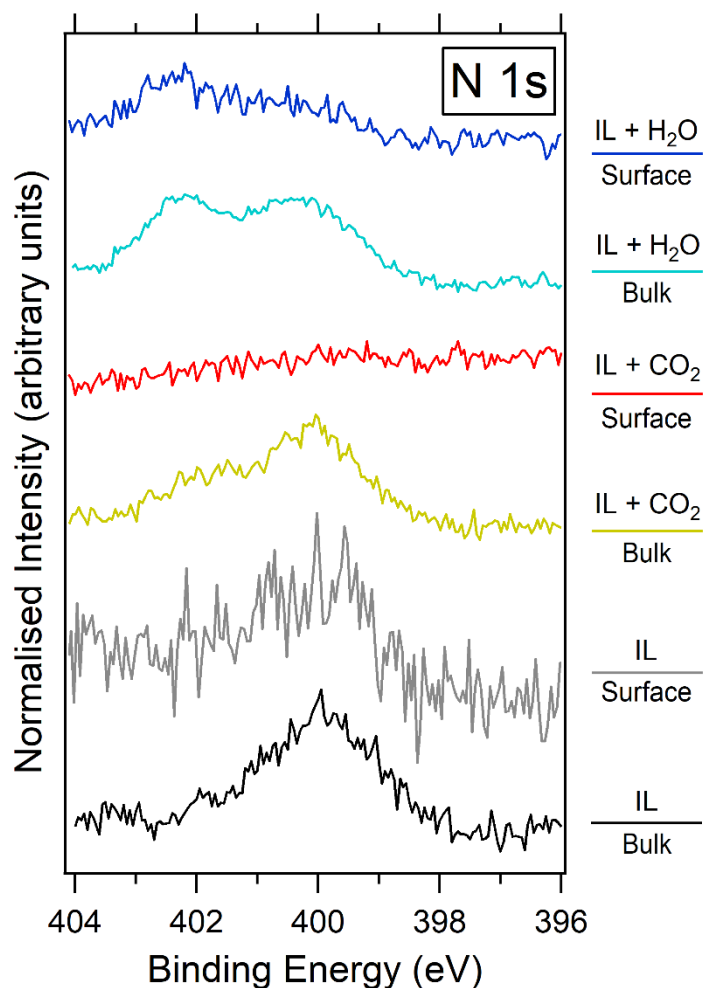
Figure 6.7. Depth profiling XPS of the N 1s region for an electrosprayed [P$_{66614}$][124Triz] thin film. The 6.2 nm thick sample was probed at two sampling depths: 4.0 nm to sample the bulk layers (denoted "Bulk") and 1.6 nm to sample the surface layers (denoted "Surface").

The absorption of H_2O results in protonation of N^1 in [124Triz]$^-$, denoted $N^{1,r}_{H_2O}$, manifesting as a feature at 402.4 eV. Relative to the main $N^{1,2}$ peak at approximately 400 eV, the intensity of $N^{1,r}_{H_2O}$ is greater when probed at the surface (dark blue line) than in the bulk (light blue line). This suggests that there is a greater concentration of protonated N atoms at the surface than in the bulk. This is also supported by the more intense $C^{3,5}$ (C atoms in the reacted anion) component at the surface when exposed to H_2O in Figure 6.6. Results from Figures 6.6 and 6.7 suggest that more H_2O-reacted species remain at the surface of the IL film, and more CO_2-reacted species diffuse through the surface to the bulk. This would explain why there is little

evidence of CO_2 absorption in Figure 6.5 (O 1s) and why H_2O absorption appeared to dominate over CO_2 absorption when the IL was exposed to a CO_2/H_2O mixture in Figure 6.4 (N 1s), because these spectra were taken at surface-sensitive photon energies of 680 eV and 550 eV, respectively.

Previous studies have found that the presence of H_2O does not significantly inhibit CO_2 absorption in thin films of $[P_{66614}][benzim]$ at near-ambient pressures [9]. This behaviour could be explained by the results presented here. Reactions between the IL and the two different gases may occur primarily at different depths in the IL film. Additionally, the timescale over which the gases absorb in the IL may play an important role here, as these timescales have been shown to vary significantly for CO_2 and H_2O in ILs (although, these studies used different ILs and atmospheric pressures as opposed to mbar used in our study) [12,13].

6.5 NEXAFS of $[P_{66614}][124Triz]$
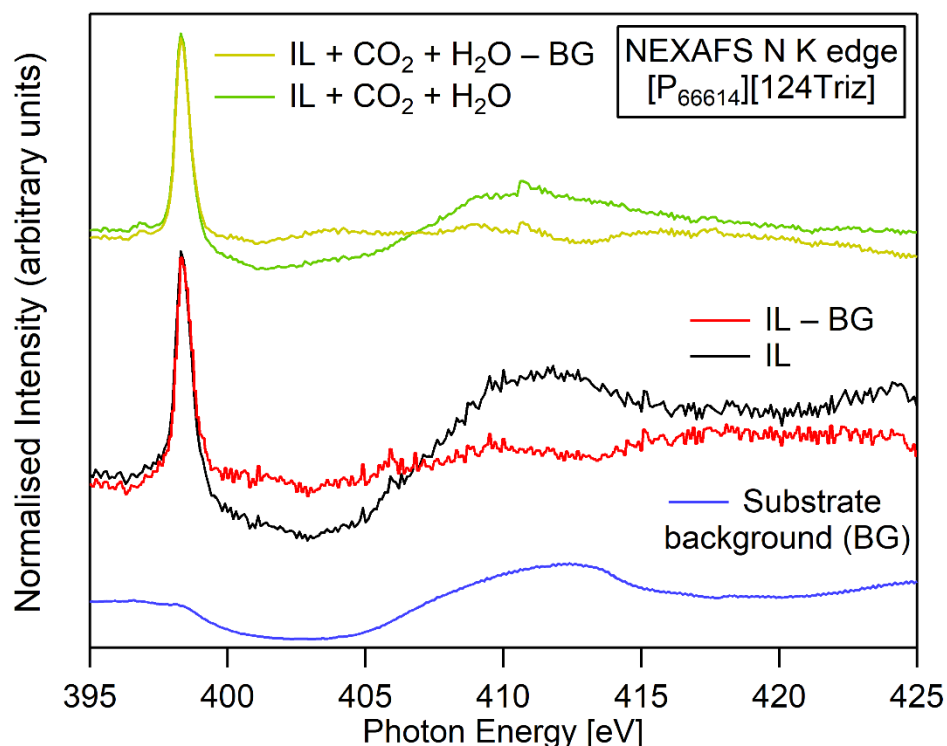
Figure 6.8. N K edge NEXAFS showing the background correction of the substrate background for the as presented IL and the IL exposed to the $CO_2 + H_2O$ gas mixture.

Experimental N K edge NEXAFS measurements were recorded for a [P_{66614}][124Triz] thin film deposited dropwise onto a tantalum sample plate. N K edge NEXAFS spectra of the as presented IL and the IL exposed to a CO_2 + H_2O mixture were first corrected for the substrate background signal. This was done by dividing the spectrum of the IL by the spectrum of the substrate signal, as shown in Figure 6.8.

N K edge NEXAFS of the as presented IL and the IL exposed to a 1 mbar CO_2 + 1 mbar H_2O mixture are shown in Figure 6.9. For the as presented IL there is a single π^* peak at a photon energy of 398.3 eV and a σ^* peak at 409.7 eV. Theoretical spectra were simulated for the isolated [124Triz]$^-$ anion and have π^* and σ^* peaks at 398.3 and 409.6, respectively. The π^* and σ^* peaks in the experimental spectrum, as well as the other small features, agree well with peak positions in the DFT spectrum, highlighted by the vertical dashed grey lines in Figure 6.9.

When the IL is exposed to the CO_2/H_2O gas mixture there is no dramatic change in the experimental spectrum compared to the IL as presented, despite changes in the theoretical DFT spectra. It's not clear why there are no dramatic changes in the spectra. At the time of the experiment, HIPPIE beamline was still in the process of commissioning the use of NEXAFS, so we suggest there could have been issues with the experimental set-up or problems with our background subtraction. There are some minor changes in the spectra worth noting. A pre-edge peak appears in the experimental IL + CO_2 + H_2O spectrum at 396.9 eV and also appears in the corresponding DFT spectrum, arising from atom $N^{2,r}$ in protonated triazolide anions (anions reacted with water, see Figure 6.11). A weak pre-edge peak has also been found for 1,2,3-triazolium based ILs with a [Tf_2N]$^-$ anion [21].
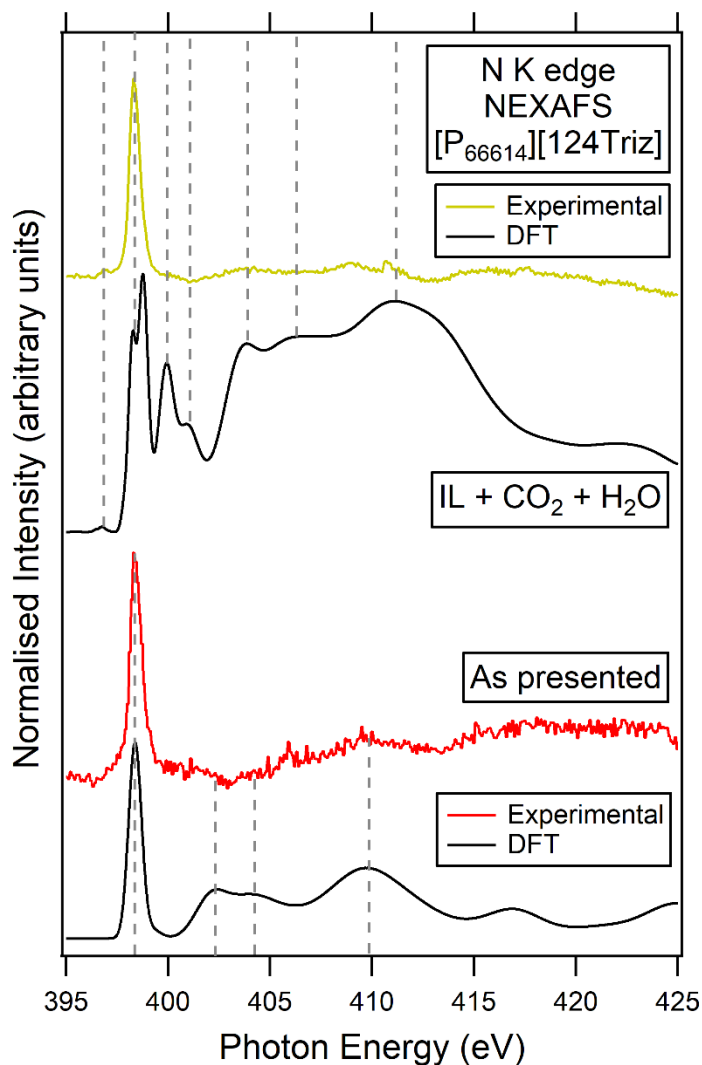
Figure 6.9. Experimental and simulated (DFT) N K edge NEXAFS spectra of [P$_{66614}$][124Triz] as presented and when exposed to 1 mbar CO_2 + 1 mbar H_2O. The vertical grey dashed lines extend from the peaks in the DFT spectra for comparison to the experimental spectra.

Simulated NEXAFS spectra were calculated for the IL [P$_{66614}$][124Triz] before (Figure 6.10) and upon exposure to a CO_2/H_2O mixture (Figure 6.11). For the IL as presented, N^1 and N^4 are equivalent, while N^2 has a similar π^* peak at 398.3 eV but a more intense σ^* peak at 409.6 eV.
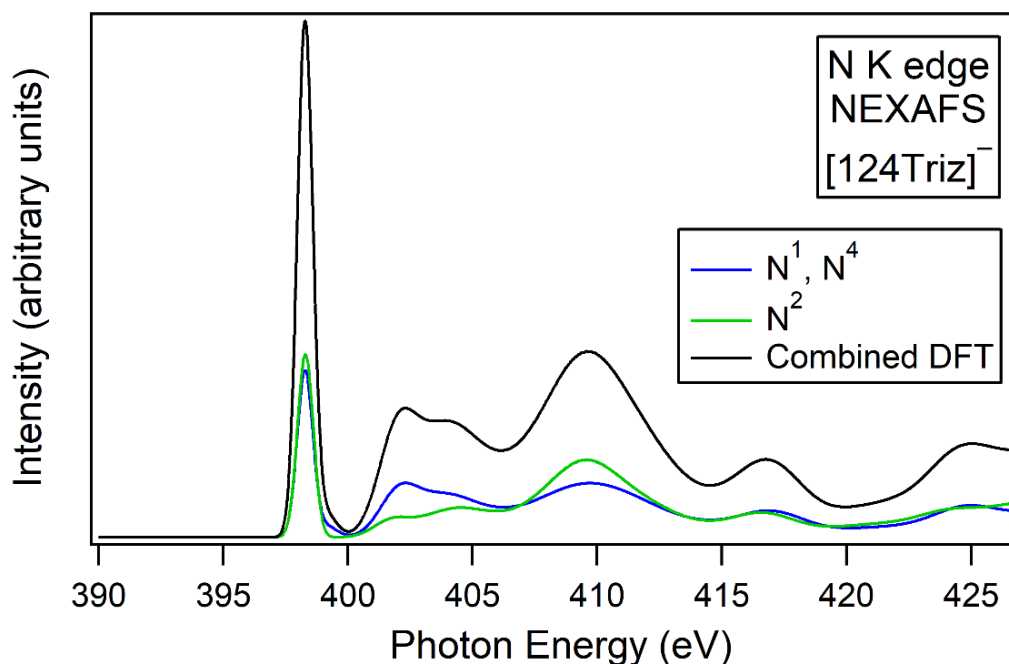
Figure 6.10. Simulated N K edge NEXAFS spectrum for $[P_{66614}][124Triz]$. The final DFT spectrum (black) is the sum of the spectra from atoms N^1 and N^3 (blue) and N^2 (green).

The IL + CO_2 + H_2O DFT spectrum in Figure 6.11 was obtained by combining the spectra for IL + CO_2 and IL + H_2O, with the assumption that the IL absorbs equal amounts of CO_2 and H_2O. We can see that the pre-edge peak in the final DFT spectrum (black line) is due to transitions from $N^{2,r}$ in protonated $[124Triz]^-$ anions (IL + H_2O). In the final DFT, atoms $N^{2,r}$ and $N^{4,r}$ have strong π^* peaks, though $N^{4,r}$ occurs at a higher photon energy than $N^{2,r}$. When the IL absorbs CO_2, H_2O, or both, there are no longer any $N^{1,r} \rightarrow \pi^*$ transitions at the reaction site. Compare this to the IL before exposure (Figure 6.10) in which each N atom contributes to the π^* peak equally, further highlighting the influence of the carbamate species.
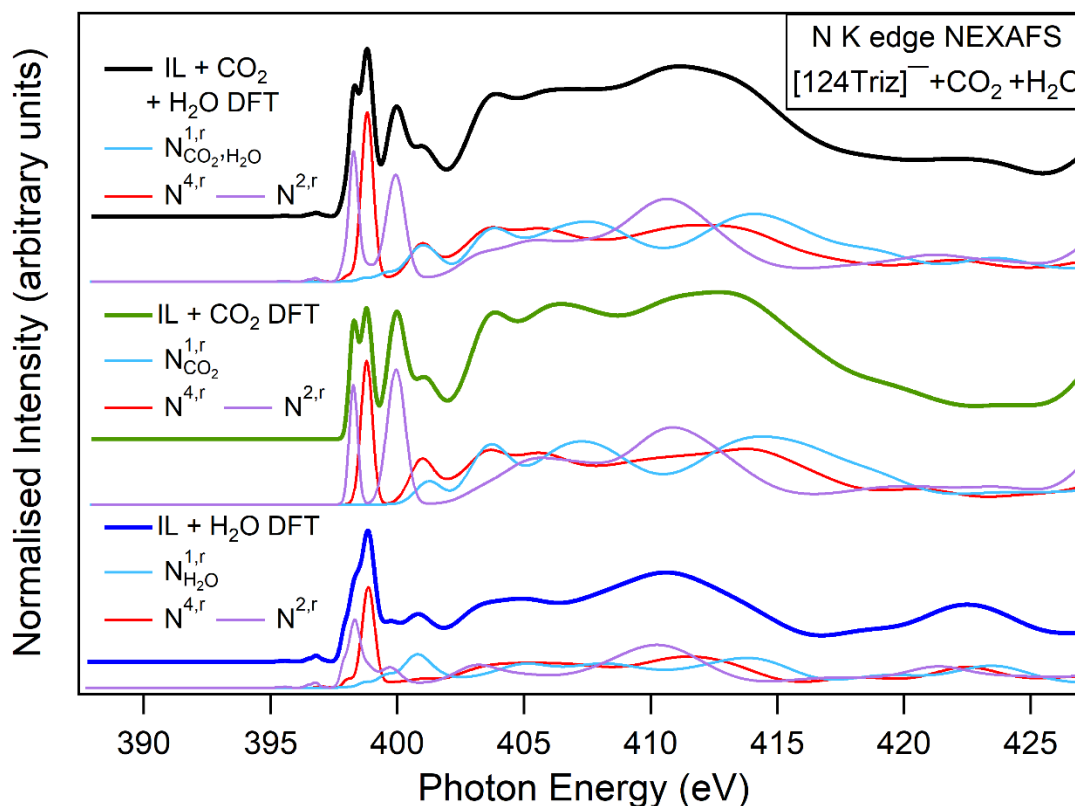
Figure 6.11. Simulated N K edge NEXAFS spectrum for $[P_{66614}][benzim]$ + CO_2 + H_2O. The final DFT spectrum (black) is the sum of the IL + CO_2 (green) and IL + H_2O (blue) spectra. Nitrogen atom labels are based on those used in Figure 6.1.

The unoccupied antibonding molecular orbitals for $[124Triz]^-$, $[124Triz]^-$ + H_2O and $[124Triz]^-$ + CO_2 are shown in Figure 6.12. These show the effect of the reaction between H_2O or CO_2 and the anion on the π^* and σ^* molecular orbitals as discussed in the NEXAFS study. The lowest unoccupied molecular orbital (LUMO), LUMO+1 and LUMO+2 are assigned to either the $1\pi^*$, $1\sigma^*$, $2\pi^*$ and $2\sigma^*$ antibonding orbitals. Using the LUMOs and DFT spectra we can assign the peaks in the experimental NEXAFS spectra in Figure 6.9 to specific transitions. In the as presented case the π^* peak at 398.3 eV is assigned to $N^{1,2,4} \rightarrow 1\pi^*$ (LUMO+2). When exposed to the gas mixture, the π^* peak at 398.3 eV is attributed to $N^{2,4} \rightarrow 1\pi^*$ (LUMO) transitions, respectively.
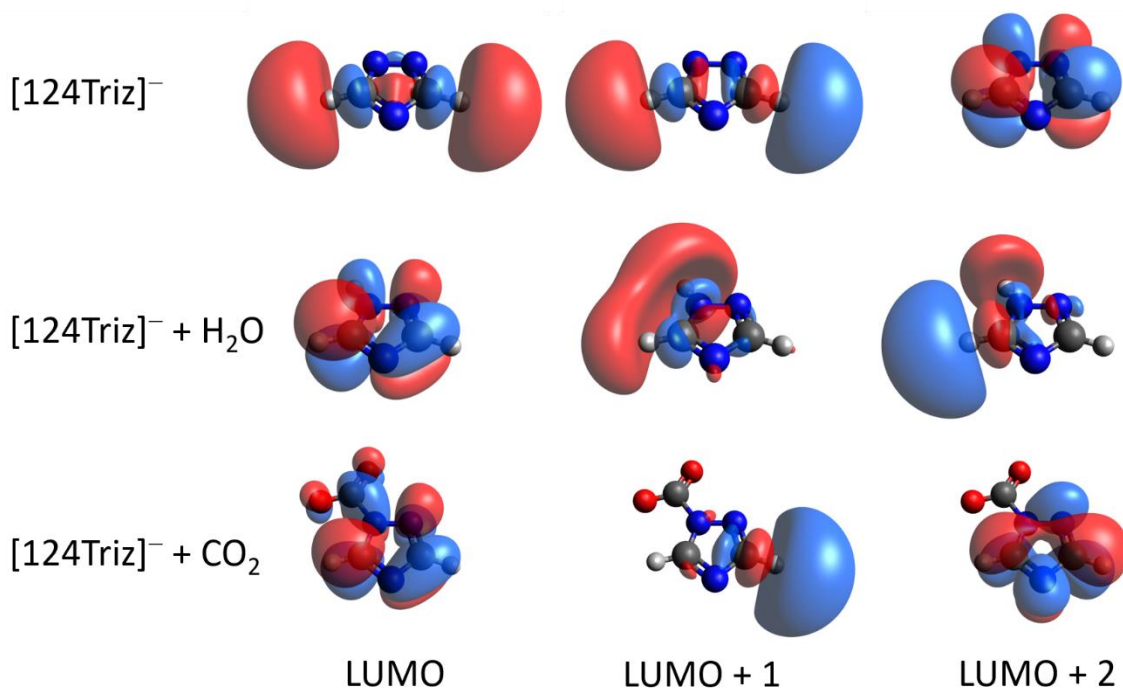
Figure 6.12. Lowest unoccupied molecular orbitals (LUMOs) of the isolated $[124Triz]^-$ anion (top row), $[124Triz]^- + H_2O$ (middle row) and $[124Triz]^- + CO_2$ (bottom row). The LUMOs are arranged in order of increasing energy (left to right).

6.6 Discussion and Conclusions

The competitive absorption between CO_2 and H_2O in electrosprayed thin films of the superbasic IL $[P_{66614}][124Triz]$ was characterised using *in situ* near-ambient pressure XPS. To the best of our knowledge, $[P_{66614}]^+$ is the largest IL ion to be successfully deposited via electrospray. Results suggest that both reacted and unreacted $[124Triz]^-$ anions reorder and diffuse through the IL thin film upon exposure to CO_2 and/or H_2O. Depth profiling XPS revealed that greater concentrations of CO_2-reacted species appear in the bulk layers of an electrosprayed IL thin film, reversibly forming carbamate on the anion. However, fewer CO_2-reacted species appear at the surface layers, and this reaction is irreversible. This is contrary to the fully reversible CO_2 reaction shown for bulk thicknesses in literature and suggests that irreversible absorption of CO_2 in thin films is largely attributed to reactions at the surface. H_2O vapour ad/absorbs in greater concentrations at the surface rather than the bulk but does not inhibit the absorption of CO_2.

Ordering of IL thin and thick films on solid surfaces has been investigated using a range of other experimental surface-sensitive techniques including angle-resolved NEXAFS [22,23], sum frequency generation (SFG) [24,25], neutron scattering [26,27], atomic force microscopy (AFM) [28], and X-ray reflectivity [29]. Our approach of using depth profiling XPS has proven to be another useful tool in analysing the interfacial behaviour of IL thin films on solid surfaces, as well as their interaction with gases. The study presented here is largely qualitative due to limitations of the technique, for example, the high levels of noise as a result of attenuation of photoelectrons through the gas combined with low counts from the use of thin films. Near-ambient pressure XPS techniques at synchrotron facilities are a relatively new development, so beamlines and endstations are still being optimised for these techniques. Additionally, further studies would be required to explore the effects of heating on the reversibility of reactions in electrosprayed IL thin films.

In our thin films, the IL/vacuum and IL/TiO$_2$ interfaces are likely to have a greater influence than they do in bulk ILs. The ordered structure of ILs at these interfaces is likely to influence specific interactions with CO$_2$/H$_2$O and affect how these gases diffuse from the vacuum interface into the bulk. N^1 and N^2 are equivalent in isolated anions, and we would still expect N^1 and N^2 to remain equivalent at the IL/vacuum interface, however, we expect different ordering at the interface compared to the bulk. The charged parts of the ions in imidazolium-based ILs have been found to form an underlayer near the IL/vacuum interface, with the alkyl chains of the cations pointing out towards the vacuum [30]. SBILs, such as those used in our experiment, have not been studied as widely in this context. In a previous XPS study of the related SBIL [P$_{66614}$][benzim], C 1s spectra showed a relatively more intense peak associated with the [benzim]$^-$ anion at grazing emission compared to normal emission, suggesting a higher concentration of [benzim]$^-$ anions at the IL/vacuum interface compared to the alkyl chains in the [P$_{66614}$]$^+$ cation [17]. This study provides evidence of SBILs forming an ordered structure at the IL/vacuum interface.

Fundamental studies of ILs at TiO$_2$ surfaces are sparse so there is very little literature for comparison [31]. Wagstaffe *et al.* studied 4 Å and 30 Å thick films of an imidazolium-based IL at the anatase TiO$_2$ (101) surface using XPS [23]. They found

that in both films the two nitrogen atoms in the imidazolium ring are chemically equivalent and were assigned to a single peak in the N 1s spectra. However, this shifted by 0.2 eV to a lower binding energy in the thinner film due to the interaction of the imidazolium cation with the TiO_2 surface. It is possible that the N^1 and N^2 nitrogen atoms in [124Triz]$^-$ may react differently with the TiO_2 surface, and this may in turn affect how these anions react with CO_2 or H_2O. If the anions were to react with the TiO_2 surface this could make them unavailable for reaction with CO_2/H_2O. A comprehensive computational study would be required to gain insights into these complex interfacial interactions.

The results presented here may have implications for thin film IL-based technologies. For example, thin films of ILs have been used to modify conventional supported catalysts, allowing the selectivity of the solid catalyst to be fine-tuned and improved (SCILL and SILP catalysis) [32]. A problem these technologies face is their sensitivity to changes at the IL-gas phase and IL-solid support interfaces [33]. Therefore, adsorption of gaseous/liquid reactants, products or contaminants in SCILL/SILP catalysts may induce changes in the surface structure of the IL thin film, potentially impacting the diffusion and selectivity for intermediate products in these catalysts [34].

6.7 References

[1]   Cole J, Henderson Z, Thomas A G, Castle C, Greer A J, Hardacre C, Scardamaglia M, Shavorskiy A and Syres K L 2023 In situ XPS of competitive CO_2/H_2O absorption in an ionic liquid *J. Phys. Mater.* **6** 045012

[2]   Rietzler F, Piermaier M, Deyko A, Steinrück H P and Maier F 2014 Electrospray ionization deposition of ultrathin ionic liquid films: [C_8C_1Im]Cl and [C_8C_1Im][Tf_2N] on Au(111) *Langmuir* **30** 1063–71

[3]   Hollingsworth N, Taylor S F R, Galante M T, Jacquemin J, Longo C, Holt K B, De Leeuw N H and Hardacre C 2015 CO_2 capture and electrochemical conversion using superbasic [P66614][124Triz] *Faraday Discuss.* **183** 389–400

[4]   Mercy M, Rebecca Taylor S F, Jacquemin J, Hardacre C, Bell R G and De Leeuw N H 2015 The addition of CO_2 to four superbase ionic liquids: a DFT study *Phys. Chem. Chem. Phys.* **17** 28674–82

[5]   Cuéllar-Franca R M, García-Gutiérrez P, Taylor S F R, Hardacre C and Azapagic A 2016 A novel methodology for assessing the environmental sustainability of ionic liquids used for CO_2 capture *Faraday Discuss.* **192** 283–301

[6]   Taylor S F R, McCrellis C, McStay C, Jacquemin J, Hardacre C, Mercy M, Bell R G and De Leeuw N H 2015 CO_2 capture in wet and dry superbase ionic liquids *J. Solution Chem.* **44** 511–27

[7]   Fairely N 2009 CasaXPS manual 2.3.15 *Casa Softw. Ltd* 1–177

[8]   Blundell R K and Licence P 2014 Quaternary ammonium and phosphonium based ionic liquids: A comparison of common anions *Phys. Chem. Chem. Phys.* **16** 15278–88

[9]   Henderson Z, Thomas A G, Wagstaffe M, Taylor S F R, Hardacre C and Syres K L 2019 Reversible reaction of CO_2 with superbasic ionic liquid [P66614][benzim] studied with in situ photoelectron spectroscopy *J. Phys. Chem. C* **123** 7134–41

[10]   Hollingsworth N, Taylor S F R, Galante M T, Jacquemin J, Longo C, Holt K B, de Leeuw N H and Hardacre C 2015 Reduction of Carbon Dioxide to Formate at Low Overpotential Using a Superbase Ionic Liquid *Angew. Chemie* **127** 14370–4

[11]   Lovelock K R J, Smith E F, Deyko A, Villar-Garcia I J, Licence P and Jones R G 2007 Water adsorption on a liquid surface *Chem. Commun.* 4866–8

[12]   Broderick A, Khalifa Y, Shiflett M B and Newberg J T 2017 Water at the Ionic Liquid-Gas Interface Examined by Ambient Pressure X-ray Photoelectron Spectroscopy *J. Phys. Chem. C* **121** 7337–43

[13]   Wang C, Luo X, Luo H, Jiang D, Li H and Dai S 2011 Tuning the basicity of ionic liquids for equimolar CO_2 capture *Angew. Chemie* **123** 5020–4

[14]   Zeng S, Zhang X, Bai L, Zhang X, Wang H, Wang J, Bao D, Li M, Liu X and Zhang S 2017 Ionic-Liquid-Based CO_2 Capture Systems: Structure, Interaction and Process *Chem. Rev.* **117** 9625–73

[15]   Syres K L, Thomas A G, Flavell W R, Spencer B F, Bondino F, Malvestuto M, Preobrajenski A and Grätzel M 2012 Adsorbate-induced modification of surface electronic structure: Pyrocatechol adsorption on the anatase TiO_2 (101) and rutile TiO_2 (110) surfaces *J. Phys. Chem. C* **116** 23515–25

[16]   Jackman M J, Thomas A G and Muryn C 2015 Photoelectron spectroscopy study of stoichiometric and reduced anatase TiO_2(101) surfaces: The effect of subsurface defects on water adsorption at near-ambient pressures *J. Phys. Chem. C* **119** 13682–90

[17]   Cole J, Henderson Z, Thomas A G, Compeán-González C L, Greer A J, Hardacre C, Venturini F, Garzon W Q, Ferrer P, Grinter D C, Held G and Syres K L 2021 Near-Ambient Pressure XPS and NEXAFS Study of a Superbasic Ionic Liquid with CO_2 *J. Phys. Chem. C* **125** 22778–85

[18]   Sorescu D C, Lee J, Al-Saidi W A and Jordan K D 2011 CO_2 adsorption on TiO_2(110) rutile: Insight from dispersion-corrected density functional theory calculations and scanning tunneling microscopy experiments *J. Chem. Phys.* **134** 1–12

[19]   Grinter D C, Graciani J, Palomino R M, Xu F, Waluyo I, Sanz J F, Senanayake S D and Rodriguez J A 2021 Adsorption and activation of CO_2 on $Pt/CeO_x/TiO_2$(110): Role of the Pt-CeOx interface *Surf. Sci.* **710** 1–8

[20]   Lewis T, Faubel M, Winter B and Hemminger J C 2011 CO_2 capture in amine-based aqueous solution: Role of the gas-solution interface *Angew. Chemie - Int. Ed.* **50** 10178–81

[21]   Lartey M, Meyer-Ilse J, Watkins J D, Roth E A, Bowser S, Kusuma V A, Damodaran K, Zhou X, Haranczyk M, Albenze E, Luebke D R, Hopkinson D, Kortright J B and Nulwala H B 2015 Branched isomeric 1,2,3-triazolium-based ionic liquids: New insight into structure-property relationships *Phys. Chem. Chem. Phys.* **17** 29834–43

[22]   Walsh J F, Dhariwal H S, Gutiérrez-Sosa A, Finetti P, Muryn C A, Brookes N B, Oldman R J and Thornton G 1998 Probing molecular orientation in corrosion inhibition via a NEXAFS study of benzotriazole and related molecules on Cu(100) *Surf. Sci.* **415** 423–32

[23]   Wagstaffe M, Jackman M J, Syres K L, Generalov A and Thomas A G 2016 Ionic Liquid Ordering at an Oxide Surface *ChemPhysChem* **17** 3430–4

[24]   Rivera-Rubero S and Baldelli S 2004 Influence of water on the surface of hydrophilic and hydrophobic room-temperature ionic liquids *J. Am. Chem. Soc.* **126** 11788–9

[25]   Baldelli S 2008 Surface structure at the ionic liquid-electrified metal interface *Acc. Chem. Res.* **41** 421–31

[26]   Bowers J, Vergara-Gutierrez M C and Webster J R P 2004 Surface Ordering of Amphiphilic Ionic Liquids *Langmuir* **20** 309–12

[27]   Bovio S, Podestà A, Lenardi C and Milani P 2009 Evidence of extended solidlike layering in [Bmim][NTf2] ionic liquid thin films at room-temperature *J. Phys. Chem. B* **113** 6600–3

[28]   Zhao W, Zhu M, Mo Y and Bai M 2009 Effect of anion on micro/nano-tribological properties of ultra-thin imidazolium ionic liquid films on silicon wafer *Colloids Surfaces A Physicochem. Eng. Asp.* **332** 78–83

[29]   Solutskin E, Ocko B M, Taman L, Kuzmenko I, Gog T and Deutsch M 2005 Surface layering in ionic liquids: An x-ray reflectivity study *J. Am. Chem. Soc.* **127** 7796–804

[30]   Lockett V, Sedev R, Bassell C and Ralston J 2008 Angle-resolved X-ray photoelectron spectroscopy of the surface of imidazolium ionic liquids *Phys. Chem. Chem. Phys.* **10** 1330–5

[31]   Cole J and Syres K L 2022 Ionic liquids on oxide surfaces *J. Phys. Condens. Matter* **34** 213002

[32]   Steinrück H P, Libuda J, Wasserscheid P, Cremer T, Kolbeck C, Laurin M, Maier F, Sobota M, Schulz P S and Stark M 2011 Surface science and model catalysis with ionic liquid-modified materials *Adv. Mater.* **23** 2571–87

[33]   Fehrmann R, Riisager A and Haumann M 2014 *Supported Ionic Liquids: Fundamentals and Applications* ed R Fehrmann, A Riisager and M Haumann (Weinheim, Germany: Wiley-VCH Verlag GmbH & Co. KGaA)

[34]   Steinrück H P and Wasserscheid P 2015 Ionic liquids in catalysis *Catal. Letters* **145** 380–97

Chapter 7. Probing Complex NO/CO$_2$ Interactions in [P$_{66614}$][Tetz] Using Near-Ambient Pressure Techniques

7.1 Introduction

Nitric oxide (NO) is one of the gases present alongside CO$_2$ in flue streams of fossil fuel-burning power plants. NO is an acidic gas and can degrade amine scrubbers, increasing their corrosivity and decreasing their lifetime for CO$_2$ capture [1]. SBILs do not degrade in the presence of NO, which makes them desirable carbon capture alternatives. However, a downside is that SBILs such as [P$_{66614}$][Tetz] and [P$_{66614}$][benzim] absorb NO and can do so irreversibly [2]. This can negatively impact the uptake of CO$_2$. It is therefore important to understand how NO competes for absorption with CO$_2$ in the SBIL. CO$_2$ capture in ILs is well documented but there are comparatively fewer studies investigating the absorption of NO in ILs.
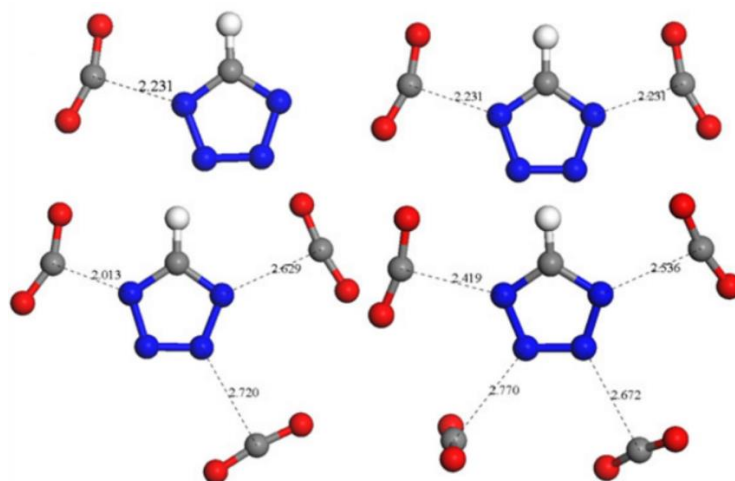
Figure 7.1. Multisite physical absorption of CO$_2$ with an isolated [Tetz]$^-$ anion. The distances between nitrogen atoms in the anion and carbon atoms in CO$_2$ are shown in units of Å. Reproduced from [3].

This chapter presents a study into the absorption of NO, CO_2 and a NO + CO_2 gas mixture in the SBIL [P_{66614}][Tetz]. [P_{66614}][Tetz] is capable of physically and chemically absorbing CO_2 and NO [4]. DFT calculations carried out by Yan-Hong *et al.* showed that interactions between CO_2 and the SBIL [P_{1114}][Tetz] can occur at multiple nitrogen sites in the [Tetz]$^-$ anion, as shown in Figure 7.1 [3]. They found that four CO_2 molecules can react with the isolated [Tetz]$^-$ anion. However, for the IL pair, [P_{1114}][Tetz], a maximum of three CO_2 molecules react at the anion because one of the bonding sites is occupied by hydrogen bonding with the cation.
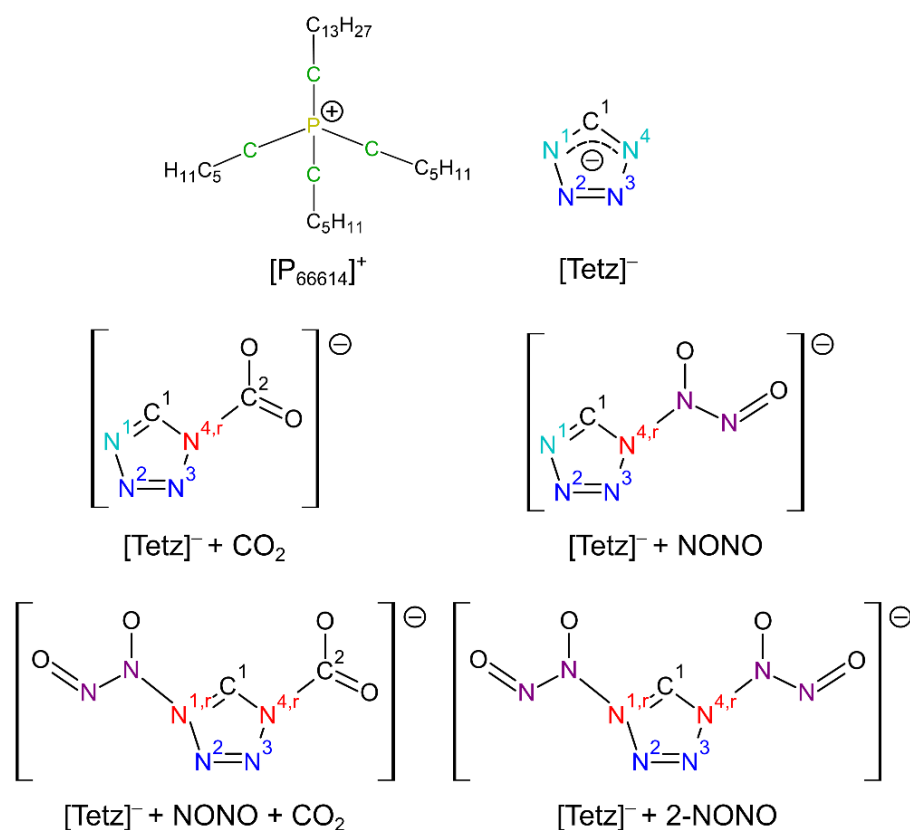
Figure 7.2. Chemical structure of the isolated [P_{66614}]$^+$ cation and [Tetz]$^-$ anion. In [P_{66614}]$^+$, C_{hetero} atoms are highlighted in green and $C_{aliphatic}$ in black. Various reactions schemes of [Tetz]$^-$ with CO_2 and/or NO are also shown. The colours of the nitrogen atoms in [Tetz]$^-$ denote four different chemical environments: N^1 and N^4 (light blue); $N^{2,3}$ (dark blue); $N^{1,r}$ and $N^{4,r}$ (red); NONO (purple).

A reaction scheme of [P_{66614}][Tetz] with CO_2, NO and a NO + CO_2 mixture is shown in Figure 7.2. Colours in this scheme highlight four different chemical environments

of nitrogen. Atoms N^2 and N^3 (dark blue) are chemically equivalent and remain in the same chemical environment after reaction with gas. N^1 and N^4 (light blue) are chemically equivalent before exposure to gas but separate into two environments upon reaction with gas. CO_2 reacts with the [Tetz]$^-$ anion at $N^{4,r}$ (red) and results in the formation of carbamate. Reaction with NO at $N^{4,r}$ forms NONOate (purple), $N^{4,r}$–(NO$^-$)–N=O. NO can react at multiple sites, for example [Tetz] + 2-NONO, in which NO is shown to react at both $N^{1,r}$ and $N^{4,r}$ in Figure 7.2. Since multisite bonding is largely based on physical interactions, we expect these are more likely to occur at higher pressures than those used in this study (3 mbar).

This chapter reports a depth profiling NAP-XPS and NEXAFS study into the absorption of CO_2 and NO in electrosprayed thin films of [P$_{66614}$][Tetz] on rutile TiO_2 (110). NEXAFS measurements are compared with computational NEXAFS spectra calculated using DFT. Quantum chemical simulations are used to visualise the unoccupied antibonding molecular orbitals to aid in assigning peaks in the NEXAFS spectra to specific electronic transitions. These results provide insights into how the orientation of IL molecules change upon exposure to gas, how absorption of gas changes with depth into the film, and the reversibility of reaction. Probing these interfacial interactions is important for understanding fundamental mechanisms of gas capture ILs. Results may also influence the performance of thin film IL-based technologies.

7.2 Experimental and Theoretical Methods

Measurements were carried out on the IL trihexyltetradecylphosphonium tetrazole ([P$_{66614}$][Tetz]) at the B07 beamline at Diamond Light Source. A thin film of [P$_{66614}$][Tetz] was deposited onto rutile TiO_2 (110) via electrospray deposition in vacuum using a Molecularspray UHV4 system. The preparation chamber had a base pressure of 1.5×10^{-9} mbar and a deposition pressure of 5.0×10^{-7} mbar. A 0.02 M [P$_{66614}$][Tetz]/ethanol solution was fed into the emitter capillary by a small backing pressure in the syringe. The emitter, syringe and tubing were cleaned prior to use by flushing with ethanol. 2.5 kV was applied to the emitter with respect to the grounded entrance capillary. The thickness of the electrosprayed thin film could not be calculated but is expected to be < 10 nm since the XPS Ti 2p signal from the TiO_2

substrate was still detected. Before depositing the IL, the rutile TiO_2 (110) surface was prepared in vacuum by cycles of Ar^+ sputtering and annealing to 700°C. Its cleanliness was confirmed using XPS survey scans.

Region	Photon energy (eV)	
	Surface ($E_{K,max}$ = 100 eV)	Bulk ($E_{K,max}$ = 600 eV)
Survey	1200	–
C 1s	390	890
N 1s	500	1000

Table 7.1 Photon energies used for depth profiling XPS. Bulk and surface sampling depths correspond to photon energies taken 100 and 600 eV above the binding energy of the region, respectively. These photon energies produce photoelectrons with maximum kinetic energies, $E_{K,max}$, of 100 and 600 eV, respectively.

NAP-XPS measurements were taken at different photon energies (summarised in Table 7.1) in order to probe the surface and bulk layers of the IL film. These have a sampling depth of 1.3 and 4.0 nm, respectively. To avoid beam damage and charging of the film, the sample was moved approximately 0.2 mm between scans to account for the beam size (90 μm × 60-100 μm). Competitive CO_2/NO absorption was investigated using NAP-XPS by exposing the IL to CO_2, NO, and a NO + CO_2 mixture, all at approximately 3 mbar. Following exposure to each of the gases, the chamber was evacuated and measurements were repeated to determine if gas absorption processes are reversible. The order of these exposure stages is given in Figure 7.3. All XPS peaks were fitted using 30:70 (Lorentzian:Gaussian) line shapes and a Shirley background, using the software CasaXPS [5]. The BE scale for all regions was calibrated to the alkyl C 1s signal at 285.0 eV [6]. All fitted peaks are quoted to ± 0.1 eV BE unless stated otherwise.
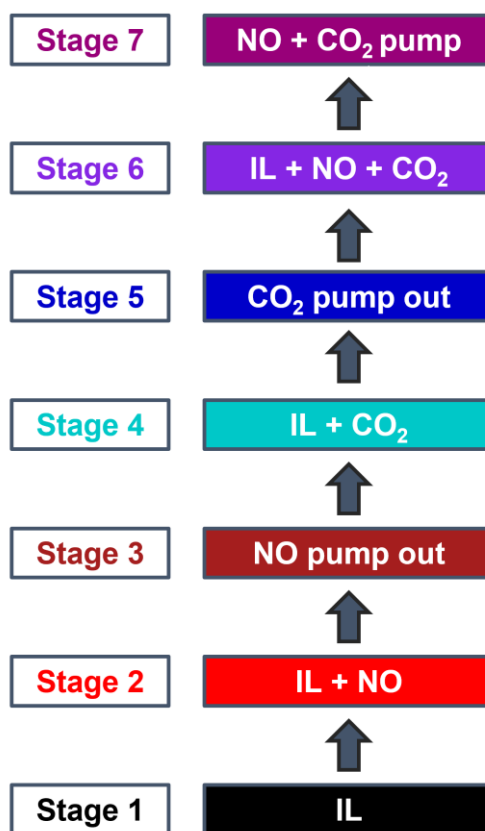
Figure 7.3. Exposure scheme for NAP-XPS measurements of $[P_{66614}]$[Tetz] exposed to CO_2 and NO gas. The pressures of the gases and gas mixture are approximately 3 mbar.

AEY C K edge and N K edge NEXAFS measurements were carried out at three X-ray incidence angles (the angle between the X-ray beam and the sample surface, θ): 43°, 53° and 63°. A wider range of angles could not be obtained due to difficulties in aligning the sample and analyser cone at extreme angles. Measurements were taken before and upon exposure to 3 mbar of CO_2, NO, and a NO + CO_2 mixture. The pressure was chosen by taking preliminary measurements and observing the signal-to-noise ratio. C K edge NEXAFS spectra were recorded over the range 280 to 310 eV by measuring the C Auger peak at a kinetic energy of 260 eV. N K edge NEXAFS spectra were recorded over the range 390 to 430 eV by measuring the N Auger peak at a kinetic energy of 375 eV. The NEXAFS spectra were intensity-normalised such that the step between 280 eV and 310 eV (for the C K edge), and between 390 eV and 430 eV (for the N K edge), is equal to unity. Spectra were normalised by division of the photon flux curve or gas phase signals as shown in Appendix B. NEXAFS results were compared with DFT simulations carried out using

the software StoBe-deMon [7]. Unoccupied molecular orbitals (MOs) were generated using ORCA and visualised in Avogadro [8–10]. Simulations were carried out in the same way as those discussed in Chapter 5. The orientation of [Tetz]⁻ anions was calculated by fitting the experimental π^* intensity taken at each θ value to the theoretical intensity plotted as a function of MO tilt angle α (see Figure 3.18 in Chapter 3). The theoretical intensity is calculated using the equations of Stöhr (Equations 3.6 – 3.8) [11]. The fitting was carried out using the software Igor Pro which uses a least squares method for the goodness of fit. Since π^* MOs point out perpendicular from the plane of the [Tetz]⁻ ring, the orientation of [Tetz]⁻ is $90° - \alpha$ with respect to the surface normal.

7.3 Angle-Resolved XPS
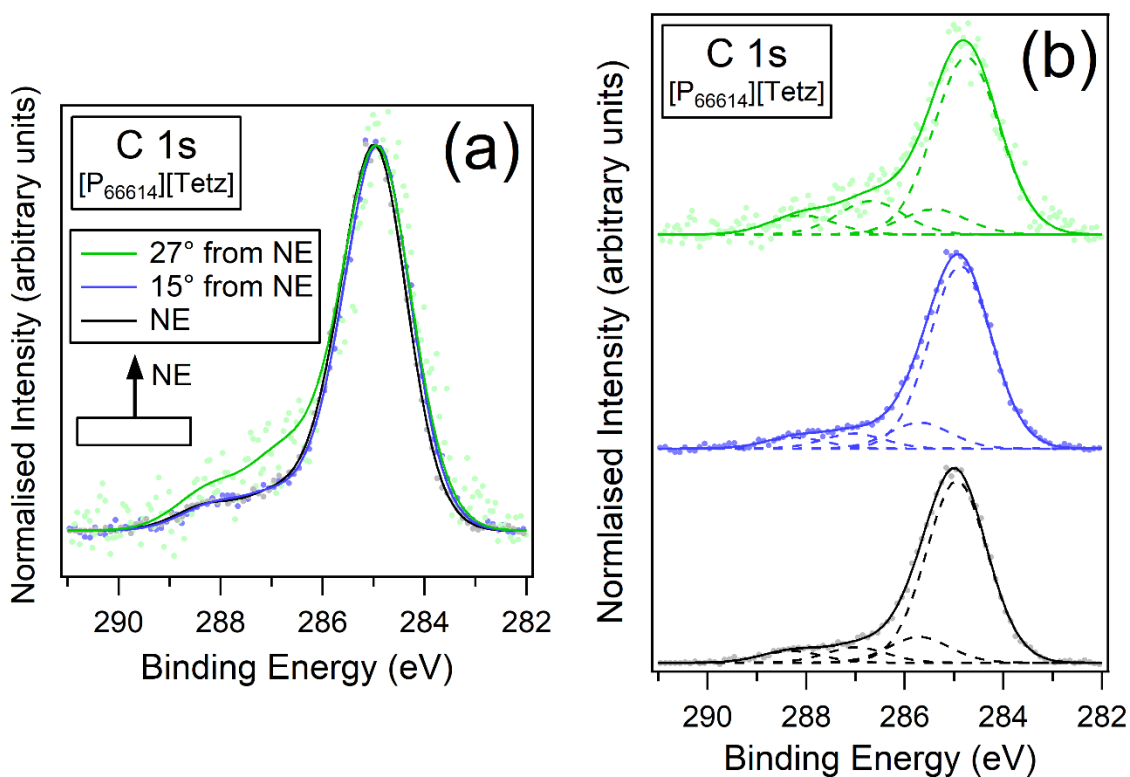
Figure 7.4. C 1s XPS of [P$_{66614}$][Tetz] recorded at a photon energy of 390 eV. Measurements were taken at normal emission (NE), 15° from NE and 27° from NE. These correspond to sampling depths of 1.34, 1.29 and 1.19 nm, respectively. (a) shows the overlayed spectra and (b) shows their fitted components.

Angle resolved XPS measurements were taken over the C 1s region for [P$_{66614}$][Tetz] as presented (Figure 7.4). Spectra were normalised to the main peak at 285.0 eV. Measurements were taken at normal emission (NE) which detects photoelectrons escaping normal from the surface. Measurements were also taken 15° from NE and 27° from NE at a photon energy of 390 eV (maximum photoelectron kinetic energy $E_{K,max}$ = 100 eV). These correspond to sampling depths of 1.34, 1.29 and 1.19 nm, respectively. The sampling depths were calculated as $3\lambda \cos(\theta_{em})$ where θ_{em} is the emission angle with respect to the surface normal and λ is the IMFP of [P$_{666614}$][Tetz]. The IMPF of [P$_{66614}$][Tetz] was calculated to be 0.45 nm for electrons with $E_{K,max}$ = 100 eV using Equation 3.15 in Chapter 3 (where the molecular weight and density of [P$_{66614}$][Tetz] are 550.9 g/mol and 0.90 g/cm^3 respectively).

The C 1s peak can be fitted with four components (summary of XPS fittings are shown in Table 7.2). The first two components occur at BEs of 285.0 and 285.8 eV. These are attributed to the two environments of carbon in [P$_{66614}$]$^+$, C$_{aliphatic}$ and C$_{hetero}$, respectively (see Figure 7.2) [6]. The component at 287.0 eV is assigned to C^1 in [Tetz]$^-$ (C–N bonds). These three components are attributed to species inherent to [P$_{66614}$][Tetz] and appear in all following C 1s spectra. The small component at 288.3 eV is believed to originate from physical interactions between residual gases in the chamber and either the carbon atom in [Tetz]$^-$ (C^1) or the TiO$_2$ substrate. The gas reaction peak at 288.3 eV and the C^1 peak at 287.0 eV are most intense at the surface-sensitive measurement θ_{em} = 27°. Since the anions are responsible for reaction with gas, this may indicate an accumulation of irreversibly reacted gases such as water at the surface.

7.4 Depth Profiling NAP-XPS of [P$_{66614}$][Tetz]

The angle resolved XPS spectra already provide some insight into the location of species with depth. Further depth profiling XPS studies were carried out by probing the IL with X-rays of different photon energies (summarised in Table 7.1). The surface and bulk sampling depths probe 1.3 and 4.0 nm into the IL film, respectively (calculated using Equations 3.2 and 3.15). The BEs of components fitted to the C 1s and N 1s peaks are shown in Table 7.2 alongside their assignments.

Region	Binding Energy (eV) (± 0.1 eV)	Assignment
C 1s	285.0	$C_{aliphatic}$
	285.8	C_{hetero}
	$287.0 \xrightarrow{NO} 286.8 \xrightarrow{CO_2,surf} 287.2$	C^1 unreacted
	288.3	C^1-NO (C^1-H_2O in Stage 1)
	289.0	Carbamate ($N^{4,r}-C^2OO^-$)
N 1s	397.3	Ti–N
	398.4 (± 0.2 eV)	N^1 (N–C–N)
	399.3	$N^{2,3}$ (N=N)
	400.5	$N^{4,r}$
	400.8	$N^{4,r} + H_2O$
	402.0	NONO

Table 7.2. XPS peak assignments for the C 1s regions over the 7 exposure stages. $\xrightarrow{NO}$ denotes chemical shifts at the surface and bulk sampling depths due to the irreversible absorption of NO. $\xrightarrow{CO_2,surf}$ denotes chemical shifts at the surface sampling depth due to the reversible absorption of CO_2 and irreversible absorption of the NO + CO_2 mixture.

7.4.1 C 1s

C 1s spectra taken before and during the gas exposure stages (Stages 1, 2, 4, 6) are shown in Figure 7.5. The fitted components of the C 1s peak are shown for the surface and bulk sampling depths. For the as presented IL in Stage 1, there is little change in the intensity of the four components with sampling depth except for a slightly more intense C^1 peak for the bulk sampling depth.

Exposing the IL to NO in Stage 2 results in a higher intensity reaction peak at 288.3 eV. C^1 does not directly participate in the formation of NONOate, however, the increase in the reaction peak intensity could be due to physical interactions between C^1 atoms and NO, resulting in a "reacted" C^1 peak with higher BE (C^1-NO). This reaction peak appears at both sampling depths but is more intense in the bulk layers. This would suggest there is a greater concentration of NO species in the deeper layers of the IL film. Additionally, the unreacted C^1 component shifts down to 286.8

eV and is more intense when probed at the bulk sampling depth. This indicates an increase in concentration of anions in the deeper layers of the IL.
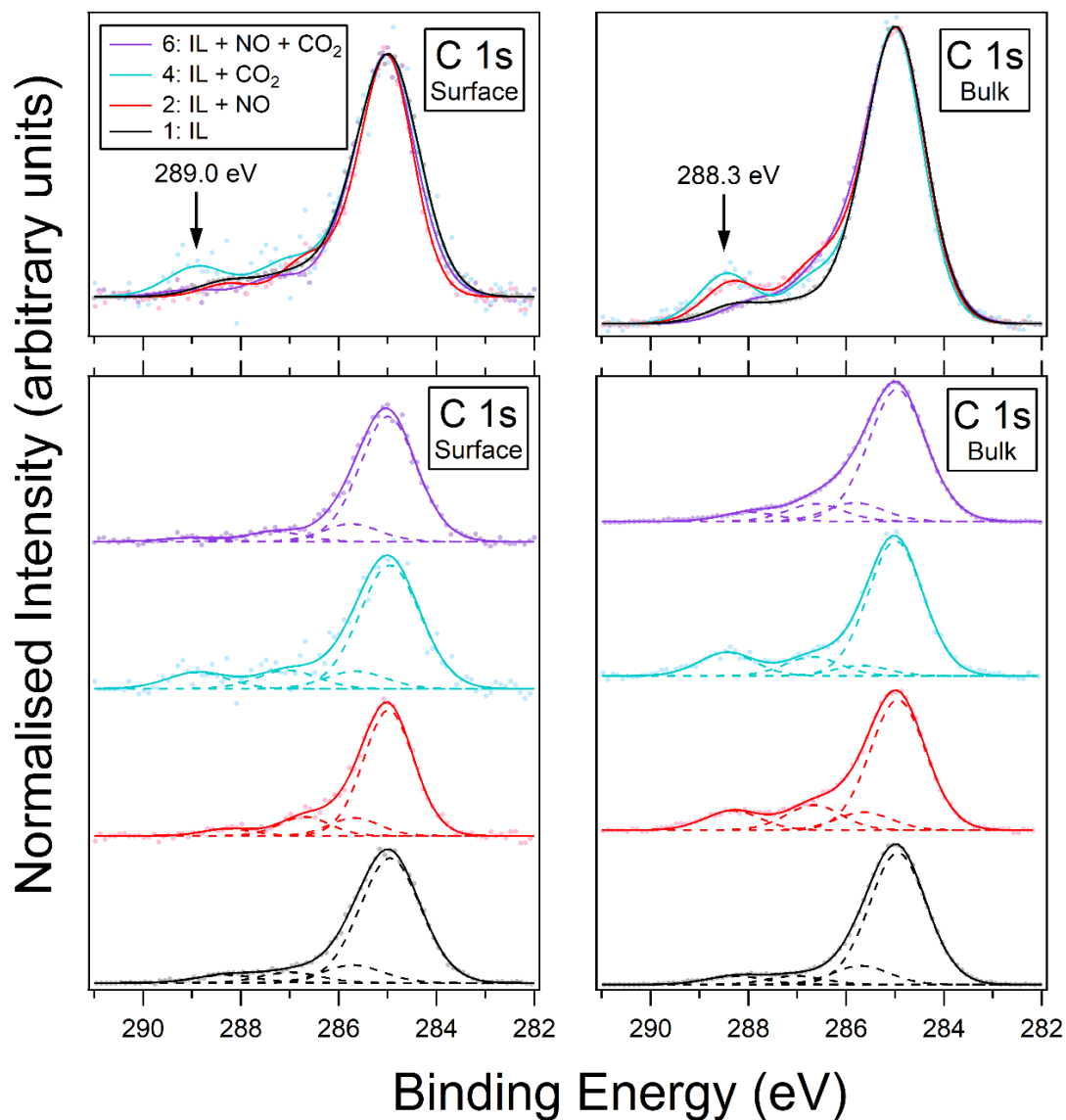
Figure 7.5. C 1s XPS of $[P_{66614}][Tetz]$ taken over 4 exposure stages: IL (1), IL + NO (2), IL + CO$_2$ (4), IL + NO + CO$_2$ (6). Measurements were recorded at a photon energy of 390 eV and 890 eV, corresponding to surface (1.3 nm) and bulk (4.0 nm) sampling depths, respectively.

In the NO pump out stage (Stage 3, shown in Figure 7.6) the reaction peak at 288.3 eV is still present at both sampling depths, showing irreversible NO absorption. When the IL is exposed to CO$_2$ in Stage 4, the reaction peak shifts in BE to 289.0 eV at the surface sampling depth but remains at 288.3 eV in the bulk (peaks

highlighted in Figure 7.5). These can be attributed to carbamate ($N^{4,r}-C^2OO^-$) and C^1-NO, respectively, and indicates that CO_2 primarily reacts at the surface while irreversibly reacted NO remains in the bulk. The reaction peaks are prominent for both the surface and bulk sampling depths. Greer *et al.* have also found that NO absorbs irreversibly in the similar SBIL [P_{66614}][benzim] using mass spectrometry [2]. They found that although NO reacts irreversibly, it did not significantly affect the uptake of CO_2. Their experiment was carried out using higher gas pressure (1 bar) containing 0.2 vol % NO and 14 vol % CO_2 in Ar (to simulate flue gas composition). Our results show that the presence of irreversibly absorbed NO inhibits CO_2 absorption in the deeper layers of the IL but not at the surface. The reason why we only see CO_2 reaction at the surface may be due to the higher concentration of NO compared to CO_2 (approximately equal number of NO and CO_2 molecules) and lower pressure (3 mbar) of the gas mixture compared to that used by Greer. When our IL is exposed to CO_2 there is also a shift in the C^1 peak to a higher BE of 287.0 eV at the surface, while C^1 remains at 286.8 eV in the bulk.

After pumping out CO_2 in Stage 5 (Figure 7.6), the surface carbamate peak at 289.0 eV disappears in place of a C^1-NO reaction peak at 288.3 eV. The C^1-NO peak remains at 288.3 eV at the bulk sampling depth between Stages 4 and 5. This behaviour suggests that CO_2 reversibly reacts at the surface and the irreversibly absorbed NO in the bulk redistributes through the IL layers after CO_2 is removed. Greer *et al.* found that it took as long as 72 hours to saturate the SBIL [P_{66614}][benzim] with NO, while only 15 minutes were required to saturate the IL with CO_2 [2]. The time between the NO pump out stage and CO_2 pump out stage in our experiment was about 18 hours, therefore, it is likely that not enough time was allowed for the NO to fully desorb. The shifted C^1 peak at the surface (287.0 eV) returns to 286.8 eV after CO_2 is pumped out which shows further evidence of reversible CO_2 absorption.

When the IL is exposed to the NO + CO_2 gas mixture in Stage 6, the carbamate peak at 289.0 eV returns at the surface but has a low intensity (and the C^1 peak shifts again to 287.2 eV). The C^1-NO peak remains at 288.3 eV in the bulk. These gas reaction peaks are small in both sampling depths. This is an unexpected result and

difficult to explain. It could imply that when the two gases compete for absorption it results in a lower uptake of both gases compared to the uptake of the gases individually. After the final pump out, the reaction peaks appear to be lower intensity than the other pump out stages.
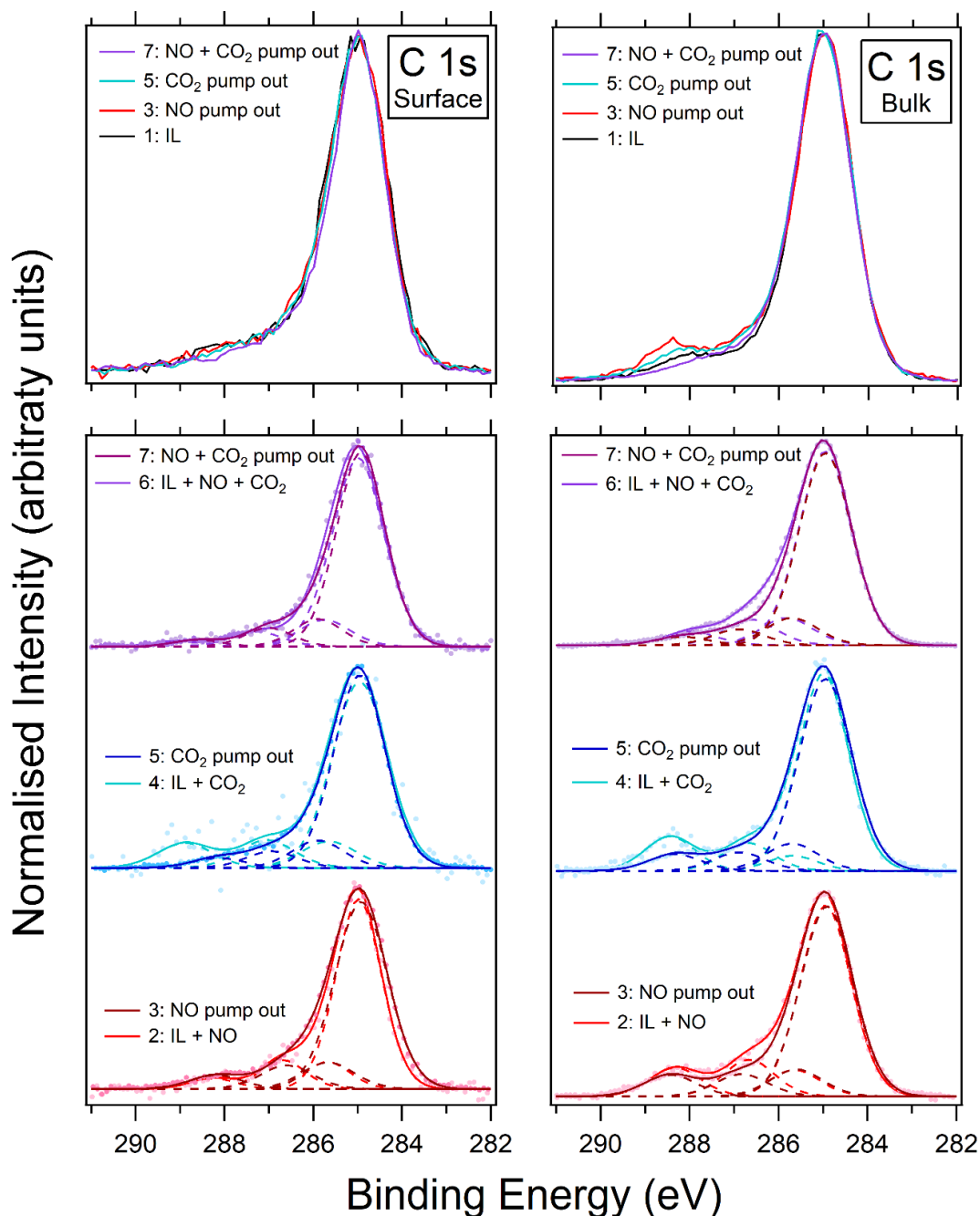
Figure 7.6. C 1s XPS of [P_{66614}][Tetz] during the gas exposure and pump out stages. Measurements were recorded at a photon energy of 390 eV and 890 eV, corresponding to surface (1.3 nm) and bulk (4.0 nm) sampling depths, respectively.

To summarise these results, the absorption of NO in [P$_{66614}$][Tetz] is not fully reversible and occurs primarily in the bulk. Following NO exposure and pump out, CO$_2$ only absorbs at the surface but does so reversibly. CO$_2$ absorption in [P$_{66614}$][Tetz] shows different behaviour to [P$_{66614}$][124Triz] discussed in Chapter 6. In [P$_{66614}$][124Triz] more CO$_2$ absorption occurred in the bulk of the IL, and this absorption was largely reversible. Less CO$_2$ absorbed in the surface layers of [P$_{66614}$][124Triz] and this absorption was irreversible. The difference in behaviour could be due to the different structure of the anions and/or to the presence of irreversibly reacted NO in the bulk layers of the [P$_{66614}$][Tetz] film before it was exposed to CO$_2$. If we had exposed [P$_{66614}$][Tetz] to CO$_2$ first, the result might have been different. This would make an interesting further study.

7.4.2 N 1s

N 1s spectra taken before and during the three gas exposure stages are shown in Figure 7.7. Spectra are shown only for the bulk sampling depth as those taken at the surface sampling depth were too weak to fit components to. The N 1s spectra were normalised to the total peak area centred around 399 eV. The peak for the electrosprayed IL in Stage 1 was fitted with four components (summarised in Table 7.2). The component at 397.3 eV is attributed to Ti–N, reactions between the anion and TiO$_2$ surface. This peak is only visible in Stage 1, suggesting that measurements were taken on a particularly thin part of the film in this stage. The component at 398.6 eV is attributed to N^1 and N^4 in the unreacted anion, as well as the chemically equivalent N^1 in the reacted anion since there is a small reaction peak at 400.8 eV (N^{4,r}). This could be due to reactions with trace amounts of residual water in the chamber [12,13].
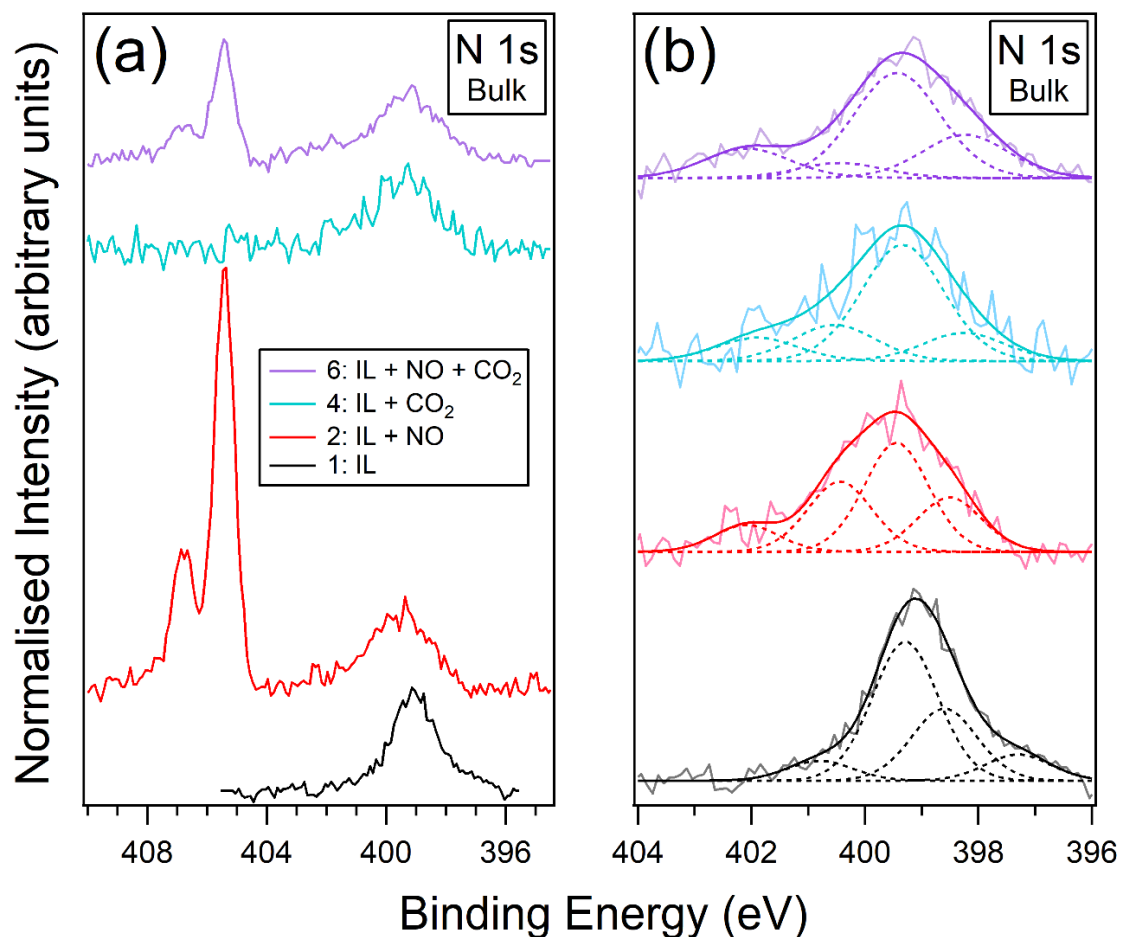
Figure 7.7. N 1s XPS of $[P_{66614}][Tetz]$ over 4 exposure stages: IL, IL + NO, IL + CO_2, IL + NO + CO_2 (a). Fitted components over a narrower BE range are shown for the same stages (b). Measurements were recorded at a photon energy of 1000 eV, corresponding to a bulk sampling depth (4.0 nm).

In the gas exposure stages IL + NO, IL + CO_2, and IL + NO + CO_2, the N 1s peak is fitted with components at 398.4 (± 0.2 eV), 399.3, 400.5 and 402.0 eV. These are attributed to N^1, $N^{2,3}$, $N^{4,r}$ and NONOate, respectively. We assume only NO absorption occurs in the bulk here since the C 1s spectra in Figures 7.5 and 7.6 showed that CO_2 only reacts at the surface. Stages 2 and 6 have a gas phase NO split peak with features at 405.4 and 406.8 eV. This characteristic split peak has a 1.4 eV separation as found in other gas phase studies in the literature [14].

In the IL + CO_2 stage, the 402.0 eV reaction peak is attributed to irreversibly absorbed NO. This corroborates evidence of irreversible NO absorption found in C

1s spectra (Figure 7.6) and in the N 1s pump out stages shown in Figure 7.8. This implies that CO_2 is incapable of replacing the irreversibly absorbed NO in the bulk. The NONOate peak at 402.0 eV remains at a similar relative area for the IL + NO and IL + CO_2 stages, while the relative area of the $N^{4,r}$ peak reduces between these stages. The reduction in this peak is likely due to a greater concentration of CO_2-reacted anions at the surface when exposed to CO_2. Note that the $N^{4,r}$ carbamate peak occurs at 401.5 eV here, however, the carbamate peak occurs at 401.1 eV in [P$_{66614}$][benzim] in Chapter 5 and 402.0 eV for [P$_{66614}$][124Triz] in Chapter 6. The difference in BE of the carbamate peak across the three ILs is likely due to their different structure.
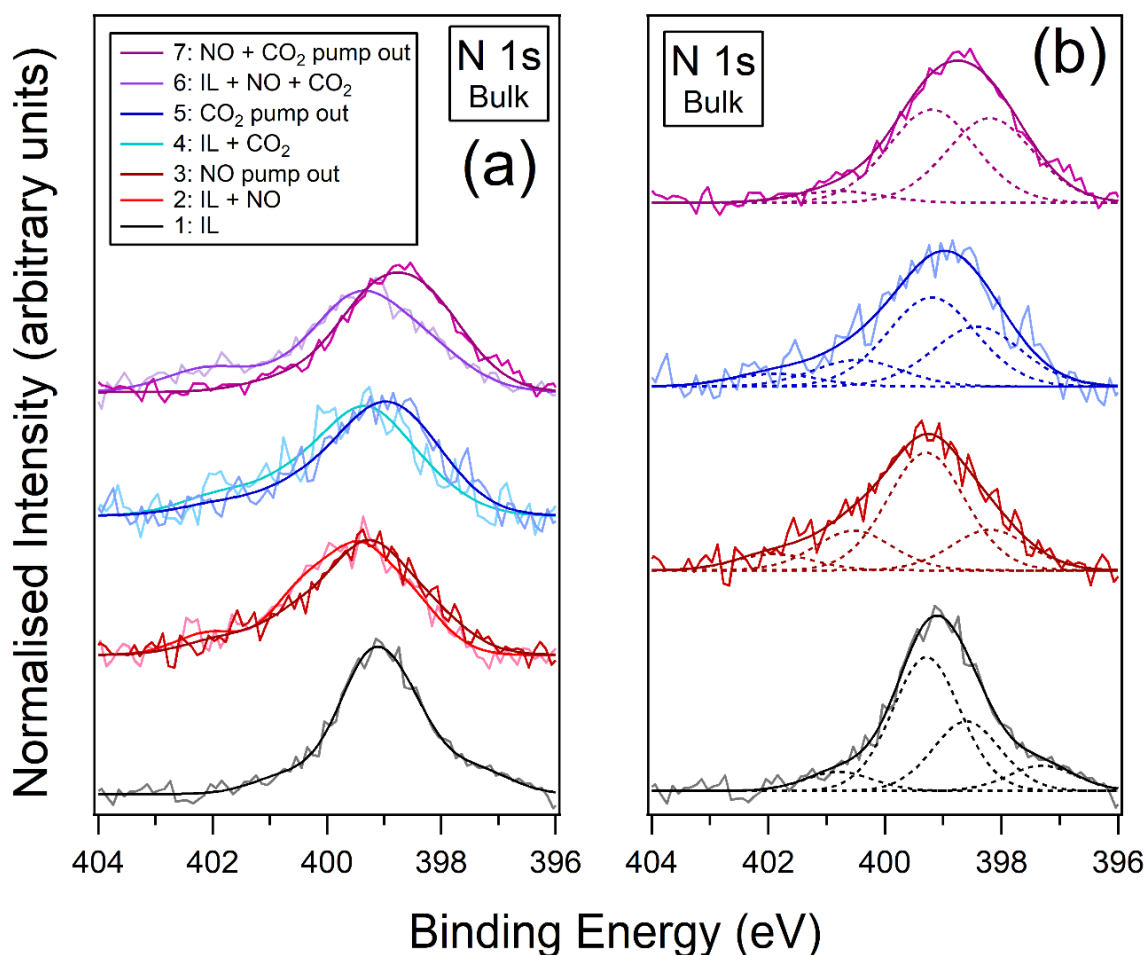
Figure 7.8. Comparison of N 1s XPS spectra of [P$_{66614}$][Tetz] taken during the gas pump out and exposure stages (a). Fitted components are shown for the pump out stages (b). Measurements were recorded at a photon energy of 1000 eV, corresponding to a bulk sampling depth (4.0 nm).

The N 1s pump out stages are shown in Figure 7.8 and are fitted with the same four components. Pumping out the gas in Stages 3 and 5 does not result in a reduction in the 402.0 eV NONOate peak. This peak only disappears after the final NO + CO_2 gas mixture pump out stage. The reason for this is not clear. The fitted components get slightly broader when the IL is exposed to CO_2 and the NO + CO_2 mixture. This suggests that there may be more chemical environments present that cannot be resolved due to the noisy nature of the spectra.

7.5 Experimental and DFT NEXAFS of [P$_{66614}$][Tetz]

C K edge NEXAFS measurements of the electrosprayed [P$_{66614}$][Tetz] thin film are shown in Figure 7.9. At each angle θ there are π^* peaks at 284.7 and 288.2 eV and a σ^* peak at 291.7 eV. Since there is only one carbon atom in [Tetz]$^-$, C^1, π^* resonances are attributed to $C^1 \rightarrow \pi^*$ transitions. The carbon atoms in [P$_{66614}$]$^+$ are part of long alkyl chains with no π bonds and therefore do not contribute to these π^* transitions. The simulated C^1 spectrum is labelled as "DFT" in Figure 7.9. It has good agreement with the experimental spectra, showing peaks at 284.7, 288.4, and 290.9 eV, respectively. Comparing the change in relative intensity of the experimental π^* peak at 284.7 eV to the σ^* peak at 291.7 eV for the three angles of incidence θ gives an indication of the orientation of the anion. The π^*/σ^* intensity ratio is maximum for $\theta = 53°$ (followed by $\theta = 63°$). Since resonances are maximised when the electric field vector is parallel to the maximum orbital amplitude of the π^* MO, results suggests that the plane of the ring in the [Tetz]$^-$ anion is oriented upright, away from the surface, rather than lying flat on the surface. This agrees with our results from Chapter 5 which indicated that anions in [P$_{66614}$][benzim] also orient upright from the surface [12]. The tilt angle of the [Tetz]$^-$ anions was calculated using the equations of Stöhr as discussed above [11]. Calculations give an orbital tilt angle of $\alpha = 80° \pm 3°$. The plane of the ring of the [Tetz]$^-$ anions are therefore oriented 10° ± 3° from the surface normal before exposure to gas.
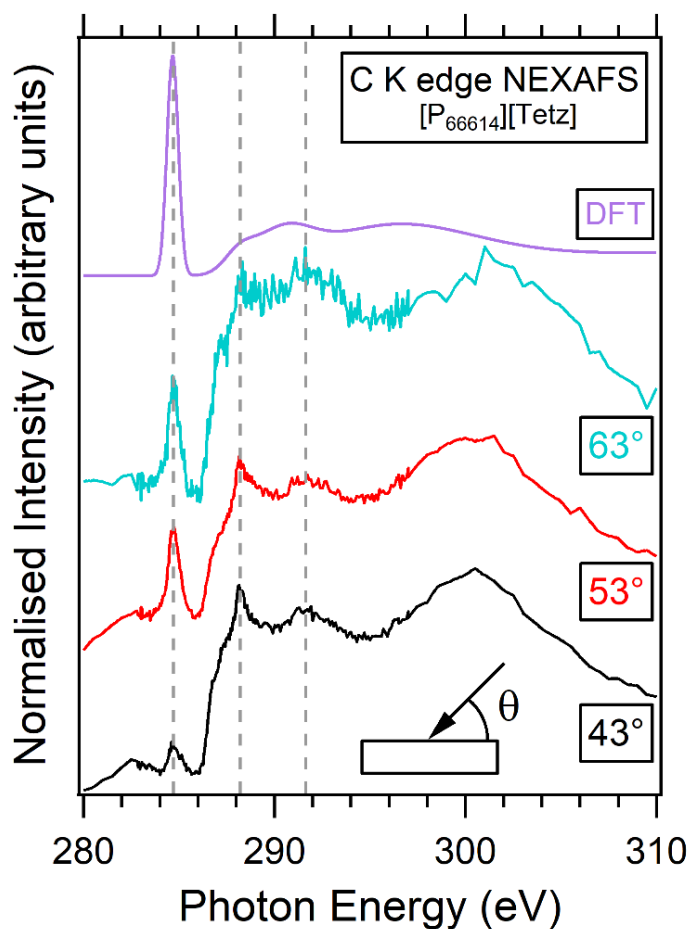
Figure 7.9. AEY C K edge NEXAFS of [P$_{66614}$][Tetz] taken at three X-ray angles of incidence (θ) from the surface. Vertical dashed lines highlight common peaks in the experimental spectra. These are compared to the theoretical NEXAFS spectrum labelled DFT.

The lowest unoccupied molecular orbitals (LUMOs) of the isolated [Tetz]⁻ anion are shown in Figure 7.10. The LUMO, LUMO+1 and LUMO+2 orbitals are similar to those calculated for [P$_{66614}$][benzim] in Chapter 5 as well as those of imidazole [15]. LUMO, LUMO+1 and LUMO+2 orbitals are assigned as 1σ*, 1π* and 2π* orbitals, respectively. The π* peaks at 284.7 and 288.4 eV can therefore be assigned as C^1 → 1π* (LUMO+1) and C^1 → 2π* (LUMO+2) transitions, respectively. The C^1 → 1σ* transition is weak and cannot be resolved in this spectrum.
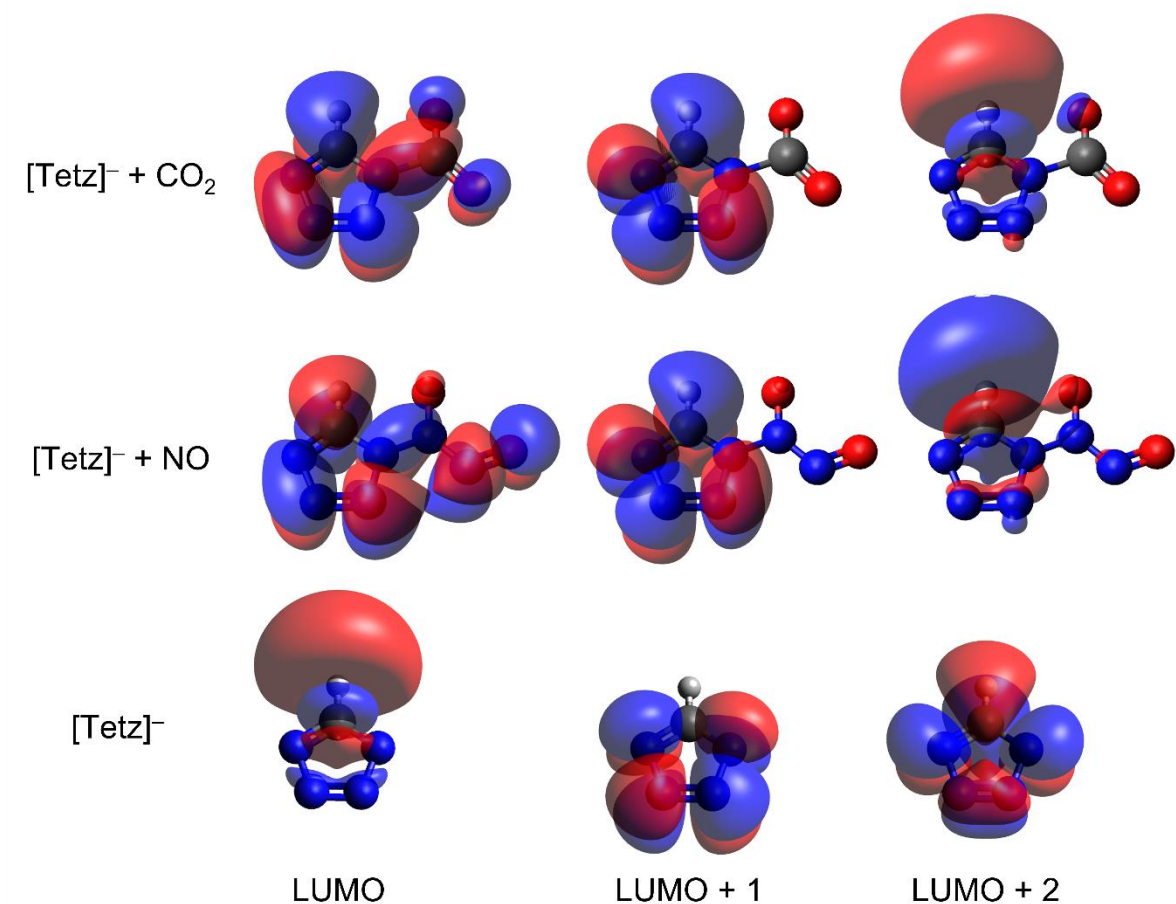
Figure 7.10. Lowest unoccupied molecular orbitals (LUMOs) of the isolated [Tetz]⁻ anion, [Tetz]⁻ + NO and [Tetz]⁻ + CO₂. The LUMOs are either π^* or σ^* antibonding unoccupied molecular orbitals.

In the N K edge spectra (Figure 7.11) there are no discernible π^* peaks. It is likely that the IL film is too thin to generate a significant N K edge signal compared to the C K edge due to the lower cross section of N to C. Alternatively, this could be due to beam damage since the NEXAFS spectra take longer than XPS measurements. N K edge NEXAFS spectra in all following exposure stages have similar high levels of noise and are therefore not discussed further.
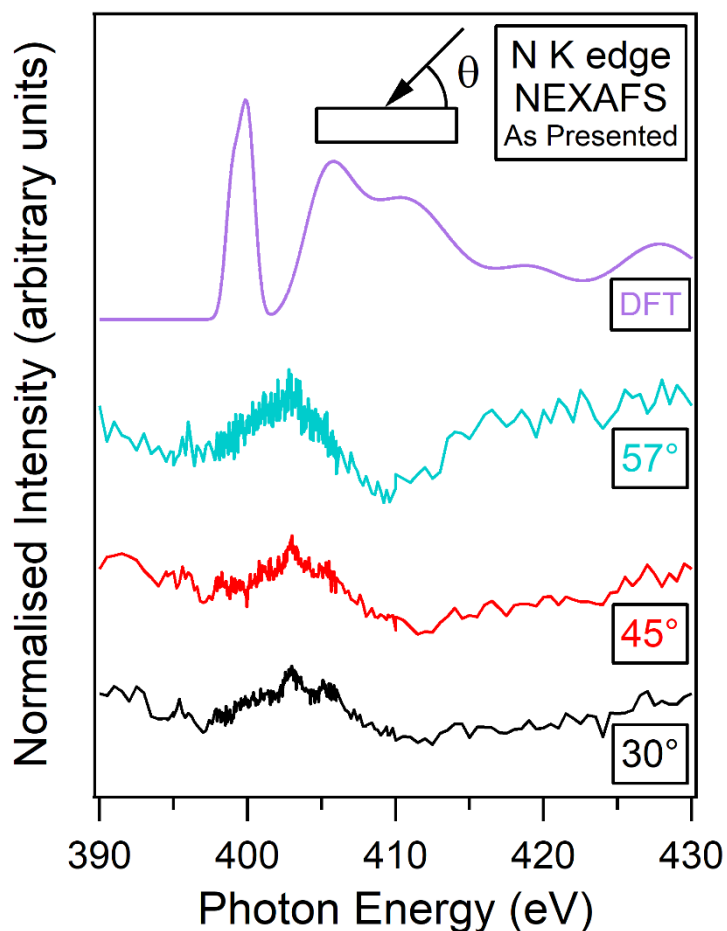
Figure 7.11. AEY N K edge [P_{66614}][Tetz] taken at three X-ray angles of incidence (θ) from the surface. The electrosprayed film appears to be too thin to produce a significant signal.

The C K edge NEXAFS of the IL exposed to 3 mbar NO (Figure 7.12) has π* peaks at 284.8 and 288.1 eV and a σ* peak at 292.5 eV. The π* peaks are at similar photon energies to those in the as presented electrosprayed IL stage. Using the LUMOs in Figure 7.10 the π* peak at 284.8 eV is attributed to C^1 → 1π* (LUMO) transitions and the 288.1 eV π* peak is assigned to C^1 → 2π* (LUMO+1) transitions. The 284.8 eV π* peak is strongest at 53°, followed by 43°. This indicates that the plane of the ring in the anions orients closer to the substrate surface compared to the pre-exposure case. This agrees with Stöhr calculations which show that the anion ring orients 37° ± 3° from the surface normal upon exposure to NO. A change in tilt angle towards the surface upon exposure to NO corroborates with results from Chapter 5 which showed reordering of [benzim]⁻ anions towards the surface upon exposure to gas (CO_2). XPS results in Figure 7.5 showed a greater concentration of NO-reacted

anions in the deeper layers of the IL film compared to the surface. Results here may suggest that the reorientation of anions upon exposure to NO is coupled with their diffusion into the deeper layers.
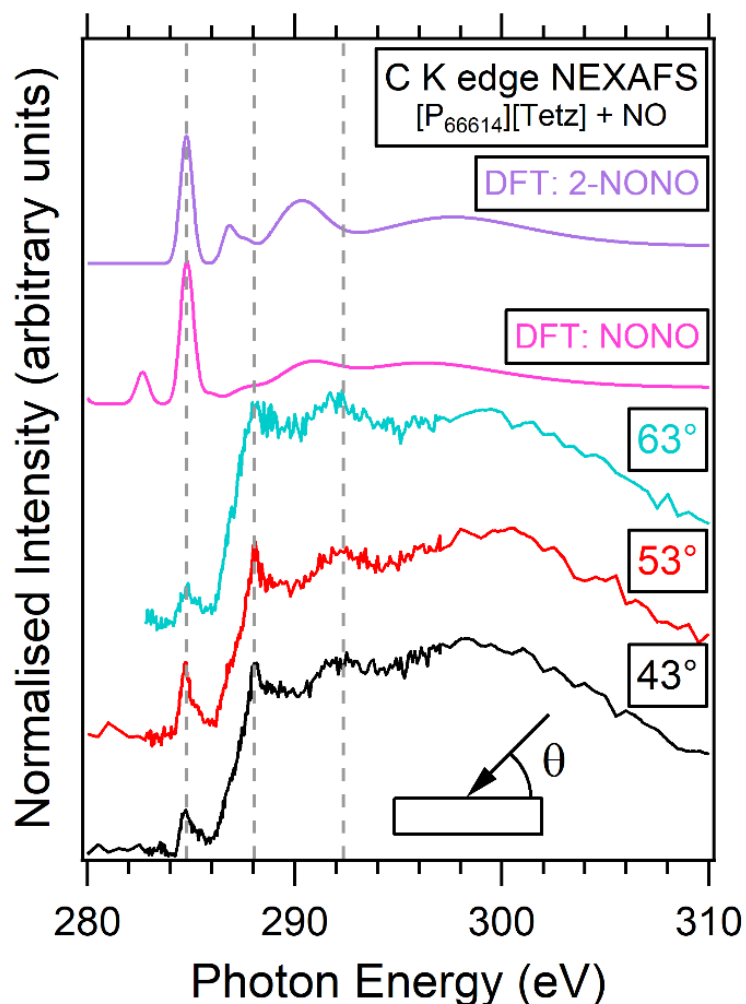
Figure 7.12. AEY C K edge NEXAFS of [P$_{66614}$][Tetz] + 3 mbar NO taken at three X-ray angles of incidence (θ) from the surface. Vertical dashed lines highlight common peaks in the experimental spectra. These are compared to theoretical NEXAFS spectra in two absorption regimes, [Tetz]$^-$–NONO and [Tetz]$^-$–2–NONO.

The experimental IL + NO C K edge NEXAFS spectra in Figure 7.12 are compared to theoretical spectra. These are modelled on either single or multiple site bonding: [Tetz]$^-$–NONO and [Tetz]$^-$–2–NONO, respectively. There is little agreement between the experimental spectra and the two theoretical DFT spectra. As discussed above, the reaction between [P$_{66614}$][Tetz] and NO is complex and involves many possible physical interactions between the IL and NO. The models used here to generate the

DFT spectra are probably too simple to account for the complex nature of these interactions.
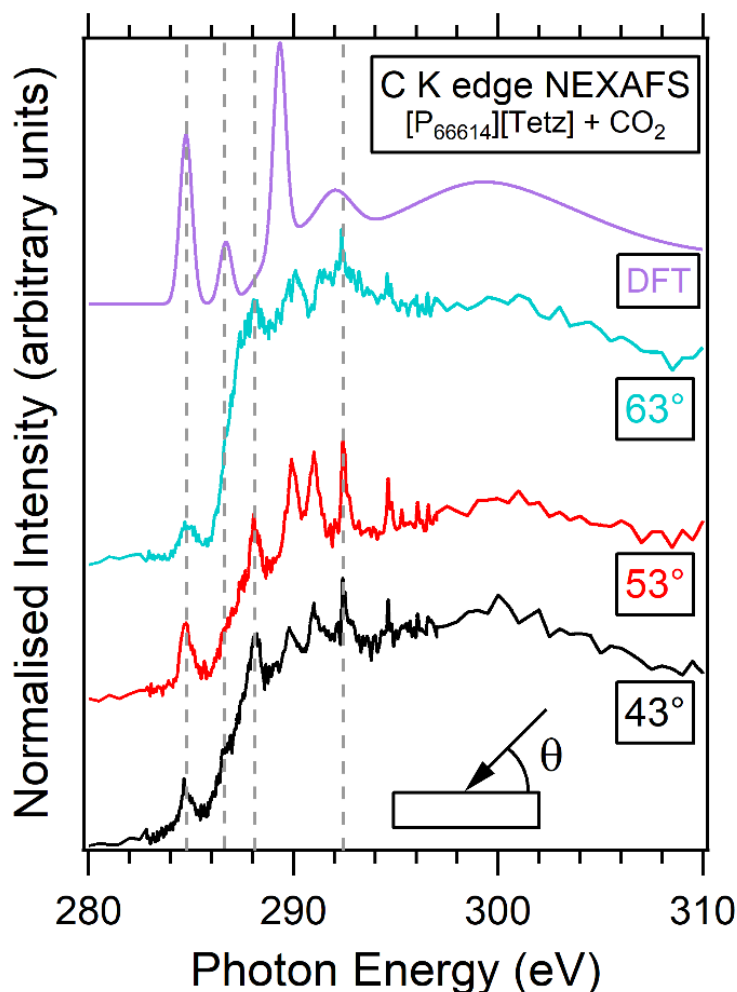
Figure 7.13. AEY C K edge NEXAFS of [P_{66614}][Tetz] + 3 mbar CO_2 taken at three X-ray angles of incidence (θ) from the surface. Vertical dashed lines highlight common peaks in the experimental spectra. These are compared to a theoretical NEXAFS spectrum labelled DFT.

Figure 7.13 shows C K edge NEXAFS spectra for IL + CO_2 at 3 mbar. The experimental spectra were corrected by dividing by the gas phase CO_2 signal, however, small discrepancies in the spectra introduced spikes into the σ^* region (shown in Appendix B) therefore we concentrate on features below ~ 290 eV where these are less prevalent. There are π^* peaks at 284.7, 286.5 (small shoulder feature) and 288.1 eV. The σ^* peak appears at 292.2 eV. Experimental spectra show good agreement with the peaks of the DFT spectrum. Comparing the IL as presented with

the IL + CO_2 C K edge NEXAFS spectra in Figures 7.9 and 7.13, respectively, there is a significant change in the DFT spectra but not in the experimental spectra. This could be because there is a convolution of reacted and unreacted anions contributing to the experimental spectra. There could also be a mixture of chemically and physically bound CO_2 and anions that are irreversibly bound to NO. The DFT spectrum has contributions from C^1 in the anion and C^2 in carbamate formed upon reaction with CO_2 (DFT spectra shown in Figure 7.14). From the DFT calculations we see that the π^* peak at 284.7 eV and small π^* shoulder at 286.5 eV in the experimental spectrum are due to excitations from C^1. C^2 contributes to higher energy π^* and σ^* resonances. The π^* peak at 288.1 eV does not closely match any of the peaks in the DFT spectrum. The π^* peak at 288.1 eV does not closely match any of the peaks in the DFT spectrum. This peak could be due to irreversibly bound NO which would explain why the DFT model does not account for this resonance. This agrees with the XPS C 1s spectra in Figure 7.6 (CO_2 pump out stage) where there is a peak at a similar BE of 288.3 eV assigned to C^1–NO. Using the LUMOs in Figure 7.10 the first two π^* peaks can be assigned as $C^1 \rightarrow$ in $1\pi^*$ (LUMO) and $C^1 \rightarrow 2\pi^*$ (LUMO+1). The main π^* peak is maximum for 53°, followed by 43°. Similar to the IL + NO stage, this indicates that the anion orients closer to the surface when exposed to CO_2 than it does pre-exposure. The [Tetz]$^-$ anion ring was calculated to orient at an angle of 64° ± 2° from the surface normal upon exposure to CO_2 (compared to 10° ± 3° pre-exposure). Results from Chapter 5 showed that [benzim]$^-$ anions orient 27° ± 5° from the surface normal, and then reorient to 54° ± 4° upon reaction with CO_2 [12]. It appears that, regardless of the anion or the gas, SBIL anions reorient closer to a rutile TiO_2 (110) surface upon exposure to CO_2 or NO. The reason for this is unclear but could be due to interactions between reacted anions and the TiO_2 substrate or the gas pressure above the IL 'pushing' the anions down towards the substrate surface.
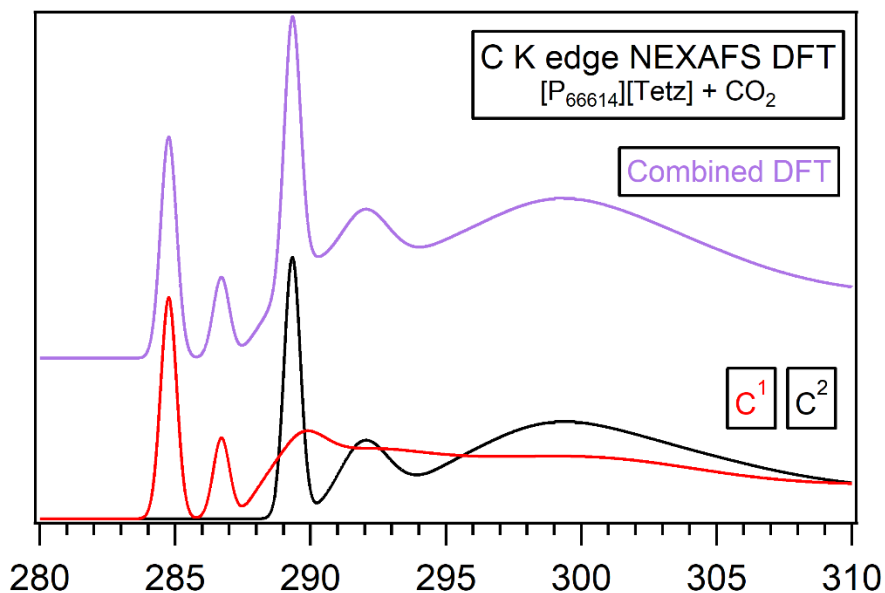
Figure 7.14. Simulated C K edge NEXAFS spectrum for the isolated [Tetz]$^-$ anion reacted with CO_2 to form carbamate. The spectra for C^1 in the anion and C^2 in carbamate are summed to give the final combined DFT spectrum.

Figure 7.15 shows C K edge NEXAFS of [P$_{66614}$][Tetz] exposed to a NO + CO$_2$ gas mixture at 3 mbar. The π^* peaks at 284.7 eV are very broad and have low intensity. This may be due to the attenuation of electrons through the gas mixture or measurements were possibly taken on a thinner part of the IL film. The C 1s and N 1s XPS spectra also showed unexpectedly small reaction peaks in the when the IL was exposed to NO + CO$_2$. The intensities of the π^* peaks are too small to fit to the Stöhr Equations to generate an angle. There appears to be a small increase in the intensity of the π^* peak with increasing θ. This would imply that the anion reorients to a more upright position when exposed to the gas mixture, however, this is tenuous given the low intensities in the spectra.
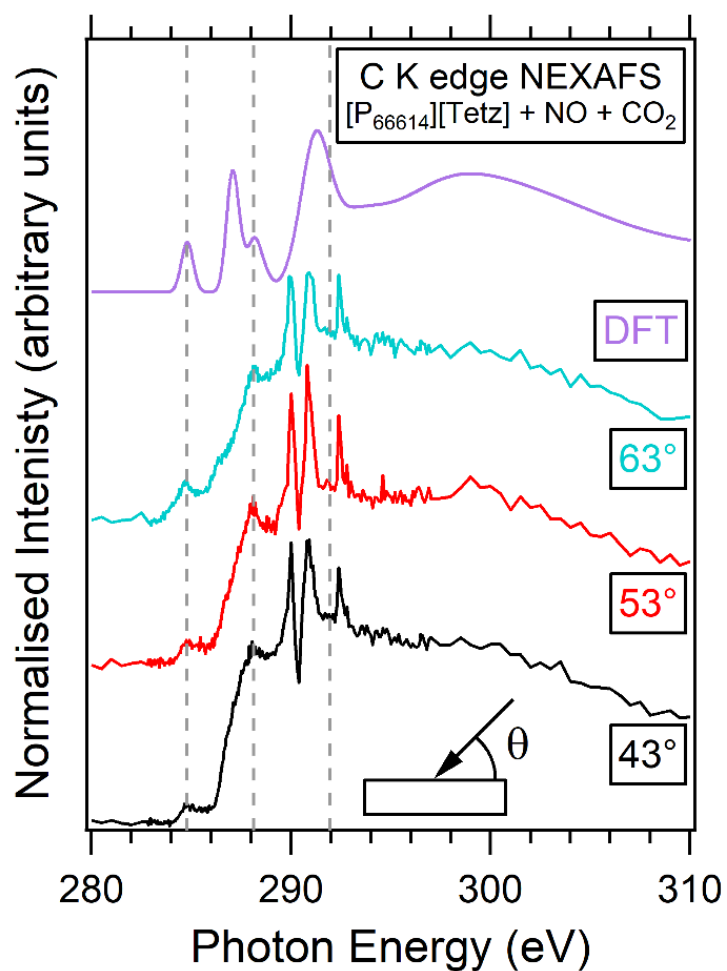
Figure 7.15. AEY C K edge NEXAFS of $[P_{66614}][Tetz]$ + 3 mbar of a NO + CO_2 mixture taken at three X-ray angles of incidence (θ) from the surface. Vertical dashed lines highlight common peaks in the experimental spectra. These are compared to a theoretical NEXAFS spectrum labelled DFT.

7.6 Discussion and Conclusions

Depth profiling NAP-XPS and angle-resolved NEXAFS were used to investigate the absorption of CO_2 and NO in thin films of the SBIL $[P_{66614}][Tetz]$. The $[P_{66614}][Tetz]$ thin film was deposited on a rutile TiO_2 (110) surface using electrospray deposition. The IL showed a reorientation of the [Tetz]⁻ anions when exposed to CO_2 or NO at 3 mbar. Angle-resolved C K edge NEXAFS revealed that the plane of the ring in the [Tetz]⁻ anion orients 10° ± 3° from the surface normal. The anions reorient to 37° ± 2° from the normal upon exposure to NO and to 64° ± 2° upon exposure to CO_2.

These results agree with those in Chapter 5 for [P_{66614}][benzim] and begin to reveal a common behaviour in the reordering of SBILs at surfaces upon exposure to gas.

The competitive absorption of CO_2 and NO was explored using depth profiling NAP-XPS. NAP-XPS measurements were taken at sampling depths of 1.3 and 4.0 nm, respectively. The absorption of NO in [P_{66614}][Tetz] involves a complex interplay of chemical and physical interactions. NO absorption is not fully reversible in the IL. CO_2 was found to only absorb at the surface of the IL due to the presence of irreversibly bound NO in the deeper layers. However, CO_2 absorption was found to be reversible. Interestingly, the NO + CO_2 gas mixture resulted in a lower uptake of gas by the IL. This complex IL/gas system appears to push the limit of the NAP-XPS technique due to the low signals measured from the electrosprayed film and the multiple chemical environments that appear at similar binding energies. Nevertheless, interesting aspects of the fundamental behaviour of the system have been revealed and this will inform the design of future IL-based technologies.

7.7 References

[1]   Greer A J, Taylor S F R, Daly H, Quesne M, Catlow C R A, Jacquemin J and Hardacre C 2019 Investigating the effect of NO on the capture of CO_2 using superbase ionic liquids for flue gas applications *ACS Sustain. Chem. Eng.* **7** 3567–74

[2]   Greer A J, Taylor S F R, Daly H, Quesne M, Catlow C R A, Jacquemin J and Hardacre C 2019 Investigating the Effect of NO on the Capture of CO_2 Using Superbase Ionic Liquids for Flue Gas Applications *ACS Sustain. Chem. Eng.* **7** 3567–74

[3]   Yan-Hong C, Yan-Fei C, Dong-Shun D, Ning A and Yong Z 2014 Difference for the absorption of SO_2 and CO_2 on [P_{nnnm}][Tetz] (n = 1, m = 2, and 4) ionic liquids: A density functional theory investigation *J. Mol. Liq.* **199** 7–14

[4]   Chen K, Shi G, Zhou X, Li H and Wang C 2016 Highly Efficient Nitric Oxide Capture by Azole-Based Ionic Liquids through Multiple-Site Absorption *Angew. Chemie - Int. Ed.* **55** 14364–8

[5]   Fairely N 2009 CasaXPS manual 2.3.15 *Casa Softw. Ltd* 1–177

[6]   Blundell R K and Licence P 2014 Quaternary ammonium and phosphonium based ionic liquids: A comparison of common anions *Phys. Chem. Chem. Phys.* **16** 15278–88

[7]   Hermann K, Pettersson L G M, Casida M E, Daul C, Goursot A, Koester A, Proynov E, St-Amant A, Salahub D R, Carravetta V, Duarte H, Friedrich C, Godbout N, Gruber M, Guan J, Jamorski C, Leboeuf M, Leetmaa M, Nyberg M, Patchkovskii S, Pedocchi L, Sim F, Triguero L and Vela A 2014 StoBe-deMon version 3.3

[8]   Neese F 2012 The ORCA program system *Wiley Interdiscip. Rev. Comput. Mol. Sci.* **2** 73–8

[9]   Neese F 2018 Software update: the ORCA program system, version 4.0 *Wiley Interdiscip. Rev. Comput. Mol. Sci.* **8** 4–9

[10]   Hanwell M D, Curtis D E, Lonie D C, Vandermeerschd T, Zurek E and Hutchison G R 2012 Avogadro: An advanced semantic chemical editor, visualization, and analysis platform *J. Cheminform.* **4** 17

[11]   Stöhr J 2003 *NEXAFS Spectroscopy* (Berlin: Springer)

[12]   Cole J, Henderson Z, Thomas A G, Compeán-González C L, Greer A J, Hardacre C, Venturini F, Garzon W Q, Ferrer P, Grinter D C, Held G and Syres K L 2021 Near-Ambient Pressure XPS and NEXAFS Study of a Superbasic Ionic Liquid with CO_2 *J. Phys. Chem. C* **125** 22778–85

[13]   Henderson Z, Thomas A G, Wagstaffe M, Taylor S F R, Hardacre C and Syres K L 2019 Reversible reaction of CO_2 with superbasic ionic liquid $[P_{66614}][benzim]$ studied with in situ photoelectron spectroscopy *J. Phys. Chem. C* **123** 7134–41

[14]   Abujarada S, Walton A S, Thomas A G, Chohan U K and Koehler S P K 2019 Adsorption site, orientation and alignment of NO adsorbed on Au(100) using 3D-velocity map imaging, X-ray photoelectron spectroscopy and density functional theory *Phys. Chem. Chem. Phys.* **21** 10939–46

[15]   Thomason M J, Seabourne C R, Sattelle B M, Hembury G A, Stevens J S, Scott A J, Aziz E F and Schroeder S L M 2015 Self-association of organic solutes in solution: A NEXAFS study of aqueous imidazole *Faraday Discuss.* **179** 269–89

Chapter 8. Conclusions and Further Work

The results presented in this thesis focus on CO_2 capture and interfacial interactions in thin films of superbasic ionic liquids using synchrotron-based techniques. This chapter discusses the conclusions drawn from results chapters 5 – 7 within the wider context of the field and provides possible avenues for continuing this work.

8.1 Conclusions of This Thesis

The aim of this work is to investigate CO_2 uptake in ionic liquids (ILs) using *in situ* synchrotron techniques and computational studies. Results give new fundamental insights into the uptake of gas, reversibility of chemical reactions and reordering of ions upon exposure to gas. We push the limits of these techniques to study the absorption of CO_2 in ultrathin films and discover how other gases compete with CO_2 at different depths in the film.

The results in Chapter 5 presented a combined *in situ* near-ambient pressure X-ray photoelectron spectroscopy (NAP-XPS) and near-edge X-ray absorption fine structure (NEXAFS) study on a multilayer thin film of trihexyltetradecylphosphonium benzimidazolide, $[P_{66614}][benzim]$, drop-cast onto rutile TiO_2 (110). This study probed the reordering of $[P_{66614}][benzim]$ upon exposure to CO_2 using NEXAFS and identified chemical reactions at the IL/gas interface using NAP-XPS. A greater concentration of CO_2-reacted anions were found in the deeper layers of the IL compared to the surface. Results also suggest that the reaction with CO_2 may not be fully reversible. NEXAFS results indicate that $[benzim]^-$ anions orient $27° \pm 4°$ from the surface normal before exposure to CO_2 and $54° \pm 4°$ from the surface normal when they react with CO_2. Theoretical NEXAFS spectra were calculated using DFT and compared to the experimental spectra, showing good agreement. DFT results were used in combination with visualised LUMOs in order to assign NEXAFS peaks to specific electronic transitions.

The study in Chapter 6 builds on the methods developed in Chapter 5 by introducing electrospray deposition, depth-profiling NAP-XPS and exposure to two gases

simultaneously. Thin films of the superbasic IL (SBIL) trihexyltetradecylphosphonium 1,2,4-triazolide, [P$_{66614}$][124Triz], were deposited onto rutile TiO$_2$ (110) using electrospray deposition. This allowed the film to be deposited in a clean UHV environment, rather than drop-cast at atmospheric pressure and resulted in films a few nanometres thick. Electrospray deposition of ILs is comparatively underutilised, and prior to the studies in this thesis has not been used to deposit large ILs such as [P$_{66614}$][124Triz]. Competitive gas absorption plays a crucial role in dictating the performance of the IL for gas capture. Therefore, the IL was exposed to CO$_2$ and H$_2$O to determine how the presence of H$_2$O affects the uptake of CO$_2$. Depth profiling NAP-XPS was used to determine how the gases react at the surface and in the deeper layers of the IL thin film. A greater concentration of CO$_2$ absorbs in the bulk layers of the [P$_{66614}$][124Triz] thin films. This is similar behaviour to that seen for [P$_{66614}$][benzim] in Chapter 5. For [P$_{66614}$][124Triz] the absorption of CO$_2$ in the deeper layers is reversible, while the fewer CO$_2$ reactions that occur at the surface do so irreversibly. The irreversible CO$_2$ absorption seen in [P$_{66614}$][benzim] therefore could be due to irreversible reactions at the IL surface. In [P$_{66614}$][124Triz], more H$_2$O was found to (reversibly) ad/absorb at the surface than in the bulk and does not inhibit CO$_2$ absorption.

The final study in Chapter 7 combines and builds on the previous chapters by using electrospray deposition and a combination of depth-profiling NAP-XPS and NEXAFS to study a more complicated SBIL/gas system. *In situ* depth profiling NAP-XPS and NEXAFS measurements of the SBIL trihexyltetradecylphosphonium tetrazole, [P$_{66614}$][Tetz], were taken upon exposure to CO$_2$, NO, and a CO$_2$ + NO mixture. A thin film of the IL was deposited on rutile TiO$_2$ (110) using electrospray deposition. A combined experimental and theoretical approach was carried out for NEXAFS analysis probing the reorientation of [Tetz]$^-$ anions upon exposure to the gases. The plane of the ring of the [Tetz]$^-$ anion orients 10° ± 3° from the surface normal before exposure to gas. This is similar to [P$_{66614}$][benzim] in Chapter 5 in which [benzim]$^-$ anions orient in a more "upright" position. The [Tetz]$^-$ anions reorient to 37° ± 2° from the normal upon exposure to NO and to 64° ± 2° upon exposure to CO$_2$. This corroborates with the behaviour of [P$_{66614}$][benzim] upon exposure to CO$_2$. Table 8.1 summarises the tilt angles of the anions in these two SBILs before and upon

exposure to gas. These results begin to reveal common behaviour in the reordering of SBILs at TiO_2 surfaces upon exposure to CO_2. In addition to the angular information, NEXAFS also highlights changes in chemical bonding upon reaction with gas. There is currently very little NEXAFS of ILs in literature, so this thesis contributes important information on how the spectroscopic fingerprint changes with structure and upon reaction with gas.

Ionic liquid	Anion tilt angle from surface normal (°)		
	As presented	CO_2	NO
$[P_{66614}][benzim]$	27 ± 5	54 ± 4	–
$[P_{66614}][Tetz]$	10 ± 3	64 ± 2	37 ± 2

Table 8.1. The orientation of the plane of the ring of $[benzim]^-$ and $[Tetz]^-$ anions in $[P_{66614}]^+$-based SBILs. Orientations are measured with respect to the rutile TiO_2 (110) surface normal and are given for the IL as presented, and when the IL is exposed to CO_2 and NO.

The competitive absorption of CO_2 and NO in $[P_{66614}][Tetz]$ was explored using depth profiling NAP-XPS in a similar approach as that used in Chapter 6. $[P_{66614}][Tetz]$ irreversibly absorbs NO, which accumulates in the bulk layers of the thin film, while CO_2 only absorbs at the surface layers. However, this CO_2 ad/absorption at the surface is reversible. $[P_{66614}][Tetz]$ shows different CO_2 capture behaviour to $[P_{66614}][benzim]$ and $[P_{66614}][124Tiz]$. These showed greater concentrations of (reversible) CO_2 absorption in the bulk while fewer CO_2 reactions occur at the surface and are irreversible. The origin of the different behaviour in $[P_{66614}][Tetz]$ is likely because the IL was first exposed to NO which irreversibly reacts with $[Tetz]^-$ anions. The irreversibly bound NO resides in the deeper layers of the IL where CO_2 absorption usually occurs in these SBILs. This suggests that CO_2 is unable to displace NO from the SBIL at these pressures.

Understanding these interfacial interactions is important for furthering the development of ILs towards widescale use in gas capture applications and IL thin film-based technologies such as SCILL/SILP catalysis, IL lubricants and corrosion

inhibitors. The following section summarises the achievements of this work and the new physical insights it provides within the wider context of current research.

8.2 Context of This Work

The work in this thesis aims to understand the driving mechanisms and interactions of IL ions with the gas phase using fundamental experimental studies. We have shown that NAP-XPS, NEXAFS and computational simulations are a powerful combination for studying the IL/gas interface. This thesis shows that NAP-XPS can be used to identify chemical reactions at the interface, and we can determine whether reactions are reversible by pumping out the surrounding gas. NEXAFS and NAP-XPS allow us to observe reordering of the IL upon exposure to gases. In real world applications, gas capture solvents are exposed to a mixture of gases alongside CO_2. There is very little literature on the competitive absorption of gases in ILs at the fundamental level [1,2]. In this work, depth profiling NAP-XPS was used to study the uptake of gases at different depths into the IL. This provides information on how the presence of one gas affects the uptake and reversibility of another. Of particular interest was the irreversible absorption of NO in $[P_{66614}][Tetz]$ which inhibited CO_2 absorption in the deeper layers of the IL film. This is in contrast to CO_2 absorption in $[P_{66614}][124Triz]$ which was reversible in the deeper layers. This depth profiling method can tell us whether gases are able to mobilise into the bulk or if they remain adsorbed at the surface, as in the case of H_2O in $[P_{66614}][124Triz]$.

Prior to this study, competitive absorption of gases in ILs has almost exclusively been studied using bulk films. Thin films of ILs are known to have highly-structured layers of ions but it is unknown how this structure can affect the uptake of gases, or how gases affect this structure. Our use of thin films allows us to explore the effects of ordering and the TiO_2 substrate on the ad/absorption of gas. For example, our results show that CO_2 irreversibly ad/absorbs in thin films of the SBIL $[P_{66614}][benzim]$ while our group's previous studies of the same SBIL deposited as a thick film show reversible CO_2 absorption [3]. It is likely that the ordered nature of the thin film, or the stronger influence of the TiO_2 substrate, may cause the irreversible reaction with CO_2. In addition, thin films of ILs are being investigated for use in other technologies such as SCILL/SILP catalysis and lubrication, where gases are in contact with the IL

layer. A change in ordering and orientation of IL ions at these surfaces upon exposure to gas could affect the diffusion of gas across the interface, physical interactions with gases, and the availability of reaction sites for chemisorption.

Previous studies of the IL/gas interface have largely been directed towards conventional imidazolium-based ILs [4]. Emerging subclasses of ILs such as SBILs have shown greater performance for gas capture applications compared to conventional ILs and deserve equal amounts of scrutiny at the molecular level. To further our understanding of SBILs for gas capture more computational studies are required alongside cutting-edge experimental surface science studies.

8.3 Further Work

As discussed in Chapter 7, the order in which the IL is exposed to certain gases plays an important role in the observed behaviour. In future work the competitive absorption between gases could be studied by switching the order in which gases are introduced to the IL. The reversibility of these reactions can be further explored by regenerating the IL by heating to approximately 80 $^\circ$C (depending on the IL). This would make an interesting comparison to regenerating the IL by pumping out the gas as done in these studies.

An area of improvement in this work would be to use a more realistic model for the IL in our density functional theory (DFT) calculations. In the current model, the charge on the anion is localised to a specific atom, and not delocalised (i.e., the model does not account for resonance effects). Additionally, only isolated anions were modelled which of course does not take into account any interionic interactions (anion/anion and anion/cation interactions). A dedicated DFT or molecular dynamics study with these improvements in mind could be carried out to investigate the mechanisms behind the reordering of anions upon exposure to different gases and gas mixtures, as well as the reversibility of these reactions.

Scaling up this study to higher pressures or using more realistic gas compositions are the next natural progressions in investigating the applicability of SBILs for gas capture in industry and power plants. A number of studies have looked at CO_2 capture in ILs using realistic flue gas compositions and pressures [5,6]. XPS cannot

be used in these types of studies as the technique is currently limited to near-ambient pressures. However, upcoming upgrades to synchrotron facilities such as the Diamond-II project and upgrades to its B07 beamline show promise for increasing operational gas pressures [7].

These studies can be naturally evolved into a device- and applications-focussed approach. ILs are currently being studied for a vast number of applications across many fields of research. SCILL and SILP catalysts use thin films of ILs to modify the catalytic reactivity of solid catalyst [8]. Reactions are believed to take place near the IL/gas interface. NAP-XPS could be used to study a model IL catalysis system. Understanding how gases interact with IL thin films, and IL thin films with solid supports, in these devices could lead to more efficient designs. In recent years, ILs are being considered for lubricants in spacecraft due to their ultra-low vapour pressures. Regulations have been recently implemented that now prohibit the use of perfluorinated compounds. There is a drive to design hydrostatically stable halogen-free ILs with improved tribological performance for both terrestrial and space applications. These will need to be understood on a fundamental level, particularly how they behave when in contact with gases compared to vacuum.

8.4 References

[1]   Lapshin D N, Jorge M, Campbell E E B, Campbell E E B and Sarkisov L 2020 On competitive gas adsorption and absorption phenomena in thin films of ionic liquids *J. Mater. Chem. A* **8** 11781–99

[2]   Taylor S F R, McClung M, McReynolds C, Daly H, Greer A J, Jacquemin J and Hardacre C 2018 Understanding the Competitive Gas Absorption of CO_2 and SO_2 in Superbase Ionic Liquids *Ind. Eng. Chem. Res.* **57** 17033–42

[3]   Henderson Z, Thomas A G, Wagstaffe M, Taylor S F R, Hardacre C and Syres K L 2019 Reversible reaction of CO_2 with superbasic ionic liquid $[P_{66614}][benzim]$ studied with in situ photoelectron spectroscopy *J. Phys. Chem. C* **123** 7134–41

[4]   Cole J and Syres K L 2022 Ionic liquids on oxide surfaces *J. Phys. Condens. Matter* **34** 213002

[5]   Greer A J, Taylor S F R, Daly H, Quesne M, Catlow C R A, Jacquemin J and Hardacre C 2019 Investigating the Effect of NO on the Capture of CO_2 Using Superbase Ionic Liquids for Flue Gas Applications *ACS Sustain. Chem. Eng.* **7** 3567–74

[6]   Taylor S F R, McCrellis C, McStay C, Jacquemin J, Hardacre C, Mercy M, Bell R G and de Leeuw N H 2015 CO_2 Capture in Wet and Dry Superbase Ionic Liquids *J. Solution Chem.* **44** 511–27

[7]   Grinter D C, Venturini F, Ferrer P, van Spronsen M A, Arrigo R, Quevedo Garzon W, Roy K, Large A I, Kumar S and Held G 2022 The Versatile Soft X-Ray (VerSoX) Beamline at Diamond Light Source *Synchrotron Radiat. News* **35** 39–47

[8]   Steinrück H P and Wasserscheid P 2015 Ionic liquids in catalysis *Catal. Letters* **145** 380–97

Appendix A

Below is an example of an input file used in the software StoBe-deMon for simulating theoretical NEXAFS spectra. The example shown in a core level excited state calculation needed to generate an N K edge NEXAFS spectrum of the atom N^1 in the IL CO_2-reacted SBIL [P_{66614}][benzim].

The first section contains information on the geometry optimised cartesian coordinates of the molecule. The final columns represent atomic number or effective nuclear charge. Following are a number of keywords and parameters of the system required to generate NEXAFS spectra. Importantly atom N1 is given a fractional occupancy of 0.5, shown here (*). The final inputs are basis set information.

```
TITLE
Benzimidazolide  +  CO2  -  N  1s  NEXAFS  -  excited  N1  using
coordinates from Avogadro
CARTESIAN ANGSTROM
O1       -0.9697950000    -2.4300920000    0.0000000000    8.   32
O2       -1.8543200000    -4.4590660000    0.0000000000    8.   32
N1       -5.5729210000    -2.7107470000    0.0000000000    7.   32
N2       -3.3187400000    -2.7454050000    0.0000000000    5.   32
C1       -5.1315520000     0.9447930000    0.0000000000    6.   32
C2       -3.7176470000     0.9464080000    0.0000000000    6.   32
C3       -3.0026100000    -0.2673170000    0.0000000000    6.   32
C4       -3.7364870000    -1.4610730000    0.0000000000    6.   32
C5       -5.1023840000    -1.4509520000    0.0000000000    6.   32
C6       -5.8388380000    -0.2708810000    0.0000000000    6.   32
C7       -4.4588550000    -3.4852840000    0.0000000000    6.   32
C8       -2.0365730000    -3.2508790000    0.0000000000    6.   32
H9       -3.1812890000     1.8864170000    0.0000000000    1.   32
H10      -1.9242870000    -0.2508390000    0.0000000000    1.   32
H11      -6.9210370000    -0.2866680000    0.0000000000    1.   32
H12      -5.6718080000     1.8824940000    0.0000000000    1.   32
H13      -4.4857560000    -4.5678700000    0.0000000000    1.   32
END
RUNTYPE START NO-OPTIMIZE
SCFTYPE DIR
POTENTIAL NONLOCAL BE88 PD86
GRID FINE
MULTIPLICITY 1
CHARGE -1
MAXCYCLES 50
ECONVERGENCE 0.000001
DCONVERGENCE 0.000001
```

```
DMIXING MDENS 0.10
DIIS NEW 7
ORBITALCHOICE 5d
NOFSYMMETRY SCFOCC EXCITED
ALFA 41
BETA 40
SYMMETRY 1
ALFA 0 1 3 0.5 (*)
BETA 0 0
END
MULLIKEN ON
XRAY XAS
REMTHRESHOLD  1.D-6
END
FILE MOLEKEL
END
A-OXYGEN (5,2;5,2)
A-OXYGEN (5,2;5,2)
A-NITROGEN (5,2;5,2)
A-NITROGEN(+5) (4,4;4,4)
A-CARBON (5,2;5,2)
A-CARBON (5,2;5,2)
A-CARBON (5,2;5,2)
A-CARBON (5,2;5,2)
A-CARBON (5,2;5,2)
A-CARBON (5,2;5,2)
A-CARBON (5,2;5,2)
A-CARBON (5,2;5,2)
A-HYDROGEN (3,1;3,1)
A-HYDROGEN (3,1;3,1)
A-HYDROGEN (3,1;3,1)
A-HYDROGEN (3,1;3,1)
A-HYDROGEN (3,1;3,1)
O-OXYGEN (7111/411/1)
O-OXYGEN (7111/411/1)
O-NITROGEN iii_iglo
O-NITROGEN(+5) (211/211/1)
O-CARBON (7111/411/1)
O-CARBON (7111/411/1)
O-CARBON (7111/411/1)
O-CARBON (7111/411/1)
O-CARBON (7111/411/1)
O-CARBON (7111/411/1)
O-CARBON (7111/411/1)
O-CARBON (7111/411/1)
O-HYDROGEN (311/1)
O-HYDROGEN (311/1)
O-HYDROGEN (311/1)
O-HYDROGEN (311/1)
O-HYDROGEN (311/1)
P-NITROGEN(+5) (3:7)
X-DUMMY
X-DUMMY
X-FIRST
```

195

```
X-DUMMY
X-DUMMY
X-DUMMY
X-DUMMY
X-DUMMY
X-DUMMY
X-DUMMY
X-DUMMY
X-DUMMY
X-DUMMY
X-DUMMY
X-DUMMY
X-DUMMY
X-DUMMY
END
```

The above calculation outputs spectra that need to be Gaussian broadened using the input file below. The width represents a linear increase in FWHM between 400 and 415 eV, beyond which the FWHM remains constant over the range.

```
Title
Broadening function for Benzimidazolide + CO2 spectrum N1
range 390 430
points 3000
width 0.9 8.0 400 415
xray xas
print
total 1
end
```

Appendix B

The C K edge NEXAFS spectra in Chapter 7 were background corrected using the photon flux curve (I_0) as shown in Figure B.1.
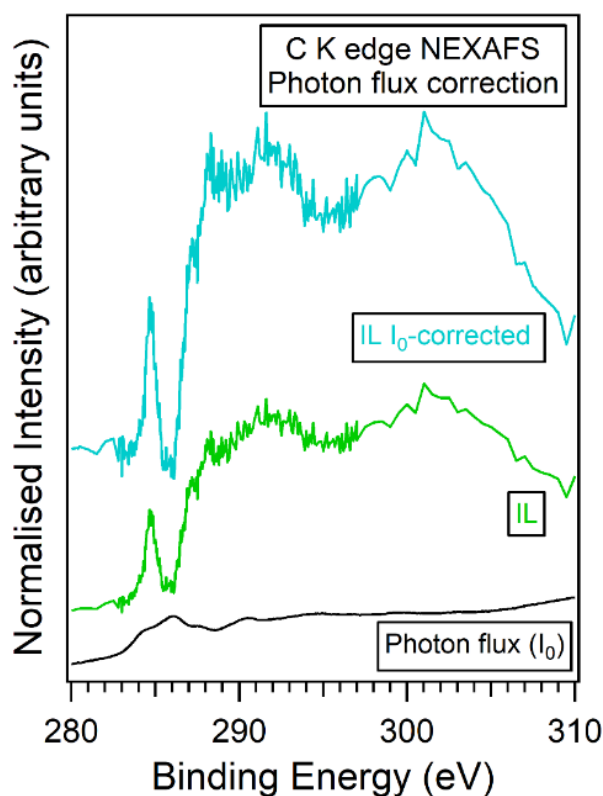
Figure B.1. Photon flux background correction for the IL [P_{66614}][Tetz].

Subsequent gas phase corrections are required to remove dips in the spectra when gas is introduced to the system. In the example in Figure B.1, [P_{66614}][Tetz] was exposed to 3 mbar CO_2. The IL signal was corrected for by division of the CO_2 signal. This removes the large dip at ~ 290 eV due to the absorption of photoelectrons by the gas. Mismatches in the data introduce unwanted spikes in the σ^* region.
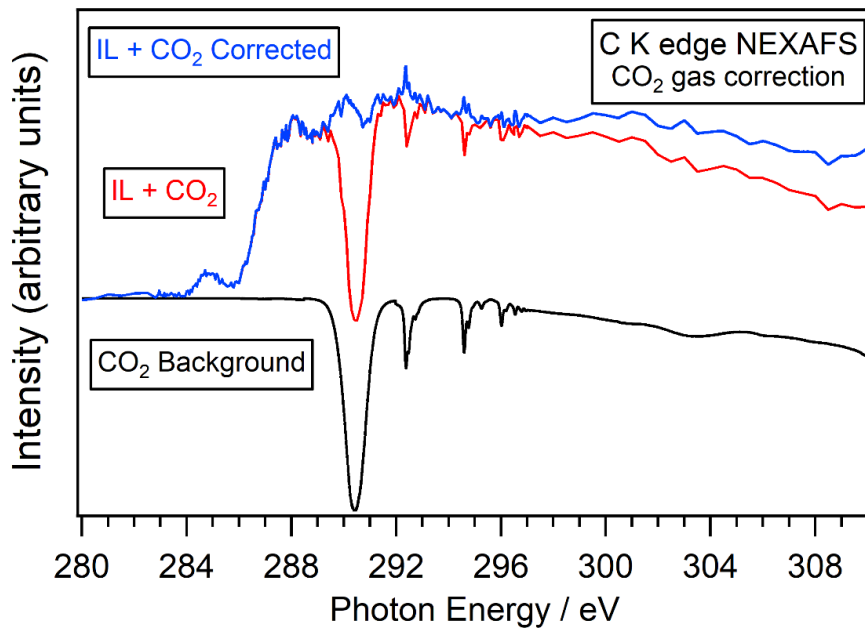
Figure B.2 CO_2 gas phase correction of [P$_{66614}$][Tetz].